Titre: Title:	Microwave Heating-Assisted Chemical Looping Ammonia Synthesis
Auteur: Author:	Kazem Adavi
Date:	2025
Type:	Mémoire ou thèse / Dissertation or Thesis
Référence: Citation:	Adavi, K. (2025). Microwave Heating-Assisted Chemical Looping Ammonia Synthesis [Thèse de doctorat, Polytechnique Montréal]. PolyPublie. https://publications.polymtl.ca/65721/

POLYTECHNIQUE MONTRÉAL

affiliée à l'Université de Montréal

Microwave heating-assisted chemical looping ammonia synthesis

KAZEM ADAVI

Département de génie chimique

Thèse présentée en vue de l'obtention du diplôme de *Philosophiae Doctor*

Génie chimique

Mai 2025

POLYTECHNIQUE MONTRÉAL

affiliée à l'Université de Montréal

Cette thèse intitulée :

Microwave heating-assisted chemical looping ammonia synthesis

présentée par **Kazem ADAVI**

en vue de l'obtention du diplôme de *Philosophiae Doctor*

a été dûment acceptée par le jury d'examen constitué de :

Jean-Philippe HARVEY, président

Gregory PATIENCE, membre et directeur de recherche

Jamal CHAOUKI, membre et codirecteur de recherche

Oumarou SAVADOGO, membre

Yaser KHOJASTEH, membre externe

DEDICATION

To my beloved parents, whose support and boundless love have been my greatest strength.

ACKNOWLEDGMENTS

I want to express my deepest gratitude to my PhD supervisor, Professor Jamal Chaouki, for his invaluable guidance and unwavering support throughout this research. His mentorship has been a beacon of light, illuminating my path and inspiring me to push the boundaries of my knowledge.

I am also profoundly grateful to Dr. Jaber Shabanian, Dr. Adrián Carrillo Garcia, and Dr. Mohammad Latifi for their insightful advice and companionship during this journey. Their contributions have enriched my research experience in countless ways. I am also thankful to all the members of the PEARL group for sharing their expertise and experiences, each discussion and collaboration has been a valuable learning opportunity.

Moreover, a special thanks to the OCP Group of Morocco for their financial support, which made this research possible.

Also, I am grateful to Mr. Santini Pace and Mario Godard for their exceptional technical assistance, which ensured the smooth progress of my experiments. Moreover, I would like to express my sincere gratitude to Mr. Gino Robin and Ms. Martine Lamarche for their support in procuring the necessary chemicals for this research. Their assistance was essential in ensuring the smooth progress of my work.

I sincerely appreciate Professor Gregory Scott Patience for presenting as my official research director. I also extend my gratitude to Professor Yaser Khojasteh, Professor Oumarou Savadogo, and Professor Jean-Philippe Harvey, members of the jury, for their time and effort in reviewing my work.

RÉSUMÉ

Remplacer les combustibles fossiles par des sources d'énergie renouvelables constitue une stratégie prometteuse pour lutter contre le réchauffement climatique. Toutefois, la nature intermittente des énergies renouvelables complique leur stockage et leur transport. L'hydrogène vert (H_2), produit à partir d'électricité renouvelable, représente une solution de stockage prometteuse. Cependant, sa forte inflammabilité et l'énergie nécessaire à sa liquéfaction ou à sa compression posent de sérieux défis. La conversion de l'hydrogène vert en ammoniac constitue une alternative plus sûre et plus pratique, réduisant jusqu'à trois fois les coûts de stockage et de transport, car l'ammoniac peut être liquéfié dans des conditions plus douces. Le procédé Haber-Bosch (HB) est largement utilisé pour la production d'ammoniac, mais il nécessite des conditions extrêmes (100–300 bar, 450–600°C) et n'est économiquement viable qu'à grande échelle (1000–5000 tonnes/jour).

Dans cette thèse, nous avons introduit la technologie de synthèse d'ammoniac par bouclage chimique assisté par chauffage micro-ondes (MHCLAS). En intégrant le chauffage micro-ondes (MW) à la synthèse d'ammoniac par bouclage chimique (CLAS), nous avons obtenu une production d'ammoniac à pression atmosphérique et à des températures de masse aussi basses que 150°C. La méthode CLAS divise la synthèse en deux étapes : la nitruration et l'hydrogénation. Lors de la nitruration, un porteur d'azote (NC) spécialement conçu est exposé à un flux de N_2, facilitant sa dissociation et la formation de nitrures. Ensuite, le NC nitruré réagit avec H_2 pour produire de l'ammoniac et régénérer le NC, complétant ainsi le cycle. Cette méthode évite l'adsorption compétitive de N_2 et H_2 sur les catalyseurs, une limite majeure du procédé HB. Pour réduire davantage la température de réaction, nous avons développé un nouveau NC et mis en œuvre un chauffage MW sélectif pour maximiser la production en maintenant une température gazeuse plus basse que celle du solide.

Dans le premier article, nous avons examiné la littérature sur la cinétique des réactions sous chauffage MW, en nous concentrant sur les écarts d'énergie d'activation, de modèles réactionnels et de facteurs préexponentiels par rapport au chauffage conventionnel. Certains chercheurs attribuent ces différences à des effets non thermiques, mais nous avons identifié des écarts dus aux points chauds, aux gradients thermiques gaz-solide et aux limites des thermocouples. Le deuxième article a approfondi ces effets par modélisation multiphysique à l'échelle microscopique. Nous

avons constaté que des vitesses de gaz plus élevées et des réactions exothermiques accentuaient les gradients thermiques, et que les thermocouples sous-estimaient les températures des solides. Les lits fixes de plus de ~3 cm de diamètre montraient également une non-uniformité accrue. Nous avons enfin montré que la profondeur de pénétration MW augmentait avec la porosité du lit, justifiant l'utilisation de lits fluidisés assistés par MW.

Dans le troisième article, nous avons sélectionné, synthétisé et optimisé des NCs pour maximiser la production d'ammoniac sous chauffage MW. Les NCs Mn-Fe et Mn-Fe-BaH_2, produits par des méthodes mécaniques ou de coprécipitation, ont facilité le transfert de l'azote entre 400–700°C (nitruration) et 150–350°C (hydrogénation), sous pression atmosphérique. Le chauffage MW a permis de maintenir de basses températures dans la phase gazeuse, réduisant la décomposition de l'ammoniac. Le NC Mn-Fe-BaH_2 a atteint un taux de production de ~36 000 µmol/g·h, surpassant les valeurs de la littérature.

Dans le quatrième article, nous avons réalisé une analyse cinétique détaillée en utilisant le NC Mn-Fe-BaH_2. Les réactions de nitruration et d'hydrogénation, menées dans un lit fluidisé chauffé par MW, ont montré de faibles énergies d'activation (27,3 kJ/mol et 25,5 kJ/mol). La nitruration suivait un modèle de contraction, tandis que l'hydrogénation était mieux décrite par le modèle d'Avrami-Erofeev.

Enfin, dans le cinquième article, nous avons simulé des réacteurs MHCLAS à l'échelle laboratoire et pilote avec COMSOL Multiphysics. À 565°C (nitruration) et 350°C (hydrogénation), environ 30 g d'ammoniac ont été produits par kg de NC. Cependant, la profondeur de pénétration des MW limitait l'agrandissement des réacteurs. Une évaluation technico-économique a été menée, proposant un design à guides d'ondes multiples pour augmenter le diamètre du réacteur de 15 à 50 cm, permettant d'utiliser jusqu'à 800 kg de NC et de produire environ 2 tonnes d'ammoniac/jour/réacteur.

ABSTRACT

Replacing fossil fuels with renewable energy helps combat global warming, but the intermittent nature of renewables makes their storage and transport challenging. Green hydrogen (H_2), produced via renewable electricity, is a promising energy storage solution. However, its high flammability and the energy required for liquefaction or compression pose significant challenges. Converting green H_2 into ammonia provides a safer, more practical alternative, reducing storage and transportation costs by up to three times since ammonia can be liquefied under milder conditions. The Haber-Bosch (HB) process is a widely used method for ammonia production. However, it requires extreme operating conditions (100–300 bar, 450–600°C) and is economically viable at large scales (1000–5000 tonnes/day).

In this thesis, we introduced microwave (MW) heating-assisted chemical looping ammonia synthesis (MHCLAS) technology. By integrating MW heating with chemical looping ammonia synthesis (CLAS), we achieved ammonia production at atmospheric pressure and bulk temperatures as low as 150°C during the ammonia synthesis stage. CLAS divides the ammonia synthesis process into two distinct stages: nitridation and hydrogenation. In the nitridation stage, a specially designed nitrogen carrier (NC) is exposed to a nitrogen gas (N_2) stream, facilitating nitrogen molecule dissociation and the formation of NC nitrides. Subsequently, in the hydrogenation stage, the nitrided NC reacts with H_2 gas, producing ammonia while regenerating the nitrogen-depleted NC, thus completing the cycle. This approach addresses the competitive adsorption of N_2 and H_2 on the catalyst surface, a major limitation of the HB process, by allowing the independent dissociation of N_2 and H_2. To further decrease the reaction temperature, which is crucial for preserving ammonia and preventing its decomposition, we developed a new NC. We implemented selective MW heating to maximize the ammonia production rate by lowering the gas phase temperature compared to the solid phase.

In the first article, we reviewed literature on reaction kinetics under MW irradiation, focusing on discrepancies in activation energy, reaction models, and pre-exponential factors compared to conventional heating. While some attribute these differences to nonthermal MW effects, others point to inaccurate temperature measurements. We found that hot spot formation, gas-solid temperature gradients, and thermocouple limitations often cause such discrepancies. For further investigation, in the second article, we used Multiphysics modeling to study MW heating effects

on gas-solid temperature gradients at the microscale. We found that higher gas velocity and exothermic reactions increased temperature differences between the gas and solid phases. Probe placement significantly affected measurements, revealing that thermocouples can underestimate solid-phase temperatures. We also confirmed that fixed beds larger than ~3 cm show greater non-uniformity due to hot spots. Finally, we found that MW penetration depth improves with higher void fractions, supporting the use of MW-assisted fluidized beds, leading to our next study on MHCLAS proof of concept.

In the third article, we focused on selecting, synthesizing, and optimizing NCs to enhance ammonia production under MW heating. We developed Mn-Fe and Mn-Fe-BaH_2 NCs via mechanical and coprecipitation methods. These NCs facilitated nitrogen transfer from a nitridation step (400–700°C) to a hydrogenation step (150–350°C), both at atmospheric pressure. MW heating enabled lower gas-phase temperatures, decreasing ammonia decomposition rate, and improving efficiency. The Mn-Fe-BaH_2 NC, especially, achieved a production rate of ~36,000 μmol/g·h, outperforming both literature values and Mn-Fe alone, while also acting as an effective MW absorber. This proof of concept led to our next study on MHCLAS kinetics.

In the fourth article, we performed a detailed kinetic analysis of the MHCLAS process, focusing on intrinsic reaction models for nitridation and hydrogenation using Mn-Fe-BaH_2 as the nitrogen carrier. Conducted in a MW-heated fluidized bed (300–630°C), the study confirmed nitridation through NC weight gain and nitride formation, while hydrogenation produced ammonia at atmospheric pressure and temperatures as low as 150°C. Selective MW heating and moderate N–NC bonding led to low activation energies (27.3 kJ/mol for nitridation, 25.5 kJ/mol for hydrogenation). The nitridation followed a contracting model, and the Avrami-Erofeev model best described hydrogenation.

In the fifth article, we applied the developed kinetic models to simulate MHCLAS reactors at lab and pilot scales using COMSOL Multiphysics. At optimal conditions (565°C nitridation, 350°C hydrogenation), about 30 g of ammonia was produced per kg of NC per cycle. However, MW penetration depth emerged as a scale-up limitation. In the final phase, we performed a techno-economic assessment and proposed a multi-waveguide design to expand reactor diameter from 15 to 50 cm, enabling up to 800 kg of NC and ~2 tons of ammonia/day per reactor.

TABLE OF CONTENTS

LIST OF TABLES

LIST OF FIGURES

LIST OF ACRONYMS

AH-CLAS	Alkali/Alkaline-earth-metal-hydride chemical looping ammonia synthesis
CH	Conventional heating
CLAS	Chemical looping ammonia synthesis
EM	Electromagnetic
EMW	Electromagnetic wave
FO	Fiber optic
HB	Haber-Bosch
IR	Infrared
ISE	Ion selective electrode
MHCLAS	Microwave heating-assisted chemical looping ammonia synthesis
MHFB	MW heating-assisted fluidized bed reactor
MPS	Mean particle size
MW	Microwave
NC	Nitrogen carrier
RXN	Reaction
SEM-EDS	Scanning electron microscopy with energy dispersive spectroscopy
TEM	Transverse electromagnetic
TGA	Thermogravimetric analysis
XRD	X-ray diffraction

LIST OF APPENDICES

CHAPTER 1 INTRODUCTION

1.1. Motivation

Progress in renewable energy harvesting technologies can decrease their implementation costs in the future. These advancements make renewable energy a practical and efficient alternative to fossil fuels for future energy demands [1,2]. However, despite these developments, the shift from fossil fuels to renewable sources is slow and insufficient to achieve the targets set by the Paris Agreement. This agreement calls for stricter regulations to cut carbon emissions, aiming for an 11% reduction between 2015 and 2050. Nevertheless, current trends indicate that global average temperatures increased by approximately 3°C, surpassing the agreement's goal of limiting the increase to 1.5°C [1,2].

Despite significant advancements in renewable energy technologies over the past decade, a key challenge remains that renewable energy transportation limits the global transition to renewables [3,4]. Although batteries offer partial solutions, they are not suitable for large-scale energy transportation from regions with abundant renewable energy [5]. In this case, liquid energy carriers are more suitable, as they can be efficiently transported by pipelines or shipping [5]. Examples include liquid H_2 [6], liquid organic H_2 carriers [7], carbon dioxide (CO_2) based chemicals [8], and ammonia (NH_3) [9]. Each of these energy carriers has its advantages and disadvantages. For instance, liquefying hydrogen is highly energy-demanding [6], CO_2-based chemical products such as methanol synthesis, are sensitive to impurities in the CO_2 stream [5,8].

Among these options, NH_3 is a promising renewable energy carrier [5,9–11]. It contains more hydrogen than methanol [9,12], and it is carbon-free [13]. In addition, ammonia storage and transportation costs are three times less than those of liquid hydrogen [13]. In addition, ammonia can be liquefied at ambient temperature with a pressure of about 10 bar (or at -30°C under atmospheric pressure). Moreover, despite the liquid hydrogen, ammonia transportation and storage infrastructures are well established [5].

NH_3 is the second largest produced chemical in the world and its annual production is between 170 and 300 million tonnes [9]. In 2023, global ammonia production was 240 million tonnes per year, and this is estimated to increase to around 300 million tonnes by 2030. Other applications of ammonia are the fertilizers production industry, refrigerants, pharmaceuticals production, and the

textiles industry. The fertilizer production sector is the largest consumer of produced ammonia, i.e., more than 85%, which provides food for nearly half of the world's population [9,14].

The well-established Haber-Bosch (HB) process for ammonia production operates under extreme conditions, such as pressures of up to 300 bar and temperatures ranging from 400°C to 600°C. These operating conditions make it economically feasible only for large-scale production, typically between 1000 and 5000 tonnes per day [15]. However, for renewable energy/green hydrogen storage and decentralized ammonia production, a production rate of just 5 to 100 tonnes per day is required. This caused an increasing demand for ammonia production technologies that can operate under milder conditions. Some promising alternatives include plasma-assisted ammonia synthesis [16,17], microwave (MW)-assisted catalytic synthesis [18,19], electrocatalysis, photocatalysis, and conventionally heated chemical looping ammonia synthesis [20]. Currently, these technologies are still in their early stages of development and showed low ammonia production rate and/or low energy efficiency compared to the HB process.

In this study, we developed a microwave heating-assisted chemical looping ammonia synthesis (MHCLAS) technology. This innovative process operates under atmospheric pressure and at temperatures as low as 150°C. The process consists of two distinct stages: nitridation and hydrogenation.

In the nitridation stage, a specially designed nitrogen carrier (NC) is exposed to a nitrogen (N_2) stream under MW irradiation, resulting in the formation of a nitrided NC. In the subsequent hydrogenation stage, the fixed nitrogen atoms within the NC structure, i.e., NC nitrides, are exposed to a H_2 stream, producing ammonia and regenerating nitrogen-depleted NCs.

This separation of nitrogen and hydrogen activation stages addresses the thermodynamic limitations associated with conventional catalytic ammonia synthesis. In the HB process, breaking the strong nitrogen-nitrogen bonds in N_2 gas requires high temperatures, which can also promote ammonia decomposition. To counter this, the HB process operates at pressures of around 200 bar.

Our approach overcomes these challenges through two key innovations:

1. Chemical looping ammonia synthesis (CLAS) eliminates the need for simultaneous nitrogen and hydrogen activation, avoiding the thermodynamic constraints.

2. MW heating selectively heats the solid phase, keeping the gas phase at a lower temperature. This targeted heating suppresses ammonia decomposition during the hydrogenation stage.

By combining these strategies, MHCLAS offers a promising alternative to traditional ammonia synthesis methods, addressing the challenges of high temperature and pressure while enhancing process efficiency.

1.2. Objectives

The general objective of this project is to develop the MHCLAS technology. To achieve this, we identified four key sub-objectives:

1. **To assess temperature distribution in gas-solid reactive and non-reactive systems under MW irradiation**

   In this sub-objective we focused on optimizing the temperature difference between gas and solid phases during MW irradiation. By maintaining a lower gas-phase temperature, secondary gas phase reactions such as ammonia decomposition can be suppressed, and energy consumption can be decreased. In addition, we investigated the impact of reaction exothermicity and endothermicity on the system's temperature distribution under MW heating.

2. **To develop a NC and MW absorber for ammonia production using MHCLAS**

   In this sub-objective, we selected and optimized NCs to maximize the ammonia production rate and enhance interaction with MWs. This stage also involved establishing the proof of concept for the MHCLAS technology.

3. **To evaluate the kinetics of nitridation and hydrogenation stages in MHCLAS**
   To advance the development of MHCLAS, we studied the reaction kinetics of the nitridation and hydrogenation stages. By eliminating/minimizing external and internal mass transfer limitations, we determined nearly intrinsic kinetic parameters, which are independent of reactor type and hydrodynamic conditions. These kinetic insights provide a solid foundation for subsequent reactor modeling and process scale-up.

4. **To model and simulate MW-heated reactors for MHCLAS technology**
   Based on the findings from previous sub-objectives, we developed a pilot-scale reactor

model to scale-up the MHCLAS technology. This final step aims to facilitate the transition from laboratory-scale development to industrial-scale implementation.

CHAPTER 2 LITERATURE REVIEW

2.1. Conventional ammonia synthesis process (HB process)

In 1908, Fritz Haber introduced a method for synthesizing ammonia by reacting H_2 and N_2 under high pressure and elevated temperatures. Later, Carl Bosch adapted and scaled this method for industrial application, leading to the construction of the first industrial ammonia production plant in 1911. This process, widely known as the Haber-Bosch (HB) process, involves the reaction of N_2 and H_2 in a 1:3 molar ratio over an iron-based catalyst, as shown in Eq. (2. 1). Since the reaction is exothermic, lower temperatures and higher pressures are optimal thermodynamically for maximizing ammonia production [21].

$$3H_2 + N_2 \leftrightarrow 2NH_3 \qquad \Delta H = -92.4\ KJ/mol \qquad (2.\ 1)$$

Figure 2. 1 illustrates the flow diagram of the HB process, which has several critical steps. The required H_2 for ammonia synthesis is generated through steam methane reforming, while secondary reformers, shift reactors, methanation reactors, and CO_2 adsorbers ensure the purification of H_2 [21]

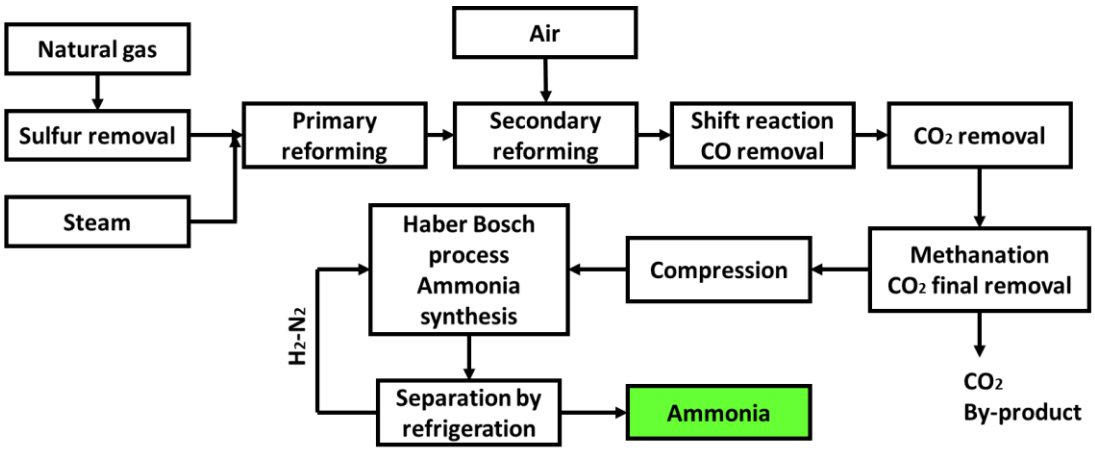

Figure 2. 1: HB process flow diagram [22]**.**

The HB process operates under demanding conditions, with temperatures ranging from 400 to 600°C and pressures between 100 and 300 bar, to activate N_2 and drive the reaction toward ammonia production. Iron-based catalysts, promoted with rhodium, play a vital role in facilitating N_2 dissociation and ammonia formation [23]. Despite the implementation of extreme operating

conditions and catalysts, the maximum ammonia yield remains limited to approximately 25±5%. To address this limitation, recycling unreacted H_2 and N_2 back into the ammonia synthesis reactor is essential. In addition, competitive adsorption of H_2 and N_2 on the catalyst's active sites can lead to hydrogen poisoning, which complicates process optimization and hinders achieving higher ammonia production rates [23].

The HB process is essential for ammonia production for various applications, but it comes with significant environmental and resource costs. It consumes approximately 5% of the global natural gas supply and 2% of global energy (30-50 GJ per ton of ammonia). In addition, the process is responsible for 1% of global CO_2 emissions, releasing about 2.3 tonnes of CO_2 per ton of ammonia [23]. Approximately 70% of the H_2 required for ammonia synthesis is derived from natural gas steam reforming, while coal (22%), fuel oil (4%), naphtha reforming (1%), and gasification account for the remaining supply [23]. Moreover, due to its harsh operating conditions and the need for high-purity feedstock to prevent catalyst deactivation [24,25], the HB process is economically viable only on a large scale, typically with production rates ranging from 1000 to 5000 tonnes of ammonia per day. However, green ammonia plants, designed to store intermittent renewable energy, typically operate at smaller scales, producing around 5-100 tonnes of ammonia per day. This makes the HB process unsuitable for green H_2 storage applications powered by renewable energy [22,23,26].

2.2. MW heating-assisted catalytic ammonia synthesis

MW heating-assisted catalytic ammonia synthesis is a method reported in literature as an alternative approach to conventional ammonia production. While it is similar in principle to the traditional HB process. However, this method utilizes MW heating instead of conventional heating. In conventional heating, the gas and solid phases typically reach the same temperature. In contrast, MW heating is selective, resulting in a higher solid-phase temperature compared to the gas phase. This temperature gradient suppresses ammonia decomposition, enabling the reaction to proceed under more moderate conditions than the HB process [18,19,27–30].

Different catalysts, such as $CsRu/CeO_2$ [27] and Ru/MgO [19], have been synthesized for MW-assisted catalytic ammonia synthesis. These reactions typically operate at lower bulk temperatures (ranging from 280°C to 400°C) compared to conventionally heated catalytic ammonia synthesis

due to the selective heating effects of MW. However, since the reaction follows the same fundamental principles as the HB process, it still requires operating pressures between up to 0.65 MPa. The reduced pressure observed in this study is attributed to the lower operational temperature achieved during the reaction, which reflects the bulk temperature, a combination of gas-phase and solid-phase temperatures [18,19,27–30]. Implementing MW heating for exothermic reactions, e.g., ammonia synthesis reaction, can help achieve the temperature needed to overcome the activation energy barrier and compensate for energy losses from hot solid particles to the cooler gas phase.

Although MW-assisted catalytic ammonia synthesis showed a higher ammonia production rate compared to the conventional HB process, certain challenges persist. Key concerns include the competitive adsorption of N_2 and H_2 and hydrogen poisoning of the catalyst surface, which can limit the efficiency and scalability of this technology.

2.3. Electrocatalysis, photocatalysis, and plasma-assisted ammonia synthesis

Electrocatalytic ammonia synthesis (EAS) is an environmentally friendly technology with low energy requirements. Unlike the HB process, EAS operates under atmospheric pressure and applies water (H_2O) as the H_2 source instead of fossil fuels [31]. In addition, renewable energy sources such as wind, solar, and hydropower can provide the necessary electricity for the process [31]. In recent years, significant research efforts have focused on enhancing the conversion efficiency and selectivity of the EAS reaction. However, despite these advancements, EAS still requires further development to compete with the industrial-scale HB process [32–34]. For even the most active catalysts, the ammonia production rate is approximately 10^{-7} mol. s^{-1}. g^{-1} [35], which is an order of magnitude lower than the rate achieved by the HB process 5×10^{-6} mol. s^{-1}. g^{-1}) [32]. The low selectivity of ammonia formation in EAS is primarily due to the H_2 evolution reaction (HER), which competes with the nitrogen reduction reaction (NRR) and is thermodynamically more favorable [32,36]. Due to the low NH_3 production rate in EAS, a large electrode surface area and a significant amount of catalyst are required to achieve meaningful outputs [32,37]. In addition, ammonia quantification is typically performed using indirect methods. These approaches involve collecting the absorption or electrolyte solution after a set period (e.g., one hour) and analyzing it with various measurement techniques. However, for more detailed

insights into reaction kinetics, the development of online detection methods for real-time ammonia monitoring is essential [32].

Harnessing abundant solar energy for nitrogen fixation is highly desirable but technically challenging. The photochemical NRR applies solar energy to drive this process [38,39]. This method uses light to generate photoexcited charges, which produce electron-hole pairs that transfer to active sites on the catalyst surface. The excited electrons then react with nitrogen to synthesize ammonia, with protons sourced from water. However, similar to the challenges faced by EAS, competition between the NRR and the HER complicates nitrogen activation [38,39]. Photocatalytic ammonia synthesis has a significantly lower production rate compared to the HB process and EAS, at approximately 10^{-9} mol. s^{-1}. g^{-1} [38,39]

Plasma processes, one of Earth's oldest natural phenomena (e.g., lightning), occur when gas is ionized by sufficient energy, such as heat [40,41]. Plasma can also be generated artificially by passing an electrical current through gases [40,41]. Among the most extensively studied applications of plasma-assisted reactors is the direct synthesis of ammonia from N_2 and H_2 [40,41]. However, due to its high energy consumption, plasma-assisted ammonia synthesis is not a viable replacement for the HB process. Thermochemical methods for ammonia synthesis are significantly more energy-efficient than plasma-based approaches, making them more practical options for green ammonia production using intermittent renewable energy in the future [42]. Furthermore, since the synthesis of ammonia from N_2 and H_2 is an exothermic reaction, utilizing thermal plasma for molecular activation is energetically unfavorable [42].

2.4. Chemical looping ammonia synthesis

Chemical looping technology has been extensively studied in the literature, primarily for applications such as fossil fuel conversion processes, including combustion, gasification, and reforming [43–47]. In recent years, there has been growing interest in applying chemical looping to ammonia synthesis [44–48]. This innovative approach breaks down the ammonia synthesis reaction ($N_2 + 3H_2 \rightarrow 2NH_3$) into two or three independent sub-reactions, enabling separate control of the nitrogen activation and ammonia formation stages [48–52]. By decoupling these steps, chemical looping ammonia synthesis (CLAS) overcomes key challenges associated with traditional catalytic methods, such as the competitive adsorption of reactants on the catalyst

surface, which often limits production rates. In addition, this approach avoids the thermodynamic constraints of ammonia synthesis and significantly decreases the required operating pressure, allowing ammonia production at atmospheric pressure in most cases. The literature identifies four main types of CLAS processes, as presented in Figure 2. 2: (i) water chemical looping ammonia synthesis (H_2O-CLAS), (ii) electrolysis chemical looping ammonia synthesis (H_2O-CELAS), (iii) hydrogen chemical looping ammonia synthesis (H_2-CLAS), and (iv) Alkali/Alkaline-Earth-Metal-Hydride Chemical Looping ammonia synthesis (AH-CLAS) [48].

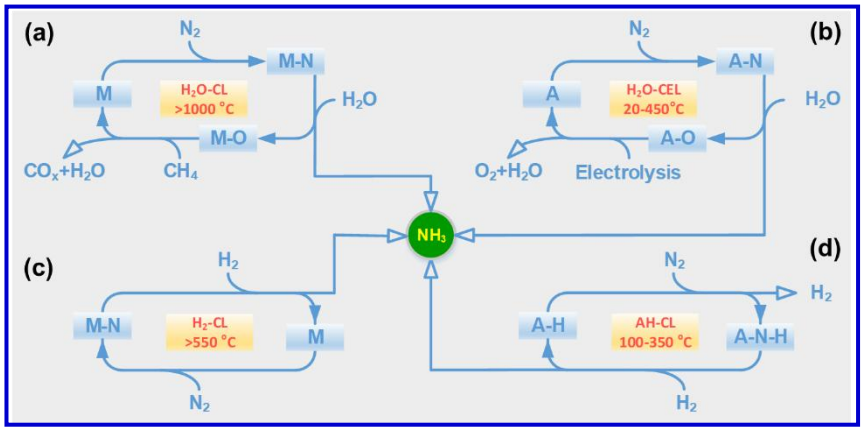

Figure 2. 2: Types of CLAS technology: (a) H_2O-CLAS, (b) H_2O-CELAS, (c) H_2-CL, and (d) AH- CLAS [48,53].

2.4.1. H_2O-CLAS and H_2O-CELAS

The H_2O-CLAS method typically involves a sequence of nitridation, oxidation, and metal hydrolysis within a chemical looping system. During this process, a metal undergoes nitridation in a N_2 atmosphere, forming a metal nitride (MeN_y). Subsequently, steam reacts with the metal nitride, hydrolyzing it to produce NH_3 and a metal oxide (MeO_x). The cycle concludes with the reduction of the metal oxide back into its metallic form (Me), enabling the loop to restart [48].

In some cases, the nitridation and reduction of MeO_x can be combined into a single step, reducing the process to just two stages. For example, the AlN/Al_2O_3 pair has been utilized for CLAS. In the first stage, Al_2O_3 reacts with active carbon (C) and N_2 gas, forming aluminum nitride (AlN) and carbon monoxide (CO). During the second stage, hydrolysis, AlN reacts with steam to produce ammonia (NH_3) and regenerate Al_2O_3, completing the cycle [54,55]. Although directly introducing H_2O into the system to supply hydrogen for ammonia production appears advantageous, the high

temperatures required for NC reduction, i.e., T> 1000°C, pose significant challenges due to the strong stability of the Me-O bond. These include elevated energy consumption and an increased risk of NC sintering, making the process less efficient [54,55].

Different single metals, such as chromium (Cr), calcium (Ca), molybdenum (Mo), zinc (Zn), magnesium (Mg), and manganese (Mn), have been employed in CLAS [3,56,57]. Their selection is largely based on their thermodynamic suitability for the different stages of the CLAS process, including nitridation, hydrolysis, and reduction. In addition, researchers considered some factors in practical considerations such as melting point, toxicity, and cost to identify the most suitable metals for the process [3].

The selection of a reducing agent for the reduction stage is crucial. Based on the thermodynamic properties of the NCs, C, methane (CH_4), and H_2 are commonly applied to reduce metal oxides or hydroxides effectively. However, the use of carbon-based reducing agents has a significant drawback: it leads to the emission of greenhouse gases, posing environmental concerns [58].

The reaction temperatures for various stages of the H_2O-CLAS process typically range between 200°C and 1000°C. However, studies have shown that utilizing bimetallic NCs can reduce the required reaction temperatures. For instance, Michalsky et al. [56] investigated Mn and Mo as NCs in a solar-driven H_2O-CLAS process for ammonia production. Figure 2. 3 illustrates the thermodynamic equilibrium for nitridation, hydrogenation, and oxidation of Mn and Mo in the H_2O-CLAS system at atmospheric pressure. The shaded regions in the figure represent exothermic reactions, indicating thermodynamically favorable conditions for product formation within the colored area [58]. To enhance nitrogen fixation at temperatures above 700°C, the metal nitride must exhibit greater stability than Mo_2N. Simultaneously, to avoid extremely high reaction temperatures, such as 1200°C, the metal oxide should be less stable than MnO [58]. Consequently, a Mn-Mo composite emerges as a promising candidate for use as a NC in ammonia production [58].

The H_2O-CELAS process operates on a principle similar to H_2O-CLAS, but with a key difference in the reduction stage. Instead of a traditional reduction method, electrolysis is used to reduce the oxide or hydroxide phase of NC. Lithium (Li) has been employed as a key element in the H_2O-CELAS approach [59]. Lien et al. [59] utilized Li in a three-stage H_2O-CELAS. The stages include:

(i) electrolysis of lithium hydroxide (LiOH), (ii) nitridation of Li, and (iii) ammonia synthesis from lithium nitride (Li_3N), and regeneration of LiOH to complete the cycle [55].

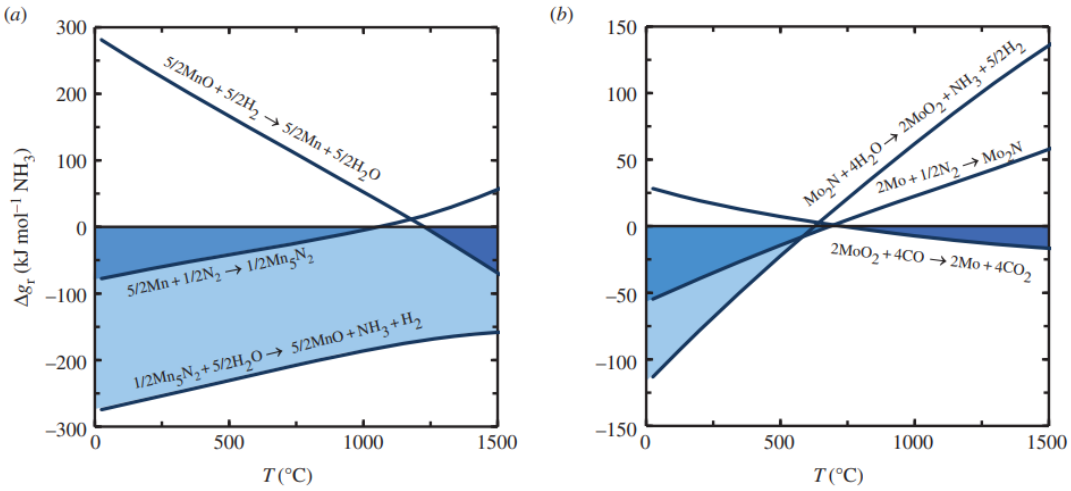

Figure 2. 3: Ammonia synthesis thermodynamic calculations by CLAS based on (a) Mn-nitride and (b) Mo-nitride [58]**.**

While many studies have focused on the selection of NCs, others have explored the impact of various promoters on enhancing NC performance. Developing NCs with minimal activity for ammonia decomposition is critical to improving ammonia production selectivity. For instance, Wu et al. [60] demonstrated that mixing zirconium dioxide (ZrO_2) with AlN effectively inhibits ammonia decomposition, thereby increasing the ammonia production rate.

2.4.2. H_2-CLAS and AH-CLAS

In H_2-CLAS and AH-CLAS systems, the process involves two sequential steps instead of the three steps observed in H_2O-CLAS and H_2O-CELAS (refer to Figure 2. 4). During the first step, the prepared NCs are subjected to an N_2 stream, leading to the incorporation of nitrogen atoms into the lattice structure of the NCs. In the second step, the nitrided NCs are exposed to H_2, resulting in ammonia production and completing the cycle. Notably, the reduction of oxides or hydroxides is absent in these systems, which lowers the reaction temperature to approximately 700°C, compared to the higher temperatures of up to 1200°C required for H_2O-CLAS [48,61].

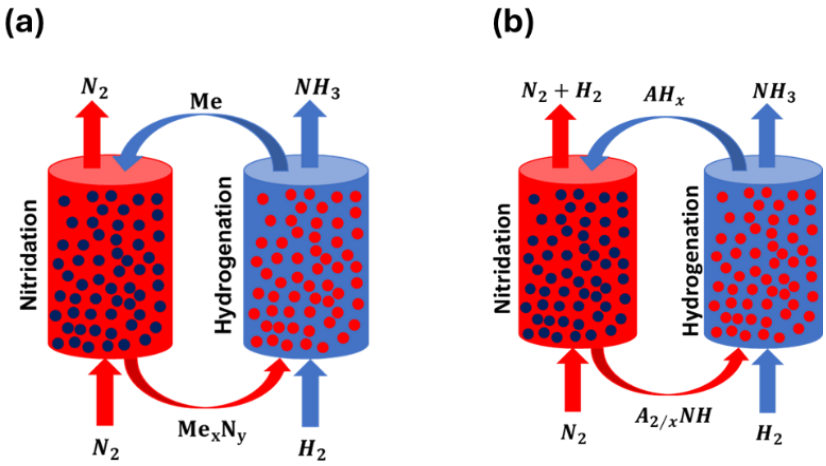

Figure 2. 4:The schematic diagram of (a) H_2-CLAS, (b) AH-CLAS ammonia synthesis [62].

The key distinction between H_2-CLAS (Figure 2. 4a) and AH-CLAS (Figure 2. 4b) lies in the type of applied NCs. H_2-CLAS implements a variety of NCs, including single-metal, bimetallic, and multimetallic, which are based on transition metals [48,63]. Conversely, AH-CLAS employs metal hydrides as NC in both nitridation and hydrogenation reactions [48].

Various metal nitrides, such as Ca_3N_2, Sr_2N, Mo_2N, and Mn_xN_y, are reported for use in H_2-CLAS [48,63]. Nitridation and hydrogenation of these compounds typically occur at temperatures exceeding 500°C. While this is significantly lower than the temperature needed for H_2O-CLAS, the hydrogenation stage at temperatures above 350°C poses a risk of ammonia decomposition. Elevated temperatures are associated with the energy demands for nitrogen activation and the reduction of thermodynamically stable metal nitrides. For example, Mohammadi et al. [64] demonstrated that Mn activated nitrogen at atmospheric pressure and approximately 700°C, forming Mn-nitride. In the subsequent step, exposing the Mn-nitride to a H_2 stream produced ammonia at around 500°C [64].

Hua et al. [65] proposed a novel approach for ammonia synthesis using a Fe-based NC. Their study evaluated the thermodynamic feasibility of Fe as NC for ammonia production. They identified optimal conditions for the nitridation stage as temperatures between 200–500°C, pressures of 5–20 bar, and a molar ratio of Fe to N_2 of 8:1. For the hydrogenation stage, the best operating conditions were reported to be temperatures of 200–400°C, pressures below 5 bar, and a NC to H_2 molar ratio of 2:3 [65]. Typically, high temperatures are required for N_2 activation, while lower temperatures suffice for the hydrogenation step [65]. Fe exhibits weaker interactions with nitrogen

compared to early transition metals such as Mn, necessitating pressures above atmospheric levels when Fe is used as a single-metal NC. According to the Sabatier principle, ideal metal nitrides for CLAS should exhibit moderate bond strength with nitrogen atoms. Early transition metals, such as Mn, form nitrides that are thermally stable, making ammonia production through hydrogenation of these nitrides challenging. Conversely, late transition metals achieve high ammonia yields at temperatures between 200–400°C, although N_2 activation at atmospheric pressure on these materials remains difficult due to their low nitrogen adsorption energy [66]. For instance, Mn demonstrates a strong capacity for nitrogen activation at ambient pressure by forming and transitioning between various nitride phases. However, Fe-based NCs perform more effectively in reactions with H_2 to produce ammonia. As a result, combining Mn and Fe nitrides emerges as a logical strategy to meet the Sabatier principle [66]. Table 2. 1 provides details on the nitridation and hydrogenation reactions of Mn-based and Fe-based NCs. Another study highlighted that the hydrogenation temperature of Mn-nitride ($Mn_6N_{2.58}$) decreased from 550°C to 400°C with the introduction of Li. This demonstrates that Li can influence the metal-nitrogen bond energy, thereby enhancing the hydrogenation process of metal nitrides [53].

Table 2. 1:Fe, Mn-based NCs nitridation and hydrogenations reactions [65]**.**

Nitridation	Hydrogenation
$8Fe + N_{2(g)} = 2Fe_4N$	$2Fe_4N + 3H_{2(g)} = 2NH_{3(g)} + 8Fe$
$4Fe + N_{2(g)} = 2Fe_2N$	$2Fe_2N + 3H_{2(g)} = 2NH_{3(g)} + 8Fe$
$2Fe_4N + N_{2(g)} = 4Fe_2N$	$4Fe_2N + 3H_{2(g)} = 2NH_{3(g)} + 2Fe_4N$
$8Mn + N_{2(g)} = 2Mn_4N$	$5/6Mn_3N_2 + H_{2(g)} = 1/2Mn5N2 + 2/3NH_{3(g)}$
$10/3Mn_4N + N_{2(g)} = 8/3Mn_5N_2$	$8/9Mn_5N_2 + H_{2(g)} = 10/9Mn_4N + 2/3NH_{3(g)}$
$3/2Mn_5N_2 + N_{2(g)} = 5/2Mn_3N_2$	$2/3Mn_4N + H_{2(g)} = 8/3Mn + 2/3NH_{3(g)}$

The catalytic performance of NCs plays a pivotal role in enhancing the ammonia production rate. Studies have shown that TMs enhance the catalytic activity of NCs by changing the bond energies between intermediate products and the NC. For example, Liu et al. [67] conducted a density functional theory (DFT) analysis to explore the influence of nickel (Ni) and Fe on a manganese nitride (Mn_4N) support for nitrogen activation. Their findings revealed that the addition of Ni and Fe significantly improved the catalytic efficiency of the NCs [67].

In the AH-CLAS process, the first stage involves the nitridation of a metal hydride in an N_2 atmosphere, resulting in the formation of imides (Eq. (2. 2)). In the subsequent stage, the imides

are reduced back to the metal hydride state in the presence of H_2, producing NH_3 and completing the cycle (refer to Figure 2. 4b) (Eq. (2. 3)) [48].

Step 1- nitridation

$$\frac{4}{x}AH_x + N_2 \rightarrow 2A_{2/x}NH + H_2 \quad \text{(x: Valence of A)} \qquad (2.\ 2)$$

Step 2- hydrogenation

$$2A_{2/x}NH + 4H_2 \rightarrow \frac{4}{x}AH + 2NH_3 \qquad (2.\ 3)$$

The concept of using the AH-CLAS method for ammonia synthesis originated from studies on NH_3 production catalyzed by Co-BaH_2. In these investigations, BaH_2 and Co-BaH_2 exhibited significant weight gain when heated under an N_2 flow in a TGA, indicating that BaH_2 acts as a nitrogen storage material. Subsequently, the nitrided Co-BaH_2 and BaH_2 were exposed to a H_2 stream using H_2-TPR analysis, and NH_3 signals were observed at temperatures exceeding 200°C (see Eq. (2. 4) and (2. 5)) [68].

$$BaH_2 + 1/2N_2 \rightarrow BaNH + 1/2H_2 \qquad (2.\ 4)$$

$$BaNH + 2H_2 \rightarrow BaH_2 + NH_3 \qquad (2.\ 5)$$

The overall reaction: $N_2 + 3H_2 \rightarrow 2NH_3$ (2. 6)

Many alkali hydrides and imides likely function similarly to the BaH_2-BaNH system in facilitating CLAS [53]. For example, the LiH/Li_2NH pair has been identified as a promising candidate for AH-CLAS ammonia synthesis due to its favorable thermodynamics during the nitridation and hydrogenation stages [53]. In addition, Chen et al. [68] studied Li_3N using TGA and reported that nitridation and hydrogenation reactions began at approximately 100°C and 170–210°C, respectively.

The energy efficiency of the AH-CLAS process largely depends on the thermodynamics of the nitridation and hydrogenation stages. Gao et al. [53] analyzed the Gibbs free energy variations for these stages across different alkali hydrides and imides (A = Ba, Ca, Mg, K, Li, and Na) under atmospheric pressure and temperatures up to 450°C (refer to Figure 2. 5). Their findings revealed that neither potassium (K) nor sodium (Na) forms imides, making them ineffective for rapid nitrogen fixation. In addition, while the hydrogenation of KNH_2 or $NaNH_2$ to ammonia is thermodynamically favorable at lower temperatures, magnesium (Mg) forms only one imide

(MgNH), and Mg_3N_2 is highly stable, making hydrogenation under mild conditions significantly more difficult [53].

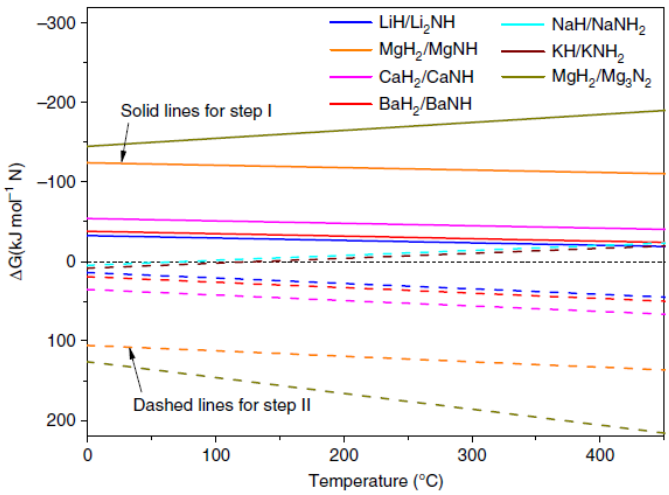

Figure 2. 5: The nitridation and the hydrogenation stages in the AH-CLAS thermodynamics [53]**.**

The MgH_2/Mg_3N_2 system exhibits a large thermodynamic gap between nitridation and hydrogenation, further complicating the process [53]. As illustrated in Figure 2. 5, the thermodynamic favorability of AH/ANH pairs for the AH-CL process follows this order: $LiH/Li_2NH > BaH_2/BaNH > CaH_2/CaNH > MgH_2/MgNH$ (Mg_3N_2) [53].

Studies have shown that incorporating certain TMs such as Ni, Co, and Pd into NCs can enhance their catalytic performance for ammonia synthesis. For example, as illustrated in Figure 2. 6a, the addition of Ni and Co to BaH_2 lowered the nitridation temperature from 300°C to approximately 200–250°C [69]. Furthermore, ammonia production was achieved at a low temperature of around 100°C and a pressure of 1.0 bar using a Ni-BaH_2/Al_2O_3 NC [48].

To better understand and differentiate the roles of chemical looping and the catalytic influence of various TM-AH systems, researchers compared NCs and catalysts in both chemical looping and conventional ammonia synthesis methods (using a H_2 to N_2 ratio of 3:1 in a tubular reactor). These experiments highlighted the catalytic impact of specific NCs. In addition, it was observed that the ammonia production rate by CLAS technology is significantly higher than catalytic approaches [69,70] (refer to Figure 2. 6b). Table 2. 2 summarizes the ammonia production rates of several TM-AH systems in both the CLAS process and conventional catalytic ammonia synthesis at

equivalent temperatures. The findings underscore the catalytic contribution of certain NCs and the effectiveness of the chemical looping process in boosting ammonia production rates.

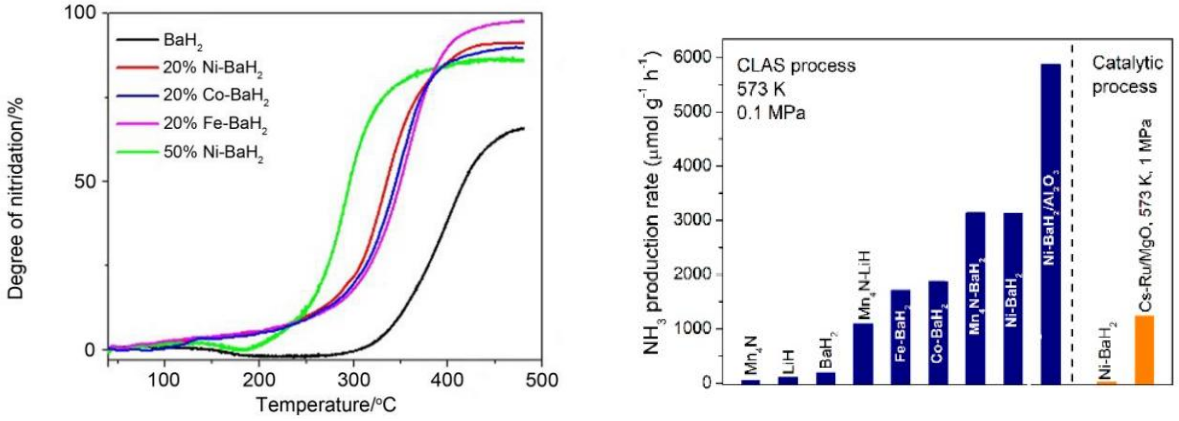

(a) **(b)**

Figure 2. 6: (a) TMs effect on nitridation of BaH_2 [53,69]**, (b) The CLAS and catalytic ammonia synthesis production rate comparison** [70]**.**

Table 2. 2: Ammonia production rate different NCs in the CLAS (P=1 bar) & catalytic process (P=10 bar) at 300°C. LiH production rate was measured at 350°C [49].

Samples	Chemical looping ($\mu molg^{-1}h^{-1}$)	Catalytic process ($\mu molg^{-1}h^{-1}$)
50% Ni-LiH	1533±50	Undetectable
LiH	105±8	Undetectable
BaH_2	198±11	Undetectable
50% Ni-BaH_2	3125±80	20±3
20 % Ni-BaH_2	2033±50	48±5
20% Co-BaH_2	1866±92	576±20
20% Fe-BaH_2	1703±70	384±13

The reactivity of certain metals can change when combined with AHs. For example, palladium (Pd) typically exhibits relatively low activity for N_2 activation due to its low adsorption energy (E_n = 0.91 eV). However, Yan et al. [71] demonstrated that LiH enhances Pd's reactivity by forming lithium-palladium hydrides, such as Li_2PdH_2 and $LiPdH_{0.7}$ (collectively referred to as [Li−Pd−H]). These compounds significantly improve the NH_3 production rate in the CLAS process [71].

Composite NCs enhance both nitridation and hydrogenation reactions. As previously noted, early TMs play a significant role in nitrogen fixation, while AHs strongly influence the hydrogenation kinetics. Feng et al. [72] introduced a multifunctional composite for the CLAS process. In their

research, nitrogen fixation occurred over Mn_4N–AH under a nitrogen stream, resulting in the formation of Mn_2N and an alkali amide (ANH). Switching to a H_2 stream facilitated the hydrogenation of the nitride phases and the reformation of Mn_4N and AH. Their findings indicated that the multifunctional Mn-AH NC improved the ammonia synthesis rate [71].

As depicted schematically in Figure 2. 7, the Mn_4N–AH NC offers three unique features: (i) both the imide (ANH) and Mn nitride function as NCs, (ii) Mn nitride acts as a NC with catalytic properties, enhancing the kinetics of nitrogen fixation and the hydrogenation of the imide, (iii) hydrides improve the kinetics of nitrogen dissociation and the subsequent hydrogenation of Mn nitride, leading to ammonia production [72].

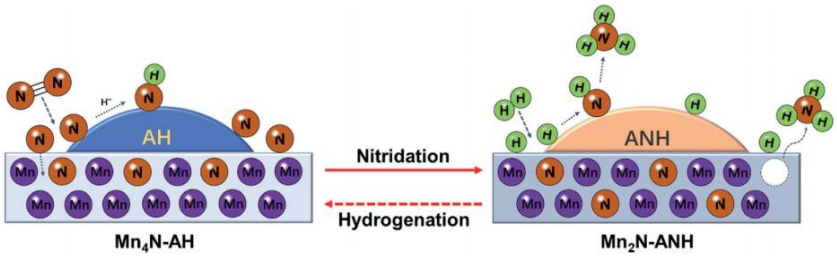

Figure 2. 7: Schematic diagram of the CLAS mediated by the MnN_x–ANH NC. AH stands for BaH_2 /LiH, and ANH denotes BaNH/Li_2NH [72]**.**

Chang et al. [73] highlighted that Mn, as an early TM, undergoes nitridation to form bulk nitride phases. However, it demonstrated negligible catalytic activity due to its strong affinities for elements such as nitrogen, oxygen, hydrogen, and carbon, which hinder the conversion of these atoms into desired products. The catalytic activity of Mn-nitride can be significantly enhanced, by an order of magnitude, with the addition of AHs [73]. Among AHs, the order of catalytic promotion is BaH_2 > LiH > KH > CaH_2 > NaH [73].

Wang et al. [74] further explored this improvement, reporting that negatively charged hydrogen atoms in LiH act as potent reducing agents, effectively removing activated nitrogen atoms from Mn-nitride. This enhancement improves catalytic activity and increases the ammonia production rate [74]. Similarly, Laassiri et al. [75] systematically investigated the potential of Mn-nitride-based materials for ammonia synthesis. They synthesized A-Mn-N NCs (A = Li, K, Fe, Co) and evaluated their reactivity by measuring ammonia production rates under H_2/N_2 streams. Their findings showed that most lattice nitrogen released during the synthesis stage reverted to N_2 rather

than forming NH_3. However, incorporating Li into the NC notably improved ammonia production [75].

Table 2. 3: NC/catalyst synthesis methods reported in the literature.

No.	NC	Synthesis procedure	Ref.
1	A-Mn-N(A=Li, Co, Fe, and K)	• A-Mn-O (A = Li, Co, Fe, and K) were synthesized by applying the coprecipitation method. 0.3 g of A-Mn-O and 1.0 g of $NaNH_2$ were mixed in an autoclave at 240°C for 36 hours, and then the solid was filtered and washed. Finally, it dried at the ambient temperature.	[75]
2	Ca_3N_2-Sr_2N	• Produced by heating Ca and Sr under a nitrogen stream and mixing them using mortar.	[77]
3	Mn-Fe/ Al_2O_3	• A certain amount of Mn powder, Fe powder, and alumina were mixed in a mortar.	[78]
4	PECVD-MnN_x	• The $MnCl_2$ evaporated at 500°C and mixed with ammonia gas. Then, the plasma ignited. After the reaction, MnN_x was found on the walls of the quartz tube.	[79]
5	Mn-LiH	• LiH and $MnCl_2$ with a molar ratio of 7:1 were ball-milled at 200 rpm for 3 hours. The remaining black solid was washed with THF three times for LiCl removal. Then, the solid was dried overnight under a vacuum.	[79]
6	PECVD-MnN_x-LiH	• PECVD-MnN_x and LiH were ball-milled for 3 hours at 200 rpm.	[79]
7	MnN_x -AHs	• Mn_4N were ball-milled with corresponding alkali/alkaline metal hydrides for 3 hours at 200 rpm under an Ar atmosphere and a molar ratio of 1:5.	[79]
8	Mn_4N–BaH_2	• Ammonia was added to 100 mg barium and 42.7 mg Mn_4N at ambient temperature. After the impregnation and ammonia removal, Mn_4N–$Ba(NH_2)_2$ solid was hydrogenated at 200°C to produce Mn_4N–BaH_2.	[80]
9	MgO or Al_2O_3-supported Ni–BaH_2	• 70% Ni/support catalyst added to a solution of barium–ammonia, and barium converted to barium amide. Ammonia was removed. The solid was exposed to a hydrogen stream at 300°C for 2 hours to produce BaH_2.	[81]
10	TM (V, Cr, Mn, Fe, Co, Ni)–LiH	• TM chloride and LiH were ball-milled at 200 rpm and 3 hours with a 7:1 molar ratio. Then, the solid was washed by THF.	[81]
11	Co_3Mo_3N	• NC produced by nitridation of $CoMoO_4.nH_2O$ that was synthesized by mixing cobalt nitrate and ammonium heptamolybdate solutions.	[82]

Some studies have also explored mechanochemical methods for ammonia synthesis, such as ball milling NCs during nitridation and hydrogenation stages [76]. This process creates highly active, low-coordinated defects through repeated collisions, facilitating N_2 activation. Since the hydrogenation stage is commonly endothermic, increasing the rotation speed or temperature boosts ammonia yield [76]. However, scaling up these processes remains a significant challenge [76].

Table 2. 3 summarizes the various NC synthesis methods reported in the literature, highlighting advancements in catalytic performance and innovative approaches for improving ammonia production rates.

2.5. Nonconventional heating methods

2.5.1. Induction and joule heating

Induction heating systems operate by applying alternating voltage to a coil, generating an alternating current (AC). This AC produces a magnetic field with a frequency matching that of the current. The magnetic field induces eddy currents in conductive materials, such as rods or particles within the coil, as well as nearby conductive objects. These eddy currents, flowing in the opposite direction to the coil current, generate heat through resistive heating [83].

To implement induction heating in reactors, a coil is positioned around the reactor bed, and magnetic or conductive particles/rods are placed inside the reactor [84]. In fixed-bed reactors, multiple coil turns are necessary to achieve a uniform magnetic field distribution throughout the bed. When transitioning to fluidized bed reactors, fewer coil turns can be used to deliver the same total power. However, challenges such as reduced coil lifetime and thermal fatigue of the reactor body remain significant issues [85].

In contrast, the Joule or resistive heating method relies on the electrical resistance of the material to convert electrical energy into heat [86]. At a fixed voltage, using a material with lower electrical resistance increases the current flow, thereby enhancing the heating power [87]. Various factors influence the electrical resistance of the bed, including superficial gas velocity, temperature, pressure, granular material composition, particle size distribution, interparticle forces, and contact resistance between particles. Joule heating offers a more uniform temperature distribution compared to induction heating. However, designing solid particles to interact efficiently with electricity, as well as optimizing reactor and electrode designs, present significant challenges [87].

2.5.2. Microwave heating

Electromagnetic (EM) waves represent a form of energy that propagates at the speed of light in a vacuum. These waves comprise electric ($\vec{E}$) and magnetic ($\vec{H}$) fields, which oscillate perpendicular to each other and to the direction of wave propagation [88–90]. EM waves are categorized by their wavelength, with the spectrum ordered from longest to shortest wavelength (or lowest to highest

frequency) as follows: (i) radio waves, (ii) MWs, (iii) infrared radiation, (iv) visible light, (v) ultraviolet radiation, (vi) X-rays, and (vii) gamma rays [88–90].

MWs occupy a specific region of the EM spectrum, with frequencies ranging from 0.3 GHz to 300 GHz and corresponding wavelengths between 100 cm and 0.1 cm [88,91]. In North America, industrial applications are limited to specific frequencies—0.915 GHz, 2.450 GHz, 5.800 GHz, and 22.00 GHz—to prevent interference with other applications. For laboratory settings, the 2.45 GHz frequency is commonly utilized due to its suitability for materials heating. At this frequency, the penetration depth, defined as the depth at which the electrical field strength falls to 38% of its surface value, is generally sufficient for most reaction systems [92].

MWs are widely utilized for their ability to heat materials efficiently, with domestic MW ovens being the most familiar example, used for cooking and heating food. Beyond household applications, recent studies have explored the use of MW heating in processing various organic and inorganic materials, including ceramics, minerals, and polymers [93–96].

MW systems typically comprise three main components: an MW source to generate radiation, an applicator to deliver the energy to the target materials, and a control system to regulate and monitor the power output. Among MW generators, the magnetron is the most used, especially in MW ovens and radar systems, due to its high efficiency, compact design, and low cost. Operating at a standard frequency of 2.45 GHz, the magnetron converts electrical energy into MW radiation [88]. The heating of materials via MW radiation can be precisely controlled by adjusting the exposure time and power level. This versatility makes MW systems valuable in a wide range of industrial and laboratory applications [88].

Maxwell's equations describe the excitation and propagation of EM waves [92]. The permittivity, also known as the dielectric constant, quantifies how dielectric materials respond to an electric field (refer to Eq. (2. 7)). In the context of dielectric materials, the magnetic field's contribution to MW heating is considered negligible. As a result, heating in such materials is driven solely by the electric field [88]. A critical parameter in assessing a material's ability to absorb MW energy is the loss tangent ($tan\delta$), refer to Eq. (2. 8). This property reflects the efficiency of MW heating in materials and plays a key role in determining their suitability for MW heating-based applications [88].

$$\varepsilon^* = \varepsilon' - j\varepsilon'' \quad (2.\ 7)$$

$$Tan\ \delta = \frac{\varepsilon''}{\varepsilon'} \quad (2.\ 8)$$

The complex permittivity (ε^*) characterizes the interaction between a material and an electric field. It comprises two components: the dielectric constant (ε'), which measures a material's ability to store electrical energy, and the dielectric loss factor (ε''), which represents energy dissipation as heat. The angle δ denotes the phase difference between the alternating electric field and the polarization response of the material.

It is important to note that a material's dielectric properties are not constant; they vary based on factors such as temperature, frequency, purity, and chemical composition [88]. Table 2. 4 provides an overview of the dielectric properties of various materials, highlighting their different responses under MW irradiation.

Table 2. 4: The dielectric properties of different materials [88]**.**

Material	$\boldsymbol{\varepsilon'}$	$\boldsymbol{\varepsilon''}$	$\boldsymbol{tan\delta}$	T (°C)	f(GHz)
Air	1.01	0.00	0.0000	25	NA
Glass	4.82	0.03	0.0054	25	3
Distillated water	78.00	12.00	0.1538	25	2.45
Quartz	4.00	0.001	0.0003	20	2.45
Methanol	32.60	21.48	0.6589	25	2.45
Polyethylene (PE)	2.26	0.01	0.0009	NA	0.915
Zinc oxide	3.00	3.00	1.0000	25	NA
Ethanol	24.30	22.86	0.9407	25	2.45
Aluminum oxide (Al_2O_3)	9.00	0.01	0.0007	25	NA
SiC (d=500 µm)	30.00	11.00	0.3700	25	2.45
Carbon active (d=20 µm)	130.00	60.00	0.4600	25	2.45
SiC tube	10.00	0.40	0.0400	25	2.45

The complex permeability (μ^*) characterizes how materials respond to a magnetic field, capturing both the storage and dissipation of magnetic energy (refer to Eq. (2. 9)). The magnetic loss tangent ($Tan\mu_\delta$), measures the efficiency with which magnetic materials convert an alternating magnetic field into heat [90]. These properties are crucial in understanding and optimizing the performance of materials in applications involving magnetic fields and heating.

$$\mu^* = \mu' - j\mu'' \quad (2.\ 9)$$

$$Tan\ \delta_\mu = \frac{\mu''}{\mu'} \quad (2.\ 10)$$

Magnetic permeability (μ') quantifies a material's ability to support the formation of a magnetic field, while the magnetic loss factor (μ'') represents energy losses due to resonance and relaxation phenomena under an alternating magnetic field. These properties influence the penetration depth of EM waves into the material. Specifically, higher permeability reduces the penetration depth, limiting the extent to which EM energy can penetrate the material [90].

We can use Eq. (2. 11) to estimate the power dissipated (P) within materials as EM energy is converted into heat [91]. Furthermore, the rate at which a material heats under MW irradiation can be described by Eq. (2. 12).

$$P = \frac{1}{2}\sigma\left|\vec{E}\right|^2 + \pi f \varepsilon_0 \varepsilon_r''\left|\vec{E}\right|^2 + \pi f \mu_0 \mu_r''\left|\vec{H}\right|^2 \quad (2.\ 11)$$

$$\frac{\Delta T}{\Delta t} = \frac{P}{\rho c_p} \quad (2.\ 12)$$

where σ represents the electrical conductivity, $\vec{E}$ is the electric field strength, f denotes the frequency, ε_0 is the permittivity of free space, μ_0 is the permeability of free space, $\vec{H}$ indicates the magnetic field strength, T is the temperature, t is the time, ρ is the material density, and C_p is the specific heat capacity of the material.

Eq.(2. 11) identifies three distinct mechanisms contributing to MW heating: Joule (or resistive) loss, dielectric loss, and magnetic loss) [91]. Joule loss, represented by the first term, is the predominant heating mechanism in materials with high electrical conductivity, such as metals [91]. This process is driven by eddy current losses generated in an alternating magnetic field and is directly related to the material's electrical conductivity. Dielectric loss, described by the second term, arises from the polarization of the material, which may involve various types of polarization, including electronic, atomic, dipolar, ionic, or interfacial polarization. Magnetic loss, represented by the third term, occurs due to mechanisms such as eddy currents, hysteresis, electron spin resonance, and domain wall motion in response to an oscillating magnetic field [91].

As illustrated in Figure 2. 8, the electric field component of an EM wave can be absorbed, transmitted, or reflected by different substances. Consequently, the interaction between MWs and

materials is typically classified into three categories: (i) Absorbing materials: These materials, which range from conductors to insulators, exhibit high dielectric loss, making them capable of absorbing EM energy and converting it into heat. They are often referred to as lossy dielectrics. (ii) Transparent materials: Characterized by low dielectric loss factors, materials such as ceramics, glass, quartz, and air exhibit minimal MW absorption. They allow MWs to pass through with little to no interaction. (iii) Opaque materials: Highly conductive materials, such as metals, fall into this category. They reflect EM waves rather than allowing absorption or transmission [88].

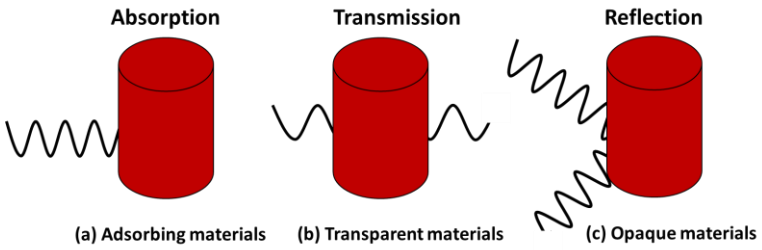

Figure 2. 8: Interaction of different materials with EM waves [88].

The EM field penetration depth refers to the distance from an object's surface where the EM field strength decreases to 38% of its initial value at the surface. This depth can be determined using Eq. (2. 13) [91]. Similarly, the power penetration depth represents the distance from the surface at which the power density drops to 38% of its surface value. Notably, the power penetration depth is half the value of the electromagnetic field penetration depth. Table 2. 5 provides the penetration depths of MWs for various materials.

$$d = \left[\frac{\omega^2 \varepsilon' \mu'}{2}\left(\sqrt{1+\frac{\sigma^2}{\omega^2 \varepsilon'^2}}-1\right)\right]^{\frac{-1}{2}} \quad , D_p = \frac{d}{2} \tag{2. 13}$$

Where d is the penetration depth of the EM field, ω is the angular frequency, and D_p is the power penetration depth.

MW heating offers rapid processing, significantly reducing both heating time and energy loss, which leads to lower overall energy consumption. In conventional heating, heat is supplied externally, and the gas phase typically reaches the same temperature as the catalyst or solid particles. This uniform heating can promote gas-phase secondary reactions, potentially lowering the yield of desired chemicals. In contrast, MW heating generates heat directly within the catalyst or solid particles due to the interaction between EM waves and the dielectric material loaded in

fixed-bed or fluidized-bed reactors. Since MWs do not directly heat the gas phase, owing to the minimal interaction between MWs and gas-phase components, a significant temperature gradient develops between the solid particles and the gas phase. This suppresses unwanted gas-phase side reactions and enhances reactor performance, leading to higher production rates of desired chemicals [97].

Table 2. 5: The penetration depth of MWs inside some studied substances at 2.45 GHz [91]**.**

Material	D_p (μm)	T (°C)	MW heating capability
Alumina (Al_2O_3)	13.0×10^6	Ambient temperature	Transparent
	5.0×10^6	590	Transparent
	0.8×10^6	980	Nearly transparent
	0.2×10^6	1340	Nearly transparent
Hematite (Fe_2O_3)	10.0×10^6	Ambient temperature	Transparent
	45.0×10^3	600	Absorber
Magnetite (Fe_3O_4)	80.0	Ambient temperature	Absorber
Water (liquid H_2O)	300×10^4	Ambient temperature	Absorber
Graphite (dp=20-80 μm)	2.0×10^4	Ambient temperature	Absorber
Silicon Carbide (SiC)	1.9×10^4	Ambient temperature	Absorber
Magnesium (Mg)	2.2	Ambient temperature	
Iron (Fe)	1.3	Ambient temperature	Reflective for the bulk of
Copper (Cu)	2.7	Ambient temperature	metals
Aluminum (Al)	1.7	Ambient temperature	Absorbers for fine particles
Nickel (Ni)	2.5	Ambient temperature	

MW heating is also highly efficient, with electrical-to-MW energy conversion efficiencies of 80–90% and MW-to-thermal energy conversion efficiencies of 70–90%. These efficiencies make MW irradiation a cost-effective heating method for industrial processes. Furthermore, the use of renewable electricity to generate MWs can enhance the sustainability of the process [91].

References

[1] Y. Wei, R. Han, C. Wang, B. Yu, Q. Liang, X. Yuan, J. Chang, Q. Zhao, H. Liao, B. Tang, J. Yan, L. Cheng, Z. Yang, Self-preservation strategy for approaching global warming targets in the post-Paris Agreement era, Nat Commun (2020) 1–13. https://doi.org/10.1038/s41467-020-15453-z.

[2] S.K. Rose, R. Richels, G. Blanford, T. Rutherford, The Paris Agreement and next steps in limiting global warming, (2017). https://doi.org/10.1007/s10584-017-1935-y.

[3] M.M. Sarafraz, F.C. Christo, Sustainable three-stage chemical looping ammonia production (3CLAP) process, 229 (2021).

[4] S.R. Bull, Renewable energy transportation technologies, (1996) 1019–1024.

[5] A. Hellman, Ammonia Synthesis : State of the Bellwether Reaction, Elsevier Ltd., 2013. https://doi.org/10.1016/B978-0-08-097774-4.00725-7.

[6] R.O. Stroman, M.W. Schuette, K. Swider-lyons, J.A. Rodgers, D.J. Edwards, Liquid hydrogen fuel system design and demonstration in a small long endurance air vehicle, Int J Hydrogen Energy 39 (2014) 11279–11290. https://doi.org/10.1016/j.ijhydene.2014.05.065.

[7] E. Environ, A future energy supply based on Liquid Organic Hydrogen Carriers (LOHC), Energy Environ Sci 4 (2011) 2767–2773. https://doi.org/10.1039/c1ee01454d.

[8] I. Ganesh, Conversion of carbon dioxide into methanol – a potential liquid fuel : Fundamental challenges and opportunities (a review), Renewable and Sustainable Energy Reviews 31 (2014) 221–257. https://doi.org/10.1016/j.rser.2013.11.045.

[9] S. Giddey, S.P.S. Badwal, C. Munnings, M. Dolan, Ammonia as a Renewable Energy Transportation Media, (2017) 10231–10239. https://doi.org/10.1021/acssuschemeng.7b02219.

[10] N.J. Duijm, F. Markert, J.L. Paulsen, Safety assessment of ammonia as a transport fuel, 2005.

[11] N. Morlanés, A technological roadmap to the ammonia energy economy: Current state and missing technologies, CHEMICAL ENGINEERING JOURNAL 408 (2021). https://doi.org/10.1016/j.cej.2020.127310.

[12] K. Räuchle, L. Plass, H. Wernicke, M. Bertau, Methanol for Renewable Energy Storage and Utilization, Energy Technology (2016) 193–200. https://doi.org/10.1002/ente.201500322.

[13] A. Yapicioglu, I. Dincer, A review on clean ammonia as a potential fuel for power generators, Renewable and Sustainable Energy Reviews 103 (2019) 96–108. https://doi.org/10.1016/j.rser.2018.12.023.

[14] Y. Gao, Y. Wu, Q. Zhang, X. Chen, N-desorption or NH3 generation of TiO2 -loaded Al-based nitrogen carrier during chemical looping ammonia generation technology, Int J Hydrogen Energy 3 (2018) 3–11. https://doi.org/10.1016/j.ijhydene.2018.07.042.

[15] Gotz Veser, Taking the pressure off, News & Views (2017) 3–4. https://doi.org/10.1038/s41560-018-0293-y.

[16] K.H.R. Rouwenhorst, H.H. Kim, L. Lefferts, Vibrationally Excited Activation of N2 in Plasma-Enhanced Catalytic Ammonia Synthesis: A Kinetic Analysis, ACS Sustain Chem Eng 7 (2019). https://doi.org/10.1021/acssuschemeng.9b04997.

[17] P. Peng, P. Chen, M. Addy, Y. Cheng, E. Anderson, N. Zhou, C. Schiappacasse, Y. Zhang, D. Chen, R. Hatzenbeller, Y. Liu, R. Ruan, Atmospheric Plasma-Assisted Ammonia Synthesis Enhanced via Synergistic Catalytic Absorption, ACS Sustain Chem Eng 7 (2019). https://doi.org/10.1021/acssuschemeng.8b03887.

[18] Y. Wang, T.S. Khan, C. Wildfire, D. Shekhawat, J. Hu, Microwave-enhanced catalytic ammonia synthesis under moderate pressure and temperature, Catal Commun 159 (2021). https://doi.org/10.1016/j.catcom.2021.106344.

[19] C. Wildfire, V. Abdelsayed, D. Shekhawat, R.A. Dagle, S.D. Davidson, J. Hu, Microwave-assisted ammonia synthesis over Ru/MgO catalysts at ambient pressure, Catal Today 365 (2021). https://doi.org/10.1016/j.cattod.2020.06.013.

[20] H. Xu, L. Zhang, S.J. Wei, X. Tong, Y. Yang, X. Ji, A novel solar system for photothermal-assisted electrocatalytic nitrate reduction reaction to ammonia, Renew Energy 221 (2024). https://doi.org/10.1016/j.renene.2023.119707.

[21] G. Veser, Taking the pressure off, Nat Energy 3 (2018). https://doi.org/10.1038/s41560-018-0293-y.

[22] L. Wang, M. Xia, H. Wang, K. Huang, C. Qian, C.T. Maravelias, G.A. Ozin, Greening Ammonia toward the Solar Ammonia Refinery, Joule 2 (2018). https://doi.org/10.1016/j.joule.2018.04.017.

[23] D.F. Swearer, N.R. Knowles, H.O. Everitt, N.J. Halas, Light-Driven Chemical Looping for Ammonia Synthesis, ACS Energy Lett 4 (2019). https://doi.org/10.1021/acsenergylett.9b00860.

[24] S. Laassiri, C.D. Zeinalipour-Yazdi, C.R.A. Catlow, J.S.J. Hargreaves, The potential of manganese nitride based materials as nitrogen transfer reagents for nitrogen chemical looping, Appl Catal B 223 (2018). https://doi.org/10.1016/j.apcatb.2017.04.073.

[25] C. Wildfire, V. Abdelsayed, D. Shekhawat, M.J. Spencer, Ambient pressure synthesis of ammonia using a microwave reactor, Catal Commun 115 (2018). https://doi.org/10.1016/j.catcom.2018.07.010.

[26] M.M. Sarafraz, F.C. Christo, Sustainable three-stage chemical looping ammonia production (3CLAP) process, Energy Convers Manag 229 (2021). https://doi.org/10.1016/j.enconman.2020.113735.

[27] A. Araia, Y. Wang, C. Jiang, S. Brown, A. Caiola, B. Robinson, J. Hu, Intuitive study on the effect of support morphology over Cs-Ru/CeO2 catalyst for microwave-initiated ammonia synthesis, Catal Commun 172 (2022). https://doi.org/10.1016/j.catcom.2022.106551.

[28] Y. Wang, C. Wildfire, T.S. Khan, D. Shekhawat, J. Hu, P. Tavadze, R. Quiñones-Fernández, S. Moreno, Effects of support and promoter on Ru catalyst activity in microwave-assisted ammonia synthesis, Chemical Engineering Journal 425 (2021). https://doi.org/10.1016/j.cej.2021.130546.

[29] A. Araia, Y. Wang, B. Robinson, C. Jiang, S. Brown, C. Wildfire, D. Shekhawat, J. Hu, Microwave-assisted ammonia synthesis over Cs-Ru/CeO2 catalyst at ambient pressure: Effects of metal loading and support particle size, Catal Commun 170 (2022). https://doi.org/10.1016/j.catcom.2022.106491.

[30] A. Araia, Y. Wang, C. Jiang, S. Brown, A. Caiola, B. Robinson, W. Li, J. Hu, Insight into Enhanced Microwave Heating for Ammonia Synthesis: Effects of CNT on the Cs-Ru/CeO2Catalyst, ACS Appl Mater Interfaces 15 (2023). https://doi.org/10.1021/acsami.3c00132.

[31] L. Hu, Z. Xing, X. Feng, Understanding the Electrocatalytic Interface for Ambient Ammonia Synthesis, ACS Energy Lett 5 (2020). https://doi.org/10.1021/acsenergylett.9b02679.

[32] G. Duan, Y. Chen, Y. Tang, K.A.M. Gasem, P. Wan, D. Ding, M. Fan, Advances in electrocatalytic ammonia synthesis under mild conditions, Prog Energy Combust Sci 81 (2020) 100860. https://doi.org/10.1016/j.pecs.2020.100860.

[33] L. Wang, M. Xia, H. Wang, K. Huang, C. Qian, C.T. Maravelias, G.A. Ozin, Greening Ammonia toward the Solar Ammonia Refinery, Joule 2 (2018) 1055–1074. https://doi.org/10.1016/j.joule.2018.04.017.

[34] A.R. Singh, B.A. Rohr, J.A. Schwalbe, M. Cargnello, K. Chan, T.F. Jaramillo, I. Chorkendor, J.K. Nørskov, Electrochemical Ammonia Synthesis -The Selectivity Challenge, Catalysts 7 (2017) 706–709. https://doi.org/10.1021/acscatal.6b03035.

[35] G. Duan, Y. Chen, Y. Tang, K.A.M. Gasem, P. Wan, D. Ding, M. Fan, Advances in electrocatalytic ammonia synthesis under mild conditions, Prog Energy Combust Sci 81 (2020). https://doi.org/10.1016/j.pecs.2020.100860.

[36] L. Hu, Z. Xing, X. Feng, Understanding the Electrocatalytic Interface for Ambient Ammonia Synthesis, Energy Letters 5 (2020) 430–436. https://doi.org/10.1021/acsenergylett.9b02679.

[37] L.F. Greenlee, J.N. Renner, S.L. Foster, The Use of Controls for Consistent and Accurate Measurements of Electrocatalytic Ammonia Synthesis from Dinitrogen, Catalysis 8 (2018) 7820–7827. https://doi.org/10.1021/acscatal.8b02120.

[38] S. Zhang, Y. Zhao, R. Shi, G.I.N. Waterhouse, T. Zhang, Photocatalytic ammonia synthesis : Recent progress and future, EnergyChem 1 (2019) 100013. https://doi.org/10.1016/j.enchem.2019.100013.

[39] S. Junwang, Progress and challenges in photocatalytic ammonia synthesis, Mater Adv 2 (2021) 264–581. https://doi.org/10.1039/d0ma00590h.

[40] S. Li, J.A. Medrano, V. Hessel, F. Gallucci, Recent Progress of Plasma-Assisted Nitrogen Fixation Research: A Review, Processes 6 (2018). https://doi.org/10.3390/pr6120248.

[41] P. Peng, P. Chen, C. Schiappacasse, N. Zhou, E. Anderson, D. Chen, J. Liu, Y. Cheng, R. Hatzenbeller, M. Addy, Y. Zhang, Y. Liu, R. Ruan, A review on the non-thermal plasma-assisted ammonia synthesis technologies, J Clean Prod 177 (2018) 597–609. https://doi.org/10.1016/j.jclepro.2017.12.229.

[42] K.H.R. Rouwenhorst, L. Le, Feasibility Study of Plasma-Catalytic Ammonia Synthesis for Energy Storage Applications, Catalysts 10 (2020).

[43] S. Abuelgasim, W. Wang, A. Abdalazeez, A brief review for chemical looping combustion as a promising CO2 capture technology : Fundamentals and progress, Science of the Total Environment 764 (2021) 142892. https://doi.org/10.1016/j.scitotenv.2020.142892.

[44] A. Lyngfelt, Chemical Looping Combustion : Status and Development Challenges, Energy & Fuels 34 (2020) 9077–9093. https://doi.org/10.1021/acs.energyfuels.0c01454.

[45] C. Lu, K. Li, H. Wang, X. Zhu, Y. Wei, M. Zheng, Chemical looping reforming of methane using magnetite as oxygen carrier : Structure evolution and reduction kinetics, Appl Energy 211 (2018) 1–14. https://doi.org/10.1016/j.apenergy.2017.11.049.

[46] Y. Lin, H. Wang, Y. Wang, R. Huo, Z. Huang, M. Liu, G. Wei, Z. Zhao, H. Li, Y. Fang, Review of Biomass Chemical Looping Gasification in China, Energy & Fuels 34 (2020) 7847–7862. https://doi.org/10.1021/acs.energyfuels.0c01022.

[47] X. Liu, H. Hong, H. Zhang, Y. Cao, W. Qu, H. Jin, Solar methanol by hybridizing natural gas chemical looping reforming with solar heat, Appl Energy 277 (2020) 115521. https://doi.org/10.1016/j.apenergy.2020.115521.

[48] K.H.R. Rouwenhorst, P.M. Krzywda, N.E. Benes, G. Mul, L. Lefferts, Chapter 4 - Ammonia Production Technologies, Elsevier Inc., 2021. https://doi.org/10.1016/B978-0-12-820560-0.00004-7.

[49] R. Juan, L. Pereira, P. Alexandros, V. Spallina, A comparative study on clean ammonia production using chemical looping based technology, Appl Energy 280 (2020) 115874. https://doi.org/10.1016/j.apenergy.2020.115874.

[50] X. Wang, M. Su, H. Zhao, Process design and exergy cost analysis of a chemical looping ammonia generation system using AlN/Al2O3 as a nitrogen carrier, Energy 230 (2021) 120767. https://doi.org/10.1016/j.energy.2021.120767.

[51] L. Burrows, P. Gao, G.M. Bollas, Thermodynamic feasibility analysis of distributed chemical looping ammonia synthesis, Chemical Engineering Journal 426 (2021) 131421. https://doi.org/10.1016/j.cej.2021.131421.

[52] R. Michalsky, P.H. Pfromm, Thermodynamics of Metal Reactants for Ammonia Synthesis from Steam , Nitrogen and Biomass at Atmospheric Pressure, Thermodynamics and Molecular-Scla Phenomena 58 (2012) 3203–3213. https://doi.org/10.1002/aic.

[53] W. Gao, J. Guo, P. Wang, Q. Wang, F. Chang, Q. Pei, W. Zhang, L. Liu, P. Chen, Chemical looping process based on metal imides as nitrogen carriers, Nat Energy 3 (2018). https://doi.org/10.1038/s41560-018-0268-z.

[54] M.E. Ga, A. Frei, M. Halmann, A. Steinfeld, P. Scherrer, Ammonia Production via a Two-Step Al2O3 / AlN Thermochemical Cycle . 2 . Kinetic Analysis, Ind. Eng. Chem. Res. (2007) 2047–2053.

[55] F. Bagja, A. Rizqi, M. Aziz, Production of ammonia as potential hydrogen carrier : Review on thermochemical and electrochemical processes, Int J Hydrogen Energy 46 (2021) 14455–14477. https://doi.org/10.1016/j.ijhydene.2021.01.214.

[56] M.G. Heidlage, E.A. Kezar, K.C. Snow, P.H. Pfromm, Thermochemical Synthesis of Ammonia and Syngas from Natural Gas at Atmospheric Pressure, I&EC (2017) 14014–14024. https://doi.org/10.1021/acs.iecr.7b03173.

[57] R. Michalsky, P.H. Pfromm, An Ionicity Rationale to Design Solid phase Metal Nitride Reactants for Solar Ammonia Production, The Journal of Physical Chemistry C 116 (2012) 23243–23251.

[58] R. Michalsky, P.H. Pfromm, A. Steinfeld, R. Michalsky, Rational design of metal nitride redox materials for solar-driven ammonia synthesis, Interface Focus 5 (2015).

[59] J.C. Lin, M. Cargnello, F. Jaramillo, J.K. Nørskov, Environmental Science Ammonia synthesis from N2 and H2O using a atmospheric pressure, Energy Environ Sci (2017) 1621–1630. https://doi.org/10.1039/c7ee01126a.

[60] Y. Wu, Y. Gao, Q. Zhang, T. Cai, X. Chen, D. Liu, M. Fan, Promising zirconia-mixed Al-based nitrogen carriers for chemical looping of NH3: Reduced NH3 decomposition and improved NH3 yield, Fuels 264 (2020). https://doi.org/10.1016/j.fuel.2019.116821.

[61] C. Mitchell, The Denitridation of Nitrides of Iron , Cobalt and Rhenium Under Hydrogen, Top Catal 56 (2013) 1963–1969. https://doi.org/10.1007/s11244-013-0133-z.

[62] B. Wang, H. Guo, X. Yin, L. Shen, N - Sorption Capability of Al2O3 -Supported Mn-/Fe-Based Nitrogen Carriers during Chemical Looping Ammonia Synthesis Technology, Energy and Fuels 34 (2020) 10247–10255. https://doi.org/10.1021/acs.energyfuels.0c01000.

[63] R. Michalsky, A.M. Avram, B.A. Peterson, P.H. Pfromm, A.A. Peterson, Chemical looping of metal nitride catalysts: low- pressure ammonia synthesis for energy storage, Chem Sci (2015) 3965–3974. https://doi.org/10.1039/c5sc00789e.

[64] W. Mohammadi, C. Huang, P.H. Pfromm, Chemical Looping of Manganese to Synthesize Ammonia at Atmospheric Pressure : Sodium as Promoter, Chem Eng Technol (2020) 2126–2133. https://doi.org/10.1002/ceat.202000154.

[65] J. Hua, K. Wang, Q. Wang, R. Peng, Feasibility of Fe - based nitrogen carrier for chemical looping ammonia synthesis : thermodynamics, J Therm Anal Calorim (2020). https://doi.org/10.1007/s10973-020-10029-x.

[66] B. Wang, H. Guo, X. Yin, L. Shen, N - Sorption Capability of Al2O3 -Supported Mn-/Fe-Based Nitrogen Carriers during Chemical Looping Ammonia Synthesis Technology, Energy and Fuels 34 (2020) 10247–10255. https://doi.org/10.1021/acs.energyfuels.0c01000.

[67] B. Liu, N. Manavi, H. Deng, C. Huang, N. Shan, V. Chikan, P. Pfromm, Activation of N2 on Manganese Nitride-Supported Ni 3 and Fe3 Clusters and Relevance to Ammonia Formation, J Phys Chem Lett 12 (2021) 6535–6542. https://doi.org/10.1021/acs.jpclett.1c01752.

[68] P. Chen, Z. Xiong, J. Luo, J. Lin, K.L. Tan, Interaction of hydrogen with metal nitrides and imides, Letters to Nature 420 (2002) 20–22.

[69] W. Gao, J. Guo, P. Chen, P. Chen, Hydrides , Amides and Imides Mediated Ammonia Synthesis and Decomposition, Chin J Chem Eng 37 (2019) 442–451. https://doi.org/10.1002/cjoc.201800586.

[70] J. Guo, P. Chen, Interplay of Alkali, Transition Metals, Nitrogen, and Hydrogen in Ammonia Synthesis and Decomposition Reactions, Accounts 54 (2021) 2434–2444. https://doi.org/10.1021/acs.accounts.1c00076.

[71] H. Yan, W. Gao, Q. Wang, Y. Guan, S. Feng, H. Wu, Q. Guo, H. Cao, J. Guo, P. Chen, Lithium Palladium Hydride Promotes Chemical Looping Ammonia Synthesis Mediated by Lithium Imide and Hydride, The Journal of Physical Chemistry C 125 (2021) 6716–6722. https://doi.org/10.1021/acs.jpcc.1c01230.

[72] S. Feng, W. Gao, Q. Wang, Y. Guan, H. Yan, H. Wu, A multi-functional composite nitrogen carrier for ammonia production via a chemical looping route †, J Mater Chem A Mater (2021) 1039–1047. https://doi.org/10.1039/d0ta10519h.

[73] F. Chang, Y. Guan, X. Chang, J. Guo, P. Wang, W. Gao, G. Wu, J. Zheng, X. Li, P. Chen, Alkali and Alkaline Earth Hydrides-Driven N2 Activation and Transfo, JACS (2018). https://doi.org/10.1021/jacs.8b08334.

[74] P. Wang, F. Chang, W. Gao, J. Guo, G. Wu, T. He, P. Chen, LiH-mediated nitrogen transfer and hydrogenation, Nat Chem (2016) 1–7. https://doi.org/10.1038/nchem.2595.

[75] S. Laassiri, C.D. Zeinalipour-yazdi, C.R.A. Catlow, J.S.J. Hargreaves, The potential of manganese nitride based materials as nitrogen transfer reagents for nitrogen chemical looping, Appl Catal B 223 (2018) 60–66. https://doi.org/10.1016/j.apcatb.2017.04.073.

[76] G. Han, F. Li, Z. Chen, C. Coppex, S. Kim, H. Noh, Z. Fu, Y. Lu, C.V. Singh, S. Siahrostami, Q. Jiang, J. Baek, Mechanochemistry for ammonia synthesis under mild conditions, Nat Nanotechnol 16 (2021). https://doi.org/10.1038/s41565-020-00809-9.

[77] R. Michalsky, A.M. Avram, B.A. Peterson, P.H. Pfromm, A.A. Peterson, Chemical looping of metal nitride catalysts: low- pressure ammonia synthesis for energy storage, Chem Sci (2015) 3965–3974. https://doi.org/10.1039/c5sc00789e.

[78] B. Wang, H. Guo, X. Yin, L. Shen, N - Sorption Capability of Al2O3 -Supported Mn-/Fe-Based Nitrogen Carriers during Chemical Looping Ammonia Synthesis Technology, Energy and Fuels 34 (2020) 10247–10255. https://doi.org/10.1021/acs.energyfuels.0c01000.

[79] F. Chang, Y. Guan, X. Chang, J. Guo, P. Wang, W. Gao, G. Wu, J. Zheng, X. Li, P. Chen, Alkali and Alkaline Earth Hydrides-Driven N2 Activation and Transformation over Mn Nitride Catalyst, JACS 140 (2018) 14766–14806. https://doi.org/10.1021/jacs.8b08334.

[80] W. Gao, J. Guo, P. Wang, Q. Wang, F. Chang, Q. Pei, W. Zhang, L. Liu, P. Chen, Production of ammonia via a chemical looping process based on metal imides as nitrogen carriers, Nat Energy 3 (n.d.). https://doi.org/10.1038/s41560-018-0268-z.

[81] P. Wang, F. Chang, W. Gao, J. Guo, G. Wu, T. He, P. Chen, Breaking scaling relations to achieve low-temperature ammonia synthesis through LiH-mediated nitrogen transfer and hydrogenation, Nat Chem (2016) 1–7. https://doi.org/10.1038/nchem.2595.

[82] D. Mckay, D.H. Gregory, J.S.J. Hargreaves, S.M. Hunter, X. Sun, Towards nitrogen transfer catalysis : reactive lattice nitrogen in cobalt molybdenum nitride, Chemical Communications 7 (2007) 3051–3053. https://doi.org/10.1039/b707913c.

[83] V. Rudnev, D. Loveless, R.L. Cook, V. Rudnev, D. Loveless, R.L. Cook, Handbook of Induction Heating, 2021. https://doi.org/10.1201/9781315117485-3.

[84] T.K. Houlding, E. V Rebrov, Application of alternative energy forms in catalytic reactor engineering, Green Process Synth 1 (2012) 19–31. https://doi.org/10.1515/greenps-2011-0502.

[85] T. Utz, K. Graichen, Optimal Control of Induction Heating Processes Using FEM Software, European Control Conference (ECC) (2015).

[86] L. J. Petrovic, Mass transfer in the flow of gases through packed beds, I&EC 7 (1968).

[87] S.S. Fedorov, M.G. Barsukov, B.S. Wells, Ultrahigh-Temperature Continuous Reactors Based on Electrothermal Fluidized Bed Concept, J Fluids Eng 138 (2016) 1–11. https://doi.org/10.1115/1.4031689.

[88] M. Gupta, W.W. Leong, Microwaves and Metals, 2007.

[89] G.J.J. Verhoeven, V. Archaeology, The reflection of two fields – Electromagnetic radiation and its role in (aerial) imaging Geert, AARGnews (2018) 10–18. https://doi.org/10.5281/zenodo.3534245.

[90] V. Palma, D. Barba, M. Cortese, M. Martino, S. Renda, E. Meloni, Microwaves and Heterogeneous Catalysis : A Review on Selected Catalytic Processes, Catalysts (2020).

[91] A. Amini, M. Latifi, J. Chaouki, Electrification of materials processing via microwave irradiation : A review of mechanism and applications, Appl Therm Eng 193 (2021) 117003. https://doi.org/10.1016/j.applthermaleng.2021.117003.

[92] S. Mutyala, C. Fairbridge, J.R.J. Paré, J.M.R. Bélanger, S. Ng, R. Hawkins, Microwave applications to oil sands and petroleum : A review, Fuel Processing Technology 91 (2010) 127–135. https://doi.org/10.1016/j.fuproc.2009.09.009.

[93] J. Tierney, J. Westman, Microwave assisted organic synthesis-a review, Tetrahedron 57 (2001).

[94] P. Prieto, A Critical Overview on the Effect of Microwave Irradiation in Organic Synthesis, THE CHEMICAL RECORD (2019) 85–97. https://doi.org/10.1002/tcr.201800059.

[95] R.R. Mishra, A.K. Sharma, A Review of Research Trends in Microwave Processing of Metal-Based Materials and Opportunities in Microwave Metal Casting A Review of Research Trends in Microwave Processing of Metal-Based Materials, Critical Reviews in Solid State and Materials Sciences 41 (2016) 217–255. https://doi.org/10.1080/10408436.2016.1142421.

[96] P. Priecel, J.A. Lopez-sanchez, Advantages and Limitations of Microwave Reactors: From Chemical Synthesis to the Catalytic Valorization of Biobased Chemicals, Sustainable Chemistry & Engineering (2019). https://doi.org/10.1021/acssuschemeng.8b03286.

[97] S. Hamzehlouia, J. Shabanian, M. Latifi, J. Chaouki, Effect of microwave heating on the performance of catalytic oxidation of n-butane in a gas-solid fluidized bed reactor, Chem Eng Sci 192 (2018) 1177–1188. https://doi.org/10.1016/j.ces.2018.08.054.

CHAPTER 3 COHERENCE OF CHAPTERS

In this thesis, we developed an innovative microwave heating-assisted chemical looping ammonia synthesis (MHCLAS) technology designed to operate under atmospheric pressure and at a temperature range of 350-630°C for the nitridation stage and 150-350°C for the hydrogenation stage. We started with a comprehensive literature review, thermodynamic analysis, and the selection of NCs. Across Chapters 4 to 9, we systematically detailed the strategy for developing and validating the MHCLAS technology, addressing the specific sub-objectives defined for this study.

- ✓ **Chapter 4:** In this chapter, published as a review paper in *Frontiers in Chemical Engineering*, we explored gas-solid reactions kinetic under MW irradiation. The study emphasized the advantages and limitations of MW heating in such reactions, proposed strategies for conducting effective kinetic studies under MW heating and discussed potential reasons for discrepancies between kinetic parameters obtained using MW and conventional heating approaches.

- ✓ **Chapter 5:** In this chapter published as a research article in *I&EC Journal*, we conducted a modeling and simulation study, validated by experimental results, to examine the temperature gradient between gas and solid phases under MW heating. The findings revealed that selective MW heating results in lower gas-phase temperatures, which is critical for minimizing ammonia decomposition during the hydrogenation stage. Parameters such as superficial gas velocities, reaction exothermicity and endothermicity, and temperature measurement techniques were analyzed. In addition, we proposed a potential optimal reactor type for studying reaction kinetics under MW irradiation.

- ✓ **Chapter 6:** Published as a research article in the *Journal of Energy Conversion and Management*, this chapter details the development and performance evaluation of various NCs under conventional and MW heating. This proof-of-concept study utilized insights from earlier chapters. We developed NCs that were both reactive in CLAS nitridation and

hydrogenation reactions and exhibited strong interactions with MWs, demonstrating the feasibility of the MHCLAS approach. We employed different techniques including thermogravimetric analysis (TGA), temperature-programmed reduction (TPR), ion-selective electrode (ISE), x-ray diffraction (XRD), and scanning electron microscopy with energy dispersive spectroscopy (SEM-EDS) to investigate/justify the nitridation and hydrogenation reactions conducted over different Mn, Fe, and Ba-based NCs.

- ✓ **Chapter 7:** In this chapter, submitted as a research paper in *Journal of Fuel*, we performed a detailed intrinsic kinetic study to evaluate the kinetics of the nitridation and hydrogenation stages. By minimizing the effects of external and internal mass transfer, we proposed intrinsic kinetic models that can serve as a foundation for further development of MHCLAS technology. We also discussed reaction models for nitridation and hydrogenation, enhancing our understanding of the MHCLAS reactions.

- ✓ **Chapter 8:** In this chapter, submitted as a research article to *Journal of Hydrogen Energy*, we applied the kinetics developed in Chapter 7 to model and simulate MW-heated fluidized bed reactors for both nitridation and hydrogenation stages. The study examined EM field distributions, temperature distributions, and gas/solid reactions conversions, providing critical insights for scaling up MHCLAS technology. These findings mark a significant step toward the industrialization of the MHCLAS process. This project showed the potential of MHCLAS as an efficient and sustainable solution for renewable energy storage.

- ✓ **Chapter 9:** In this chapter, we conducted a preliminary/general techno-economic assessment, highlighting potential challenges in scaling up the MHCLAS reactor, such as the limitation of MW penetration depth. These findings provide valuable insights into the key constraints that must be addressed for the successful industrialization of MHCLAS technology.

CHAPTER 4: ARTICLE 1-KINETIC STUDY OF MULTIPHASE REACTIONS UNDER MICROWAVE IRRADIATION: A MINI-REVIEW

Kazem Adavi [1], Ahmadreza Amini [1], Mohammad Latifi [1], Jaber Shabanian [1, 2], Jamal Chaouki [1, 3, *]

[1] Process Engineering Advanced Research Lab (PEARL), Department of Chemical Engineering, Polytechnique Montreal, P. O. Box 6079, Station Centre-Ville, Montreal, (Quebec) Canada, H3C 3A7

[2] Heirloom, 125 Valley Dr., Brisbane, California, 94005, United States

[3] Technology Development Cell (Tech-Cell) Department, Mohammed VI Polytechnic University, Ben Guerir, Morocco

[*] Corresponding author: Tel. +1 (514) 340-4711 X 4034, fax: +1 (514) 340-4159,

E-mail: jamal.chaouki@polymtl.ca

(Published on November 1st, 2022, Frontiers in Chemical Engineering, DOI: https://doi.org/10.3389/fceng.2022.1059160)

Abstract

Microwave (MW) heating is rapid, selective, and volumetric, and it is a compelling non-conventional heating approach for driving chemical reactions. The effect of MW irradiation on the kinetics of thermal/catalytic reactions is still under debate. A group of researchers reported that the effect of MW heating on reaction kinetics is highlighted through the non-thermal effects of MWs on kinetic parameters and reaction mechanisms in addition to the thermal effect. However, another group attributed the observations to the thermal effect only. In the present work, we summarized and critically synthesized available information in the literature on the subject. It can be concluded that MW heating has solely the thermal effect on gas-solid reactions, and the variations of kinetic parameters are related to the direct and indirect impacts of that. Temperature measurement limitations, physical structure variation, and non-uniform temperature distribution are the primary sources of the discrepancy in previous studies. In ionic liquid-solid reactions, the presence of electromagnetic fields can affect the movement of ions/polar molecules which can be considered a non-thermal effect of MWs. However, the effect of MW absorption by solid/catalyst, and the formation of hot spots must be taken into account to avoid potential discrepancy. Therefore, further theoretical/experimental studies are required to clarify the effect of MWs on liquid-solid reactions. In addition, developing reliable temperature measurement methods and isothermal reaction domain are required for an accurate kinetic study during MW irradiation.

Keywords: Microwave irradiation, reaction kinetics, thermal effect, non-thermal effect, temperature measurement, hot spot.

4.1. Introduction

Compared to conventional heating, microwave (MW) heating is an effective heat supply approach for chemical and material processes. Electromagnetic (EM) properties of materials, including permittivity, permeability, penetration depth, and electrical conductivity play critical roles in absorbing MWs and their conversion to thermal energy [1,2]. In the conventional heating of a multi-phase system, an external source supplies heat, and the whole system, including solid particles, gas/liquid, and reactor walls, are at similar temperatures. Therefore, non-desired secondary reactions likely occur in the fluid phase, reducing the desired chemicals' production rate and process efficiency [3]. In the MW heating approach, however, heat is generated in the body of certain phases (commonly solid particles) owing to the high penetration depth of MWs and their interaction with dielectric material loaded in the reactors. MWs cannot directly heat the gas phase due to their negligible interactions with this phase [3,4]. Therefore, a considerable temperature gradient between the solid particles (either inert or catalyst) and fluid suppresses the fluid-phase side reactions, favors the production of desired chemicals, and likely leads to higher selectivity and conversion [3–6]. The rapid and selective features of MW heating also decrease the treatment time and energy loss during the process [2]. The effects of MW irradiation on various multiphase (gas/liquid-solid phases) reaction systems are presented in Table 4.1.

Despite the applications of MW heating in multiphase systems, its effect on the kinetics of these reactions is still under debate. The main discrepancy is the presence of non-thermal effects, i.e., the interaction of MWs with materials at atomic/subatomic level and electron donation enhancement, in addition to the thermal effects, i.e., selective heating and formation of hotspots. In the present communication, we reviewed the impacts of MW heating on the reaction kinetics of multiphase reactions reported in the literature. We critically compared the experimental procedures in various references to propose the potential sources of discrepancy in the kinetic results.

Table 4.1: Impact of MW heating on multiphase reactions.

No.	Process	Reactor ID (mm)/ sample amount (g or ml)	Temperature measurement technique	Heating approach	MW effect			Ref.
					Conversion	Selectivity	Reaction Temp.	
1	Methane decomposition	22 mm	Pyrometer	Direct	↑[a]	↑	NA[b]	[7]
2	Methane oxidation	5 mm	Pyrometer +metallic thermocouple	Direct	↑	↑	↓[c]	[8]
3	Methane dry reforming	5-30 mm	Pyrometer	Hybrid	↑	↑	NA	[9]
4	Methane dehydroaromatization	8 mm	IR	Direct	↑	NA	↓	[10]
5	Methanol steam reforming	24 mm	Fiber optic probe	Direct	↑	↑	↓	[11]
7	H_2S decomposition	2 g	Metallic thermocouple	Direct	↑	NA	NA	[12]
8	CO oxidation	0.1 g	Fiber optic probe	Direct	↑	NA	NA	[13]
9	Propane oxidation	16 mm	Pyrometer	Hybrid	↑	NA	↓	[14]
10	n-butane oxidation	24 mm	Pyrometer	Hybrid	↑	↑	NA	[3]
11	SO_2 reduction	20 mm	Metallic thermocouple	Direct	↑	NA	NA	[15]
12	Ethane valorization	8 mm	Pyrometer	Hybrid	↑	↑	↓	[6]
16	Upgrading stranded shale gas to aromatics	10 mm	Pyrometer	Direct	↑	NA	↓	[16]
17	Synthesis of phytosterol esters	200 ml	NA	Hybrid	↑	NA	↓	[17]
18	Sodium tetrahydridoborate ($NaBH_4$) hydrolysis	15 mm	NA	Hybrid	↑	NA	↓	[18]

a: increasing, b: not applicable, c: decreasing

4.2. Kinetics of gas/liquid-solid reactions

According to the literature, MW heating has mainly thermal effects on reaction kinetics. For instance, hot spots generated during the MW treatment of solid beds enhance the reaction rate as their temperature is significantly higher than the average bed (or bulk) temperature [1,4]. These hot spots can form microcracks inside the solid materials, and enhance internal mass transfer. For

instance, Amini et al. [4] reported that MWs selectively heat some components of iron oxide minerals, generating a temperature gradient between different components within an ore particle. Accordingly, micro-cracks are generated through the ore, enhancing gas diffusion into the ore, and improving the apparent kinetics of the reduction reaction [4].

In some discrepant cases, the non-thermal effect of MWs is also reported as a driving force in accelerating reactions [19]. For instance, Omran et al. [4] reported a decrease in the activation energy (E) in Eq.(4.1)) during carbothermic reduction of zinc oxide and zinc ferrite which occurs at a lower temperature compared to conventional heating. Also, Fukushima et al. [20] studied the reduction of CuO to Cu_2O under MW heating. They reported that, compared to the conventional heating, E decreases to 2/3 and 1/3 under E-field and H-field, respectively due to the non-thermal effect of MWs which likely enhances the electron donation and micro-plasma formation. In contrast, others believe that decreasing the activation energy is due to underestimating hot spots temperatures [1,3]. Accordingly, the measured temperature was the bulk temperature, while catalyst/solid particles had noticeably (50 to 300°C) higher temperatures owing to selective heating via MWs [1–3,21]. Eq. (4.1) shows the general equation for reaction rate and its parameters.

$$R_i = k_0 \exp\left(\frac{-E}{RT}\right) f(C_i) \tag{4.1}$$

where R_i is the reaction rate of component i, k_0 is the pre-exponential factor, R is the universal gas constant, T is the absolute temperature, and C_i is the concentration of component i.

In the case of k_0, both the increase [22,23] and decrease [24–26] have been reported under MW heating. However, k_0 is known as collision frequency that should not decrease under MW heating [21]. In MW transparent fluids, no change is expected in the k_0 compared to the conventional heating approach. The Effects of MW heating on the kinetic parameters of some thermal/catalytic reactions for gas/liquid-solid systems are presented in Table 4.2. Reactor diameter/sample amount, temperature measurement technique, and heating approach (direct: directly heating the sample via MWs, or hybrid: mixing the sample with MW receptor materials, such as silicon carbide (SiC) and activated carbon to heat the sample indirectly) are investigated in this paper.

Table 4.2: kinetic studies of gas/liquid-solid systems under MW irradiations.

Process	Reactor ID (mm)/ mass (g)	Temperature measurement technique	Changes compared to conventional heating		Rate controlling mechanism	Heating approach	Ref.
			E	K_0			
Methanol reforming	8 mm	Metallic thermocouple (top of the bed)	No change	No change	No change	Hybrid	[27]
Thermal pyrolysis of bamboo sawdust	45 mm	Grounded metallic thermocouple (center of the bed)	↓	↓	NA	Hybrid	[24]
Char steam gasification	20 mm	Grounded metallic thermocouple (center of the bed)	↓	↓	No change (SCM[a], VRM[b])	Direct	[25]
Iron production via hydrogen-reduction of Iron(II) sulfide – calcium oxide (FeS-CaO) mixture	35 mm	Radiation thermometer	↓	NA	• Conventional: reaction rate-limiting, and then diffusion rate limiting. • MW heating: gas diffusion rate-limiting	Direct	[4]
Reduction of chromium ore fines containing coal	65 mm	Metallic thermocouple	↓	NA	No change	Direct	[26]
Carbothermic reduction of zinc oxide and zinc ferrite	NA	Metallic thermocouple on top of the sample	↓	NA	NA	Hybrid	[28]
Pyrolysis of waste printed circuit boards	40 g sample in MW-TGA	Metallic thermocouple	↓	↓	Under MW heating, reaction order decreased	Hybrid	[29]
Pyrolysis of lignocellulosic biomass	Quartz crucible (3-5 g)	Metallic thermocouple	↓	↓	NA	Hybrid	[30]
Reduction of copper oxide (CuO)	Pelletized particles (8×2 mm)	IR[c] thermometer	↓	↓	NA	Direct	[20]
Pyrolysis of wood sawdust for phenolic rich compounds	NA	IR thermometer	↓	NA	NA	Hybrid	[31]
Paper cups pyrolysis	15	Metallic thermocouple	No change	No change	At a high heating rate, decomposition of cellulose was direct from feedstock to products rather than producing intermediates	Hybrid	[32]

Table 4.2 (cont'd): kinetic studies of gas/liquid-solid systems under MW irradiations.

$NaBH_4$ hydrolysis	15	NA	↓	↓	By increasing heating rate under MW irradiation reaction order decreased	Direct	[18]
Synthesis of phytosterol esters	200 ml	NA	↓	↑	NA	Direct	[42]

a: shrinking core model, b: volume reaction model, c: infrared

4.3. Potential sources of discrepancy

Variations of reaction kinetic parameters in multiphase reactions under MW heating compared to conventional heating have potential reasons, such as reactor diameter/sample amount in a kinetic study [33], heating approach (direct or hybrid) [34], temperature measurement [34,35], physical structure variation due to materials exposure to MWs [4], and interaction of MWs with polar molecules and free radicals [36]. These sources are discussed below.

4.3.1. Effects of reactor diameter/sample amount and heating approach

The uniform temperature distribution in the reaction domain is essential to increase the accuracy of estimated kinetic parameters. Temperature non-uniformity in the bed is observed on both the macro-scale and micro-scale. The macro-scale temperature gradient of the bed is changed by variation of the sample's location in the cavity, the ratio of the waveguide to cavity impedances, and materials properties (affecting penetration depth). The main reason for the micro-scale temperature non-uniformity/hot spots is the difference in dielectric properties of materials in the bed [1,37].

Smaller reactor sizes and a few grams of solid mass are preferred to have a more uniform temperature distribution (see Figure 4.1), while effects of external and internal mass transfer limitations are eliminated/minimized either by increasing gas/liquid velocity or decreasing particle size, respectively [33]. To provide a uniform temperature distribution, we recommend applying a reactor diameter smaller than 10 mm (around 1/12 of MW wavelength at a frequency of 2.45 GHz), in fixed bed reactors adopted for intrinsic kinetic studies. In addition, employing fluidized bed reactors is another solution for an accurate kinetic study due to minimizing temperature non-uniformity [38,39]. Impedance matching between the waveguide and cavity eliminates microwave reflection and minimizes the bed's macro-scale temperature gradient.

Heating of materials with weak MW interactions, e.g., plastics and biomass, in MW heating systems is challenging [34]. Therefore, the hybrid heating approach is typically applied. However, due to variations in dielectric properties, it forms hot spots at MW receptors in the bed. For instance, pyrolysis of 40 g waste printed circuit board in an MW-thermogravimetric analyzer resulted in both macro and micro scales hot spots during MW-assisted hybrid heating [29]. Also, MW-assisted pyrolysis of bamboo sawdust in a fixed bed reactor with a diameter of 45 mm (around 1/3 of the MW wavelength at 2.45 GHz) resulted in the formation of macro-scale hot spots [24].

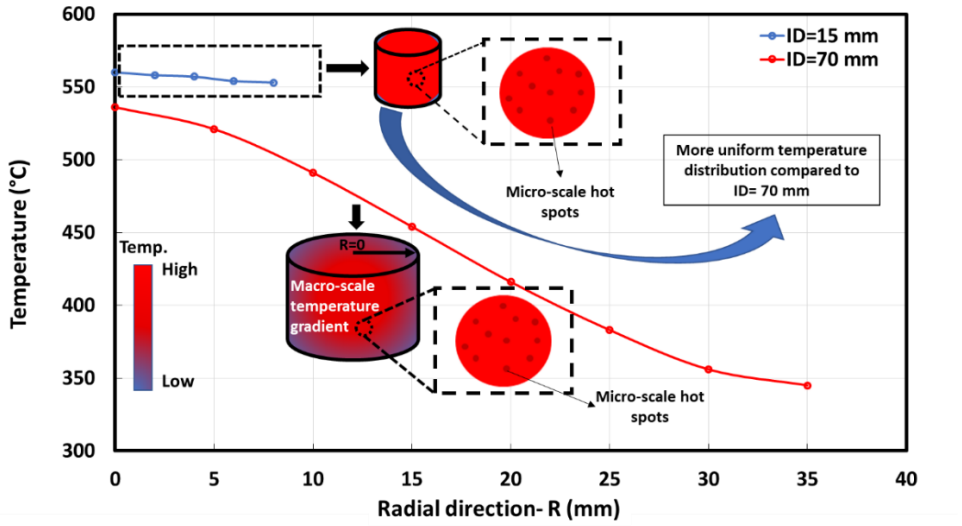

Figure 4.1: Effect of the internal reactor diameter (15 and 70 mm) on temperature distribution in a mixture of paper cups and graphite (adapted from ref. [33]).

4.3.2. Effect of temperature measurement

Most MW reactors work based on temperature control mode, where the sample is heated to and kept at the desired temperature by coupling the feedback from an appropriate temperature measurement technique to the impedance tuner in the MW waveguide [35,40]. However, accurate temperature measurement of the gas/liquid and solid phases under MW heating is one of the critical issues in kinetic studies [35,40]. If the temperature is underestimated, the kinetic results show a fake enhancement.

Currently, no technique can accurately measure the gas/liquid and solid local temperatures during MW heating [41]. Various techniques, including grounded and shielded metallic thermocouples [35], fiber optic probes [40], IR [35], polymeric [35], molecular [35], and air thermometers [21],

as well as radiometry methods [41] are employed in MW heated reactions. For kinetic studies, we need at least one contact sensor, e.g., thermocouple and fiber optic probe, or some other MW transparent sensors, to track the temperature changes during MW treatment of multiphase systems [35]. Critical remarks regarding different temperature measurement techniques for MW heating systems are summarized in Table 4.3.

Table 4.3: Temperature measurement techniques in MW processing.

Technique	Main remarks	Ref.
Polymeric thermometer	• Limited for measuring the solid surface temperature • Inaccurate for gas-phase temperature measurement, especially during a reaction	[18]
Molecular thermometer	• Unsuitable for gas-solid reactions	[35]
Metallic thermocouple	• Interference with MWs • Spark formation • The difficulty in measuring local hot-spots temperature	[35]
Fiber optic probes	• More accurate than IR and metallic thermocouples • Immune to interference with MWs (depends on its design) • Limited temperature range (0-300°C) • Fragile • Expensive	[40]
IR-thermography	• Inaccurate due to the emissivity change during the reactions	[35]
Radiometry method	• Antenna made of planar printed steel that causes Interference with MWs	[41]
Air thermometer	• No interference with MWs • The difficulty in measuring local hot-spots temperature • Fragile	[21]

4.3.3. Effect of MWs interactions with polar molecules and free radicals

The activation energy is a characteristic of a chemical reaction implying the minimum required energy to initiate the reaction between reactants. Thus, a deep insight into the interactions (e.g., vibrations, disassociations, etc.) at an atomic scale under MW irradiation is essential to investigate their dependency on MWs.

Patil et al. [42] reported that the reaction rate constant for microwave-assisted transesterification of oil on BaO catalyst is 98 times higher than conventional reaction. Although they provided no discussion/justification, it seems they ignored the potential interaction between BaO catalyst and microwaves that leads to a higher temperature at the catalyst surface compared to the bulk temperature (i.e., hot spot formation). Barium oxide is a non-polar dielectric material with potential defects, including vacancies and interstitials, which couple with microwaves to convert its energy into heat [43]. Khujaev et al. [44] reported that the complete dissolution of BaO in HCl under

microwave irradiation at 385 W takes less than 2.5 min, whereas it requires more than 20 min in conventional heating methods, indicating a significant interaction between microwaves and BaO. Accordingly, a higher reaction rate during microwave transesterification is attributed to the higher local temperature at the catalyst surface compared to the measured temperature, i.e., the bulk temperature, whereas the catalyst temperature is the same as the bulk temperature during conventional heating [44].

In addition, in liquid-solid MW heating-assisted reaction systems, MWs interactions can potentially affect ions and polar molecules. These interactions might result in a variation of kinetic parameters compared to conventional heating. For instance, the activation energy of Sodium tetrahydridoborate ($NaBH_4$) hydrolysis under MW heating (46.8 kJ/mol) is lower than that obtained under the conventional heating approach (66.9 kJ/mol) [18]. The authors attributed this to the interaction between MW electric field and OH^- ions that accelerate hydrolysis which was confirmed by a high-level pre-exponential factor (2.08×10^3 L/mol.min) under MW irradiation. In the study by Yang et al. [45], accelerating ions under MW heating was also reported. However, the MW absorption capability of the solid/catalyst was ignored in these studies. If the solid absorbs MWs, the improved kinetics in a liquid-solid system under MW irradiation is likely attributed to the formation of hot spots in the solid component, which provides a higher local temperature compared to the bulk. Moreover, the formation of intermediate products with MW interaction, which is locally heated, affected reaction kinetics by their rotation [32].

Unlike the gas phase, which is relatively transparent to MWs, liquid materials containing polar molecules or ions interact with MWs. Accordingly, a liquid ion's dipolar/rotational movement on a solid's surface can change the reaction pathway/mechanism [18]. However, further theoretical/experimental works are needed to study the interaction of ions and polar intermediate with MWs in liquid-solid systems.

4.4. Future study

The development of new temperature measurement techniques, preferably non-intrusive ones, e.g., wireless thermometers, for local temperature measurement in MW systems is essential. In addition, the morphology variation of solid materials should be monitored under MW heating processes. Applying computational approaches like density functional theory (DFT), to investigate the effect of EM field on polar molecules in solid-liquid systems and consequently its impact on reaction kinetics/mechanism is an important concept that needs to be covered in future studies.

4.5. Conclusion

The effect of MW heating on the kinetic parameters of gas/liquid-solid reactions was reported in the literature. Underestimation and even sometimes overestimation of the reaction temperature in the reaction domain due to hot spots formation at micro and macro scales, and difficulty in measurement of these temperatures are the main sources of discrepancy in MW heating kinetic studies. Therefore, to the best of the authors' knowledge, there is no evidence in the literature confirming the presence of the non-thermal effect of MWs on the kinetics of gas-solid reactions, by now. Fixed bed reactors with a smaller diameter, e.g., 10 mm or operation under fluidized bed mode are suggested for kinetic studies to avoid noticeable temperature gradients within the reactor. However, changing the morphology of solid materials under MW heating can affect apparent kinetic parameters when the internal mass transfer controls the reaction rate. In liquid-solid systems with ions and polar molecules, electromagnetic fields likely accelerate the molecule's movement, which might affect the reaction rate; however, the interaction of MWs with solid/catalyst should also be considered for potential hot spot formation to avoid an inaccurate kinetics evaluation.

References

[1] A. Amini, M. Latifi, J. Chaouki, Electrification of materials processing via microwave irradiation : A review of mechanism and applications, Appl Therm Eng 193 (2021) 117003. https://doi.org/10.1016/j.applthermaleng.2021.117003.

[2] M. Gupta, W.W. Leong, Microwaves and Metals, 2007.

[3] S. Hamzehlouia, J. Shabanian, M. Latifi, J. Chaouki, Effect of microwave heating on the performance of catalytic oxidation of n-butane in a gas-solid fluidized bed reactor, Chem Eng Sci 192 (2018) 1177–1188. https://doi.org/10.1016/j.ces.2018.08.054.

[4] A. Amini, K. Ohno, T. Maeda, K. Kunitomo, A kinetic comparison between microwave heating and conventional heating of FeS-CaO mixture during hydrogen-reduction, Chemical Engineering Journal 374 (2019) 648–657. https://doi.org/10.1016/j.cej.2019.05.226.

[5] G.D. Stefanidis, A helicopter view of microwave application to chemical processes : reactions , separations , and equipment concepts, Rev Chem Eng (2014). https://doi.org/10.1515/revce-2013-0033.

[6] B. Robinson, A. Caiola, X. Bai, V. Abdelsayed, D. Shekhawat, J. Hu, Catalytic direct conversion of ethane to value-added chemicals under microwave irradiation, Catal Today 356 (2020) 3–10. https://doi.org/10.1016/j.cattod.2020.03.001.

[7] A. Domínguez, B. Fidalgo, Y. Fernández, J.J. Pis, J.A. Menéndez, Microwave-assisted catalytic decomposition of methane over activated carbon for CO2 -free hydrogen production, Int J Hydrogen Energy 32 (2007) 4792–4799. https://doi.org/10.1016/j.ijhydene.2007.07.041.

[8] Microwave effect on partial oxidation of methane to syngas, React.Kinet.Catal.LeR. 66 (1999) 381–386.

[9] T.T.P. Pham, K.S. Ro, L. Chen, D. Mahajan, T. Ji, S.U.P.M. Ashik, Microwave - assisted dry reforming of methane for syngas production : a review, Springer International Publishing, 2020. https://doi.org/10.1007/s10311-020-01055-0.

[10] X. Bai, P.D. Muley, T. Musho, V. Abdelsayed, B. Robinson, A. Caiola, D. Shekhawat, C. Jiang, J. Hu, A combined experimental and modeling study of Microwave-assisted methane dehydroaromatization process, Chemical Engineering Journal 433 (2022) 134445. https://doi.org/10.1016/j.cej.2021.134445.

[11] T. Durka, G.D. Stefanidis, T. Van Gerven, A.I. Stankiewicz, Microwave-activated methanol steam reforming for hydrogen production, Int J Hydrogen Energy 36 (2011) 12843–12852. https://doi.org/10.1016/j.ijhydene.2011.07.009.

[12] J. Chen, J. Zhu, W. Xu, Y. Chen, J. Zhou, Highly efficient H2 and S production from H2 S decomposition via microwave catalysis over a family of TiO2 modified MoxC microwave catalysts, Fuel Processing Technology 226 (2022) 107069. https://doi.org/10.1016/j.fuproc.2021.107069.

[13] H. Einaga, Y. Nasu, M. Oda, H. Saito, Catalytic performances of perovskite oxides for CO oxidation under microwave irradiation, CHEMICAL ENGINEERING JOURNAL 283 (2016) 97–104. https://doi.org/10.1016/j.cej.2015.07.051.

[14] A. Ramirez, J.L. Hueso, R. Mallada, J. Santamaria, Microwave-activated structured reactors to maximize propylene selectivity in the oxidative dehydrogenation of propane, Chemical Engineering Journal 393 (2020) 124746. https://doi.org/10.1016/j.cej.2020.124746.

[15] X. Xia, X. Zhao, P. Zhou, T. Feng, C. Ma, Z. Song, Reduction of SO2 to elemental sulfur with carbon materials through electrical and microwave heating methods, Chemical Engineering & Processing: Process Intensification 150 (2020) 107877. https://doi.org/10.1016/j.cep.2020.107877.

[16] X. Bai, B. Robinson, C. Killmer, Y. Wang, L. Li, J. Hu, Microwave catalytic reactor for upgrading stranded shale gas to aromatics, Fuel 243 (2019) 485–492. https://doi.org/10.1016/j.fuel.2019.01.147.

[17] Y. Zhang, T. Zhang, Y. Zhang, Z. Wu, P. Zhang, R. Liu, M. Chang, X. Wang, Microwave-assisted catalytic synthesis of phytosterol esters, Int J Food Sci Technol 57 (2022) 3162–3170. https://doi.org/10.1111/ijfs.15649.

[18] A. Ekinci, Ö. Şahin, S. Horoz, Kinetics of catalytic hydrolysis of NaBH, Journal of the Australian Ceramic Society (2022) 113–121. https://doi.org/10.1007/s41779-021-00673-3.

[19] J. Hu, C. Wild, A.E. Stiegman, R.A. Dagle, D. Shekhawat, V. Abdelsayed, X. Bai, H. Tian, M.B. Bogle, C. Hsu, Y. Luo, S.D. Davidson, Y. Wang, Microwave-driven heterogeneous catalysis for activation of dinitrogen to ammonia under atmospheric pressure, Chemical Engineering Journal 397 (2020). https://doi.org/10.1016/j.cej.2020.125388.

[20] J. Fukushima, K. Kashimura, S. Takayama, M. Sato, S. Sano, Y. Hayashi, H. Takizawa, In-situ kinetic study on non-thermal reduction reaction of CuO during microwave heating, Mater Lett 91 (2013) 252–254. https://doi.org/10.1016/j.matlet.2012.09.114.

[21] S. Farag, J. Chaouki, A modified microwave thermo-gravimetric-analyzer for kinetic purposes, Applied Thermal Engineering Journal 75 (2015) 65–72. https://doi.org/10.1016/j.applthermaleng.2014.09.038.

[22] G.D. Yadav, I. V Borkar, Kinetic Modeling of Microwave-Assisted Chemoenzymatic Epoxidation of Styrene, BIOENGINEERING, FOOD, AND NATURAL PRODUCTS 52 (2006) 1235–1247. https://doi.org/10.1002/aic.10700.

[23] Kinetics of Isothermal Ethanol Adsorption onto a Carbon Molecular Sieve under Conventional and Microwave Heating, Chem Eng Technol (2012) 761–768. https://doi.org/10.1002/ceat.201100153.

[24] Q. Dong, Y. Xiong, Bioresource Technology Kinetics study on conventional and microwave pyrolysis of moso bamboo, Bioresour Technol 171 (2014) 127–131. https://doi.org/10.1016/j.biortech.2014.08.063.

[25] Q. Liu, H. He, H. Li, J. Jia, G. Huang, B. Xing, Characteristics and kinetics of coal char steam gasification under microwave heating, Fuel 256 (2019). https://doi.org/10.1016/j.fuel.2019.115899.

[26] W. She-bin, Kinetics of Voluminal Reduction of Chromium Ore Fines Containing Coal by Microwave Heating, LOURNAL OF IRON AND STEEL RESEARCH 15 (2008) 10–15. https://doi.org/10.1016/S1006-706X(08)60258-7.

[27] W.L. Perry, A.K. Datye, A.K. Prinja, L.F. Brown, J.D. Katz, Microwave Heating of Endothermic Catalytic Reactions : Reforming of Methanol, AIChE Journal 48 (2002).

[28] M. Omran, T. Fabritius, E. Heikkinen, T. Vuolio, Y. Yu, G. Chen, Y. Kacar, Microwave catalyzed carbothermic reduction of zinc oxide and zinc ferrite : effect of microwave energy on the reaction activation energy, RSC Adv (2020) 23959–23968. https://doi.org/10.1039/d0ra04574h.

[29] J. Sun, W. Wang, Z. Liu, Q. Ma, C. Zhao, C. Ma, Kinetic Study of the Pyrolysis of Waste Printed Circuit Boards Subject to Conventional and Microwave Heating, Energies (Basel) 5 (2012) 3295–3306. https://doi.org/10.3390/en5093295.

[30] Y. Huang, P. Chiueh, W. Kuan, S. Lo, Microwave pyrolysis of lignocellulosic biomass : Heating performance and reaction kinetics, Energy 100 (2016) 137–144. https://doi.org/10.1016/j.energy.2016.01.088.

[31] H. Luo, L. Bao, L. Kong, Y. Sun, Bioresource Technology Low temperature microwave-assisted pyrolysis of wood sawdust for phenolic rich compounds : Kinetics and dielectric properties analysis, Bioresour Technol 238 (2017) 109–115. https://doi.org/10.1016/j.biortech.2017.04.030.

[32] S. Benzennou, J.P. Laviolette, J. Chaouki, Microwave effect on kinetics of paper cups pyrolysis, Can J Chem Eng (2020) 1757–1766. https://doi.org/10.1002/cjce.23752.

[33] S. Benzennou, J.P. Laviolette, J. Chaouki, Kinetic Study of Microwave Pyrolysis of Paper Cups and Comparison with Calcium Oxide Catalyzed Reaction, AIChE Journal 65 (2020). https://doi.org/10.1002/aic.16471.

[34] X. Ren, M. Shanb, H. Zhu, W. Ao, H. Zhang, Challenges and opportunities in microwave-assisted catalytic pyrolysis of biomass : A review, Appl Energy 315 (2022) 118970. https://doi.org/10.1016/j.apenergy.2022.118970.

[35] L.S. Gangurde, G.S.J. Sturm, T.J. Devadiga, A.I. Stankiewicz, G.D. Stefanidis, Complexity and Challenges in Noncontact High Temperature Measurements in Microwave-Assisted Catalytic Reactors, I&EC (2017) 13379–13391. https://doi.org/10.1021/acs.iecr.7b02091.

[36] M. Wan, H. Yue, J. Notarangelo, H. Liu, F. Che, Deep Learning-Assisted Investigation of Electric Field−Dipole Effects on Catalytic Ammonia Synthesis, JACS 2 (2022) 1338–1349. https://doi.org/10.1021/jacsau.2c00003.

[37] A. Ramirez, J.L. Hueso, R. Mallada, J. Santamaria, In situ temperature measurements in microwave-heated gas-solid catalytic systems . Detection of hot spots and solid-fluid temperature gradients in the ethylene epoxidation reaction, Chemical Engineering Journal 316 (2017) 50–60. https://doi.org/10.1016/j.cej.2017.01.077.

[38] S. Farag, J. Chaouki, A modified microwave thermo-gravimetric-analyzer for kinetic purposes, 75 (2015) 65–72. https://doi.org/10.1016/j.applthermaleng.2014.09.038.

[39] S. Samih, J. Chaouki, Development of a Fluidized Bed Thermogravimetric Analyzer, AIChE Journal 61 (2015) 84–89. https://doi.org/10.1002/aic.

[40] C.O. Kappe, How to measure reaction temperature in microwave-heated transformations, Chem Soc Rev (2013) 4977–4990. https://doi.org/10.1039/c3cs00010a.

[41] H.M. Nguyen, J. Sunarso, C. Li, G.H. Pham, C. Phan, S. Liu, General Microwave-assisted catalytic methane reforming : A review, Appl Catal A Gen 599 (2020) 117620. https://doi.org/10.1016/j.apcata.2020.117620.

[42] P. Patil, V.G. Gude, S. Pinappu, S. Deng, Transesterification kinetics of Camelina sativa oil on metal oxide catalysts under conventional and microwave heating conditions, Chemical Engineering Journal 168 (2011) 1296–1300. https://doi.org/10.1016/j.cej.2011.02.030.

[43] V.A. Bolotov, V. v. Chesnokov, Y.Y. Tanashev, V.N. Parmon, The oxidative dehydrogenation of ethane: Convectional vs microwave heating of Ba - containing catalysts, Chemical Engineering and Processing - Process Intensification 129 (2018) 103–108. https://doi.org/10.1016/j.cep.2018.05.006.

[44] S. Khujaev, A. Vasidov, E.A. Markelova, Extraction of the 131Cs from neutron irradiated barium oxide under microwave radiation, J Radioanal Nucl Chem 298 (2013) 435–438. https://doi.org/10.1007/s10967-013-2687-4.

[45] X. Yang, K. Cheng, G. Jia, Microwave heating and non-thermal effects of sodium chloride aqueous solution, Mol Phys 8976 (2020). https://doi.org/10.1080/00268976.2019.1662505.

CHAPTER 5: ARTICLE 2-TEMPERATURE DISTRIBUTION ASSESSMENT IN GAS-SOLID REACTIVE AND NONREACTIVE SYSTEMS HEATED BY MICROWAVES

Kazem Adavi, Jaber Shabanian, Jamal Chaouki*

Process Engineering Advanced Research Lab (PEARL), Department of Chemical Engineering, Polytechnique Montreal, P. O. Box 6079, Station Centre-Ville, Montreal, (Quebec) Canada, H3C 3A7

**Corresponding author: Tel. +1 (514) 340-4711 X 4034, fax: +1 (514) 340-4159, E-mail: jamal.chaouki@polymtl.ca*

(Published on June 22nd, 2023, Industrial & Engineering Chemistry Research, DOI: https://doi.org/10.1021/acs.iecr.3c00575)

Abstract

Research studies have shown that selective heating of different phases in gas-solid systems exposed to microwave (MW) irradiations leads to a temperature gradient between gas and MW absorber solids. This can suppress undesired secondary gas-phase reactions and yield apparent kinetic improvements and energy savings. However, the effects of reaction exothermicity/endothermicity, gas velocity, temperature probe location at the micro-scale, and MW penetration depth in fixed beds on the temperature difference between solid and gas phases exposed to MWs and temperature distribution in the fixed beds are poorly understood. Highlighting these effects was targeted in this study and accomplished with the help of multiphysics simulations by COMSOL Multiphysics (5.6). The corresponding COMSOL model was initially verified and validated by data collected from literature and those obtained experimentally by the authors in this study. Simulation results from the verified and validated model indicated that the temperature gradient between gas and MW absorber solid increases by increasing the gas velocity or switching from an endothermic reaction to a no-reaction and/or exothermic reaction. In addition, the collected results show non-uniform temperature distribution in a fixed bed reactor made of MW absorber particles irradiated by MWs due to the limited penetration depth of MWs and hot spot formation. This operational deficiency makes the large-scale design of this type of reactor very challenging for MW heating-assisted reactions.

5.1. Introduction

Chemical and metallurgical industries significantly contribute to global warming since they produce a large amount of carbon dioxide (CO_2) annually [1–4]. One of the main sources of produced CO_2 is the combustion of fossil fuels to supply their required energy/feedstocks. This problem can partly be tackled by applying process electrification integrated with renewable electricity. Electromagnetic waves (EMWs) from renewable energy sources can help decrease the rate of CO_2 emissions compared to the conventional heating approach supplied by fossil fuels or even renewable energy [5,6]. Applying EMWs can enhance reaction selectivity/yield. It can, hence, result in a lower energy consumption/carbon footprint for the separation process and the overall process, accordingly. EMWs contain electrical (E) and magnetic (H) fields with propagation speeds similar to light in a vacuum and oscillating perpendicular to each other [7–9]. Microwave (MW) is a certain type of electromagnetic (EM) wave having a wavelength in the range of 1 m to 1 mm and a frequency in the range of 300 MHz to 300 GHz [7,10]. For laboratory trials, a frequency of 2.45 GHz is preferred since the penetration depth, i.e., the depth in an object at which electric field strength reaches 37% of its value at the surface of the object, achieved under this frequency, is adequate for most reactive conditions. In addition, 2.45 GHz is among the allowed frequencies in North America for industrial/laboratory applications to prevent interference with other applications [11].

As schematically depicted in Figure 5.1, heat transfer in the conventional heating approach is from the surface of a solid object to its core due to the shallow penetration depth of infrared waves [7,10]. However, materials are not following the same phenomena when exposed to MWs. A higher penetration depth of MWs in materials compared to that of infrared waves results in their volumetric heating [12–14]. In the MW heating approach, because of heat loss from the surface, the central temperature is commonly higher compared to the surface temperature, which leads to heat transfer from the center of the object to its surface [7,15]. In addition, volumetric heating by MWs happens when the solid particle size of a MW absorber material is optimally smaller than the MW's penetration depth [7].

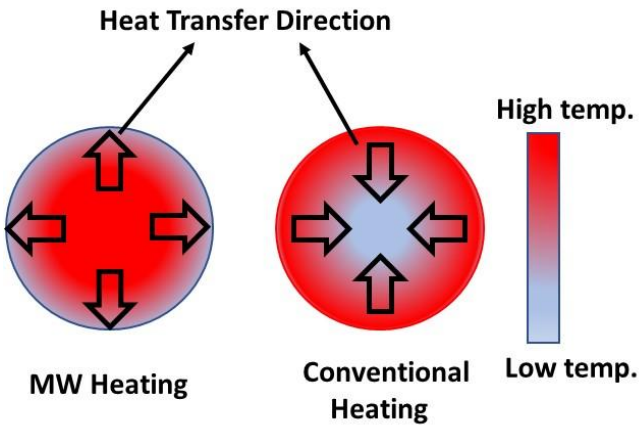

Figure 5.1: Schematic representations of temperature distributions in a MW receptor particle heated by MW heating and conventional heating approaches.

Materials exposed to MW heating can be categorized into three main groups. They are (i) transparent materials through which MWs pass with negligible interaction, (ii) reflective materials, which MWs reflect from their surfaces due to the small penetration depths of EMWs inside these materials, and (iii) MW absorber materials with a high dielectric loss factor, which represents the materials' capability of converting EMW energy to heat. Since in gas-solid systems, the gas phase is transparent to MWs, and the solid phase is commonly designed to be MW absorbers, EMWs directly interact with solid materials which results in their selective and rapid heating. The selective and rapid heating characteristics of the MW heating approach decrease the processing time and energy consumption [10,16].

While the MW heating approach is rapid, it also yields a higher selectivity and reaction rate compared to conventional heating owing to the selective heating and hot-spot formation [17,18]. Different dielectric properties of gas and solid result in the selective MW heating of solids and, thus, the formation of a temperature difference between the gas and solid phases. This temperature difference, with a lower gas phase temperature in comparison with the solid phase temperature, can result in the suppression of secondary (undesired) reactions if they happen in the gas phase [18]. Researchers believe that decreasing the activation energy in gas-solid catalytic/non-catalytic reactions is owing to the underestimation in hot-spot temperatures rather than non-thermal effects, and the intrinsic activation energy of the reaction does not change under MW irradiation [10]. In addition, both the increasing and decreasing of the pre-exponential factor of reaction kinetics under MW irradiation were reported in literature. However, since MWs can potentially improve agitation

and the pre-exponential factor represents the collision frequency in a specific reaction, its reduction under MW heating is questionable [10,19,20]. Moreover, no theoretical proof and accurate experimental observations were reported to accurately answer the MW effect on chemical reaction improvement [19,20]. Interested readers are encouraged to check out the recent review by Adavi et al. [21] for further details.

To maximize MW absorption by MW responsive materials and temperature uniformity throughout the cavity (i.e., a metallic structure applied to confine EMWs) and to prevent MW reflection to the waveguide, a 3-stub tuner can be applied in the waveguide. The 3-stub tuner helps with impedance matching between the waveguide and MW cavity. The impedance of EMWs is the ratio of the transverse components of the electrical field to those of the magnetic field. Transverse components are those perpendicular to the direction of EMWs propagation [21]. The impedance of the cavity can be affected by variations in voidage, diameter, and height of the loaded sample (i.e., the gas-solid mixture in a gas-solid reactor, also called the bed), as well as its electrical conductivity. Decreasing the electrical conductivity of the bed and increasing its voidage increase the impedance of the bed by changing the effective properties of the MW absorber bed (refer to Section 5.2.2.1). Therefore, its impedance can be closer to the impedance of air, i.e., 377 ohms, often present in the waveguide. In addition, increasing bed dimensions in the cavity can change the electromagnetic field distribution in the bed and, hence, the impedance of the cavity. A smaller bed diameter and height are recommended for beds with a smaller penetration depth to prevent MW reflection to the waveguide. However, for materials with a high penetration depth, a higher bed diameter and height are applicable [22].

One of the main challenges in MW heating-assisted systems is the accurate measurement of the solid and gas temperatures. Currently, no technique is reported in literature to effectively measure the local temperatures of gas and solid phases under MW heating [17]. This limitation has a crucial influence on the gas-solid reactive systems since the temperature of the hot spots on the solid surface are vital factors to explain the absence or presence of non-thermal effects of MWs [17,23,24]. Available techniques for temperature measurements in MW heated systems are metallic thermocouple [17,25–27], infrared (IR) thermography [17,28], pyrometer [28,29], fiber optic probe [28,29], air thermometer [30], radiometry method [17,31], polymeric thermometer [17], wireless thermocouple [32], and Raman spectroscopy [28,33].

Applications of the MW heating approach for endothermic reactions have been extensively investigated in literature. However, there is limited information about the effect of the MW heating approach on the local temperature difference between solid and gas phases in exothermic reaction systems. Therefore, micro-scale temperature measurement/estimation is essential in MW heated systems to understand the effects of process parameters, e.g., superficial gas velocity (U_g) and reaction heat ($\dot{Q}_{rxn}$) on the local temperature difference between gas and solid phases. In addition, MW heating has been extensively employed in lab-scale fixed-bed reactors. Dissipated power distributions in these reactors and MWs penetration depth under different bed voidages are, however, not reported in detail in literature. This information is crucial to understand sources of discrepancies between kinetic parameters obtained under conventional and MW heating approaches.

To investigate the effects of $\dot{Q}_{rxn}$, U_g, and temperature measurement probe location at micro-scale on the temperature gradient between gas and solid phases, as well as the estimation of microwave penetration depth and temperature distribution in fixed beds heated by MWs, a multiphysics model was initially developed in COMSOL Multiphysics (5.6) (Section 5.2). Upon verifying and validating the model with available data from literature and those collected in this study (Section 5.5.1), numerical simulations (details in Section 5.5.3) were accomplished to estimate the temperature gradient between gas and solid phases (i) in the reactive (with different possibilities for the heat of reaction) and/or non-reactive gas-solid systems (Section 5.5.3), (ii) at different temperature probe locations from the particle surface d (Section 5.5.4), and (iii) at different U_g (section 5.5.5). In addition, power dissipation/temperature distribution and MW penetration depth under different bed voidages in a MW-heated fixed-bed reactor are reported in Section 5.5.6.

5.2. Model Development

COMSOL Multiphysics can help investigate temperature distribution in MW-heated gas-solid systems on the micro-scale, which is limited to being measured experimentally due to the lack of proper measurement techniques. In this section and Section 5.3, COMSOL Multiphysics modeling and simulation details, including assumptions, governing equations, simulated geometries, boundary conditions, and grid independency analysis are reported.

5. 2.1. Assumptions

The general assumptions made in this study to develop a model that can estimate micro-scale temperature distribution in MW heating gas-solid reactive/non-reactive systems are reported in the following list:

(i) Silicon carbide (SiC) is considered as MW absorber and catalyst support, and the properties of the catalyst are assumed to be similar to SiC.
(ii) Manganese nitridation reaction is considered as the model for the exothermic reaction.
(iii) Hydrogenation of the manganese nitride reaction is applied as the model for the endothermic reaction.
(iv) Fluid properties are calculated as a function of temperature, and they are applied from the available values in the database of COMSOL Multiphysics.
(v) MW receptor properties, including permittivity, permeability, heat capacity, thermal conductivity, and density, are considered constant.
(vi) We neglected the magnetic heat loss in the MW absorber, and solely the electrical component of MWs is considered for the MW receptor heating.

5.2.2. Governing equations

As presented in Figure 5.2, a set of equations with suitable boundary conditions should be solved to model and simulate the gas-solid reactive/non-reactive system. Initially, Maxwell's equation was solved to calculate the electromagnetic field distribution. Then, the Navier stocks, continuity, energy balance, and mass balance equations were solved simultaneously. For the calculation of local gas velocity $\vec{u}$, the Navier stocks and continuity equations were solved. The calculated $\vec{u}$ was subsequently applied to mass and energy balance equations to estimate chemical species compositions and local temperatures, respectively. In the following, the temperature distribution was applied to the Navier stocks equation for the calculation of gas properties. The mentioned equations are presented in detail in Sections 5.2.2.1–5.2.2.4.

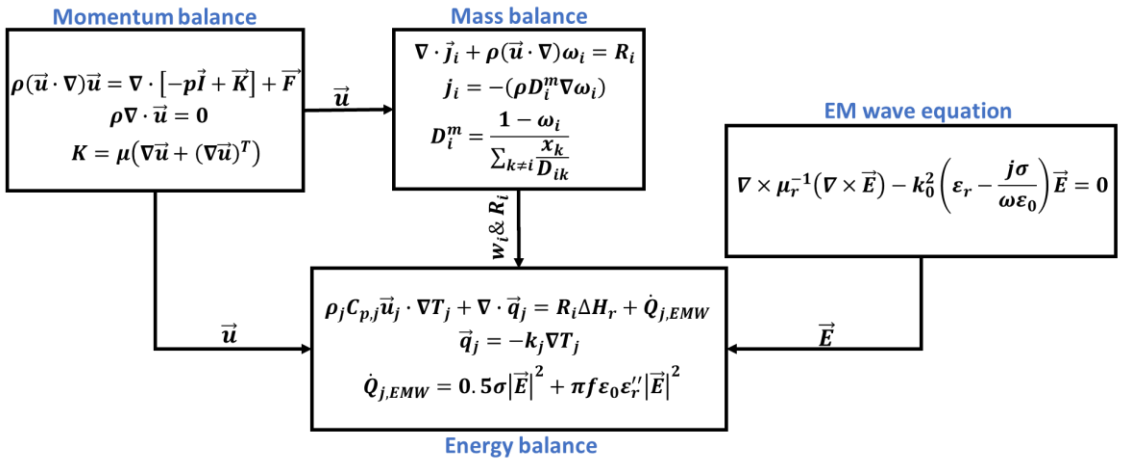

Figure 5.2: Employed equations and their corresponding relationships to estimate local temperatures in a MW heated gas-solid system in this study.

5.2.2.1. EM wave equation (Maxwell equation)

The EMW (Maxwell) equation, Eq. (5.1), was applied and solved for the local electromagnetic field calculation [5].

$$\nabla\times\mu_{r,eff}^{-1}(\nabla\times\vec{E})-\left(\frac{c}{\omega}\right)^2\left(\varepsilon_{r,eff}-\frac{j\sigma_{eff}}{\omega\varepsilon_0}\right)\vec{E}=0 \tag{5.1}$$

where $\vec{E}$, μ_r, and ε_r are the electrical field strength, the relative permittivity, and the relative permittivity, respectively. σ, ω, and ε_0 show the electrical conductivity, angular frequency, absolute permeability in free space, respectively. Subscript eff shows effective parameters. σ_{eff} and $\varepsilon_{r,eff}$ can be calculated by Eqs. (5.2) and (5.3) as follows:

$$\sigma_{eff}=\varepsilon\sigma_F+(1-\varepsilon)\sigma_s \tag{5.2}$$

$$\varepsilon_{r,eff}=\varepsilon\varepsilon_{r,F}+(1-\varepsilon)\varepsilon_{r,s} \tag{5.3}$$

where ε represents the bed voidage, and subscripts s and F refer to solid and fluid phases, respectively. Power dissipation ($\dot{Q}_{MW}$) can be estimated as a function of $\vec{E}$ by applying Eq. (5.4) [10].

$$\dot{Q}_{j,EMW}=0.5\sigma_{eff}|\vec{E}|^2+\pi f\varepsilon_0\varepsilon_{r,eff}''|\vec{E}|^2 \tag{5.4}$$

where f is the frequency.

5.2.2.2. Momentum balance

The Navier stocks, Eq. (5.5), and continuity, Eq. (5.6), equations were applied for estimations of $\vec{u}$ and the pressure profile [5].

$$\rho_g(\vec{u}\cdot\nabla)\vec{u} = \nabla\cdot\left[-p\vec{I}+\vec{K}\right] \tag{5.5}$$

$$\rho_g\nabla\cdot\vec{u} = 0 \tag{5.6}$$

where p is the pressure, $\vec{I}$ is the unit vector, ρ_g is the gas density, and μ is the gas viscosity. $\vec{K}$ is the viscous momentum transfer term, which can be estimated as follows [34]:

$$\vec{K} = \mu(\nabla\vec{u} + (\nabla\vec{u})^T) \tag{5.7}$$

5.2.2.3. Mass balance

The mass balance equation, Eq. (5.8), was applied and solved to calculate the local composition of chemical species [35].

$$\nabla\cdot\vec{j}_i + \rho(\vec{u}\cdot\nabla)w_i = R_i \tag{5.8}$$

where $\vec{j}_i$ is the diffusive mass transfer flux of species i, w_i is the mass fraction of species i, R_i is the reaction rate of species i, and D_i is the diffusion mass transfer coefficient of species i. $\vec{j}_i$ can be calculated as follows [35]:

$$\vec{j}_i = -(\rho D_i^m\nabla w_i) \tag{5.9}$$

where D_i^m is the diffusion mass transfer coefficient of species i in the mixture that can be calculated as follows [35]:

$$D_i^m = \frac{1-w_i}{\sum_{k\neq i}\frac{x_k}{D_{ik}}} \tag{5.10}$$

where x_k is the mole fraction of species k.

The reversible manganese nitridation and hydrogenation reactions, referring to assumptions (ii) and (iii), were considered as follows [12]:

$$Mn + N_{2(g)} \rightleftharpoons Mn_4N \qquad \Delta H_r = (-0.0001 \times T^2 + 0.094 \times T - 263.25)\ kJ/mol \tag{5.11}$$

$$Mn_4N + H_{2(g)} \rightleftharpoons Mn + NH_{3(g)} \qquad \Delta H_r = = (8 \times 10^{-8} \times T^2 - 0.0675 \times T - 86.088)\ kJ/mol \tag{5.12}$$

where T is the reaction temperature.

5.2.2.4. Energy balance

The energy balance equation, Eq. (5.13), was coupled with the mass balance, Navier Stocks, continuity, and Maxwell equations for the calculation of local temperature in the gas-solid system [35].

$$\rho_j C_{p,j} \vec{u}_j \cdot \nabla T_j + \nabla \cdot \vec{q}_j = \dot{Q}_{j,EMW} + \dot{Q}_{rxn} \tag{5.13}$$

where ρ_j, $C_{p,j}$, T_j, and $\vec{q}_j$ are the density, heat capacity, temperature, and conductive heat flux of phase j (gas or solid). $\dot{Q}_{rxn}$ can be calculated as follows:

$$\dot{Q}_{rxn} = \Delta H_r R_i \tag{5.14}$$

where ΔH_r is the reaction enthalpy change. $\vec{q}_j$ is calculated as follows [10]:

$$\vec{q}_j = -k_j \nabla T_j \tag{5.15}$$

where k_j is the thermal conductivity of phase j. A summary of the governing equations and their relationships are presented in Figure 5.2.

5.3. Numerical simulation

5.3.1. Geometry and model parameters

We applied a SiC monolith (see Figure 5.3a.1) similar to what was employed in the study performed by Malhotra et al. [5] for verification and validation of the developed model by results reported in the same study. Monolith has 21 square channels with a size of 1.3 mm × 1.3 mm and a length of 15 mm. A cylindrical cavity with an inner diameter of D= 105mm and length of L=85 mm equipped with a coaxial port located in the central height of the cavity, where the EM field is maximum, was employed. The mode type of the coaxial port is transverse electromagnetic (TEM) in which both electric and magnetic fields are transverse. A quartz tube with a diameter of D_b=10 mm and height of L=85 mm was placed in the center of the cavity, and a monolith (for model verification and validation and subsequent parametric studies) or a single SiC particle (for parametric studies) was alternatively located at its central height (see Figure 5.3).

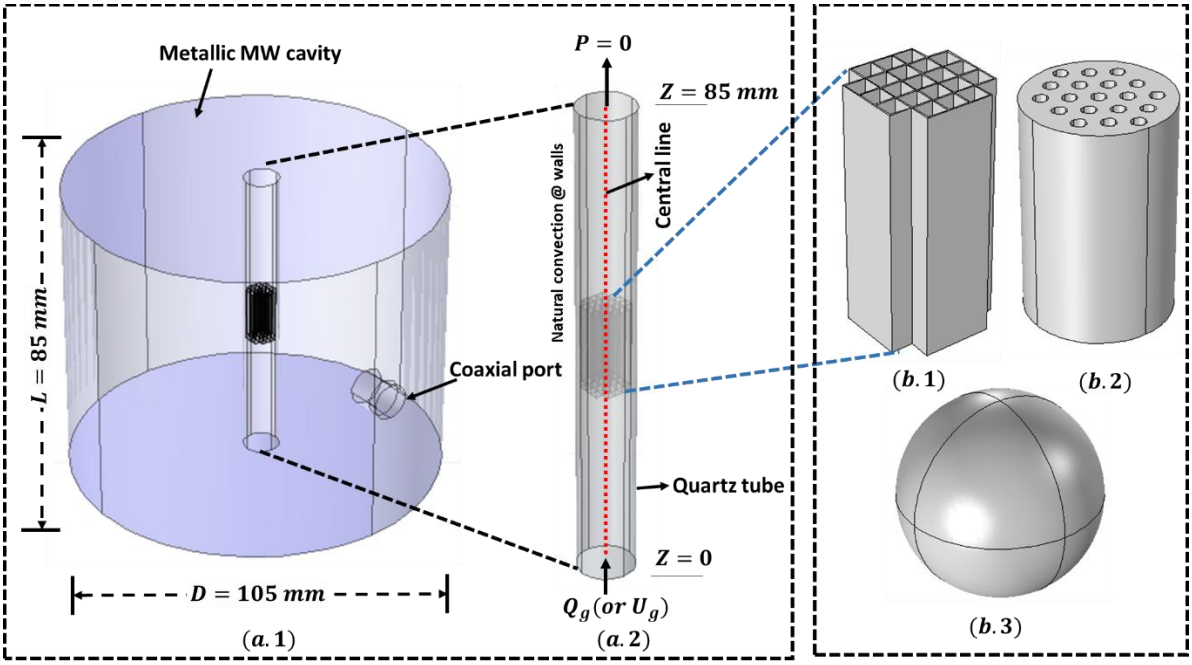

Figure 5.3: a.1 and a.2 are schematic representations of the MW heating system and quartz tube, respectively adopted for model verification and validation and parametric studies in this work; b.1 is the multichannel monolith applied for model verification and validation from the work of Malhotra et al. [5]**, b.2 and b.3 are the multi-hole monolith and the single particle employed in the present work for subsequent parametric simulations, respectively.**

A multi-hole SiC monolith with a D=10 mm and H_b=15 mm with 19 circular holes having a diameter of 1 mm (see Figure 5.3b.2) was selected for the investigation of the MW heating effect on temperature distribution in gas-solid systems in comparison with a conventional heating

approach. A spherical particle that was 500 µm in size (see Figure 5.3b.3) was applied to study the effect of MW heating on the temperature gradient between solid and gas phases at the micro-scale.

As shown in Figure 5.4a, to examine the effects of MW heating on temperature distribution in packed SiC particles, beds with a diameter range from D_b=10 to 60 mm and a length of H_b=30 mm were heated under MW. In addition, a fixed bed with a D=1 m and H_b=1 m was applied to study the effect of ε on the penetration depth of MWs in the bed (see Figure 5.4b). Parameters that were employed for the COMSOL simulations in the present work are reported in Table 5.1.

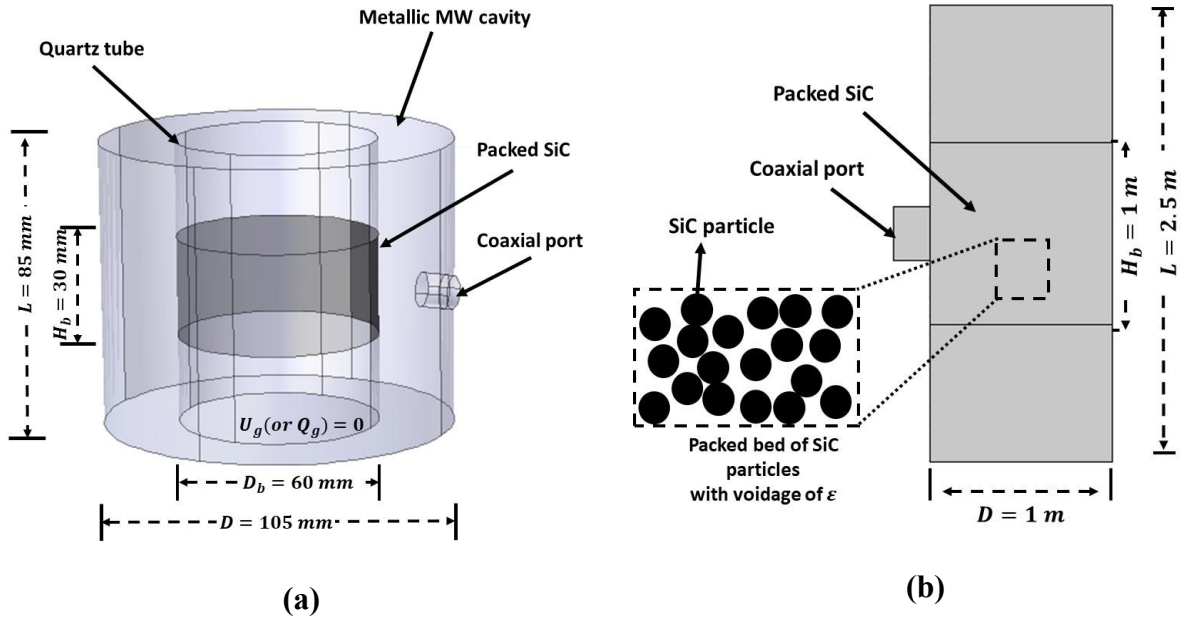

Figure 5.4: Schematic representation of MW heated packed SiC particles in this work; (a) 3D model of a SiC fixed bed, (b) 2D model of a SiC fixed bed.

Table 5.1: Model's parameters of the present work.

Parameter	Value	Reference
SiC permeability, $\mu_{r,SiC}$ [-]	1	*
SiC permittivity, ε_{SiC} [F/m]	9.72-2.3j	[5]
SiC density, ρ_{SiC} [Kg/m^3]	3216	*
SiC electrical conductivity, σ_{SiC} [S/m]	100	[5]
SiC heat capacity, C_p [J/kg.K]	690	*
SiC thermal conductivity, k_{SiC} [W/mK]	50	[5]
Air permeability, $\mu_{r,Air}$ [-]	1	*
Air permittivity, ε_{Air} [F/m]	1	*
Nitridation reaction rate, R_1 [µmol/g.h]	$2.84 \times 10^8 exp\left(\frac{-47150}{RT}\right)(1-X)$	[12]

Table 5.1 (cont'd): Model's parameters of the present work.

Hydrogenation reaction rate, R_2 [μmol/g.h]	$1.57 \times 10^9 exp\left(\frac{-58240}{RT}\right)(1-X)$	[12]
MW input power, P_0 [W]	50-5000	[5]
Superficial gas velocity, U_g [m/s]	0-3	*

* Corresponding values were employed from COMSOL Multiphysics' database.

5.3.2. Boundary conditions

Impedance boundary condition was considered for the metallic cavity to decrease the computational cost, and a coaxial port was defined to supply MWs to the cavity. In addition, first-order scattering boundary conditions were defined at the inlet and outlet of the tube to prevent reflection artifacts.

The Navier Stocks equation was solved with a specific Q_g or U_g at the inlet and zero-gauge pressure (P=0) at the outlet of the quartz tube. The mass balance equation was also considered with pure N_2 at the inlet and no mass flux at the outlet for the reactive system in the axial direction. The manganese nitridation and manganese nitride hydrogenation reactions were considered in the MW absorber domain. For energy balance, the gas was at 25 ˚C at the inlet of the tube with no heat flux conditions at the outlet. The quartz tube was exposed to room temperature, where it loses heat to the ambient. Natural heat convection from the quartz external wall (see Figure 5.3) and the radiative heat transfer from the monolith/particle are two additional heat loss sources from the monolith/particle to the environment. The natural convection heat transfer coefficient was estimated by Eq. (5.16) at the external surface of the quartz tube [36].

$$Nu_L = \frac{h_L L}{k_g} = \frac{4}{3}\left(\frac{7Ra_L Pr}{5(2+21Pr)}\right)^{0.25} + \frac{4(272+315\mathrm{Pr})\mathrm{L}}{35(64+63Pr)\mathrm{D}} \tag{5.16}$$

where the Nu_L shows the Nusselt number, h_L denotes the free convection heat transfer coefficient, Pr is the Prandtl number, and Ra_H is the Rayleigh number.

5.3.3. Grid independency analysis

For grid independency analysis, different number of cells were considered to identify the optimum cell number that helps minimize computational cost, while providing an acceptable accuracy of results. Meshing was applied to ensure that at least six grid cells per wavelength (around 12.2 cm in the air) in the MW cavity are employed. Cell sizes of extremely fine, extra fine, finer, fine, and normal, which are available in COSMOL's settings, were considered for this analysis (see Figure 5.5 for further details and their corresponding cell numbers). Free tetrahedral cells were considered in all domains, including bed, cavity, and waveguide. The absorbed power was considered as the reference value to investigate the effect of cell number or the corresponding cell size on the calculated results. The value of absorbed power was calculated by applying volume integration of heat loss per unit of volume on the MW absorber bed domain for different cell numbers in the grid independency analysis here. The optimized number of cells of 486,785 (see Figure 5.5) was considered for simulations of monolith 1 (Figure 5.3b.1), and its average mesh quality based on the volume versus length quality measure technique was 0.962. The volume versus length quality measure technique is based on the quotient of element volume and element edge length that is available in COMSOL Multiphysics. With the same procedure, 385,158 (mesh quality=0.953) and 375,847 (mesh quality=0.971) cells were identified as the optimal ones for simulations of monolith 2 (Figure 5.3b.2) and the single-particle (Figure 5.3b.3), respectively.

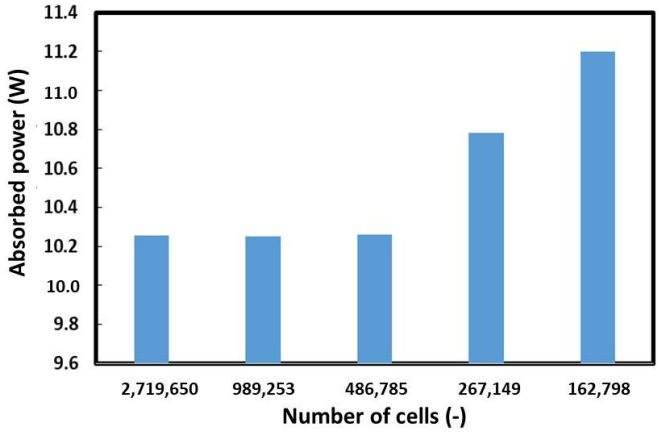

Figure 5.5: Mesh independency results for SiC monolith 1 system for extremely fine (2,719,650 cells), extra fine (989,253 cells), finer (486,785 cells), fine (267,149 cells), and normal (162,798 cells) mesh sizes.

5.4. Experimental in this study

A MW cavity with dimensions of 33×22.5×32.5 cm (depth × height × width) was applied in this study to validate the temperature of a SiC foam with ε, D, and H_b of 0.65, 4 cm, and 2 cm, respectively. The schematic representation of the adopted experimental setup in this study for the collection of additional experimental data for supplementary model validation is presented in Figure 5.6. The unit had a magnetron capable of supplying MWs with a frequency of 2.45 GHz and power of 1 KW. The SiC foam was placed in the MW cavity as depicted in Figure 5.6. A grounded metallic thermocouple (k-type with a diameter of 2 mm) was applied for measuring the local temperature of the upper surface of the SiC foam exposed to MW irradiations (see Figure 5.6). Employing a grounded metallic thermocouple can reduce the risk of spark formation resulting from the interference of EMWs with the thermocouple during an experiment.

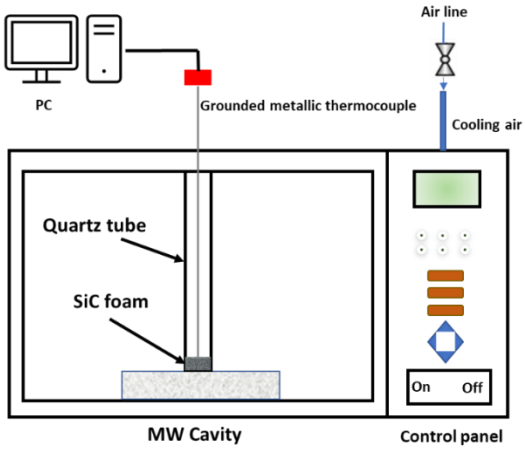

Figure 5.6: Schematic representation of the adopted experimental setup in this study.

5.5. Results and Discussion

5.5.1. Model verification and validation

The developed model was verified and validated successfully by employing simulation and experimental results obtained by COMSOL Multiphysics, metallic thermocouple, and IR camera readings reported in the study of Malhotra et al. [5]. Input MW power was fixed at 120 W, and gas with a temperature of 25 ˚C and a Q_g of 100 SCCM (U_g=2 cm/s) was defined at the inlet of the quartz tube, like what was defined in Malhotra et al.'s model [5]. The gas and solid axial temperatures at the central line along the axis (refer to Figure 5.3) calculated in the developed model in this study are shown in Figure 5.7. They agree with the results from the Malhotra et al.

model for the same monolith, which can be regarded as model verification. Since the wall of the tube is in contact with air at 25 ˚C, the monolith's sidewall temperature, which is estimated in this work, is lower compared to the axial temperature (see Figure 5.7). These results are in good agreement with results measured by applying the IR camera in the Malhotra et al. study [5] (model validation). The rapid increase of the axial temperature in the interval, where the monolith was located, i.e., Z=35-50 mm, indicates the selective heating of the monolith in the MW heated system.

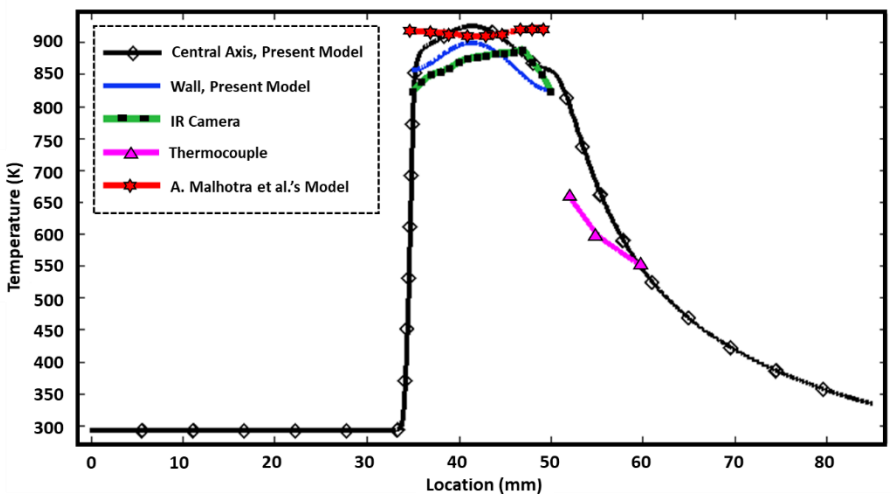

Figure 5.7: Developed model verification and validation by applying simulation and experimental results presented in the work of Malhotra et al. [5].

Malhotra et al. located a thermocouple 50 mm after the monolith to measure the gas phase temperature passed through the monolith [5]. Both experimental results [5] and those estimated from the developed model in this work indicate a rapid decrease in temperature, i.e., around 90−180 K within 2−5 mm above the heated monolith's upper surface (model verification and validation). These results are consistent with available data in literature, where a decrease of 150 K was detected by a pyrometer and an IR camera 2 mm above the monolith [37].

For further model validation, the developed model was adopted to simulate the MW cavity described in Section 5.4 (see Figure 5.6). The predicted local temperatures over time by the model were validated by the acquired experimental results (see Section 5.4 for more details). For temperature evaluation by applying COMSOL Multiphysics, a point probe was located on the upper surface of the SiC foam similar to what was achieved experimentally. The predicted

temperatures by the model were compared to the experimental data and the results are shown in Figure 5.8, where good agreement is evident between the simulation and experimental results. Therefore, the developed COMSOL model was successfully validated based on the additional and independent experimental data confirming its comprehensiveness. A slight deviation between experimental and simulation results can be related to the limited ability of metallic thermocouples to accurately measure the local temperature under MW irradiations.

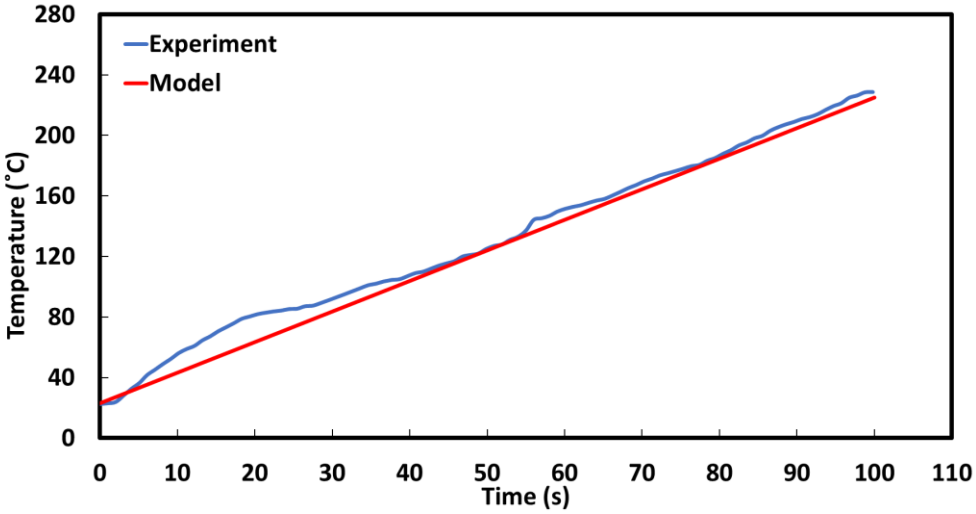

Figure 5.8: Validation of developed model by applying experimental data obtained in this study.

5.5.2. Comparison of conventional and MW heating approaches

COMSOL simulations were attempted for monolith 2 (Figure 5.3b.2) in the quartz tube under non-reactive conditions to compare the effects of conventional and MW heating approaches on gas and solid temperature distributions (see Figure 5.9 for results). To study the conventional heating approach effect on the temperature distribution in a gas-monolith system, the tube wall was either completely (Figure 5.9a) or partially along the axis of the monolith (Figure 5.9b) and kept at a constant temperature, i.e., 727 °C. In the conventional heating approach, heating is from the wall toward the tube center. Therefore, the wall temperature is higher than that along the axis of the tube. This temperature difference increases with Q_g. At Q_g=20 SCCM, relatively uniform local gas and solid temperatures exist along the axis (Figure 5.9a.1 and 5.9b.1). At Q_g=100 SCCM, however, the local temperatures of the gas and solid phases along the axis were lower than those at near-wall locations (Figure 5.9a.2 and 5.9b.2).

A rapid gas temperature decrease above the monolith's top surface and the temperature difference between gas and solid in monolith holes are observed in Figure 5.9c.1 and 5.9c.2. These indicate the MW heating approach's effectiveness in suppressing the secondary reactions that can happen in the gas phase. However, in the conventional heating approach, the entire gas-solid system was heated, which increases the risk of gas phase secondary reactions [38,39].

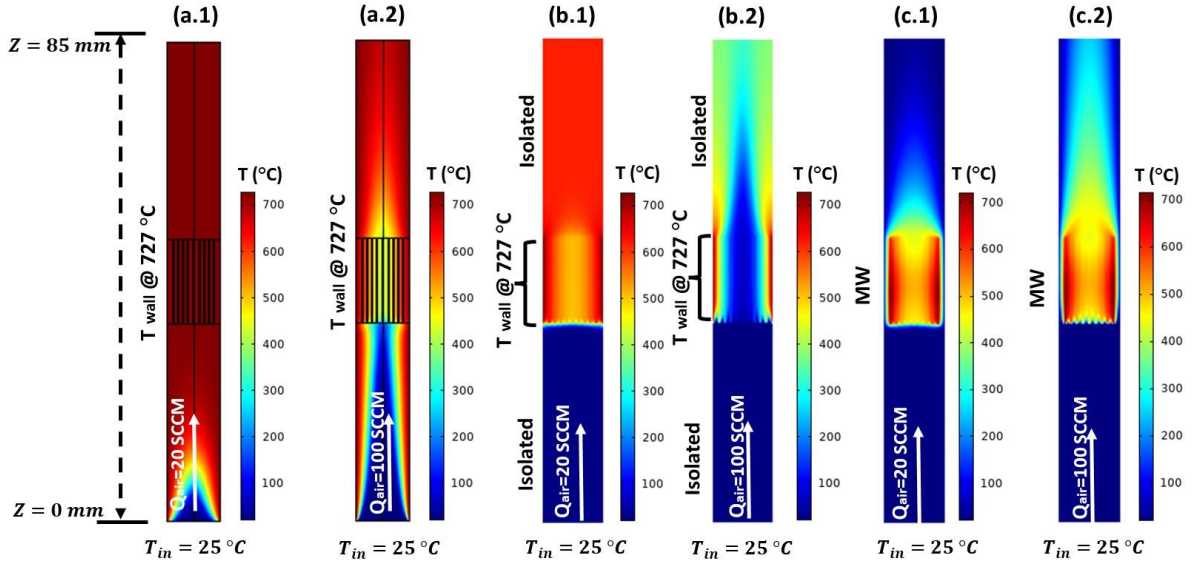

Figure 5.9: Variations of local gas and solid (monolith 2) temperatures at different inlet Q_g, (a) conventional heating approach and the whole wall was kept at a constant temperature of 727 °C and U_g=0.4, 2 cm/s, (b) conventional heating approach and only unit wall corresponding to the monolith height was kept at a constant temperature of 727 °C, while other parts are isolated, and U_g=0.4, 2 cm/s, (c) MW heating approach with U_g=0.4, 2 cm/s.

As illustrated in Figure 5.9c, in the MW heating approach, increasing the gas flow rate from 20 SCCM (U_g=0.4 cm/s) to 100 SCCM (U_g=2 cm/s) yields a slight temperature decrease (20-50 °C) in the monolith at a fixed inlet power and 100 sec into the simulation. However, a more pronounced temperature decrease (100-250 °C) in the monolith can be observed for the conventional heating approach (see Figure 5.9a and Figure 5.9b) for the same change in the Q_g, inlet power, and simulation time. These findings reveal that in the range of Q_g explored here, the solid-phase temperature is less sensitive to the inlet gas flow rate at a fixed inlet power under the MW heating approach than the conventional heating approach.

5.5.3. Effect of reaction heat on the temperature gradient between gas and solid phases

To investigate the effect of $\dot{Q}_{rxn}$ on the local temperature gradient between gas and solid phases heated by MWs, a spherical particle (rather than a monolith) was placed in the cavity (see Figure 5.3). This evaluation was accomplished at different U_g and a d of 1 mm away from the particle surface at 100 sec into the simulation. Three cases, including endothermic, exothermic reaction, and no reaction, were considered. Irrespective of the heat of the reaction (endothermic, exothermic or no reaction), the MW heating approach can provide an appreciable temperature gradient between solid and gas phases (see Figure 5.10). By switching from endothermic reaction to no reaction to exothermic reactions, the temperature difference between gas and solid phases increases. The local temperature difference between solid and gas phases under no reaction conditions for U_g=3 m/s is 268 °C. For the assumed endothermic and exothermic reactions, referring to assumptions (ii) and (iii) in Section 5.2.2, the local temperature difference between gas and solid phases is 258 °C and 276 °C, respectively. There was additional heat generation inside the particle under exothermic reactions to what is provided by MW heating resulting in a higher temperature gradient between gas and solid phases because of higher solid temperature. This effect is expected to be intensified by increasing the particle size due to a lower particle surface area per its mass.

Results presented in this section recommend that the MW heating approach can be applied for a wide range of reactions, including endothermic, e.g., steam and dry methane reforming, and exothermic reactions, e.g., methanol synthesis [17,40], while taking advantage of its thermal effect to enhance the desired product selectivity/yield.

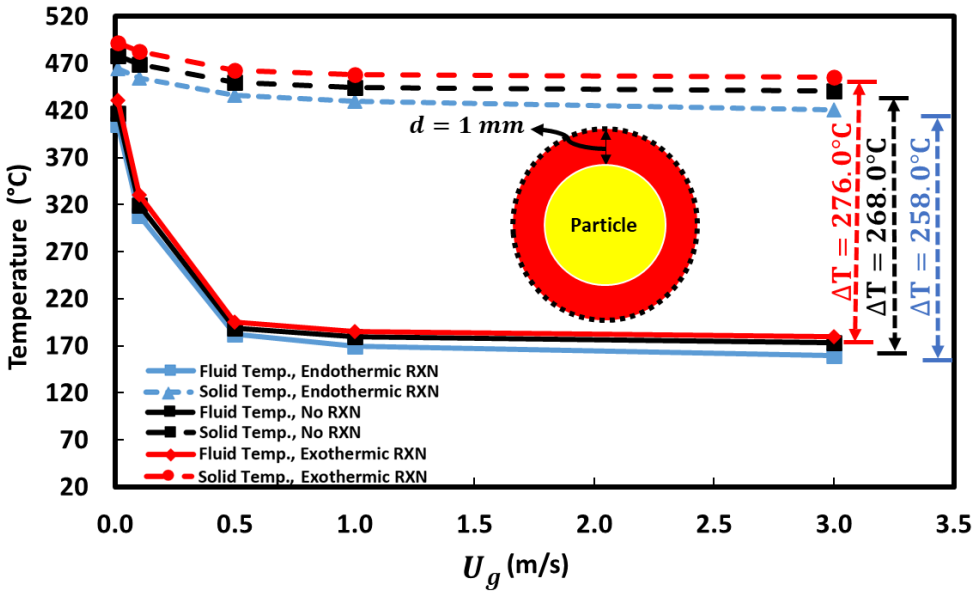

Figure 5.10: Effect of $\dot{Q}_{rxn}$ at different U_g on the temperature gradient between gas and the MW absorber solid particle for endothermic reactions, no reaction, and exothermic reactions.

5.5.4. Effect of temperature probe location at micro-scale on the temperature difference between MW absorber solid and gas phases

To investigate the temperature probe location at the micro-scale effect on the temperature difference between gas and solid phases, the same MW absorber particle studied in the previous section (see Figure 5.3) at 100 sec into the simulation was considered. A non-reactive system was adopted, and U_g was set at 0.5 m/s, while input power was adjusted to 400 W. The local temperature difference between MW heated solid and gas was estimated based on the temperature integral average on the particle surface and a virtual sphere at different d; the latter corresponded to the gas temperature (see Figure 5.11).

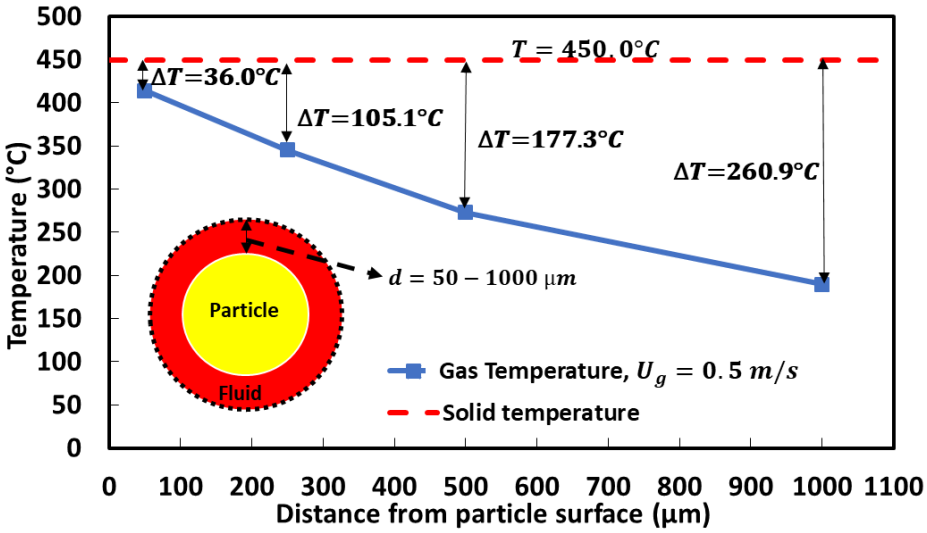

Figure 5.11: Temperature probe location at the micro-scale effect on the temperature difference between MW heated solid and gas phases.

Results presented in Figure 5.11 indicate that the temperature probe location noticeably changes the calculated local temperature difference between gas and solid phases. For example, at d=50 µm the temperature difference between the gas and solid is 36 °C, while it increases to 261 °C at d=1000 µm. These results show the significant effect of local temperature measurement probe dimensions and their location on the local temperature difference that can be measured between gas and the MW absorber solid. Therefore, for measuring temperature accurately in MW heated systems, the thermometer's size (especially diameter) and its location should be adjusted carefully [30,41].

5.5.5. Effect of superficial gas velocity on the temperature gradient between gas and solid phases

A non-reactive system was considered to investigate the effect of U_g on the temperature gradient between gas and the MW absorber solid particle. Air was considered as the passing fluid over the particle and the input power of the MW was set at 400 W, at 100 sec in the simulation. As mentioned in Section 5.3.1, the selected particle was 500 µm in size and it was placed in a quartz tube at the center of the MW cavity, where the electromagnetic field is at its maximum (see Figure 5.3).

The gas-phase temperature was calculated by the integral average of temperature on the sphere with a 1 mm distance from the particle surface. Solid and gas temperatures decrease with U_g (See

Figure 5.12). However, the extent of temperature decrease in the gas phase is higher than that of the solid phase upon increasing U_g. For instance, by changing U_g from 0.01 m/s to 1 m/s, the solid temperature decreases from 478 °C to 434 °C, while the gas temperature decreases from 416 °C to 147 °C. The different behaviors of gas and solid temperatures by increasing U_g cause a nonlinear increase of the temperature gradient between gas and solid phases with U_g. Similar trends were reported in the study by Hamzehlouia et al. [18] when U_g varied in the range of 3.4-10 cm/s for a MW-heated fluidized bed. Hence, in the case of gas-solid reaction systems with undesired secondary reactions in the gas phase, a higher U_g results in greater suppression of these undesired reactions and increases the yield of the desired products.

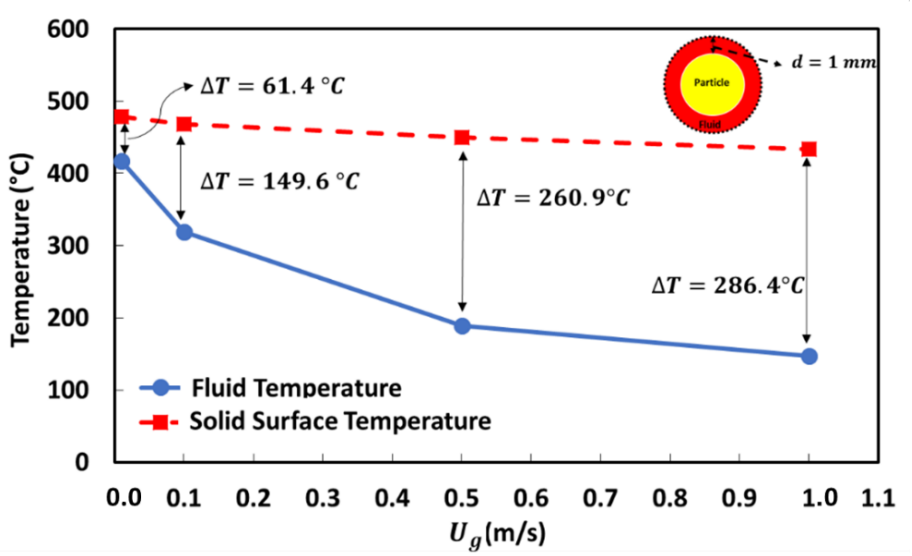

Figure 5.12: Effect of superficial gas velocity on the temperature gradient between gas and the MW absorber solid particle under MW irradiation.

5.5.6. Effects of bed voidage on power dissipation and MW penetration depth in a fixed bed

To investigate the effect of ε on the MW heating efficiency in fixed beds, a non-reactive system was considered. A quartz tube with a fixed bed of SiC particles was located in the middle of the cavity (see Figure 5.4a) and an input MW power of 5 kW was considered for this evaluation at 100 sec into the simulation. By increasing ε, power dissipation density is decreased (see Figure 5.13b; note for the color bar scales). In addition, due to impedance mismatching between the waveguide and cavity, we can observe a non-uniform power dissipation in the bed, while the pattern of power dissipation varies by changing ε. The appearance of hot spots in the bed is the result of non-uniform

temperature distribution, which can cause particle (sometimes as a catalyst) sintering and the undesired species formation in reactive systems. Solid mixing in dense fluidized bed reactors helps overcome the issues associated with hot spot formations in MW-heated beds [18].

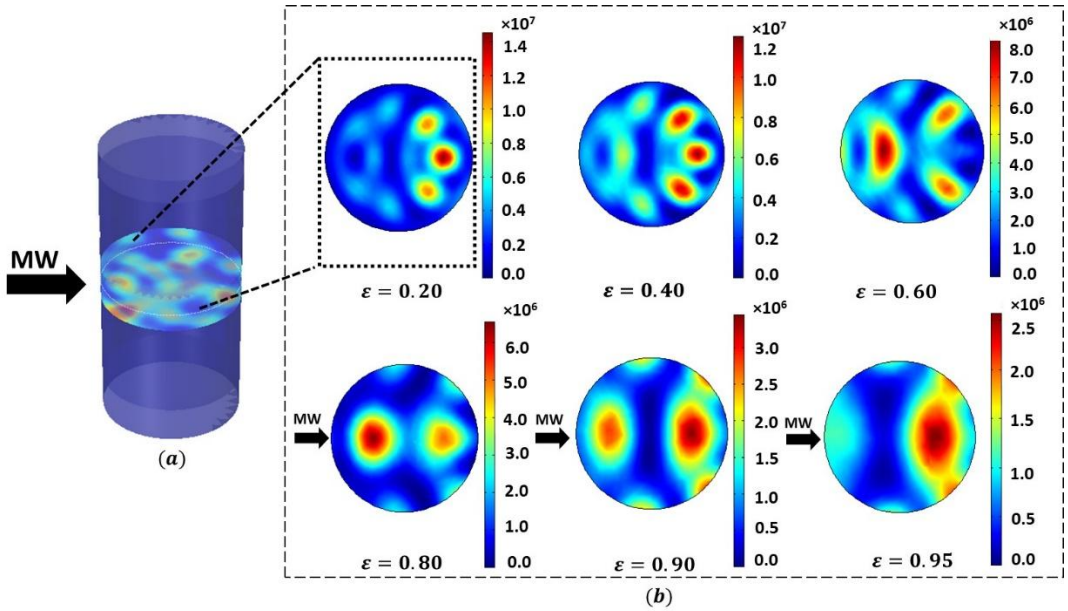

Figure 5.13: Effect of bed voidage on power dissipation (W/m^3) in a MW heated fixed-bed reactor with a packed SiC MW absorber.

Some studies reported that kinetic parameters change under MW heating due to the non-thermal effect of MW heating in addition to the thermal effect [21]. However, results presented in Figure 5.13 show that non-uniformity in heat dissipation inside the reactor can result in the underestimation/overestimation of temperature. Temperature underestimation/overestimation in a MW-heated reactor can result in a lower or higher apparent activation energy compared to when the reactor is heated conventionally. These are sources of discrepancy for kinetic parameters comparison obtained under conventional and MW heating approaches. In addition, the presence of elements/compounds with different dielectric properties in the solid phase and applying hybrid heating, i.e., employing a MW absorber, such as SiC or activated carbon, for heating materials that have poor interactions with MWs, can result in micro-scale hot spots. They can, accordingly, affect apparent kinetic parameters [21].

Macro-scale hot spots, observed in the results discussed in this section, and the micro-scale hot spots discussed above can potentially change the physical structure of the solid phase during gas-solid reaction kinetic studies. Variations of solid phase physical structure under MW heating can

affect apparent kinetic parameters. When the internal mass transfer is the reaction rate-limiting step, the appearance of micro-fractures inside solid particles can cause lower apparent activation energy compared to what can be obtained for conventional heating [21]. Therefore, minimizing micro- and macro-scale hot spots is a promising approach for estimations of intrinsic reaction kinetic parameters. Macro-scale hot spots can be partially eliminated by applying efficient solid mixing, like what can be achieved in well-mixed fluidized bed reactors [21].

The bed's dimensions have a direct effect on temperature non-uniformity under MW heating, and its optimization is essential for the impedance matching of the waveguide and MW cavity to maximize MW absorption. Results presented in

Figure 5.14 indicates that decreasing the reactor diameter causes a less non-uniform temperature distribution in the packed SiC particles. Therefore, kinetic parameters obtained from reaction kinetic studies in thinner fixed bed reactors with greater control on temperature uniformity are preferred/more accurate.

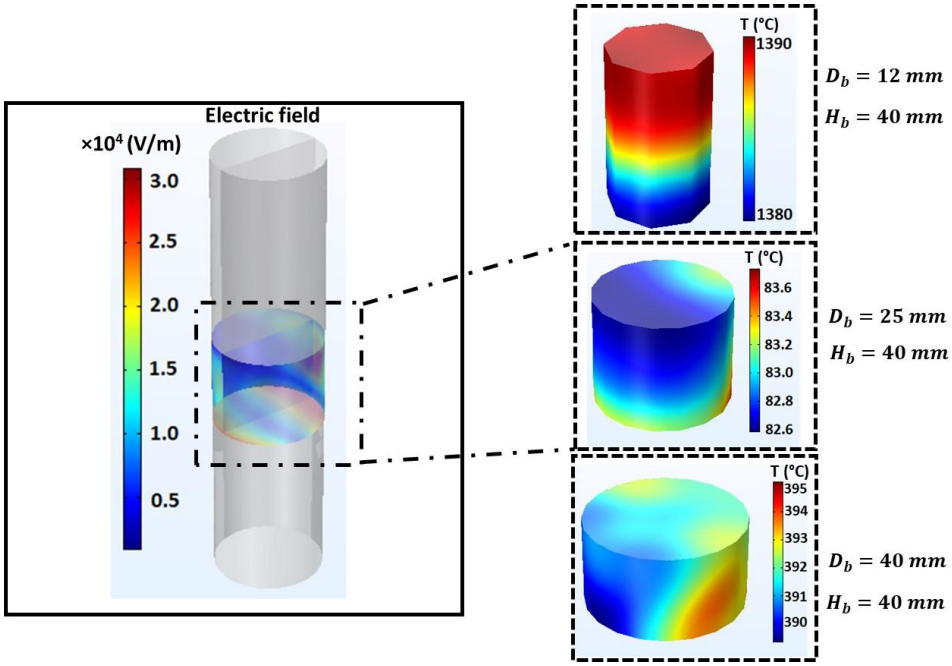

Figure 5.14: Reactor diameter effect on temperature distribution in the packed SiC particles.

To study the effect of ε on the penetration depth of MWs, a 2D quartz tube with packed SiC particles was exposed to MWs (see Figure 5.4b). The relative electrical field strength was calculated based on the electrical field strength along the radial direction divided by the electrical field strength on the outer surface of the bed at the contact boundary of the waveguide and the bed.

The length at which the electrical field strength in the bed decreases to 37% of its value on the contact area of the waveguide and the bed was considered as the penetration depth of MWs in the bed. Figure 5.15 shows by increasing ε, the MW penetration depth is increased. For the geometry studied here, the penetration depth of MWs for ε=0.4 is approximately 9 cm, while it reaches 52 cm for ε=0.9. These results indicate that because of the limited MW penetration depth in packed beds, these units should be designed carefully if they are planned to be heated by MWs.

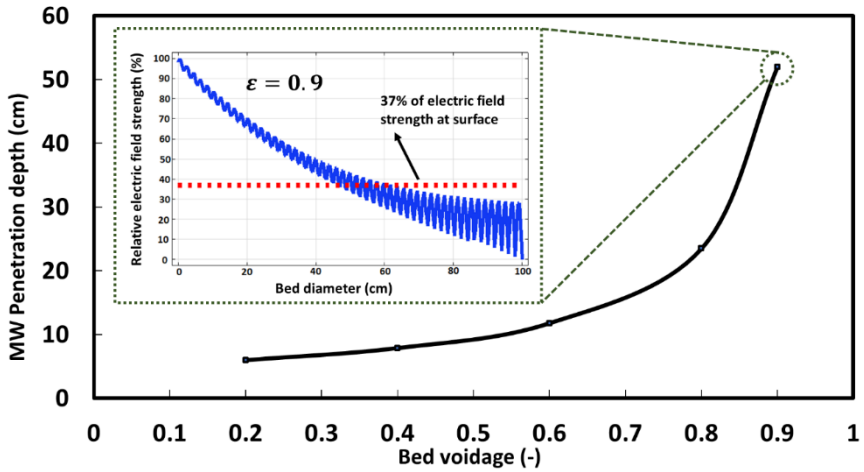

Figure 5.15: Effect of bed voidage on the MW penetration depth in the MW heated fixed-bed.

The power dissipation distribution (see Figure 5.13) and penetration depth of MWs (see Figure 5.15) calculated in this section can be applied to fluidized beds operating at various regimes, such as bubbling, turbulent, and fast fluidization regimes [42].

5.6. Conclusion

In this study, a multiphysics model, which integrates mass, heat, and momentum balance, as well as Maxwell equations, developed in COMSOL Multiphysics (5.6) was initially verified and validated. It was subsequently applied for the estimation of micro-scale and macro-scale temperature distributions in MW-heated gas-solid systems, which are restricted to being measured experimentally. The new model helps reach the following conclusions:

(i) The selective heating feature of the MW heating approach leads to a significant temperature gradient between gas and solid phases compared to the conventional heating approach.

(ii) The temperature gradient between gas and MW-heated solid phases increases by switching from an endothermic reaction to no reaction to an exothermic reaction in the gas-solid system. Hence, the MW heating approach can be effectively applied for a wide range of reactions irrespective of their heat of reactions.

(iii) Temperature gradient between gas and solid phases increases by increasing the superficial gas velocity.

(iv) Non-uniform power dissipation in fixed bed reactors can result in hot spot formations and non-uniform temperature distribution that can affect the estimated apparent kinetic parameters, which yield challenges in intrinsic kinetic studies on a lab scale. Applications of very thin fixed bed reactors or small dense fluidized bed reactors with an acceptable solid mixing are recommended under MW heating to help determine intrinsic reaction kinetic parameters.

(v) MW penetration depth increases in a packed/fluidized bed reactor by increasing the bed voidage. Precautions should be taken to prevent (a significant) temperature gradient in an industrial-scale fixed bed reactor owing to the limited MW penetration depth in these units when heated by MWs.

CRediT authorship contribution statement

Kazem Adavi: Conceptualization, Methodology, Validation, Investigation, Writing - original draft, Software, Visualization, Data-curation. **Jaber Shabanian**: Conceptualization, Methodology, Writing - review & editing, Project administration, Funding acquisition. **Jamal Chaouki:** Resources, Supervision, Writing - review & editing, Funding acquisition.

Acknowledgment

The authors gratefully acknowledge the financial support provided for this research study by the OCP Group of Morocco.

Nomenclature

Acronyms

EMW	Electromagnetic wave
FO	Fiber optic
IR	Infrared
MW	Microwave
RXN	Reaction
TEM	Transverse electromagnetic

Symbols

$C_{p,j}$	Heat capacity of phase j [J/kg.K]
d	Temperature probe location [mm]
D_b	Bed diameter [m]
D	Cavity diameter [m]
D_i^m	Diffusion coefficient of species i in the mixture [m^2/s]
E	Electrical field [V/m]
F	External force [N]
H_b	Bed height [m]
j_i	Definitive Mass flux [$mol/m^2.s$]
k_j	Thermal conductivity of phase j [W/m.K]
p	Pressure [Pa]
Pr	Prandtl number [-]
Ra_H	Rayleigh number [-]
R_1	Nitridation reaction rate [µmol/g.h]
R_2	Hydrogenation reaction rate [µmol/g.h]
$Q_{j,EMW}$	Heat dissipation density [W/m^3]
q_j	Conductive heat flux [W/m^2]
T_j	Temperature of phase j [K]
X	Solid phase conversion [-]
x_k	Mole fraction of species k [-]

Greek letters

ΔH_r	Reaction enthalpy [J/mol]
ε_r	Relative permittivity [-]
ε''	Dielectric loss factor [-]
ε_0	Permittivity in vacuum [-]
μ	Gas viscosity [Pa.s]
μ_r	Relative permeability [-]
ρ	Gas density [kg/m^3]

L	Length [m]	ρ_j	Density of phase j [kg/m^3]
L_b	Bed height [m]	σ	Electrical conductivity [S/m]
u	Gas velocity [m/s]	ω_i	Mass fraction of species i [-]
U_g	Intel gas velocity [m/s]		
Nu_H	Nusselt number [-]		

References

[1] V.M.S. Santos, J.F.P. Gomes, J.C.M. Bordado, R.A.F. Tom, Assessment of the impact of the European CO2 emissions trading scheme on the Portuguese chemical industry, 38 (2010) 626–632. https://doi.org/10.1016/j.enpol.2009.06.066.

[2] A. Otto, T. Grube, D. Stolten, Closing the loop : captured CO 2 as a feedstock in the chemical industry, Environ Sci Technol (2015) 3283–3297. https://doi.org/10.1039/c5ee02591e.

[3] H. Li, H. Zhou, K. Liu, X. Gao, X. Li, Retrofit application of traditional petroleum chemical technologies to coal chemical industry for sustainable energy efficiency production, Energy 218 (2021) 119493. https://doi.org/10.1016/j.energy.2020.119493.

[4] Z. Ge, Q. Sun, L. Xue, T. Yang, The influence of microwave treatment on the mode I fracture toughness of granite, Eng Fract Mech 249 (2021) 107768. https://doi.org/10.1016/j.engfracmech.2021.107768.

[5] A. Malhotra, W. Chen, H. Goyal, P.J. Plaza-gonzalez, I. Julian, J.M. Catala-civera, D.G. Vlachos, Temperature Homogeneity under Selective and Localized Microwave Heating in Structured Flow Reactors, I&EC (2021).

[6] S.D. Anuar Sharuddin, F. Abnisa, W.M.A. Wan Daud, M.K. Aroua, A review on pyrolysis of plastic wastes, Energy Convers Manag 115 (2016) 308–326. https://doi.org/10.1016/j.enconman.2016.02.037.

[7] M. Gupta, W.W. Leong, Microwaves and Metals, 2007.

[8] G.J.J. Verhoeven, V. Archaeology, The reflection of two fields – Electromagnetic radiation and its role in (aerial) imaging Geert, AARGnews (2018) 10–18. https://doi.org/10.5281/zenodo.3534245.

[9] V. Palma, D. Barba, M. Cortese, M. Martino, S. Renda, E. Meloni, Microwaves and Heterogeneous Catalysis : A Review on Selected Catalytic Processes, Catalysts (2020).

[10] A. Amini, M. Latifi, J. Chaouki, Electrification of materials processing via microwave irradiation : A review of mechanism and applications, Appl Therm Eng 193 (2021) 117003. https://doi.org/10.1016/j.applthermaleng.2021.117003.

[11] S. Mutyala, C. Fairbridge, J.R.J. Paré, J.M.R. Bélanger, S. Ng, R. Hawkins, Microwave applications to oil sands and petroleum : A review, Fuel Processing Technology 91 (2010) 127–135. https://doi.org/10.1016/j.fuproc.2009.09.009.

[12] S. Feng, W. Gao, Q. Wang, Y. Guan, H. Yan, H. Wu, H. Cao, J. Guo, P. Chen, A multi-functional composite nitrogen carrier for ammonia production via a chemical looping route, J Mater Chem A Mater 9 (2021) 1039–1047. https://doi.org/10.1039/d0ta10519h.

[13] R.-J. Chen, N. Qiao, M. Arowo, H.-K. Zou, G.-W. Chu, Y. Luo, B.-C. Sun, J.-F. Chen, Modeling for Temperature Distribution of Water in a Multiwaveguide Microwave Reactor, Ind Eng Chem Res 59 (2020) 4762–4774. https://doi.org/10.1021/acs.iecr.9b04748.

[14] H. Goyal, A. Mehdad, R.F. Lobo, G.D. Stefanidis, D.G. Vlachos, Scaleup of a Single-Mode Microwave Reactor, Ind Eng Chem Res 59 (2020) 2516–2523. https://doi.org/10.1021/acs.iecr.9b04491.

[15] H. Marion, M. Jr, Q. Bu, J. Liang, Y. Liu, H. Mao, A. Shi, H. Lei, R. Ruan, A review of catalytic microwave pyrolysis of lignocellulosic biomass for value-added fuel and chemicals, Bioresour Technol 230 (2017) 112–121. https://doi.org/10.1016/j.biortech.2017.01.059.

[16] C. Wildfire, V. Abdelsayed, D. Shekhawat, R.A. Dagle, S.D. Davidson, J. Hu, Microwave-assisted ammonia synthesis over Ru / MgO catalysts at ambient pressure, Catal Today 365 (2021) 103–110. https://doi.org/10.1016/j.cattod.2020.06.013.

[17] H.M. Nguyen, J. Sunarso, C. Li, G.H. Pham, C. Phan, S. Liu, General Microwave-assisted catalytic methane reforming : A review, Appl Catal A Gen 599 (2020) 117620. https://doi.org/10.1016/j.apcata.2020.117620.

[18] S. Hamzehlouia, J. Shabanian, M. Latifi, J. Chaouki, Effect of microwave heating on the performance of catalytic oxidation of n-butane in a gas-solid fluidized bed reactor, Chem Eng Sci 192 (2018) 1177–1188. https://doi.org/10.1016/j.ces.2018.08.054.

[19] Q. Liu, W. He, M. Aguedo, X. Xia, W. Bai, Y. Dong, Microwave-assisted alkali hydrolysis for cellulose isolation from wheat straw : Influence of reaction conditions and non-thermal effects of microwave, Carbohydr Polym 253 (2021). https://doi.org/10.1016/j.carbpol.2020.117170.

[20] S. Horikoshi, N. Serpone, On the influence of the microwaves ' thermal and non-thermal effects in titania photoassisted reactions, Catal Today 224 (2014) 225–235. https://doi.org/10.1016/j.cattod.2013.10.056.

[21] K. Adavi, A. Amini, M. Latifi, J. Shabanian, J. Chaouki, Kinetic study of multiphase reactions under microwave irradiation: A mini-review, Frontiers in Chemical Engineering 4 (2022). https://doi.org/10.3389/fceng.2022.1059160.

[22] G. Atanasova, N. Atanasov, Tuning, coupling and matching of a resonant cavity in microwave exposure system for biological objects, in: Electromagn Biol Med, 2013: pp. 218–225. https://doi.org/10.3109/15368378.2013.776432.

[23] S. Horikoshi, A. Osawa, S. Sakamoto, N. Serpone, General Control of microwave-generated hot spots . Part V . Mechanisms of hot-spot generation and aggregation of catalyst in a microwave-assisted reaction in toluene catalyzed by Pd-loaded AC particulates, Appl Catal A Gen 460–461 (2013) 52–60. https://doi.org/10.1016/j.apcata.2013.04.022.

[24] X. Zhang, D.O. Hayward, Applications of microwave dielectric heating in environment-related heterogeneous gas-phase catalytic systems, 359 (2006) 3421–3433. https://doi.org/10.1016/j.ica.2006.01.037.

[25] L.S. Gangurde, G.S.J. Sturm, T.J. Devadiga, A.I. Stankiewicz, G.D. Stefanidis, Complexity and Challenges in Noncontact High Temperature Measurements in Microwave-Assisted Catalytic Reactors, I&EC (2017) 13379–13391. https://doi.org/10.1021/acs.iecr.7b02091.

[26] M. Science, Measurement of temperature during microwave heating, (1991) 571–573.

[27] L. Li, Z. Yang, J. Chen, X. Qin, X. Jiang, F. Wang, Performance of bio-char and energy analysis on CH 4 combined reforming by CO 2 and H 2 O into syngas production with assistance of microwave, Fuel 215 (2018) 655–664. https://doi.org/10.1016/j.fuel.2017.11.107.

[28] C.O. Kappe, How to measure reaction temperature in microwave-heated transformations, Chem Soc Rev (2013) 4977–4990. https://doi.org/10.1039/c3cs00010a.

[29] T. Chudoba, J. Wojnarowicz, Current Trends in the Development of Microwave Reactors for the Synthesis of Nanomaterials in Laboratories and Industries : A Review, Crystals Review (2018). https://doi.org/10.3390/cryst8100379.

[30] S. Farag, J. Chaouki, A modified microwave thermo-gravimetric-analyzer for kinetic purposes, Applied Thermal Engineering Journal 75 (2015) 65–72. https://doi.org/10.1016/j.applthermaleng.2014.09.038.

[31] P. Cresson, C. Ricardi, L. Dubois, S. Vaucher, T. Lasri, J. Pribetich, Temperature Measurement by Microwave Radiometry ., I2MTC 2008 - IEEE International Instrumentation and Measurement Technology Conference (2008).

[32] D. Luan, J. Tang, P.D. Pedrow, F. Liu, Z. Tang, Performance of mobile metallic temperature sensors in high power microwave heating systems, J Food Eng 149 (2015) 114–122. https://doi.org/10.1016/j.jfoodeng.2014.09.041.

[33] B.A. Lapshinov, Temperature measurment methods in microwave heating technologies, Measurment Techniques 64 (2021) 20–28. https://doi.org/10.1007/s11018-021-01954-w.

[34] H. Nokhbatolfoghahaei, M. Bohlouli, K. Adavi, Z. Paknejad, M. Rezai Rad, M.M. khani, N. Salehi-Nik, A. Khojasteh, Computational modeling of media flow through perfusion-based bioreactors for bone tissue engineering, Proc Inst Mech Eng H 234 (2020) 1397–1408. https://doi.org/10.1177/0954411920944039.

[35] Y. Mehdizadeh Chellehbari, K. Adavi, J. Sayyad Amin, S. Zendehboudi, A numerical simulation to effectively assess impacts of flow channels characteristics on solid oxide fuel cell performance, Energy Convers Manag 244 (2021). https://doi.org/10.1016/j.enconman.2021.114280.

[36] J.W.& Sons, Convective heat transfer, 2013.

[37] I. Julian, H. Ramirez, J.L. Hueso, R. Mallada, J. Santamaria, Non-oxidative methane conversion in microwave-assisted structured reactors, Chemical Engineering Journal 377 (2019) 119764. https://doi.org/10.1016/j.cej.2018.08.150.

[38] A. Ramirez, J.L. Hueso, R. Mallada, J. Santamaria, Microwave-activated structured reactors to maximize propylene selectivity in the oxidative dehydrogenation of propane, Chemical Engineering Journal 393 (2020) 124746. https://doi.org/10.1016/j.cej.2020.124746.

[39] I. Julian, C.M. Pedersen, A.B. Jensen, A.K. Baden, J.L. Hueso, A. V Friderichsen, H. Birkedal, R. Mallada, J. Santamaria, From bench scale to pilot plant : A 150x scaled-up configuration of a microwave-driven structured reactor for methane dehydroaromatization, Catal Today 383 (2022) 21–30. https://doi.org/10.1016/j.cattod.2021.04.013.

[40] E. Meloni, M. Martino, A. Ricca, V. Palma, Ultracompact methane steam reforming reactor based on microwaves susceptible structured catalysts for distributed hydrogen production, Int J Hydrogen Energy 46 (2020) 13729–13747. https://doi.org/10.1016/j.ijhydene.2020.06.299.

[41] G.D. Stefanidis, A helicopter view of microwave application to chemical processes : reactions , separations , and equipment concepts, Rev Chem Eng (2014). https://doi.org/10.1515/revce-2013-0033.

[42] D. Chisalita, A. Cormos, Dynamic simulation of fl uidized bed chemical looping combustion process with iron based oxygen carrier, Fuel 214 (2018) 436–445. https://doi.org/10.1016/j.fuel.2017.11.025.

CHAPTER 6: ARTICLE 3-MICROWAVE HEATING-ASSISTED CHEMICAL LOOPING AMMONIA SYNTHESIS OVER Mn-Fe AND Mn-Fe-BaH_2 NITROGEN CARRIERS

Kazem Adavi [a], Zhaohui Chen [b], Adrian Carrillo Garcia [a], Jaber Shabanian [a], and Jamal Chaouki [a,c,*]

[a] Process Engineering Advanced Research Lab (PEARL), Department of Chemical Engineering, Polytechnique Montreal, P. O. Box 6079, Station Centre-Ville, Montreal, (Quebec) Canada, H3C 3A7

[b] State Key Laboratory of Mesoscience and Engineering, Institute of Process Engineering Chinese Academy of Sciences, Beijing 100190, China

[c] University Mohamed VI Polytechnique, Benguerir, Morocco

[*] Corresponding author: Tel. +1 (514) 340-4711 X 4034, fax: +1 (514) 340-4159, E-mail: jamal.chaouki@polymtl.ca

(Published on February 1st, 2025, Energy Conversion and Management, DOI: https://doi.org/10.1016/j.enconman.2024.119434)

Abstract

Ammonia, a promising hydrogen carrier, holds significant potential for advancing the storage and transportation of renewable energy and facilitating the decarbonization of industry, transportation, and households. Conventional ammonia synthesis technologies, like Harber-Bausch technology, often operate under harsh operating conditions and/or with low production rates or encounter substantial thermodynamic limitations, impeding their scalability. In this study, we developed a new ammonia synthesis technology based on microwave heating-assisted chemical looping to minimize these challenges. We applied synthetic nitrogen carriers, i.e., Mn-Fe and Mn-Fe-BaH_2 synthesized by mechanical and/or coprecipitation approaches, to transport lattice nitrogen from a nitridation step (at atmospheric pressure and 400 °C) to a hydrogenation step (at atmospheric pressure and 150-350 °C), where ammonia was produced. The simultaneous application of microwave heating and chemical looping resulted in a lower gas-phase temperature compared to the solid phase within a gas-microwave absorber solid system. With this strategy, we minimized undesirable secondary gas-phase reactions, circumvented thermodynamic limitations associated with ammonia production, and achieved a significantly higher ammonia production rate compared to conventional heating methods. The Mn-Fe-BaH_2 nitrogen carrier demonstrated a higher ammonia production rate, i.e., around 36,000 μmol/g.h under MW heating, surpassing previously reported values in literature and the Mn-Fe nitrogen carriers synthesized in this work.

Keywords: Chemical looping; Hydrogen carrier; Ammonia; Microwave heating; Nitrogen carrier; Nitridation.

6.1. Introduction

Progress in renewable energy technologies has highlighted a lack of appropriate energy carriers, which is restricting global advances toward renewable energy [1,2]. Batteries may cover some aspects of the problem [3]; however, they are less suitable for large-scale transportation from regions with abundant renewable energy sources, such as solar, wind, and hydropower [4]. The application of solid-state energy carriers, particularly metal hydrides, as direct renewable energy storage materials faces significant obstacles [5]. These challenges are primarily due to the high costs associated with the storage and transportation of metal hydrides, as well as their significant safety risks [6]. Furthermore, technical complexities, especially the limitations in mass transfer within solid materials during hydride formation, further hinder their practical application [7]. As a result, liquid energy carriers are generally preferred for bulk transport via pipelines or maritime routes [4]. Among these, ammonia (NH_3) is a particularly promising candidate as a renewable energy carrier [8]. It contains 17.5 wt.% hydrogen (H_2), i.e., 40% more than methanol, which is another common liquid energy carrier [9]. The storage cost of NH_3 is three times lower than H_2 [10], and ammonia can provide more than 50% more energy than natural gas (NG) [11]. Ammonia can be liquefied by increasing the pressure to about 10 bar at room temperature or temperatures lower than -33 °C at atmospheric pressure. Unlike liquefied H_2, the pipeline and shipping infrastructure for liquid ammonia in the industrial sector is well established [12,13]. Different ammonia synthesis technologies are Haber-Bosch (HB) [14], microwave (MW) heating-assisted catalytic ammonia synthesis in a single reactor [15], electrocatalysis [16], photochemical [16], plasma-assisted [17], and chemical looping ammonia synthesis (CLAS) [18].

HB technology operates at relatively harsh operating conditions, i.e., pressure ranging from 100 to 300 bar and temperatures ranging from 400 to 600 °C, for nitrogen (N_2) activation and shifting the reaction toward ammonia production [19,20]. The HB plants are economically efficient at large scale, i.e., an ammonia production rate of more than 1000 tonnes/day [21,22]. In addition, expensive iron-based catalysts are required to dissociate N_2 molecules. Since green ammonia, i.e., ammonia produced by green H_2 obtained from water electrolysis, synthesis plants need to operate

at a production rate of around 30-100 tonnes of ammonia/day to store intermittent renewable energy. HB technology is a less suitable candidate for green H_2 storage when applying renewable energy [23].

In MW heating-assisted catalytic ammonia synthesis in a single reactor, chemisorption competition between N_2 and H_2 on the surface of the catalyst can be observed [24,25]. In this technology, high-temperature hot spots required for nitrogen dissociation can result in ammonia decomposition [15].

Electrocatalysis ammonia synthesis and photochemical technology are two eco-friendly technologies with low energy consumption [26,27]. These technologies can produce ammonia under atmospheric pressure [28]. However, their reaction rate is 10 to 100 times lower than that of the HB technology [29,30]. In addition, conventional catalytic ammonia synthesis technologies, e.g., HB, have a higher energy efficiency than plasma-assisted ammonia synthesis, and they are more feasible alternatives for green ammonia synthesis by applying intermittent renewable energy in the future [31].

CLAS decouples ammonia synthesis reaction into two or three independent sub-reactions, typically conducted in two or three reactors operated sequentially, that allow independent control of N_2 activation on nitrogen carrier (NC) and ammonia formation steps [32,33]. It circumvents the thermodynamic limitation of conventional catalytic ammonia production, i.e., the importance of harsh operating conditions to prevent ammonia decomposition and decrease operating pressure [34]. This technology also eliminates the competitive adsorption of reactants on the catalyst, which generally limits ammonia production in catalytic ammonia synthesis technologies [35]. Therefore, the CLAS technology synthesizes ammonia under considerably friendlier conditions, usually atmospheric pressure, compared to conventional catalytic technologies. Different types of CLAS technologies are (i) water chemical looping ammonia synthesis (H_2O-CLAS), (ii) chemical electrolysis looping (H_2O-CEL) [34], (iii) hydrogen chemical looping ammonia synthesis (H_2-CLAS), and (iv) alkali/alkaline-earth-metal-hydride chemical looping ammonia synthesis (AH-CLAS) [32,36].

H_2O-CLAS technology commonly consists of nitridation, oxidation, and metal hydrolysis in a chemical loop or cycle, typically accomplished in three reactors [37]. The literature reported a wide range of nitrogen/oxygen carriers, such as those containing chromium (Cr), calcium (Ca),

molybdenum (Mo), zinc (Zn), aluminum (Al), manganese (Mg), and manganese (Mn), for the H_2O-CLAS technology [38,39]. Due to the high temperature of the reduction stage (i.e., > 1000 °C) for a highly stable metal oxide reduction, applying a composite of two or more metals as a NC is a promising solution to decrease the reduction temperature. For instance, in the study by Michalsky et al. [40], the authors adopted Mn and Mo as NCs for solar-driven H_2O-CLAS. The modification led to an NC-N bond that is weaker than the Mn-N bond but stronger than the Mo-N bond during the hydrogenation stage [40]. Moreover, in the reduction stage, the NC-O bond is less stable than the Mn-O bond, resulting in a lower reduction temperature. This selection is based on the Sabatier principle in catalytic systems. According to this principle, the strength of metal-O bonds must be balanced: they should not be so strong that they require excessively high temperatures to break, which could degrade the NC. Conversely, if the bonds are too weak, the system may lack the stability needed during the nitridation stage, ultimately hindering the ability to complete the cycle and efficiently produce ammonia [39].

The H_2O-CEL technology, like the H_2O-CLAS, applies H_2O for the H_2 supply in ammonia production. However, in the H_2O-CEL, the reduction step of NCs is achieved through electrolysis.

H_2-CLAS has two stages, nitridation and hydrogenation [24]. In the former stage, a metal undergoes nitridation by producing nitrogen-rich metal nitride in the N_2 atmosphere [41]. Subsequently, it is reduced to a metallic or nitrogen-depleted state and ammonia in the presence of a H_2 stream [32,42]. Several metal nitrides, such as calcium nitride (Ca_3N_2) [43], molybdenum nitride (Mo_2N) [44], Iron nitride (Fe_2N) [42], strontium nitride (Sr_2N) [43], and Manganese nitride (Mn_xN_y) [45], are reported in literature as NCs for the H_2-CLAS technology. However, nitridation and hydrogenation reactions for these NCs commonly occur at temperatures higher than 500 °C [32,43]. Barium hydride/barium amide (BaH_2/$Ba(NH_2)_2$) and lithium hydride/ lithium amide (LiH/Li_2NH) pairs are potential NCs for AH-CLAS ammonia synthesis due to their favorable thermodynamics, i.e., Gibbs free energy $\Delta G < 0$, in the nitridation and hydrogenation steps [46]. In addition, doping transient metals, such as nickel (Ni), cobalt (Co), and palladium (Pd), to NCs can decrease nitridation and hydrogenation temperatures [47].

Existing technologies, such as the HB process, MW heating-assisted catalytic ammonia synthesis in a single reactor, electrocatalytic, photocatalytic, plasma-assisted ammonia synthesis, and conventionally heated CLAS technologies, either have low production rates or require high

operational temperatures that cause ammonia decomposition under atmospheric pressure. Thus, introducing a new technology that operates at low temperatures, i.e., below 350 °C for hydrogenation stage, and atmospheric pressure is crucial. Minimizing the gas-phase temperature and developing a solid/catalyst that functions at lower temperatures can be key solutions to this problem.

In this study, we introduced a MW heating-assisted CLAS (MHCLAS) technology (see Figure 6.1). We also introduced a novel Mn-Fe-BaH_2 NC that demonstrates a promising performance in ammonia production under MW irradiations. In the new technology, we exposed synthesized MW absorber-NC to MWs in a nitrogen stream, resulting in nitrogen molecule dissociation and the formation of nitride NCs within the 300-700 °C temperature range. We, then, exposed these nitrided carriers to H_2 to yield ammonia and nitrogen-depleted carriers at temperatures as low as 150 °C. This technology, which separates nitrogen dissociation from ammonia formation along with MW heating to maintain lower gas phase temperatures, overcomes thermodynamic barriers in conventional catalytic ammonia production at atmospheric pressure. It also offers several advantages, including decreased energy consumption, enhanced ammonia production rates, the ability to produce ammonia at atmospheric pressure and lower temperatures compared to conventional technologies, ammonia production decentralization, and the implementation of renewable electricity resulting in zero carbon emissions. These advantages make the MHCLAS technology a promising candidate for ammonia production decentralization. MW heating, known for its selective, rapid, and volumetric heating, directly heats MW absorber solid particles in the proposed technology, while maintaining lower gas-phase temperatures. This temperature difference minimizes undesired ammonia decomposition reactions. In addition, the application of MW heating in the proposed technology enables process electrification, offering a promising avenue for applying renewable electricity to decarbonize and decentralize chemical processes.

A schematic representation of the proposed technology, detailing potential energy and feedstock supply sources, nitridation and hydrogenation stages, a comparison between microwave and conventional heating, and applications of the resulting ammonia product, is illustrated in Figure 6.1.

We present experimental details, including the selection strategy for NCs, synthesis approaches of selected NCs, and procedures for the performance evaluation of synthesized NCs in Section 6.2.

In Section 6.3, we discuss the results obtained from the characterization of the synthesized NCs, the heating capabilities of the synthesized NCs under MW irradiation, and nitridation and hydrogenation performances of the synthesized NCs.

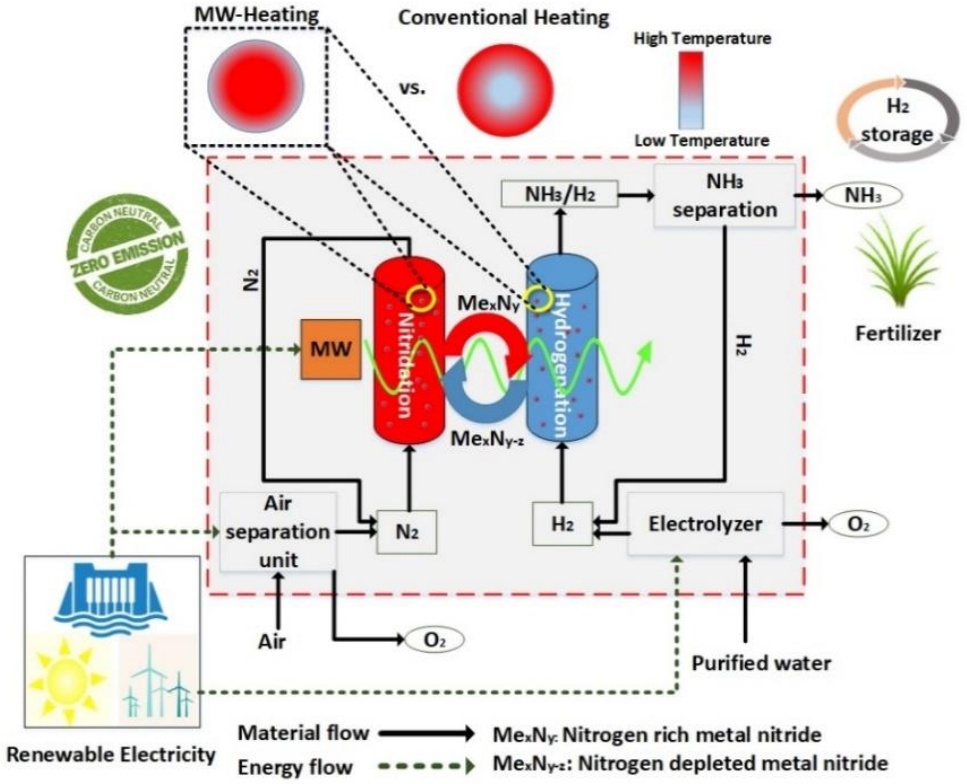

Figure 6.1: A schematic representation of MHCLAS technology.

6.2. Experimental

6.2.1. Nitrogen carrier selection

A Mn-Fe composite has a different NC-N bond strength compared to Fe-N and Mn-N bonds. These composites are expected to exhibit a stability profile between Mn nitride and Fe nitride, rendering them promising candidates for diverse applications [48]. The Mn-N bond is stronger than the Fe-N bond, and this phenomenon is associated with the number of d-electrons in the metal. The higher the number of d-electrons, the weaker the metal-N bond, with Mn having 5 d-electrons and Fe having 6. However, application a composite of both metals results in a NC-N bond that is weaker than the Mn-N bond but stronger than the Fe-N bond. This balance facilitates the hydrogenation

reaction at a lower temperature. Fe alone does not form a stable bond with nitrogen under atmospheric pressure [39].

The presence of Fe within the NC holds the potential to enhance its magnetic properties and elevate the heating efficiency under MW irradiation. This augmentation stems from the dual contribution of magnetic and electrical fields, collectively fostering an increase in the sample temperature.

Benefiting from other compounds to improve the activity of synthesized NCs is important. In this regard, barium hydride (BaH_2) exhibits a notable effectiveness in ammonia synthesis with the CLAS technology under conventional heating conditions [49]. Despite its efficacy in CLAS technology and the possession of a crystalline structure, BaH_2 is not an ideal material for MW absorption. Materials with higher concentrations of defect sites demonstrate superior MW absorption capabilities, and increasing crystallinity tends to diminish MW heating efficiency. Nevertheless, there is potential improvement through the development of a composite material that incorporates Mn, Fe, and BaH_2. This composite has the prospect of enhancing the overall performance of MHCLAS technology by a skillful balancing activity and MW heating capabilities, thus optimizing its utility in ammonia synthesis applications.

6.2.2. Synthesis of NCs

6.2.2.1. Mn-Fe NCs synthesis

We adopted mechanical and coprecipitation approaches to synthesize Mn-Fe NCs. In the mechanical approach, we mixed Mn powder and Fe powder, both from Sigma Aldrich, at a 4:1 mass ratio in a mortar for 20 min. We prepared the mixed sample in an inert atmosphere with argon to prevent NC contamination by oxygen. The mechanical synthesis preactivated the NC and avoided any additional activation steps.

For Mn-Fe NCs synthesis via the coprecipitation approach, we mixed iron nitrite solution ($Fe(NO_3)_3 9.H_2O$, Sigma Alrich, purity ≥99.95%, CAS No.: 7782-61-8, 10 M) with manganese nitrate ($Mn(NO_3)_2 4.H_2O$, Sigma Aldrich, purity ≥99.95%, CAS No.: 20694-39-7, 10 M) and sodium carbonate solution (Na_2CO_3, Sigma Alrich, purity ≥99.5%, CAS No.: 497-19-8, 10 M) as a precipitation agent with a mass ratio of 1:1.5:3, respectively. We optimized the synthesized NCs' recipe, in particular, material ratios, in this study based on preliminary studies to maximize ammonia production rates, while ensuring efficient heating under MW irradiations. We gradually

added the precipitation agent to the mixture to maximize the homogeneity of the synthesized NC. We continuously stirred the solution, while preserving its temperature at 80 °C. We filtered and washed the produced suspension three times with deionized water and dried it at 120 °C overnight. We then calcined the dried NC for 3 hours at 500 °C in an electrical furnace.

6.2.2.2. Mn-Fe-BaH2 NCs synthesis

To synthesize the Mn-Fe-BaH_2 NC by the coprecipitation approach, we prepared a 10 M sodium carbonate solution (Sigma Aldrich). We then added Barium fluoride (BaF_2) powder (Sigma Aldrich, purity ≥98.0%, CAS No.: 7787-32-8, mesh: 325) to the solution, and stirred the mixture at 80 °C for 30 minutes. We subsequently introduced a mixture of 5 M iron nitrite solution (Sigma Aldrich) and 5 M manganese nitrate (Sigma Aldrich) in a gradual manner to ensure a homogeneous distribution. We adjusted BaF_2:$Mn(NO_3)_2$:$Fe(NO_3)_3$:Na_2CO_3 mass ratio at 1:4:1:5, optimized based on the preliminary investigations attempted in this study. We finally filtered and washed the resulting suspension three times with deionized water, and dried the sample overnight at 120 °C.

6.2.3. Characterization of synthesized NCs

We analyzed the synthesized NCs by X-ray diffraction (XRD) analysis (Bruker D8 Advance) with Cu $K\alpha$ radiation to identify the synthesized phases and verification of Mn-Fe composite formation. The scanned range was from 10˚ to 90˚ with a 2θ rate of 10˚/min. Scanning electron microscopy with energy dispersive X-ray spectroscopy (SEM-EDS) analysis (JEOL JSM-7600F) was applied for the morphology study of synthesized NCs and analyzing the uniformity of elements in synthesized NCs. We applied inductively coupled plasma optical emission spectroscopy (ICP-OES) analysis (Agilent 5110-SVDV) to study the elemental composition of synthesized NCs. Prior to this analysis, we diluted 0.1 g of NC in hydrochloric acid (HCL) (6M) and heated the resulting solution at 100 °C for 1 hour.

6.2.4. Experiment procedure

In the case of NCs synthesized via the coprecipitation approach, we initially activated or reduced the NCs. We performed all tests with a NC having a particle size in the range of around 40 to 75 µm. For coprecipitation-derived Mn-Fe and Mn-Fe-BaH_2 NCs, we performed the

activation/reduction step in a laboratory-scale MW heating-assisted fluidized bed reactor (MHFB) setup at 900 °C for 45 minutes with a gaseous mixture of CH_4 (10 vol.%, supplied from Canadian Air Liquid with 99.92% purity), H_2 (5 vol.%, supplied by a Peak Scientific hydrogen generator, 99.9999% H_2 purity), and N_2 (balance, supplied from Canadian Air Liquid with 99.99% purity). Subsequently, the H_2 gas was passed through the reactor at 300 °C for another additional 60 min. During this stage, H_2 and CH_4 can reduce oxide phases into their metallic counterparts leading to the formation of BaH_2 in the Mn-Fe-BaH_2 NC.

To investigate the mass variation of NC during the nitridation reaction, we employed a thermogravimetric analysis (TGA) instrument (TA Instruments Waters- TGA 550). For this characterization, we placed 10 mg of NC in a platinum pan and subjected it to a nitrogen stream at a flow rate of 40 ml/min and a heating rate of 5 °C /min, up to 800 °C. We recorded the mass gain of NC at 0.1 second intervals.

We applied a temperature programmed reduction (TPR) analysis to measure the reduction in temperature of produced nitrided NCs and ammonia formation from nitrided NCs. For this analysis, we placed 0.3 g of NC in a U-shaped quartz tube and heated it at 10 °C/min from room temperature to 600 °C. The thermal conductivity detector (TCD) measured H_2 consumption at different temperatures.

To study the MW absorption and activity, we loaded 10 g of synthesized NCs leading to an approximately 3±1 cm bed height and exposed them to 1100 kW of MW irradiations in a laboratory-scale MHFB reactor. The reactor consisted of a 2.86 cm ID quartz reactor with a MW power set in the range of 110-1100 W that was placed in a metallic cavity (stainless steel 306). We monitored the temperature profile of the sample with a grounded, type K, metallic thermocouple (yielding the bulk temperature) positioned at the dense bed center along the axis (Figure 6.2). In addition, a pyrometer was employed to measure the solid phase temperature which is positioned in the center of the dense bed along the axis as depicted in Figure 6.2. To mitigate the risk of magnetron damage, spark formation, and arcing, we cooled the magnetron with an air stream and cold water circulated through MW-transparent tubes to absorb any excess MW irradiations in the cavity. To maximize safety precautions, we employed a MW detector to identify any MW leakage and safeguarded the experimental setup with a MW absorber shield. We adjusted the operating temperature in the MW heating setup by manipulating the MW power (110 to 1100 W). The bed

temperature stabilized at an equilibrium state, allowing for the occurrence of the reaction within a temperature tolerance of around ±5 °C.

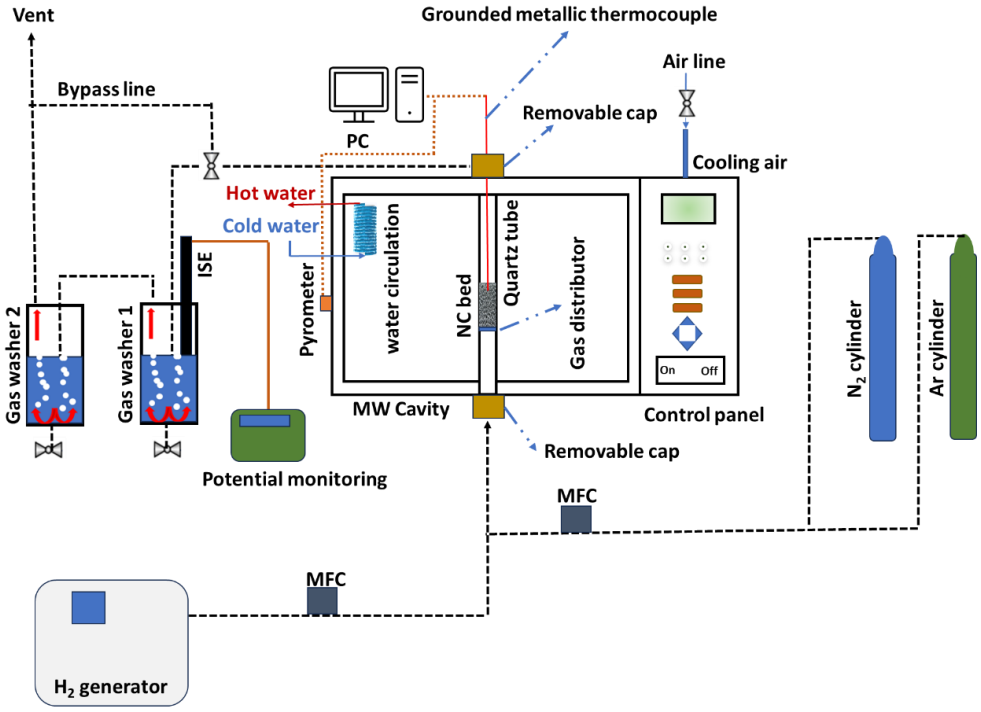

Figure 6.2: A schematic representation of the adopted laboratory-scale MHFB reactor.

For CLAS experiments, we initially nitrided NCs by passing a pure nitrogen stream through the reactor with a superficial gas velocity of $U_g = 6.5\ cm/s$. After completing the nitridation process, we cooled the reactor to room temperature. We then switched the inlet gas to H_2, supplied by a H_2 generator, 20 vol.% balanced with Argon at $U_g = 7.0\ cm/s$ to initiate the hydrogenation reaction.

To compare the performances of MW and conventional heating methods in ammonia synthesis, we also adopted a laboratory-scale fluidized bed reactor (stainless steel reactor with a 2.86 cm ID) that was heated by induction heating. A schematic representation of the employed conventionally heated reactor is presented in Figure 6.3. The generated heat in the reactor wall by the induction heating was transferred to the bed inventory by conventional heat transfer mechanisms. We placed two type K metallic thermocouples at the dense bed center along the axis and on the reactor wall at the axial center to continuously monitor and control the temperature. We monitored temperature differences in axial and radial directions by displacing the inner metallic thermocouple. Results showed a negligible temperature difference in the bed in fluidization mode. We kept nitridation

and hydrogenation stage parameters the same as those with the MHFB setup. We initially exposed NC to the N_2 stream to produce nitrided NC. In the next stage, we passed the H_2 gas through the bed to produce ammonia. In Table 6.1, we summarized experimental parameters for performance evaluations of synthesized NCs under conventional and MW heating methods.

We added a quartz wool at the reactor exit to ensure that all solids remain in the reactor during its operation. In addition, we monitored the weight change of loaded NCs by passing Ar gas through the reactor at a $U_g = 9.0\ cm/s$. The monitored bed inventory variation revealed a negligible weight change.

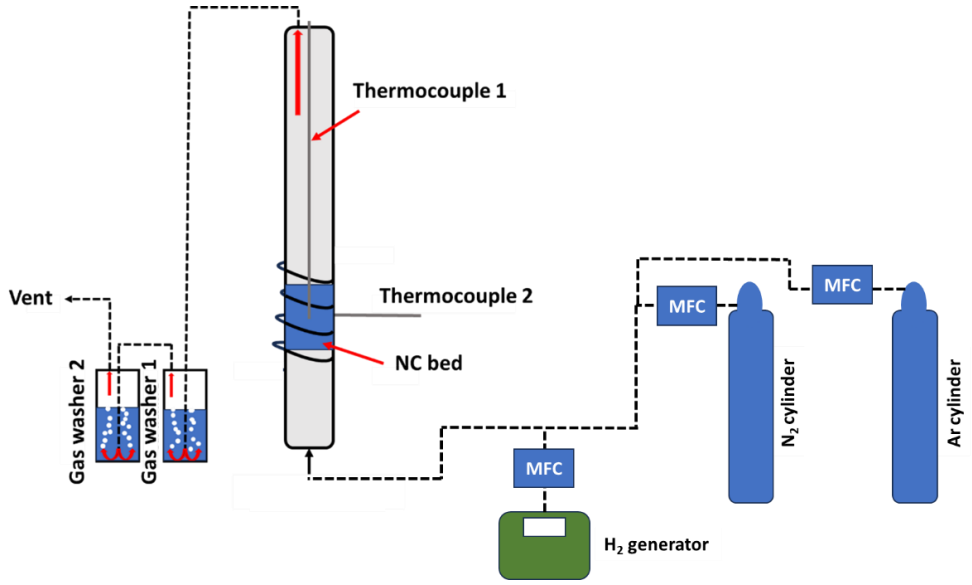

Figure 6.3: A schematic representation of the adopted laboratory-scale conventional heating-assisted reactor.

To quantify the generated ammonia, we passed the resulting gas through two successive gas washers, each containing 400 ml of deionized water (Figure 6.2). To facilitate a complete dissolution of ammonia in the water, by forming ammonium hydroxide, we immersed the gas washers in an ice-water mixture to lower their temperature. We subsequently employed a pre-calibrated ion-selective electrode (ISE) to determine an overall ammonia production. The ISE was designed to detect and measure the concentration of ammonium ions in the concentration range between 0.03 to 70,000 ppm at 22 ±2 °C. We adopted the second gas washer to ensure that we captured nearly all produced ammonia in the first gas washer.

Table 6.1: Experimental parameters for performance evaluations of synthesized NCs under conventional and MW heating methods.

Parameter	Value
Reactor conditions	
Quartz inner reactor diameter (MW heating)	2.86 cm
Stainless steel reactor inner diameter (conventional heating)	2.86 cm
Metallic thermocouple type	Type K & grounded
MW power	110-1100 W
Nitridation stage	
Initial NCs mass	5-10 g
Nitridation duration time	10 min
$U_{g-Nitridation}$	6.5 cm/s
Nitridation temperature	350-700 °C
Hydrogenation stage	
Hydrogenation duration time	5 min
$U_{g-Hydrogeneation}$	7.0 cm/s
Hydrogenation temperature	150-350 °C

6.3. Results and discussion

6.3.1. Characterizations of synthesized NCs

SEM and EDS mappings of the synthesized Mn-Fe NC through the mechanical approach are shown in Figure 6.4a. The mechanical approach yielded a non-uniform particle size, from 1 to 103 µm as presented in Figure 6.4a.1, and elemental distributions of Mn (Figure 6.4a.2) and Fe (Figure 6.4a.3). However, achieving a uniform particle size distribution, coupled with a homogeneous distribution of Mn and Fe elements, is anticipated to enhance the consistency of NC properties during nitrogen fixation and ammonia formation stages. The interaction between Mn and Fe metals plays a crucial role in modifying the surface energy of the synthesized NCs to decrease nitridation and hydrogenation stage temperatures. The bond between nitrogen and the Mn-Fe NC is stronger than the Fe-N bond but weaker than the Mn-N bond. At atmospheric pressure, Fe does not form a nitride phase due to the weakness of its bond with nitrogen, while Mn-N requires higher temperatures (i.e., T> 500 °C) for reduction during the hydrogenation stage. However, combining Mn and Fe in the NC composite enables the formation of a NC-N bond that can be reduced at a lower temperature under a H_2 atmosphere due to the synergy of both metals [39].

SEM-EDS results of the coprecipitation approach for the Mn-Fe NC presented in Figure 6.4b.2 and Figure 6.4b.3 indicate a uniform elemental distribution of Mn and Fe in the NC. The more uniform distribution and, hence, the interaction between Mn and Fe results in the production of a nitrided NC that is less stable than manganese nitride and more stable than iron nitride.

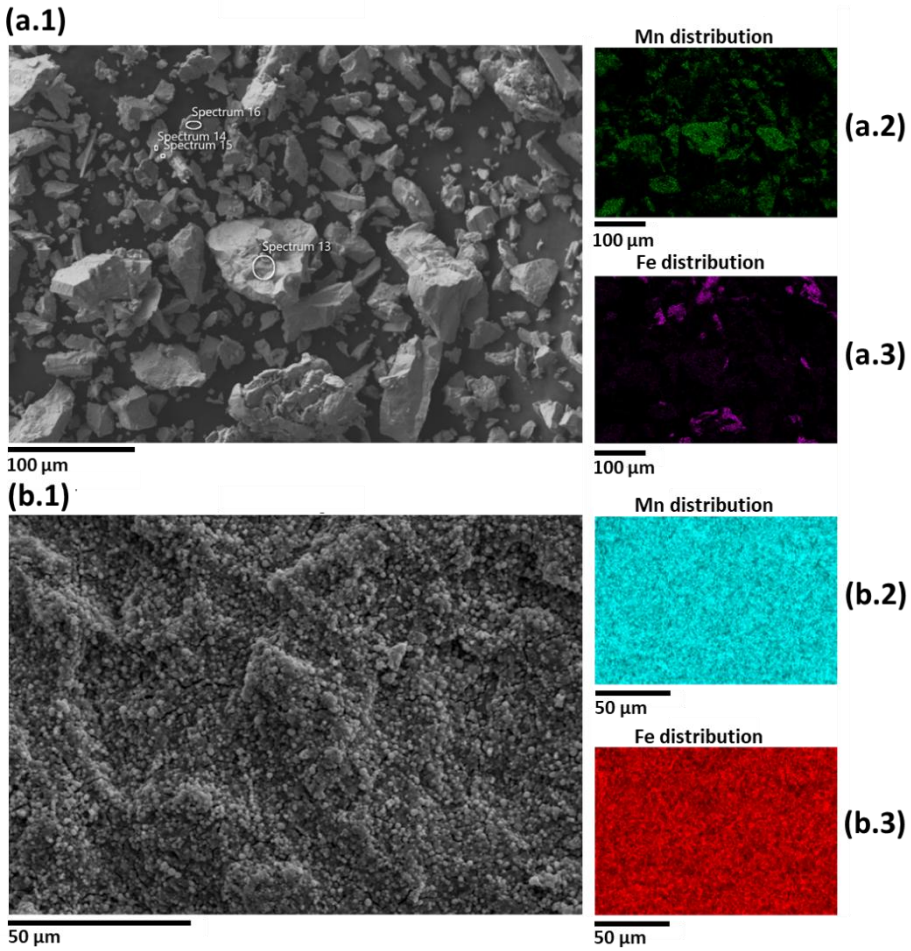

Figure 6.4: (a) SEM micrograph and EDS mappings of Mn and Fe in Mn-Fe: mechanical NC: (a.1) SEM micrograph, (a.2) Mn EDS mapping, and (a.3) Fe EDS mapping. (b) SEM micrograph and EDS mappings of Mn and Fe in Mn-Fe: coprecipitation NC: (b.1) SEM micrograph, (b.2) Mn EDS mapping, and (b.3) Fe EDS mapping.

The mean particle size (MPS) of the synthesized NCs was calculated by applying Digimizer image analyzer software. Accordingly, we considered 100 particles in each micrograph. The MPS of the synthesized NC by the coprecipitation approach was 2.1 µm (0.5-3 µm), refer to. Figure 6.4b.1. However, we measured a MPS of 20 µm for the NC synthesized by applying the mechanical approach (1-103 µm). The non-uniform particle size along with the weak interaction between Mn and Fe metals in the NC synthesized by the mechanical approach may thus result in the non-

uniformity of nitrogen fixation in the nitridation stage and a lower ammonia formation in the hydrogenation stage. However, the implementation of the coprecipitation approach improves Mn and Fe element distribution in the NC, which can result in a higher ammonia formation.

In the coprecipitation approach, the formation of a high degree of supersaturation during the crystallization reaction leads to the generation of primary nuclei within the synthesis solution [50]. These solid particles serve as active sites for secondary nucleation, thus facilitating the subsequent formation of larger particles [51]. The elevated mixing rate employed during the crystallization reaction plays a crucial role in promoting the creation of particles characterized by enhanced elemental uniformity. In addition, in the synthesis of the Mn-Fe-BaH_2 NC, we strategically incorporated BaF_2 particles through doping as secondary nucleation sites to initiate the nucleation phenomena within the synthesized NC.

BaH_2 attracted attention as a prospective NC for ammonia synthesis through chemical looping technology [46]. Its crystalline structure, however, poses challenges in achieving effective heating when subjected to MW irradiation. The application of BaH_2 within the Mn and Fe composite, synthesized through a coprecipitation approach, has also demonstrated a homogeneous elemental distribution within the NC (see Figure 6.5). Figure 6.5a.1-6.5a.4 shows the elemental distribution of Mn, Fe, and barium (Ba). Notably, Figure 6.5a.5 reveals the presence of sodium (Na) and fluorine (F) elements in the NC due to the NC synthesis procedure. Due to the high level of fluoride electronegativity, the presence of this element with 6 wt.% could potentially increase the nitrogen dissociation rate in the nitridation step. Studies in the literature report that the presence of fluoride in the structure of the NC enhances the electron-donating ability of the catalyst, thereby promoting ammonia synthesis [52].

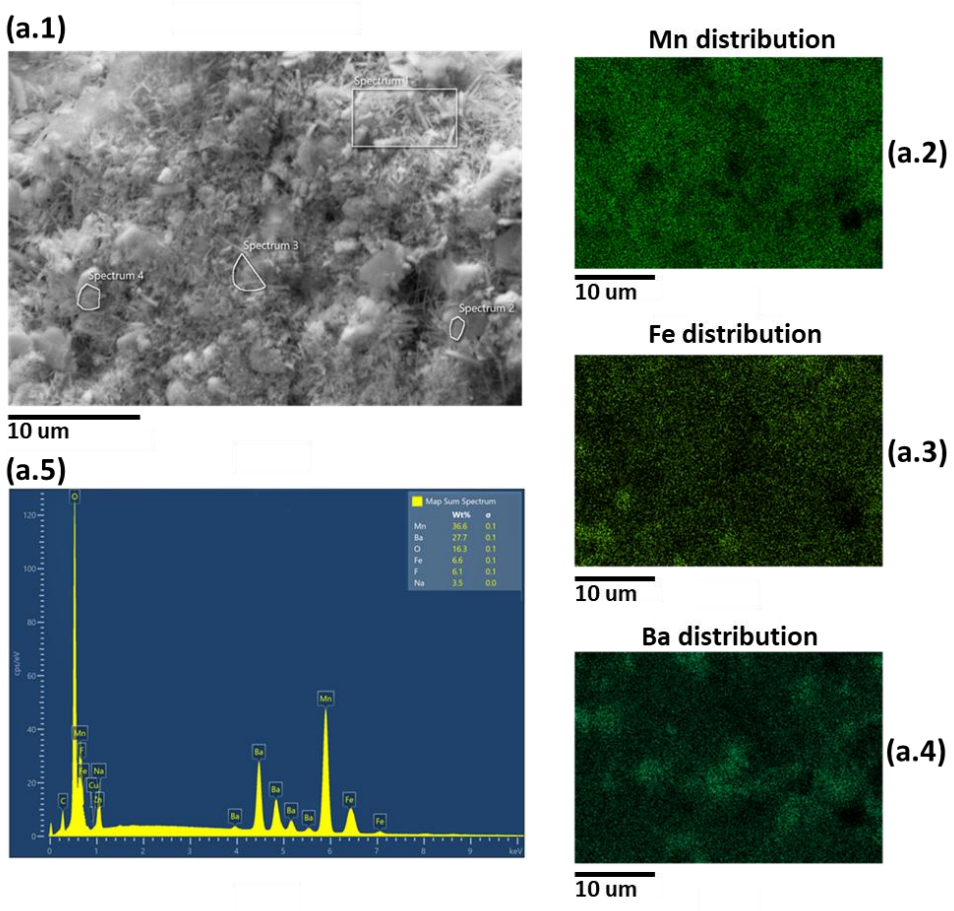

Figure 6.5: SEM micrograph and EDS mappings of the synthesized Mn-Fe-BaH_2 NC by the coprecipitation approach: (a.1) SEM micrograph, (a.2) Mn EDS mapping, (a.3) Fe EDS mapping, (a.4) Ba EDS mapping, and (a.5) EDS spectrum.

We adopted the ICP-OES analysis to measure the elemental distribution of NC synthesized by applying the coprecipitation approach. Mn, Fe, and Ba concentrations of synthesized NCs measured by ICP-OES analysis are reported in Table 6.2. In the mechanically synthesized Mn-Fe NC, Mn accounted for approximately 79 wt.%, with Fe comprising about 21 wt.%. Conversely, the coprecipitation approach yielded a Mn-Fe NC with 41 wt.% Mn and 23 wt.% Fe, with the remaining being attributed to oxygen. The synthesized Mn-Fe-BaH_2 NC by coprecipitation approach is comprised of approximately 34 wt.% Mn, 5.6 wt.% Fe, and 29 wt.% Ba, with the remainder being oxygen, Na, and F, thus confirming the surface composition that was obtained by EDS analysis (Figure 6.5a.5).

Table 6.2: A summary of the elemental analysis of synthesized NCs by ICP-OES.

NC	Mn (wt.%)	Fe (wt.%)	Ba (wt.%)	Balance
Mn-Fe: Mechanical	79.1	20.9	0.0	-
Mn-Fe: Coprecipitation	41.0	23.0	0.0	O
Mn-Fe-BaH_2: Coprecipitation	34.2	5.6	29.0	O, Na, F

The results of the XRD analysis confirmed the formation of Mn, Fe, and Ba-based NCs for the coprecipitation and mechanical approaches (see Figure 6.6). They indicate that when synthesized by the coprecipitation approach, the NC contains oxide phases, while the NC contains Mn and Fe in their metallic forms when it is synthesized by the mechanical approach. The latter finding confirms that mechanically mixed Mn-Fe metals were not contaminated by oxygen during the mixing.

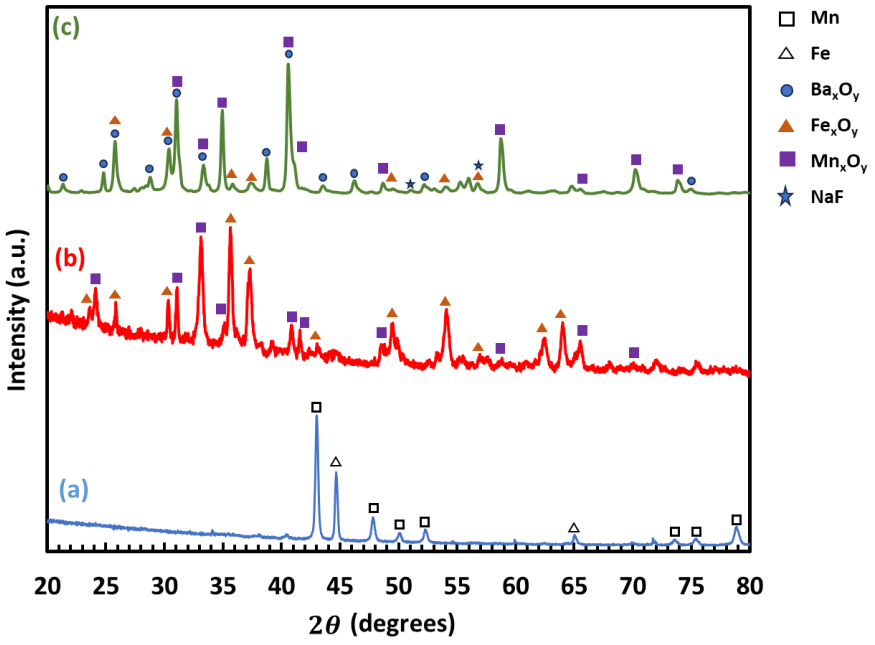

Figure 6.6: XRD patterns of synthesized NCs (a) Mn-Fe: mechanical, (b) Mn-Fe-based: coprecipitation, (c) Mn-Fe-Ba-based: coprecipitation.

6.3.2. MW heating capability of synthesized NCs

To investigate the heating rate of synthesized NCs under MW irradiation, we employed an experimental setup (see Figure 6.2) of 10 g of activated NC and injected nitrogen into the reactor as a reactive and fluidization agent. We measured the resulting bulk temperature (T_b) increase by applying a grounded metallic thermocouple.

The observed heating rate of the synthesized NCs exhibited a notable dependence on the dielectric properties of the synthesized materials. Bulk temperature measurement results of synthesized NCs exposed to MW irradiations are illustrated in Figure 6.7, where all three NCs showed a heating capability under MW irradiations. We observed heating rates of approximately 22 °C/sec, 12 °C/sec (before reaching equilibrium temperature), and 4 °C/sec for Mn-Fe-coprecipitation, Mn-Fe-BaH_2 coprecipitation NCs, and Mn-Fe-mechanical, respectively. The Mn-Fe NC synthesized by the coprecipitation approach showed the best heating capability under MW irradiation among the synthesized NCs. Electrical field dissipation, magnetic field dissipation due to the presence of Fe, and Joule heating are heating mechanisms that contribute to the NCs-MW absorbers' heating process [53].

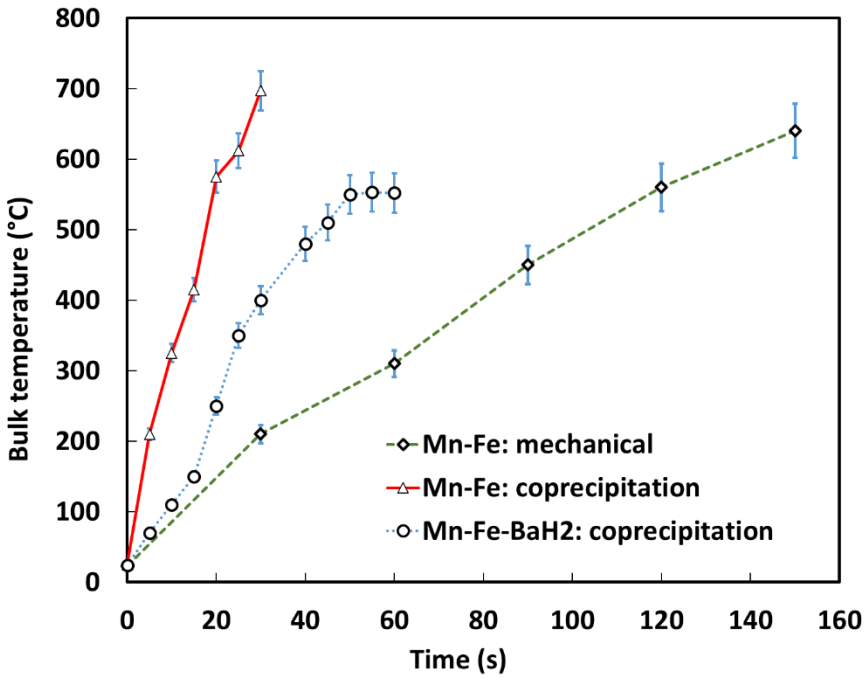

Figure 6.7: Bulk temperature of synthesized NCs under MW irradiation as a function of time (MW power: 1100 W).

The presence of a thin oxide layer on the surface of powdered metals was reported to significantly enhance particle heating under MW irradiation [54]. This phenomenon explains the higher heating

rate of Mn-Fe NC synthesized via the coprecipitation method compared to the mechanical approach. In addition, the crystalline structure of BaH_2 and its limited interaction with MWs result in a lower heating rate for Mn-Fe-BaH_2 NC synthesized through coprecipitation, compared to Mn-Fe NC synthesized by the same method. Although BaH_2 is not an effective MW absorber, it is a promising NC. By incorporating BaH_2 with Mn and Fe elements, we synthesized a NC with an enhanced MW heating capabilities and improved activity.

When the particles in the bed reach an equilibrium bulk temperature, where the dissipated heat within the particles equals the heat transferred to the gas phase and surrounding environment, the bulk temperature remains constant. In the case of Mn-Fe-BaH_2 NC, we achieved the equilibrium bulk temperature after 50 seconds, at a bulk temperature of around 540 °C. This trend aligns with findings reported in the literature [54].

The application of a dense fluidized bed in conjunction with MW irradiations favors the temperature uniformity experienced by the MW absorber bed inventory during exposure to MW irradiations. In addition, one can adjust/enhance the MW penetration depth within the bed by adjusting the bed voidage [55] to maximize MW absorption by the bed inventory. These advantages underscore the importance of considering fluidized beds as a promising reactor type for optimizing MW-driven processes.

6.3.3. Nitridation stage

The initial stage in the CLAS involves nitrogen fixation and the generation of lattice nitrogen. The nitridation reaction mechanism begins with the adsorption of N_2 molecules onto the surface of the NC, followed by their dissociation into nitrogen atoms. These nitrogen atoms subsequently diffuse into the NC structure, resulting in the formation of nitrided phases [56,57]. Studies have shown that the presence of Fe atoms within the NC structure decreases the diffusion energy barrier, thereby promoting the formation of the nitrided phase [43]. We subjected activated NCs to a nitrogen stream under conventional heating by applying a TGA, conventionally heated fluidized bed reactor, and under MW heating by employing a MHFB reactor. TGA results indicated a significant weight increase in synthesized NCs by mechanical and coprecipitation approaches under a N_2 stream (Figure 6.8). This confirms that nitridation was taking place on the synthesized NCs. We observed a minimal weight gain for Fe, which agrees with thermodynamic investigations

for the nitridation stage. Studies suggest that the Fe-N bond is weak, making the thermodynamic feasibility of the iron nitride phase formation unlikely under atmospheric pressure. Nonetheless, the literature indicates that elevating the pressure, up to 5 bars, may enhance the development of iron nitride phases [49].

Results presented in Figure 6.8 show that Fe powders exhibited a negligible weight gain when subjected to a N_2 stream, primarily due to the instability of the Fe-N compound at atmospheric pressure and elevated temperatures. However, the presence of Fe within the NC could decrease the stability of Mn-N, thereby facilitating the hydrogenation stage. The bond between nitrogen and the Mn-Fe composite is stronger than that with Fe alone, allowing nitrogen atoms to be stabilized more effectively. The weaker NC-N bond compared to the Mn-N bond, however, requires less energy and a lower temperature for nitrogen reduction during the hydrogenation stage [39]. The synthesized Mn-Fe NC by mechanical approach showed a weight gain of up to 6.5 wt.% when heated to 800 °C due mainly to the presence of Mn. In contrast, the synthesized Mn-Fe NC by the coprecipitation approach exhibited a non-monotonous trend and weight gain of 5.5 wt.% upon heating to 800 °C. For this sample, the nitridation rate decreased at temperatures above 600 °C, due likely to residual oxide phases within the NC. In the presence of residual oxide phases in the NC structure, some reaction sites were already occupied by oxygen, thus decreasing the amount of nitrogen that could react during the nitridation stage. This residual oxygen came from unreacted oxygen left over from the activation stage, where a mixture of CH_4 and H_2 streams was applied to reduce oxide phases. The oxide phases, mainly MnO, remain stable under the H_2 stream and contribute to the heating of solid particles during MW irradiation [58]. In addition, the inclusion of BaH_2 in the NC resulted in a significantly higher fixed nitrogen content, reaching up to 7.5 wt.% when the sample was heated to 800 °C under identical conditions.

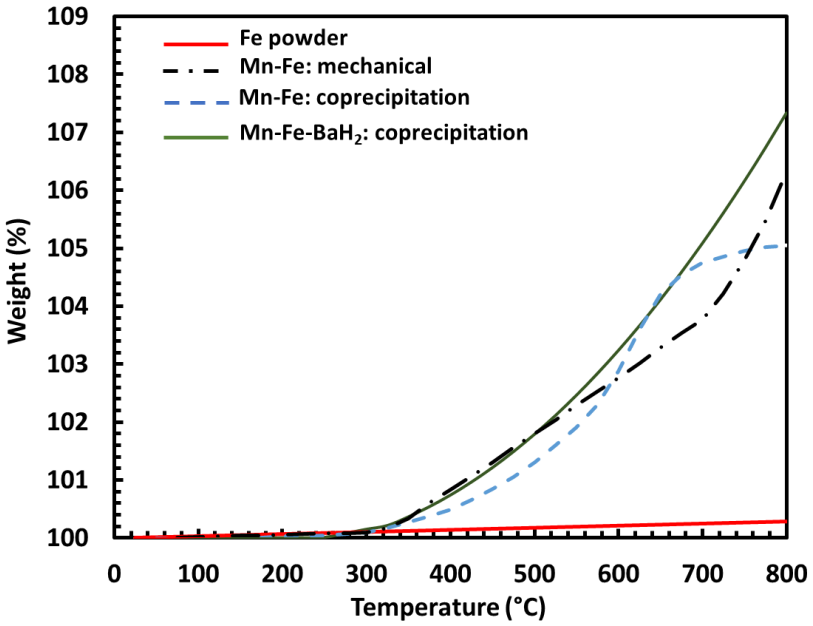

Figure 6.8: Nitridation performances of synthesized NCs and elemental Fe in TGA.

Results of the comparative analysis of weight gain by synthesized NCs subjected to conventional and MW heating at identical bulk temperatures (350, 400, and 700 °C) are presented in Figure 6.9. They highlight that the application of the MW heating method led to higher nitrogen content in the NCs compared to samples treated under the conventional heating method. We can attribute this to a higher solid phase temperature than the bulk temperature under MW irradiation. In the conventional heating method, the bulk temperature is often very similar to the temperatures of solid and gas phases. However, under MW irradiations, the solid phase temperature measured by the pyrometer reached 415, 480, and 850 °C for corresponding bulk temperatures of 350, 400, and 700 °C, respectively.

The MW heating method introduces the possibility of generating micro-scale hot spots on the surface of solid NCs, thereby enhancing the dissociation of nitrogen molecules. The nitridation stage is classified as an exothermic reaction. Despite its exothermic nature, the MW heating method offers advantages, such as the formation of micro-scale hot spots facilitating nitrogen dissociation, lower energy consumption, rapid heating, and volumetric heating [55]. As presented in Figure 6.9, we recorded a higher weight gain for the Mn-Fe-BaH_2 NC compared to other NCs indicating a significant enhancement in nitrogen fixation attributed to the presence of BaH_2 within the NC structure. In addition, an increase in nitridation temperature from 400 to 700 °C resulted

in a small increase in the NCs' weight gain in Mn-Fe-BaH_2 NC (refer to Figure 6.9b and Figure 6.9c).

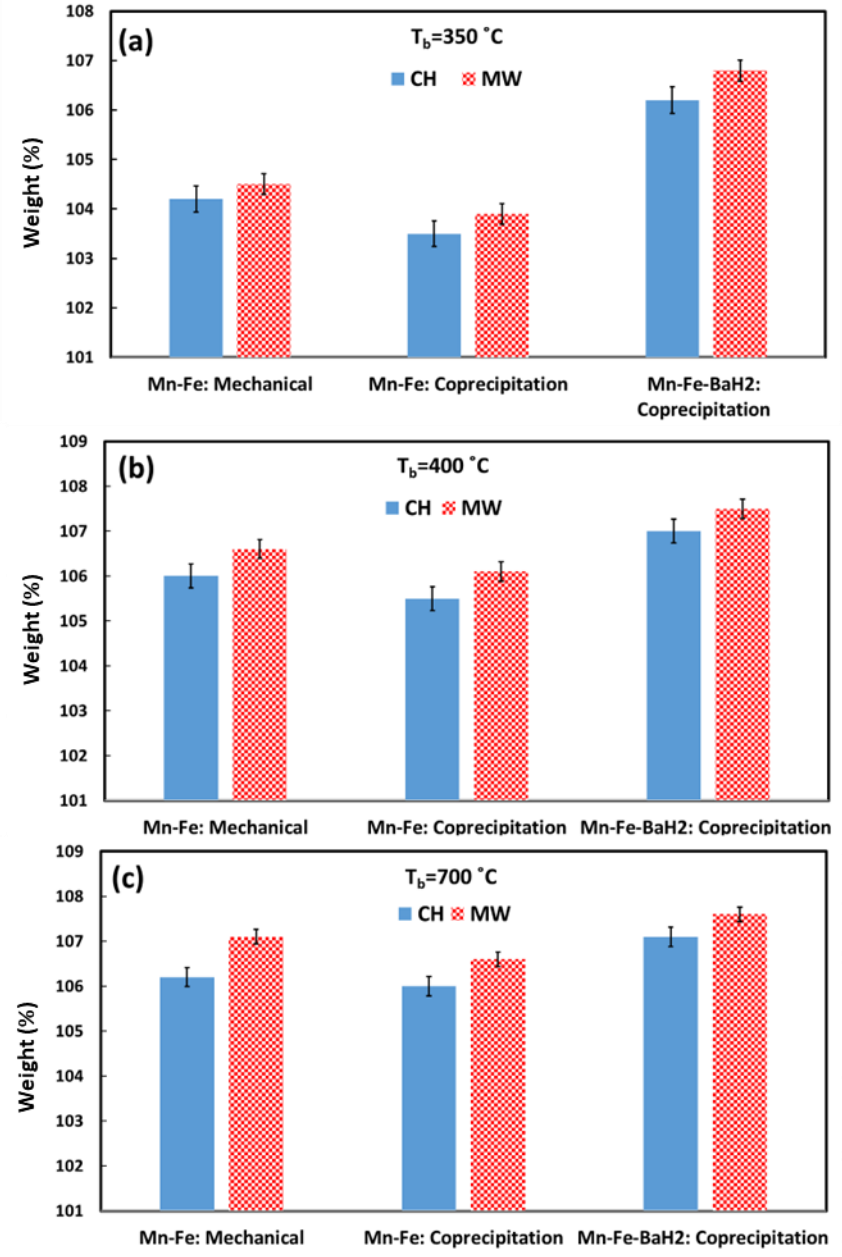

Figure 6.9: Weight gain of synthesized NCs in the nitridation stage under conventional and MW heating for (a) T_b=350 °C, (b) T_b=400 °C, and (c) T_b=700 °C after 20 min of nitridation.

SEM and EDS results of collected samples after nitridation under MW irradiation are presented in Figure 6.10. The presence of small Mn particles in the domain of Fe particles increases the presence of nitrogen elements in these areas. This phenomenon is attributed to the comparatively weak bond strength between Fe and nitrogen. These results confirm that under atmospheric

pressure, Fe under both conventional heating (refer to TGA results in Figure 6.8) and MW heating (Figure 6.10) has a lower nitrogen fixation compared to other composite NCs. The weak involvement of Fe in the nitridation stage shows the inefficiency of the Mn-Fe NC synthesized by the mechanical approach to form uniform nitrogen distribution.

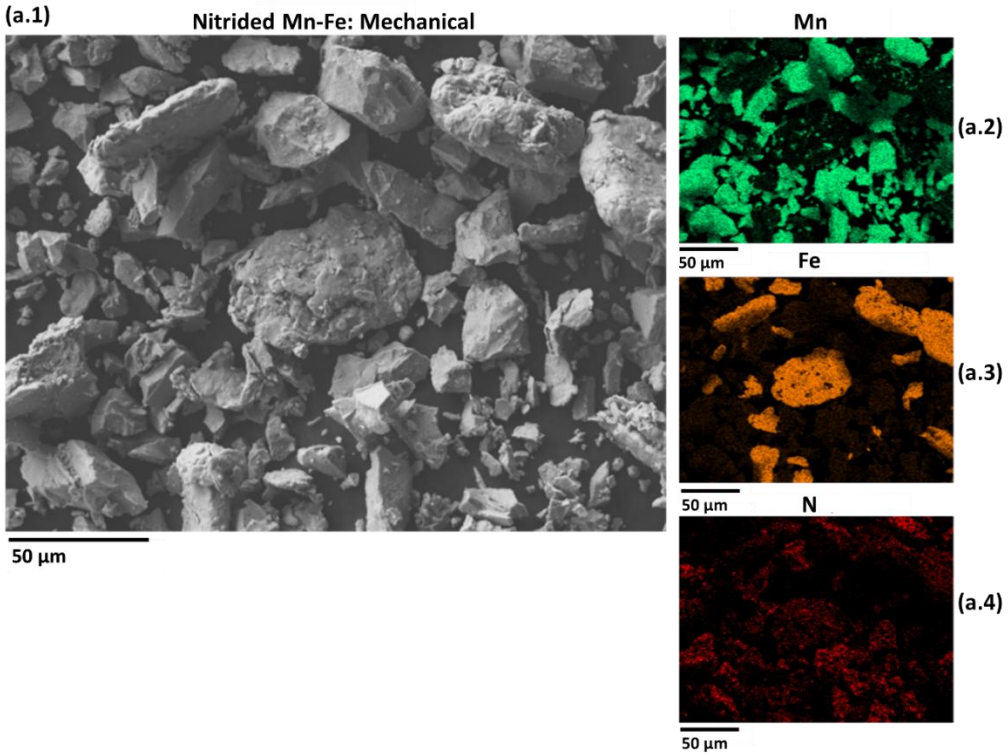

Figure 6.10: SEM analysis and EDS mappings of the nitrided Mn-Fe: mechanical NC under MW heating at T_b = 400 °C: (a.1) SEM image, (a.2) Mn EDS mapping, (a.3) Fe EDS mapping, and (a.4) nitrogen EDS mapping.

The coprecipitation-based synthesis of NCs, in contrast to the mechanical synthesis approach, yielded a uniform distribution of nitrogen elements due to a more moderate bonding between the NC and nitrogen. This could be attributed to the homogeneity between different elements in the coprecipitation NC synthesis approach. We presented SEM and EDS results of the synthesized Mn-Fe-BaH_2 NC through the coprecipitation approach nitrided under MW heating in Figure 6.11. A uniform elemental distribution of Mn, Fe, and Ba is discernible within the nitride phase of the Mn-Fe-BaH_2 NC. BaH_2 is effective in enhancing the nitrogen fixation rate, consequently contributing to the formation of the nitride state in the synthesized NC. This increase yields a superior level of nitrogen fixation when compared to Mn-Fe NCs. The production of barium amid

(BaNH) and Mn_3N_2 as a result of BaH_2 and Mn nitridation could be the main reason for the higher nitrogen fixation when applying the Mn-Fe-BaH_2 NC (see Figure 6.12).

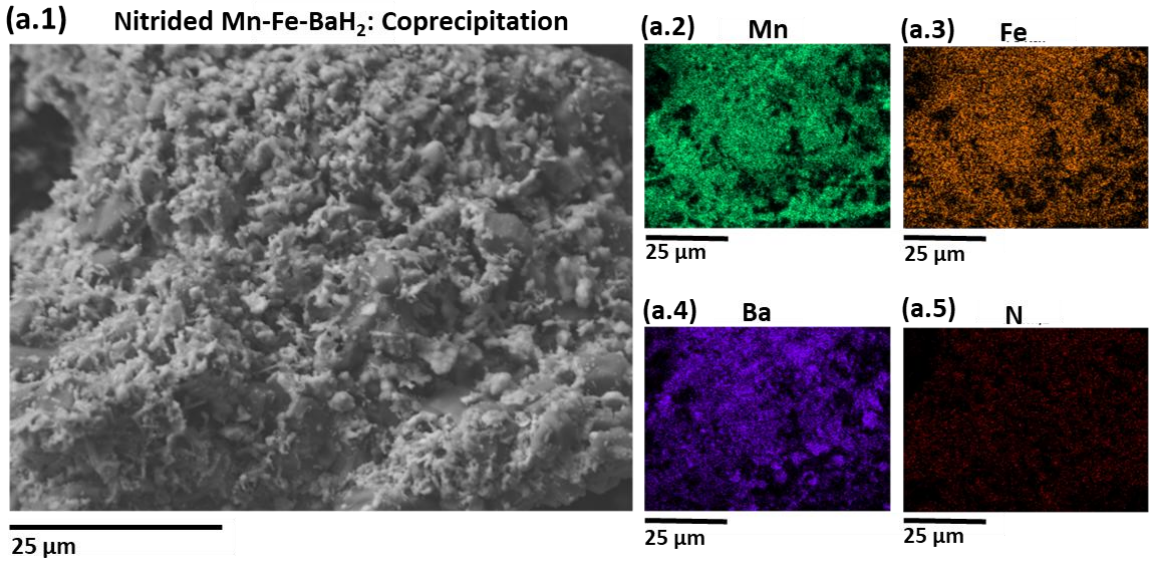

Figure 6.11: (a.1) SEM analysis, and EDS mappings of (a.2) Mn, (a.3) Fe, (a.4) Ba, and (a.5) nitrogen elements of the synthesized Mn-Fe-BaH2 NC by coprecipitation approach nitrided under MW heating at Tb=400 °C.

We presented the XRD analysis results of nitrided Mn-Fe: mechanical, Mn-Fe: coprecipitation NCs, and Mn-Fe-BaH_2: coprecipitation treated under MW irradiation at T_b=400 °C in Figure 6.12. The results of Figure 6.12a (for Mn-Fe-mechanical NC) indicate the predominant formation of manganese nitrides (Mn_4N) as the primary nitride phase within the NC structure. In addition, the iron nitride was not detected, which suggests a limited interaction between Mn and Fe, resulting in the exclusive formation of Mn_4N.

The results presented in Figure 6.12b highlight the formation of iron nitride (Fe_8N) during the nitridation process, indicating the active involvement of iron in the nitridation reaction for Mn-Fe: coprecipitation while Mn_4N and $MnN_{0.388}$ were the predominant manganese phases in the NC.

Figure 6.12c shows the nitrided Mn-Fe-BaH_2 NC, verifying the formation of Mn_4N, Mn_3N_2, and BaNH. Incorporating Ba into the NC structure promoted the formation of Mn_3N_2 as the dominant manganese nitride phase, which was absent in both Mn-Fe: mechanical and Mn-Fe: coprecipitation methods. This contributes to the greater weight gain of Mn-Fe-BaH_2 at lower temperatures (i.e., T_b<400 °C). In addition, the presence of MnO in the NC, produced via coprecipitation, represents the oxide phase that remains after the activation stage. MnO is a well-known MW absorber, and

its inclusion in the NC structure enhances its heating efficiency under MW irradiation [58]. MnO remains stable under hydrogenation operation conditions in an H_2 stream. In addition, it has been reported that stable oxides can promote single-metal nitrides, thereby improving ammonia production properties [35].

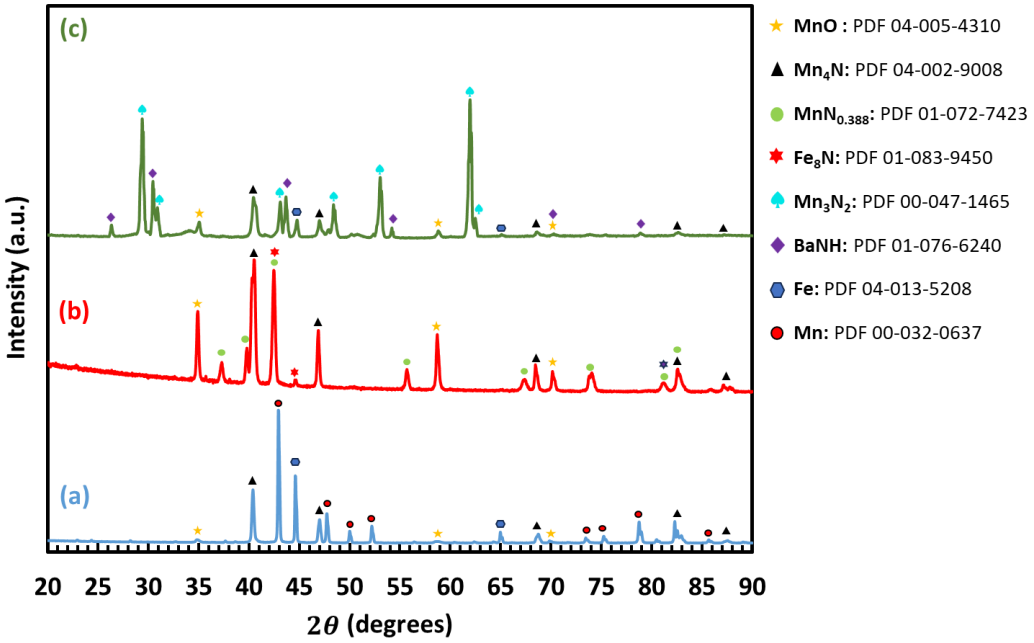

Figure 6.12: XRD pattern of the nitrided, (a) Mn-Fe: mechanical, (b) Mn-Fe: coprecipitation, and (c) Mn-Fe-BaH_2: coprecipitation (nitridation at T_b=400 °C under MW irradiation).

6.3.4. Hydrogenation stage

The hydrogenation of nitrided NCs leads to the generation of ammonia and the production of nitrogen-depleted NCs. R1 and R2 describe the hydrogenation of nitrided Mn-Fe and Mn-Fe-BaH_2 NCs, where a is the number of nitrogen atoms that are involved in the reaction.

$$Fe_xMn_yN_{z_{(s)}} + 1.5aH_{2_{(g)}} \rightarrow Fe_xMn_yN_{z-a_{(s)}} + aNH_{3_{(g)}} \quad \textbf{(R1)}$$

$$Fe_xMn_yN_zBaNH_{(S)} + 1.5aH_{2_{(g)}} \rightarrow Fe_xMn_yN_{z-a}BaH_{2_{(S)}} + (a+1)NH_{3_{(g)}} \quad \textbf{(R2)}$$

We investigated the hydrogenation performances of NCs leading to ammonia production under both conventional and MW heating conditions in different instruments/units, including the H_2-TPR, and conventional heating and MHFB reactors.

The results of H_2-TPR analyses of nitrided NCs are shown in Figure 6.13. They indicate that nitrided Mn-Fe-BaH_2 exhibited a lower hydrogenation temperature compared to nitrided Mn-Fe

by mechanical and coprecipitation approaches. The hydrogenation of nitrided Mn-Fe-BaH_2 started at around 70 °C and its maximum was at 270 °C. This observation is attributed to a more moderate bond between nitrogen and NC, i.e., NC-N, in the case of synthesized Mn-Fe-BaH_2 by the coprecipitation approach. In the case of synthesized Mn-Fe by the coprecipitation approach, hydrogenation started at approximately 180 °C and maximized at about 350 °C. For synthesized Mn-Fe by the mechanical approach, hydrogenation started at around 280 °C and reached its maximum at 375 °C. These findings align with those reported in the study by Wang et al. [45], where the TPR analysis of nitrided MnFeAl NC produced by mechanical approach indicated an H_2-TPR peak occurring around 350-420 °C. The incorporation of Fe and BaH_2 compounds within the NC framework resulted in a decrease in the required hydrogenation temperature due to the formation of a less stable NC-N bond compared to the highly stable Mn-N bond. Consequently, the hydrogenation reaction can be conducted at a lower temperature, mitigating the risk of ammonia decomposition.

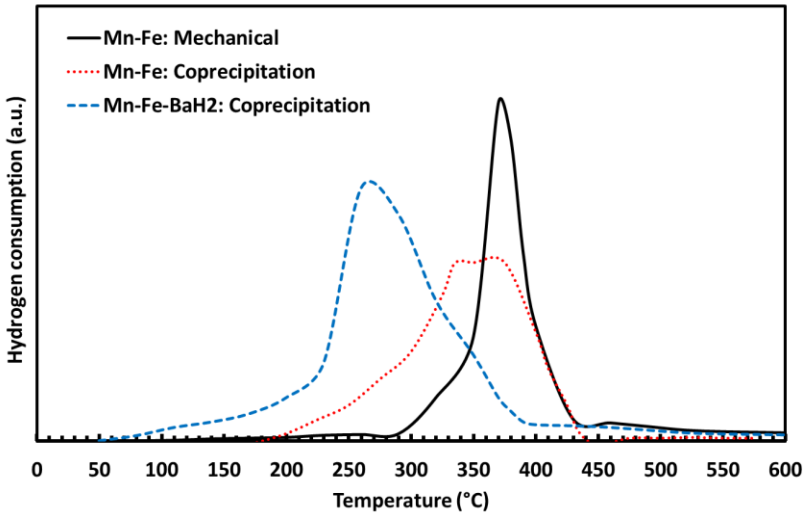

Figure 6.13: H_2-TPR analyses of synthesized NCs in this study nitrided before the hydrogenation step (nitridation at T_b=400 °C under MW irradiation).

We employed the conventional heating reactor described in Section 6.2.3 to investigate the hydrogenation performances of synthesized NCs under conventional heating conditions. To assess the impact of MW heating on ammonia production rates, we compared results obtained from the MHFB setup (described in Section 6.2.3) with those from the conventional heating reactor. We compared ammonia production rates, calculated based on Eq. (6.1), for various NCs heated by conventional and MW heating methods in Figure 6.14. The nitridation temperature was set to T_b

= 400 °C for both conventional and MW heating approaches. In the conventional approach, the temperatures of the solid and bulk phases are equal, whereas under MW heating, the solid temperature reached 505 °C in the nitridation stage. In addition, during the hydrogenation stage, the reaction was conducted at T_b = 350 °C, corresponding to a solid temperature of 415 °C under MW irradiation. Results indicated that for all tested NCs, the application of MW heating significantly enhanced the ammonia production rate compared to the conventional heating method. For instance, the ammonia production rate for the Mn-Fe-BaH_2 NC under conventional heating was 11391 µmol/g.h, while it was 35793 µmol/g.h with MW heating. The difference between the ammonia production rate under MW and conventional heating conditions decreased from the Mn-Fe-BaH_2 NC synthesized by the coprecipitation approach to the Mn-Fe NC synthesized by the mechanical approach. The Mn-Fe-BaH_2 NC exhibited the highest ammonia production rate among the studied NCs. This could be attributed to the presence of BaH_2 in its composition. The presence of BaH_2 enhances the electron-donating capability of NCs during both the nitridation and hydrogenation reactions. During the hydrogenation stage, the hydrogen atoms within the NC structure, e.g., BaNH, enable hydrogenation to occur at lower temperatures or result in higher ammonia production rates at the same temperature. This effect explains the increased ammonia production rate observed for Mn-Fe-BaH_2 NC.

$$\textbf{Production rate} = \frac{\textbf{Amount of produced ammonia}}{\textbf{NC weight} \times [\textbf{Hydrogenation time}]} \quad \textbf{(6.1)}$$

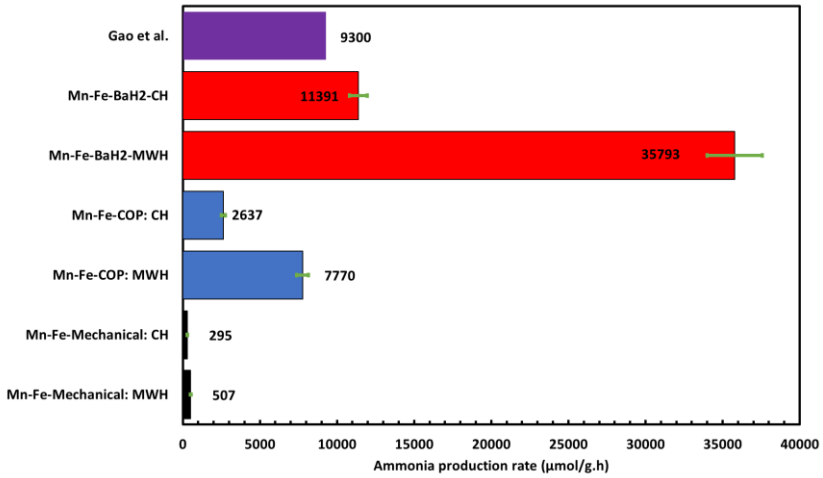

Figure 6.14: Ammonia production rates of synthesized NCs tested under MW irradiation and conventional heating conditions (nitridation at T_b=400 °C and hydrogenation at T_b=350 °C) and Ni-BaH_2 NC tested under conventional heating conditions from the study by Gao et al. [59].

When comparing our results with those reported in literature, e.g., in the study by Gao et al. [59] when adopting the Ni-BaH_2 NC, the Mn-Fe-BaH_2 NC prepared in this study and tested under MW heating conditions led to a considerably higher ammonia production rate, see Figure 14. Gao et al. [59] prepared the Ni-BaH_2 NC by the ball milling approach and were able to achieve an approximate 9300 μmol/g.h based on hydrogenation time under conventional heating at 300 °C.

The predominant factor contributing to the higher rate of ammonia production under MW irradiation compared to conventional heating is the lower gas phase temperature in the MW heating system. Despite conventional heating, where both gas and solid phases are uniformly heated to the reaction temperature, MW irradiations selectively heat solids, maintaining a lower temperature in the gas phase. This selective heating decreases the risk of post-formation ammonia decomposition. The temperature difference between gas and solid phases can vary with variables, such as bed hydrodynamics, operating temperature, particle diameter, and electromagnetic properties.

Challenges in independent monitoring of gas and solid phase temperatures are the main reason for the discrepancy between results obtained under MW heating and those obtained under conventional heating. A grounded metallic thermocouple for temperature measurement during MW irradiations measures the temperature pertaining to the gas-solid mixture that is generally higher than the gas phase but lower than the solid phase temperature. This phenomenon leads to the underestimation of the solid phase temperature, consequently resulting in a higher observed ammonia production rate under MW irradiations when compared to conventional heating with similar bulk temperatures. In addition, the introduction of MW heating induces the formation of hot spots at both micro and macro scales. Micro-scale hot spots arise from variations in the dielectric properties of different elements within the synthesized NCs, increasing the ammonia production rate by facilitating nitrogen dissociation. However, macro-scale hot spots emerge due to limitations in penetration depth, wave dissipation, impedance mismatching between bed and cavity, and non-uniform electrical field intensity.

The influence of temperature on the ammonia production rate of the Mn-Fe-BaH_2 NC under MW irradiations is presented in Figure 6.15. The ammonia production rate was measured at T_b= 350, 300, 250, 200, and 150 °C which corresponds to T_s= 420, 360, 290, 240, and 180 °C, respectively. Results show that under MW heating conditions, ammonia synthesis is achievable even at temperatures as low as T_b= 150 °C for the Mn-Fe-BaH_2 NC. We observed a higher ammonia

production rate upon increasing the hydrogenation temperature (Figure 6.15), which is primarily attributed to the increase in the reaction rate with the operating temperature. The rate of hydrogenation reaction experiences an increase with the temperature. The application of MW heating, coupled with the temperature difference between gas and solid phases, yields a higher temperature at the active sites of the solid phase. A lower temperature in the gas phase suppresses the ammonia decomposition reaction, thus increasing the overall ammonia production rate.

In conventional ammonia synthesis methods, such as the HB technology, ammonia production typically reaches thermodynamic equilibrium. At atmospheric pressure and temperatures above 250 °C, the produced ammonia tends to undergo complete decomposition. However, the coupled implementation of MW heating and CLAS technology enables ammonia production at atmospheric pressure while significantly reducing the risk of decomposition. MHCLAS technology divides the ammonia synthesis reaction into two sequential steps: nitridation and hydrogenation. This approach overcomes the thermodynamic limitations of conventional ammonia synthesis. However, in conventional CLAS, the hydrogenation stage operates at temperatures as high as 500 °C, which raises the risk of ammonia decomposition. The introduction of the new Mn-Fe-BaH_2 NC, operating effectively within a bulk temperature range of 150 to 350 °C, minimizes the decomposition risk of synthesized ammonia, providing a more stable and efficient alternative.

The application of the Mn-Fe-BaH_2 NC, synthesized by the coprecipitation approach, has demonstrated a notable decrease in the hydrogenation reaction temperature compared to conventional NCs reported in literature. Comparable results are reported in the study by Hattori et al. [60] on catalytic ammonia synthesis by employing BaH_2-BaO/Fe/CaH_2 catalyst under conventional heating. However, by integrating chemical looping with MW heating for Mn-Fe-BaH_2 NC in the present study, the ammonia production rate was approximately ten times higher than that observed in Hattori's study.

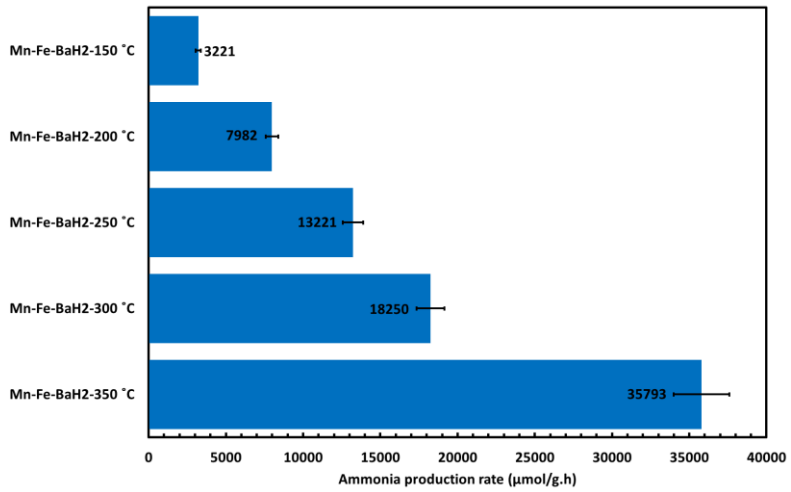

Figure 6.15: Effect of temperature on the ammonia production rate for the Mn-Fe-BaH_2 NC under MW heating conditions (nitridation at T_b=400 °C).

6.4. Conclusion

In this study, we formulated three NCs mainly composed of Mn and Fe for application in MHCLAS technology to produce ammonia. The technology operated at atmospheric pressure and temperatures ranging from 350 to 700 °C for the nitridation reaction and 150 to 350 °C for the hydrogenation stage. We synthesized NCs by mechanical and coprecipitation approaches, which included Mn-Fe NCs synthesized by the two approaches and the Mn-Fe-BaH_2 NC synthesized by the coprecipitation approach. We had uniform NCs in terms of size and elemental distribution by the co-precipitation approach and they outperformed nitridation and overall ammonia production compared to the mechanical approach.

The application of selective MW heating led to a temperature difference between gas and solid phases, which suppressed undesirable gas-phase reactions, like ammonia decomposition. It, hence, resulted in an increased ammonia production for both Mn-Fe and Mn-Fe-BaH_2 NCs compared to conventional heating conditions. We achieved a maximum ammonia production rate of 35793 µmol/g.h with nitridation at 400 °C and hydrogenation at 350 °C. Under MW heating conditions, the ammonia production by the Mn-Fe-BaH_2 NC was initiated at temperatures as low as 150 °C. The presence of BaH_2 in the NC structure caused ammonia production at a lower temperature, i.e., as low as 150 °C. The findings of this study will pave the way for the scale-up of an effective ammonia production technology by integrating selective MW heating with a novel Mn-Fe-BaH_2 NC and chemical looping concept and its decentralization.

CRediT authorship contribution statement

Kazem Adavi: Conceptualization, Methodology, Validation, Formal analysis, Investigation, Data-curation, Writing - original draft, Visualization. **Zhaohui Chen:** Conceptualization, Writing - review & editing. **Adrian Carrillo Garcia:** Methodology, Investigation, Writing - review & editing. **Jaber Shabanian:** Conceptualization, Methodology, Writing - review & editing, Project administration. **Jamal Chaouki:** Conceptualization, Resources, Supervision, Writing - review & editing, Funding acquisition.

Acknowledgment

The authors gratefully acknowledge the financial support provided for this research study by the OCP Group of Morocco.

References

[1] M.M. Sarafraz, F.C. Christo, Sustainable three-stage chemical looping ammonia production (3CLAP) process, Energy Convers Manag 229 (2021). https://doi.org/10.1016/j.enconman.2020.113735.

[2] S.R. Bull, Renewable energy transportation technologies, Renew Energy 9 (1996). https://doi.org/10.1016/0960-1481(96)88453-9.

[3] S.O. Amrouche, D. Rekioua, T. Rekioua, S. Bacha, Overview of energy storage in renewable energy systems, Int J Hydrogen Energy 41 (2016) 20914–20927. https://doi.org/10.1016/j.ijhydene.2016.06.243.

[4] A. Hellman, K. Honkala, S. Dahl, C.H. Christensen, J.K. Nørskov, Ammonia Synthesis: State of the Bellwether Reaction, in: Comprehensive Inorganic Chemistry II (Second Edition): From Elements to Applications, 2013. https://doi.org/10.1016/B978-0-08-097774-4.00725-7.

[5] S.S. Bhogilla, Numerical simulation of metal hydride based thermal energy storage system for concentrating solar power plants, Renew Energy 172 (2021). https://doi.org/10.1016/j.renene.2021.03.109.

[6] C.M. Rangel, V.R. Fernandes, A.J. Gano, Metal hydride-based hydrogen production and storage system for stationary applications powered by renewable sources, Renew Energy 197 (2022). https://doi.org/10.1016/j.renene.2022.07.103.

[7] J. Sunku Prasad, P. Muthukumar, Design and performance analysis of an annular metal hydride reactor for large-scale hydrogen storage applications, Renew Energy 181 (2022). https://doi.org/10.1016/j.renene.2021.09.109.

[8] H. Xu, L. Zhang, S.J. Wei, X. Tong, Y. Yang, X. Ji, A novel solar system for photothermal-assisted electrocatalytic nitrate reduction reaction to ammonia, Renew Energy 221 (2024). https://doi.org/10.1016/j.renene.2023.119707.

[9] S. Giddey, S.P.S. Badwal, C. Munnings, M. Dolan, Ammonia as a Renewable Energy Transportation Media, ACS Sustain Chem Eng 5 (2017). https://doi.org/10.1021/acssuschemeng.7b02219.

[10] N. Morlanés, S.P. Katikaneni, S.N. Paglieri, A. Harale, B. Solami, S.M. Sarathy, J. Gascon, A technological roadmap to the ammonia energy economy: Current state and missing technologies, Chemical Engineering Journal 408 (2021). https://doi.org/10.1016/j.cej.2020.127310.

[11] A. Yapicioglu, I. Dincer, A review on clean ammonia as a potential fuel for power generators, Renewable and Sustainable Energy Reviews 103 (2019) 96–108. https://doi.org/10.1016/j.rser.2018.12.023.

[12] M. Tawalbeh, S.Z.M. Murtaza, A. Al-Othman, A.H. Alami, K. Singh, A.G. Olabi, Ammonia: A versatile candidate for the use in energy storage systems, Renew Energy 194 (2022). https://doi.org/10.1016/j.renene.2022.06.015.

[13] T. Gu, S.S. Araya, C. Yin, V. Liso, Exploring decentralized ammonia synthesis for hydrogen storage and transport: A comprehensive CFD investigation with experimental validation and parametric study, Energy Convers Manag 295 (2023). https://doi.org/10.1016/j.enconman.2023.117604.

[14] K. Smart, Review of Recent Progress in Green Ammonia Synthesis: Decarbonisation of fertiliser and fuels via green synthesis, Johnson Matthey Technology Review 66 (2022). https://doi.org/10.1595/205651322X16334238659301.

[15] E. Fu, F. Gong, S. Wang, C. Liu, P. Yang, Y. Jing, R. Xiao, Ni-Mn-N derived composite nitrogen carriers for enhanced chemical looping ammonia production, Fuel Processing Technology 252 (2023). https://doi.org/10.1016/j.fuproc.2023.107971.

[16] N. Salmon, R. Bañares-Alcántara, Green ammonia as a spatial energy vector: A review, Sustain Energy Fuels 5 (2021). https://doi.org/10.1039/d1se00345c.

[17] K. Adavi, A. Amini, M. Latifi, J. Shabanian, J. Chaouki, Kinetic study of multiphase reactions under microwave irradiation: A mini-review, Frontiers in Chemical Engineering 4 (2022). https://doi.org/10.3389/fceng.2022.1059160.

[18] Z. Liu, Q. Yu, H. Wang, J. Wu, S. Tao, Selecting nitrogen carriers used for chemical looping ammonia generation of biomass and H2O by thermodynamic method, Int J Hydrogen Energy 48 (2023) 4035–4051. https://doi.org/10.1016/j.ijhydene.2022.10.197.

[19] A. Edrisi, Z. Mansoori, B. Dabir, Using three chemical looping reactors in ammonia production process e A novel plant configuration for a green production, Int J Hydrogen Energy 39 (2014) 8271–8282. https://doi.org/10.1016/j.ijhydene.2014.03.119.

[20] C. Wild, V. Abdelsayed, D. Shekhawat, M.J. Spencer, Ambient pressure synthesis of ammonia using a microwave reactor, Catal Commun 115 (2018) 64–67. https://doi.org/10.1016/j.catcom.2018.07.010.

[21] Q. Wang, J. Guo, P. Chen, Recent progress towards mild-condition ammonia synthesis, Journal of Energy Chemistry 36 (2019) 25–36. https://doi.org/10.1016/j.jechem.2019.01.027.

[22] Z. Sun, Y. Zhang, H. Huang, Y. Luo, L. Lin, L. Jiang, Modeling and simulation of dynamic characteristics of a green ammonia synthesis system, Energy Convers Manag 300 (2024). https://doi.org/10.1016/j.enconman.2023.117893.

[23] S. Feng, W. Gao, Q. Wang, Y. Guan, H. Yan, H. Wu, H. Cao, J. Guo, P. Chen, A multi-functional composite nitrogen carrier for ammonia production via a chemical looping route, J Mater Chem A Mater 9 (2021) 1039–1047. https://doi.org/10.1039/d0ta10519h.

[24] Y. Zhao, Y. Zhao, J. Wang, W. Bao, L. Chang, Highly simplified and efficient process for methanol and ammonia synthesis from coke-oven gas and pulverized coke using chemical looping technology, Int J Hydrogen Energy 48 (2023) 39330–39346. https://doi.org/10.1016/j.ijhydene.2023.08.055.

[25] S.W. Brown, B. Robinson, Y. Wang, C. Wildfire, J. Hu, Microwave heated chemical looping ammonia synthesis over Fe and CoMo particles, J Mater Chem A Mater 10 (2022) 15497–15507. https://doi.org/10.1039/d2ta03241d.

[26] S. Zhang, Y. Zhao, R. Shi, G.I.N. Waterhouse, T. Zhang, Photocatalytic ammonia synthesis : Recent progress and future, EnergyChem 1 (2019) 100013. https://doi.org/10.1016/j.enchem.2019.100013.

[27] S. Junwang, Progress and challenges in photocatalytic ammonia synthesis, Mater Adv 2 (2021) 264–581. https://doi.org/10.1039/d0ma00590h.

[28] L. Hu, Z. Xing, X. Feng, Understanding the Electrocatalytic Interface for Ambient Ammonia Synthesis, Energy Letters 5 (2020) 430–436. https://doi.org/10.1021/acsenergylett.9b02679.

[29] G. Duan, Y. Chen, Y. Tang, K.A.M. Gasem, P. Wan, D. Ding, M. Fan, Advances in electrocatalytic ammonia synthesis under mild conditions, Prog Energy Combust Sci 81 (2020) 100860. https://doi.org/10.1016/j.pecs.2020.100860.

[30] L. Wang, M. Xia, H. Wang, K. Huang, C. Qian, C.T. Maravelias, G.A. Ozin, Greening Ammonia toward the Solar Ammonia Refinery, Joule 2 (2018) 1055–1074. https://doi.org/10.1016/j.joule.2018.04.017.

[31] K.H.R. Rouwenhorst, L. Le, Feasibility Study of Plasma-Catalytic Ammonia Synthesis for Energy Storage Applications, Catalysts 10 (2020).

[32] K.H.R. Rouwenhorst, P.M. Krzywda, N.E. Benes, G. Mul, L. Lefferts, Chapter 4 - Ammonia Production Technologies, Elsevier Inc., 2021. https://doi.org/10.1016/B978-0-12-820560-0.00004-7.

[33] L. Burrows, P. Gao, G.M. Bollas, Thermodynamic feasibility analysis of distributed chemical looping ammonia synthesis, Chemical Engineering Journal 426 (2021) 131421. https://doi.org/10.1016/j.cej.2021.131421.

[34] E. Fu, F. Gong, S. Wang, R. Xiao, Chemical Looping Technology in Mild-Condition Ammonia Production: A Comprehensive Review and Analysis, Small 20 (2024). https://doi.org/10.1002/smll.202305095.

[35] S. Brown, J. Hu, Review of chemical looping ammonia synthesis materials, Chem Eng Sci 280 (2023). https://doi.org/10.1016/j.ces.2023.119063.

[36] Y. Gao, Y. Wu, Q. Zhang, X. Chen, G. Jiang, D. Liu, N-desorption or NH3 generation of TiO2-loaded Al-based nitrogen carrier during chemical looping ammonia generation technology, Int J Hydrogen Energy 43 (2018) 16589–16597. https://doi.org/10.1016/j.ijhydene.2018.07.042.

[37] R. V. Kappagantula, G.D. Ingram, H.B. Vuthaluru, Effectiveness of Three Reactor Chemical Looping for ammonia production using Aspen Plus simulation, Int J Hydrogen Energy 61 (2024) 1340–1355. https://doi.org/10.1016/j.ijhydene.2024.02.238.

[38] M.G. Heidlage, E.A. Kezar, K.C. Snow, P.H. Pfromm, Thermochemical Synthesis of Ammonia and Syngas from Natural Gas at Atmospheric Pressure, I&EC (2017) 14014–14024. https://doi.org/10.1021/acs.iecr.7b03173.

[39] R. Michalsky, P.H. Pfromm, An Ionicity Rationale to Design Solid phase Metal Nitride Reactants for Solar Ammonia Production, The Journal of Physical Chemistry C 116 (2012) 23243–23251.

[40] R. Michalsky, P.H. Pfromm, A. Steinfeld, R. Michalsky, Rational design of metal nitride redox materials for solar-driven ammonia synthesis, Interface Focus 5 (2015).

[41] Z. Gong, T. Zhang, N. Li, Y. Yang, S. Liu, J. Zheng, Z. Yu, S. Yang, Progress in design and application research of nitrogen carrier in chemical looping ammonia synthesis technology, Ranliao Huaxue Xuebao/Journal of Fuel Chemistry and Technology 52 (2024) 512–524. https://doi.org/10.1016/S1872-5813(23)60397-4.

[42] C. Mitchell, The Denitridation of Nitrides of Iron , Cobalt and Rhenium Under Hydrogen, Top Catal 56 (2013) 1963–1969. https://doi.org/10.1007/s11244-013-0133-z.

[43] R. Michalsky, A.M. Avram, B.A. Peterson, P.H. Pfromm, A.A. Peterson, Chemical looping of metal nitride catalysts: low- pressure ammonia synthesis for energy storage, Chem Sci (2015) 3965–3974. https://doi.org/10.1039/c5sc00789e.

[44] S. Yang, T. Zhang, Y. Yang, B. Wang, J. Li, Z. Gong, Z. Yao, W. Du, S. Liu, Z. Yu, Molybdenum-based nitrogen carrier for ammonia production via a chemical looping route, Appl Catal B 312 (2022). https://doi.org/10.1016/j.apcatb.2022.121404.

[45] B. Wang, X. Yin, P. Wang, L. Shen, Chemical looping ammonia synthesis at atmospheric pressure benefiting from synergistic effect of Mn- and Fe-based nitrogen carriers, Int J Hydrogen Energy 48 (2023). https://doi.org/10.1016/j.ijhydene.2022.10.132.

[46] J. Guo, P. Chen, Interplay of Alkali, Transition Metals, Nitrogen, and Hydrogen in Ammonia Synthesis and Decomposition Reactions, Accounts 54 (2021) 2434–2444. https://doi.org/10.1021/acs.accounts.1c00076.

[47] W. Gao, J. Guo, P. Chen, P. Chen, Hydrides , Amides and Imides Mediated Ammonia Synthesis and Decomposition, Chin J Chem Eng 37 (2019) 442–451. https://doi.org/10.1002/cjoc.201800586.

[48] L. Zhou, X. Li, Q. Li, A. Kalu, C. Liu, X. Liu, W. Li, Advances in Nitrogen Carriers for Chemical Looping Processes for Sustainable and Carbon-Free Ammonia Synthesis, ACS Catal 13 (2023) 15087–15106. https://doi.org/10.1021/acscatal.3c03717.

[49] W. Gao, R. Wang, S. Feng, Y. Wang, Z. Sun, J. Guo, P. Chen, Thermodynamic and kinetic considerations of nitrogen carriers for chemical looping ammonia synthesis, Discover Chemical Engineering 3 (2023). https://doi.org/10.1007/s43938-023-00019-4.

[50] K. Adavi, A. Molaei Dehkordi, Synthesis and polymorph controlling of calcite and aragonite calcium carbonate nanoparticles in a confined impinging-jets reactor, Chemical Engineering and Processing - Process Intensification 159 (2021). https://doi.org/10.1016/j.cep.2020.108239.

[51] K. Adavi, D. Tahery, M. Khajouei, M. Latifi, High local supersaturation formation for precipitated calcium carbonate synthesis by applying a rotating disk reactor, Brazilian Journal of Chemical Engineering (2023). https://doi.org/10.1007/s43153-023-00423-x.

[52] M. Hattori, S. Iijima, T. Nakao, H. Hosono, M. Hara, Solid solution for catalytic ammonia synthesis from nitrogen and hydrogen gases at 50 °C, Nat Commun 11 (2020). https://doi.org/10.1038/s41467-020-15868-8.

[53] A. Amini, M. Latifi, J. Chaouki, Electrification of materials processing via microwave irradiation: A review of mechanism and applications, Appl Therm Eng 193 (2021). https://doi.org/10.1016/j.applthermaleng.2021.117003.

[54] M. Khodabandehloo, J. Shabanian, J.P. Harvey, J. Chaouki, Microwave heating-assisted chemical looping dry reforming of methane, Int J Hydrogen Energy 71 (2024) 1380–1391. https://doi.org/10.1016/j.ijhydene.2024.05.295.

[55] K. Adavi, J. Shabanian, J. Chaouki, Temperature Distribution Assessment in Gas-Solid Reactive and Nonreactive Systems Heated by Microwaves, Ind Eng Chem Res 62 (2023). https://doi.org/10.1021/acs.iecr.3c00575.

[56] W. Mohammadi Aframehr, P.H. Pfromm, Activating dinitrogen for chemical looping ammonia Synthesis: Mn nitride layer growth modeling, Chem Eng Sci 252 (2022). https://doi.org/10.1016/j.ces.2021.117287.

[57] W. Mohammadi Aframehr, P.H. Pfromm, Activating dinitrogen for chemical looping ammonia synthesis: nitridation of manganese, J Mater Sci 56 (2021). https://doi.org/10.1007/s10853-021-06079-7.

[58] P. Hu, S. Dong, X. Li, J. Chen, X. Zhang, P. Hu, S. Zhang, A low-cost strategy to synthesize MnO nanorods anchored on 3D biomass-derived carbon with superior microwave absorption properties, J Mater Chem C Mater 7 (2019). https://doi.org/10.1039/c9tc02182e.

[59] W. Gao, J. Guo, P. Wang, Q. Wang, F. Chang, Q. Pei, W. Zhang, L. Liu, P. Chen, Chemical looping process based on metal imides as nitrogen carriers, Nat Energy 3 (2018). https://doi.org/10.1038/s41560-018-0268-z.

[60] M. Hattori, N. Okuyama, H. Kurosawa, M. Hara, Low-Temperature Ammonia Synthesis on Iron Catalyst with an Electron Donor, J Am Chem Soc 145 (2023). https://doi.org/10.1021/jacs.2c13015.

CHAPTER 7: ARTICLE 4-KINETIC STUDY OF MICROWAVE HEATING-ASSISTED CHEMICAL LOOPING AMMONIA SYNTHESIS OVER Mn-Fe-Ba-BASED NITROGEN CARRIER

Kazem Adavi [a], Adrian Carrillo Garcia [a], Jaber Shabanian [a], Mohammad Latifi [a], and Jamal Chaouki [a, b,*]

[a] Process Engineering Advanced Research Lab (PEARL), Department of Chemical Engineering, Polytechnique Montreal, P. O. Box 6079, Station Centre-Ville, Montreal, (Quebec) Canada, H3C 3A7.

[b] University Mohamed VI Polytechnique, Benguerir, Morocco.

[*] Corresponding author: Tel. +1 (514) 340-4711 X 4034, fax: +1 (514) 340-4159, E-mail: jamal.chaouki@polymtl.ca

Submitted to Fuel (Feb 6th, 2025)

Abstract

Microwave heating-assisted chemical looping ammonia synthesis (MHCLAS) has emerged as a promising alternative to conventional ammonia production technologies, e.g., Haber-Bosch. Kinetic studies associated with the MHCLAS are very limited in literature. In this study, we investigated the stability and kinetic behavior of Mn-Fe-BaH2 nitrogen carriers (NCs) in a microwave heating-assisted fluidized bed reactor. Preliminary assessments demonstrated that ammonia production remained consistent at a nitridation bulk temperature of 565 °C and a hydrogenation temperature of 320 °C. For the kinetic studies, we focused on two sequential reactions of nitridation and hydrogenation. We performed the nitridation reaction in a temperature range of 300 to 630 °C, where weight gain and the formation of nitride phases confirmed the reaction progression. We adopted the corresponding information in the kinetic study. We conducted the subsequent hydrogenation of the nitrided NC in the same reactor. It yielded a higher ammonia production at atmospheric pressure compared to those reported in literature under conventional heating. The unique selective heating properties of microwaves, combined with moderate bonding between the NC and nitrogen atoms, resulted in low apparent activation energies for both reactions, i.e., 25.6 and 23.7 kJ/mol for the nitridation and hydrogenation reactions, respectively. The nitridation reaction followed the contracting kinetic models, while the Avrami-Erofeev-3 kinetic models most effectively describe the hydrogenation reaction. The reaction models developed for the nitridation and hydrogenation stages in this work are independent of

reactor hydrodynamics or type, making them important for advancing reactor modeling and MHCLAS technology scaling up in the future.

Keywords: Microwave; Hydrogen storage; Ammonia synthesis; Chemical looping; Nitridation kinetic; Hydrogenation kinetic.

7.1. Introduction

Ammonia serves as an excellent hydrogen (H2) carrier, enabling the safe and effective transportation and storage of H2 under mild conditions. Unlike liquid H2, which requires extreme conditions, ammonia can be stored at atmospheric pressure and relatively moderate temperatures as low as -33°C [1–4]. This capability yields a threefold decrease in costs associated with H2 storage as a promising renewable energy carrier when comparing it with conventional H2 storage approaches, e.g., liquid H2 storage approaches. Consequently, recent studies have focused on various technologies for ammonia production by employing environmentally friendly green H2 [5].

Haber-Bosch (HB) technology, i.e., a conventional technology for ammonia production practiced at commercial scale, operates under harsh operating conditions, typically at pressures and temperatures of 100-300 bar and 400-600 °C, respectively [6–8]. Ammonia synthesis through electrocatalysis and photocatalysis exhibits a relatively low production rate and challenges in the accurate quantification and purification of ammonia [9–11]. While plasma-assisted ammonia synthesis has widely been explored for nitrogen (N2) dissociation, its viability is limited by the exothermic nature of ammonia production reaction, making it less favorable as the primary candidate [1,12,13]. Researchers implemented microwave (MW) heating for a single-stage catalytic ammonia synthesis. Due to the selective heating properties of MWs, they helped obtain a higher ammonia production rate compared to conventional heating methods [3,14]. However, competitive adsorption of N2 and H2 molecules on the catalyst surface remains the main issue for ammonia synthesis under MW heating [15].

Chemical looping ammonia synthesis (CLAS) consists of either two, i.e., nitridation and hydrogenation, or three, i.e., reduction, nitridation, and hydrogenation, sequential reactors, has shown promising results in enhancing ammonia production under atmospheric pressure. Various

ammonia synthesis scenarios exist within CLAS, such as water (H2O)-CLAS [3], H2-CLAS [10,14], and alkali/alkaline hydride (AH)-CLAS [16–18]. The H2O-CLAS involves high temperatures, reaching up to 1000 °C, necessary for the reduction of oxidized nitrogen carriers (NCs) [19]. The temperature ranges for the H2-CLAS and AH-CLAS technologies for the nitridation (200-750 °C) and the hydrogenation stages (150-700 °C) depend on the specific type of NC that was involved in these reactions [2,3,10,19]. Various NCs have been utilized in H2-CLAS, such as manganese (Mn), cobalt-molybdenum (CoMo), iron (Fe), barium hydride (BaH2), lithium hydride (LiH), and calcium hydride (CaH2) [3]. In our recent study [20], we demonstrated that synthesized Mn-Fe-BaH2 NC in the study had a promising performance in ammonia production among the highlighted NCs when adopted in a MW heating-assisted chemical looping ammonia synthesis (MHCLAS) technology. A schematic representation of the proposed MHCLAS technology is presented in Figure 7.1. In the first step, i.e., nitridation, the developed NC goes under the nitridation reaction, and nitrogen atoms are fixed in the NC structure. In the second step, i.e., hydrogenation, the nitrided NC is exposed to a H2 stream, producing ammonia and nitrogen-depleted NC. The synthesized Mn-Fe-BaH2 NC exhibited strong interaction with MWs, enabling direct and efficient heating by MWs. The selective heating properties of MWs resulted in a lower gas-phase temperature compared to the solid phase, thus effectively suppressing the ammonia decomposition reaction. It led to high rates of ammonia production under both conventional, i.e., 11000 µmol/g.h at 350 °C, P=1 atm, and MW, i.e., 36000 µmol/g.h at 350 °C, P=1 atm, heating conditions [20].

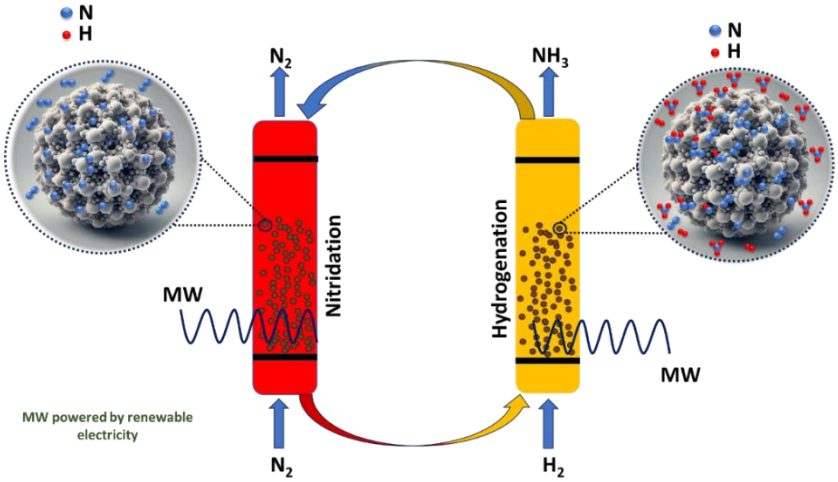

Figure 7.1: Schematic representation of nitridation and hydrogenation reactions under MW heating [20].

Studying nitridation and hydrogenation kinetics of Mn-Fe-BaH2 NC as a promising NC, in particular, under MW heating, is essential for the successful scale-up of MHCLAS technology. To the best of the authors' knowledge, there are very limited studies on the kinetics of ammonia synthesis through the CLAS technology, and one can also identify a research gap in the kinetics of MHCLAS. In particular, most studies on the kinetics of CLAS under conventional heating focused on model-free approaches for estimating activation energies of involved reactions. These approaches fail to provide reaction models/mechanisms, and there is a significant gap in the data concerning the kinetics of MHCLAS technology in ammonia synthesis, both based on the model-free and model-fitting approaches [21].

In this work, we studied apparent and intrinsic kinetics of nitridation and hydrogenation reactions for Mn-Fe-BaH2 NC under MW heating based on gas-solid bulk (T_b) and solid (T_s) temperatures, while minimizing the effects of external and internal mass transfer resistances for the intrinsic kinetics. T_b refers to the temperature of the gas and solid phases mixture, whereas T_s specifically denotes the temperature of the solid phase. Due to the selective heating effect of microwaves, the solid temperature is typically higher than the bulk temperature. We evaluated the kinetic parameters by applying data from a grounded metallic thermocouple to measure T_b and a pyrometer/IR camera for T_s. For the nitridation reaction kinetics, we measured NC mass gain. For the hydrogenation reaction kinetics, we quantified ammonia production during the hydrogenation stage by employing a calibrated ion-selective electrode (ISE). In Section 7.2, we detailed the adopted experimental methodology for kinetic study, including materials and NC characterization (Section 7.2.1), experimental setup and procedure (Section 7.2.2), and ammonia quantification (Section 7.2.3), as well as the development of kinetic models (Section 7.2.4). In Section 7.3, we presented results of temperature uniformity evaluation in MW heated fluidized bed reactor (Section 7.3.1), analysis of NC stability (Section 7.3.2), mass transfer limitations (Section 7.3.3), kinetics of nitridation (Section 7.3.4) and hydrogenation reactions (Section 7.3.5), kinetic models performance evaluation (Section 7.3.6), and NC performance comparison (Section 7.3.7).

7.2. Experimental methodology

7.2.1. Materials and NC characterization

In this study, we applied Mn-Fe-BaH2 NC produced by adopting the coprecipitation approach. A mixture of barium fluoride (BaF2), manganese nitrate (Mn(NO3)2), iron nitrate (Fe(NO3)3), and

sodium carbonate (Na2CO3) was prepared in a molar ratio of 1:4:1:5, which was already optimized for highest activity in our previous study [20]. The resulting mixture was dried at 120 °C. Subsequently, the NC was activated under MW irradiation at T_b=900 °C in a gas mixture consisting of 10 vol.% methane (CH4), 5 vol.% H2, and N2 as the balance gas for 45 minutes. Following this, the gas flow was switched to hydrogen at T_b=300 °C for an additional 60 minutes. Please refer to Adavi et al. [20] for detailed information on the synthesis procedure of this NC.

The Mn-Fe-BaH_2 NC demonstrated the highest ammonia production rate compared to those reported in the literature and those tested by the authors in their previous study, highlighting its potential for further process development [20]. We adopted N2 gas (99.99% purity, supplied by Canadian Air Liquide), Argon (Ar) gas (99.99% purity, supplied by Canadian Air Liquide), and deionized water.

The synthesized NC had a mean particle size of around 35 μm, following the results of its particle size distribution (PSD) measurement with a particle size analyzer, Mastersizer 3000 (refer to Figure 7.2). To obtain detailed information on the chemical composition of the NC, we digested it with 6 M hydrochloric acid (HCl) at 100 °C and analyzed it with an inductively coupled plasma optical emission spectroscopy (ICP-OES), Agilent 5110-SVDV. The normalized composition before reduction and nitridation of the NC was 50 wt.% Mn, 8 wt.% Fe, and 42 wt.% barium (Ba). We performed scanning electron microscopy with energy dispersive X-ray spectroscopy (SEM-EDS), JEOL JSM-7600F, analysis to study the morphology and elemental distribution of synthesized NC. To measure the surface area of the synthesized NC, we applied Brunauer-Emmett-Teller (BET) analysis, model: Autosorb-1. Prior to the BET measurements, the samples were degassed under vacuum at 150 °C for 4 hours. In addition, the minimum fluidization velocity U_{mf} measured for synthesized NCs at ambient conditions, i.e., atmospheric pressure and 22 °C, was 2.5 cm/s.

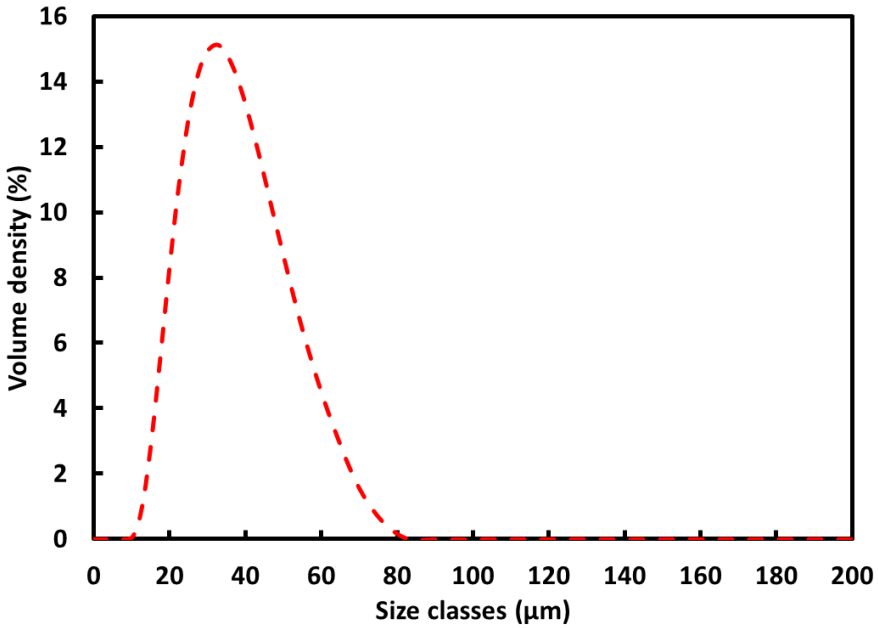

Figure 7.2: PSD of synthesized Mn-Fe-BaH_2 NC by applying particle size analyzer.

7.2.2. Experimental setup and procedure

To study apparent and intrinsic kinetics of nitridation and hydrogenation reactions of Mn-Fe-BaH_2 NC adopted for MHCLAS technology, we applied a laboratory-scale MW heating-assisted fluidized bed (MHFB) setup made of quartz, as shown in Figure 7.3. We monitored T_b in the reaction zone by a grounded metallic thermocouple and T_s by a pyrometer. We placed the metallic thermocouple at the center of the bed inventory along the axis, and the pyrometer pointed to the center of the bed height. We developed intrinsic reaction kinetics by minimizing the effects of both external and internal mass transfers, and estimating kinetic parameters based on T_s under MW heating conditions. When any of these conditions are not met, the reaction kinetic parameters should instead be referred to as apparent kinetic parameters.

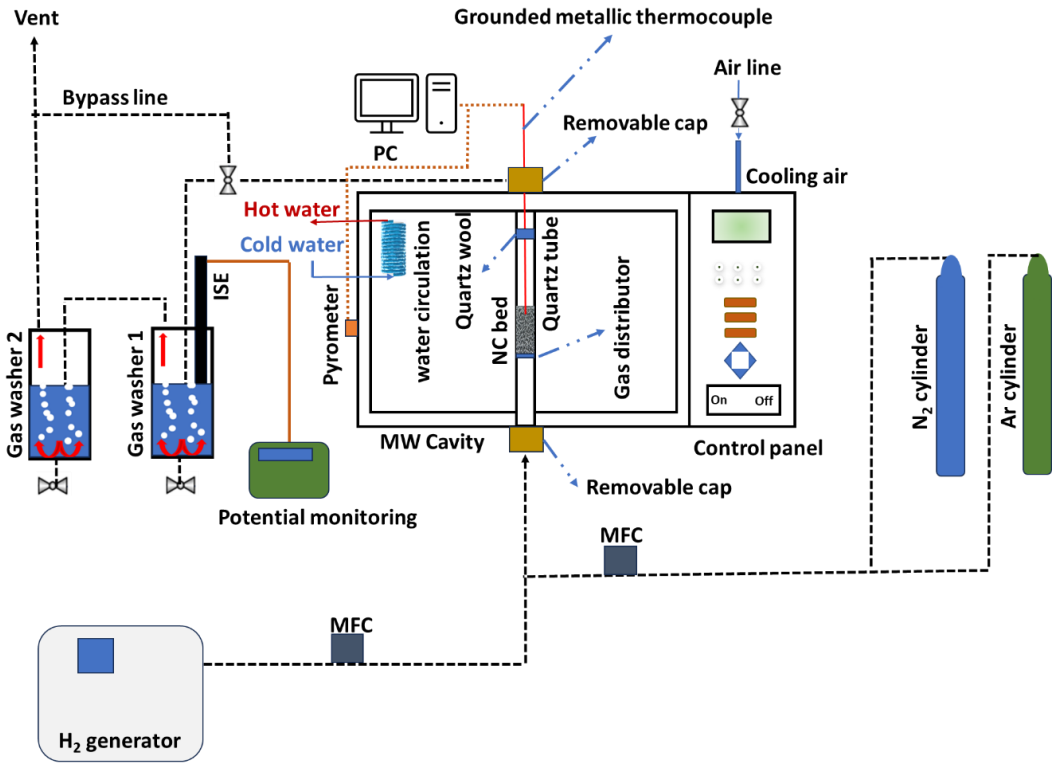

Figure 7.3: Experimental setup for nitridation and hydrogenation kinetic studies under MW irradiation.

The application of a grounded metallic thermocouple helped minimize the risk of spark formation. We also implemented water circulation and cooling air to minimize the risk of magnetron overheating. For the nitridation step, we loaded either 2.5 g of NC along with 7.5 g of alumina, 5 g of NC together with 5 g of alumina, 10 g or 20 g of NC without alumina into a quartz reactor positioned within the MW cavity with a dense bed height of around 2.5-4.0 cm under the conditions explored here. Masses of 10 and 20 g were applied for the nitridation stage, followed by mass measurement to maximize the mass measurement accuracy. The quartz reactor, alumina, and distributor were transparent to MWs at operating conditions applied in this work, allowing NC solid particles to be directly heated by MWs. The synthesized NC demonstrated excellent heat generation when exposed to MW irradiations, due mainly to its favorable dielectric properties [20].

During the nitridation step, we passed N_2 through the reactor bed, maintaining a T_b in the range of 360-630 °C. We monitored the mass gain of NC at 2-minute intervals between 4-12 min of reaction time by applying

a scale with an accuracy of 0.1 mg with an initial NC mass of 10 or 20 g. To decrease measurement errors, we measured the total mass of the reactor, including the quartz reactor and NCs. We placed quartz wool at the reactor outlet to prevent particle loss. Before the nitridation reaction and starting associated measurements, we flushed the reactor by Ar at room temperature with a superficial gas velocity U_g of 9 cm/s and confirmed mass consistency. Throughout the nitridation and hydrogenation reactions, we adjusted the inlet gas flow rate by a LabView program, ensuring the reactor remained in fluidized mode. XRD results for samples collected after the nitridation reaction confirmed that the NCs remained free from contamination during material handling [20].

Between nitridation and hydrogenation steps, we passed Ar through the reactor to cool down NCs to room temperature and started the hydrogenation step after reaching the corresponding T_b in the range of 150-320 °C. During the hydrogenation stage, we passed H_2 produced by a H_2 generator (Peak Scientific hydrogen generator with 99.9999% H_2 purity) with a 20 vol. % Ar as the balance gas through the nitrided NC at T_b ranging from 150 to 320 °C. We monitored the produced ammonia both online and offline by applying a calibrated ISE. For online measurements, we monitored the variation in electrode potential throughout the reaction, providing valuable insights into the reaction rate at different times. In contrast, offline measurements involved recording the final electrode potential at the end of the reaction. We kept the electrode potential variation in the second gas washer around ±5 V, indicating that ammonia was almost fully absorbed in the first gas washer (see Section 7.2.4 for further details). We presented adjusted experimental parameters for the kinetic study of MHCLAS technology, while adopting Mn-Fe-BaH_2 NC, in Table 7.1.

In this study, we adopted an isothermal approach for kinetic study by preheating NC to the desired reaction temperature under an Ar atmosphere in kinetic experiments. Once the temperature stabilized at the target level, we switched the inlet gas stream to reactive gases, i.e., N_2 for nitridation reaction and a H_2/Ar mixture for hydrogenation reaction.

Table 7.1: Experimental parameters employed in the current study.

Parameter	Value
Quartz reactor diameter (cm)	2.86
NC's initial weight in the nitridation stage (g)	2.5, 5, 10, 20
NC's initial weight in the hydrogenation stage (g)	2.5, 5, 10
MW power (W)	110-1100
Nitridation stage U_g (cm/s)	6.5
Hydrogenation stage U_g (cm/s)	7.0
Nitridation T_b range (°C)	360-630
Hydrogenation T_b range (°C)	150-350
Nitridation stage pressure	Atmospheric pressure
Hydrogenation stage pressure	Atmospheric pressure
Nitridation reaction time (min)	12
Hydrogenation reaction time (min)	5

7.2.3. Ammonia quantification

Employing ammonia quantification techniques with low detection limits is essential for kinetic studies of the hydrogenation stage in MHCLAS technology. Researchers adopted different ammonia quantification techniques in literature, including the Berthelot technique, ion conductivity measurement (IC), proton nuclear magnetic resonance (H NMR), gas chromatography, colorimetric techniques, and mass spectrometry. The Berthelot technique, also known as the indophenol technique, is a well-established water-based colorimetric analysis with a low detection limit for ammonia (NH_3). However, it is labor-intensive and sensitive to experimental conditions, such as PH and impurities. IC measurement allows for automated analysis but is unsuitable for electrochemical ammonia synthesis due to ion interference and is limited to concentrations above 0.1 ppm [22,23]. Quantitative H NMR and ultra-performance liquid chromatography-mass spectrometry (UPLC-MS) detect ammonium ions by acidifying ammonia solutions or employing derivatizing agents, like dansyl chloride [23]. Gas chromatography offers a rapid analysis with a 5-minute duration and a detection limit of approximately 150 ppb v/v, with Sulfinert lines to decrease ammonia physisorption [23]. The colorimetric technique with a UV spectrophotometer can detect ammonia at levels

as low as 17 ppm by passing ammonia through water [24]. Mass spectrometry is a rapid-response technique that can be effectively utilized for ammonia quantification. Its fast response time makes it particularly suitable for real-time, online monitoring of ammonia levels [25].

In this study, we employed a calibrated ISE to measure ammonia concentration by applying offline and online measurements. For the offline measurement, we analyzed the ammonia concentration in samples from gas washers 1 and 2 (see Figure 7.3), each containing 400 ml of deionized water. To minimize ammonia absorption and decrease measurement errors, we made all piping from the reactor exit to the gas washers from Teflon. The application of stainless steel for the reactive system under study here can lead to ammonia adsorption on the tube surfaces, resulting in an underestimation in ammonia quantification [26]. To ensure that gas flow through the gas washer did not affect the electrode potential measurements, we conducted a blank test. The test confirmed that the presence of bubbles in the gas washer during electrode potential measurement had no impact on the results.

7.2.4. Kinetic models

Kinetics of non-catalytic gas-solid reactions (when the solid phase is reactive) can effectively be modeled by applying various reaction models presented in literature [27–29]. The most common non-catalytic reaction models documented in literature include nucleation models, diffusion models, reaction order models, and geometrical contraction models (or shrinking core models) [28–30]. One can examine these models in both integral and differential forms, as detailed in Table 7.2.

Table 7.2: Principal reaction models describing non-catalytic gas-solid reactions [27–29]**.**

Reaction model	**Differential form, $f(\alpha)$**	**Integral form, $g(\alpha) = kt$**	**Equation no.**
	Nucleation models		
Power law	$2\alpha^{1/2}$	$\alpha^{1/2}$	(7.1)
	$3\alpha^{2/3}$	$\alpha^{1/3}$	(7.2)
	$4\alpha^{3/4}$	$\alpha^{1/4}$	(7.3)
	$2/3\alpha^{-1/2}$	$\alpha^{3/2}$	(7.4)
Avrami-Erofeev	$2(1-\alpha)[-\ln(1-\alpha)]^{1/2}$	$[-\ln(1-\alpha)]^{1/2}$	(7.5)
	$3(1-\alpha)[-\ln(1-\alpha)]^{2/3}$	$[-\ln(1-\alpha)]^{1/3}$	(7.6)
	$4(1-\alpha)[-\ln(1-\alpha)]^{3/4}$	$[-\ln(1-\alpha)]^{1/4}$	(7.7)

Table 7.2 (cont'd): Principal reaction models describing non-catalytic gas-solid reactions [27–29].

	Diffusion models		
One dimensional diffusion	$1/2\alpha^{-1}$	α^2	(7.8)
Two-dimensional diffusion	$[-ln(1-\alpha)]^{-1}$	$(1-\alpha)\ln(1-\alpha)+\alpha$	(7.9)
Three-dimensional diffusion	$3/2(1-\alpha)^{2/3}\left[1-(1-\alpha)^{1/3}\right]^{-1}$	$\left[1-(1-\alpha)^{1/3}\right]^2$	(7.10)
	Reaction order models		
Zero-order	1	α	(7.11)
Mampel (first order)	$1-\alpha$	$-\ln(1-\alpha)$	(7.12)
Second order	$(1-\alpha)^2$	$[1/(1-\alpha)]-1$	(7.13)
Third order	$(1-\alpha)^3$	$(1/2)[(1-\alpha)^{-2}-1]$	(7.14)
	Geometrical contraction models		
Contracting cylinder	$2(1-\alpha)^{1/2}$	$1-(1-\alpha)^{1/2}$	(7.15)
Contracting sphere	$3(1-\alpha)^{2/3}$	$1-(1-\alpha)^{1/3}$	(7.16)

One can present a general form of nitridation and/or hydrogenation reaction rate as a function of temperature T, apparent activation energy $E_{a,i}$, pre-exponential constant $k^*_{0,i}$, universal gas constant R, and reaction model $f(\alpha_i)$ as follows [31]:

$$\frac{d\alpha_i}{dt} = k^*_{0,i} exp\left(-\frac{E_{a,i}}{R}\left(\frac{1}{T}-\frac{1}{T_r}\right)\right) f(\alpha_i) \tag{7.17}$$

where $i =$ (subscript) N or H refers to the nitridation and hydrogenation stage, respectively. Nitridation and hydrogenation conversion fractions, i.e., α_N and α_H, can be calculated by applying Eqs. (7.18) and (7.19) as follows:

$$\alpha_N = \frac{m_{i,N} - m_{0,N}}{m_{\infty,N} - m_{0,N}} \tag{7.18}$$

$$\alpha_H = \frac{C_{i,NH_3} - C_{0,NH_3}}{C_{\infty,NH_3} - C_{0,NH_3}} \tag{7.19}$$

where m_0 is the initial mass of NC in the nitridation stage, m_i is the mass of the NC at $t = t_i$ of nitridation, and m_∞ is the final mass of the NC if it is fully nitrided (maximum theoretical nitrogen content, i.e., 13.5

wt.% associated with formation of manganese nitride (Mn_3N_2), barium imide (BaNH), and iron nitride (Fe_4N)[20]). C_{0,NH_3} is the initial concentration of ammonia, C_{i,NH_3} is the ammonia concentration at $t = t_i$ in the gas washer 1 since the amount of ammonium hydroxide in the gas washer 2 is negligible, and C_{∞,NH_3} is the concentration of ammonia when the nitrided NC is theoretically fully reduced (i.e., 3900 μmol/g_{NC}).

By applying the integral form of non-catalytic reaction models, we have Eqs. (7.20) and (7.21) as follows [31]:

$$g(\alpha_i) = \int \frac{d\alpha_i}{f(\alpha_i)} = k_i t \tag{7.20}$$

$$g(\alpha_i) = k_{0,i}^{*} exp\left(-\frac{E_{a,i}}{R}\left(\frac{1}{T} - \frac{1}{T_r}\right)\right) t \tag{7.21}$$

We performed the non-linear statistical analysis based on the least-squares method, where we calculated the residual sum of squares (RSS) of the tested reaction model in the model-fitting approach (see Eq. (7.22)).

$$RSS_{Model\ fitting} = \frac{1}{n}\sqrt{\sum_{i=1}^{i=n}\left(g(\alpha_i)_{exp} - g(\alpha_i)_{model}\right)^2} \tag{7.22}$$

where $g(\alpha_i)_{exp}$ and $g(\alpha_i)_{model}$ are the calculated values that we obtained from experimental data and the tested reaction model, respectively, and n represents the number of points employed in the model fitting. Kinetic models with the lowest RSS are the most appropriate candidates to accurately represent reaction mechanism.

To evaluate performances of developed kinetic models, we employed a different set of kinetic data from what we adopted during the model development by the model-fitting approach. We, hence, applied Eq. (7.23) to calculate the corresponding RSS during the model performance evaluation stage.

$$RSS_{Model\ performance} = \frac{1}{m}\sqrt{\sum_{i=1}^{i=m}\left(\alpha_{i_{exp}} - \alpha_{i_{model}}\right)^2} \tag{7.23}$$

where m represents the number of experimental data points adopted in the model performance evaluation step. $\alpha_{i_{exp}}$ and $\alpha_{i_{model}}$ are conversion fractions calculated by applying experimental results and developed models, respectively.

7.3. Results and discussion

7.3.1. Temperature distribution in the MHFB

To accurately determine kinetic parameters, it is critical to have a uniform temperature distribution in both radial and axial directions of the particulate bed. We set the position of the metallic thermocouple at two different bed heights (i.e., $0.5H_b$ and $0.3H_b$ relative to the distributor plate, where H_b is the dense bed height) to monitor T_b at different positions within the bed of NCs. Obtained results, presented in Figure 7.4, demonstrate a temperature difference of less than 2% in the axial direction at $0.5H_b$ and $0.3H_b$. We monitored IR camera readings, and they confirmed a temperature gradient of less than 1% across the radial direction. These findings confirm that we successfully achieved isothermal conditions in our experimental setup, allowing the corresponding temperature data to be applied for kinetic parameter calculations. Numerous studies applied fixed-bed reactors to investigate the kinetics of gas-solid reactions under MW irradiations [32–34]. However, the application of non-tiny fixed-bed reactors, e.g., ID greater than 10 mm, when heated by MWs, intensifies temperature gradients within the bed, leading to the formation of hot spots [35,36]. These hot spots can result in inaccurate temperature measurements, potentially affecting the calculated kinetic parameters [37]. However, the application of a dense MHFB enhances temperature uniformity within the bed while helping minimize the impact of external mass transfer resistances [38–40].

We presented the temperature profile of NCs during the nitridation stage at 500 °C in Figure 7.4, while we observed similar trends for other temperatures in both nitridation and hydrogenation stages. T_b increased initially and reached a plateau, indicating a thermal equilibrium within the bed between NCs and gas phase.

We started nitridation and hydrogenation reactions at this/similar equilibrium stage with minimal temperature uniformity issues.

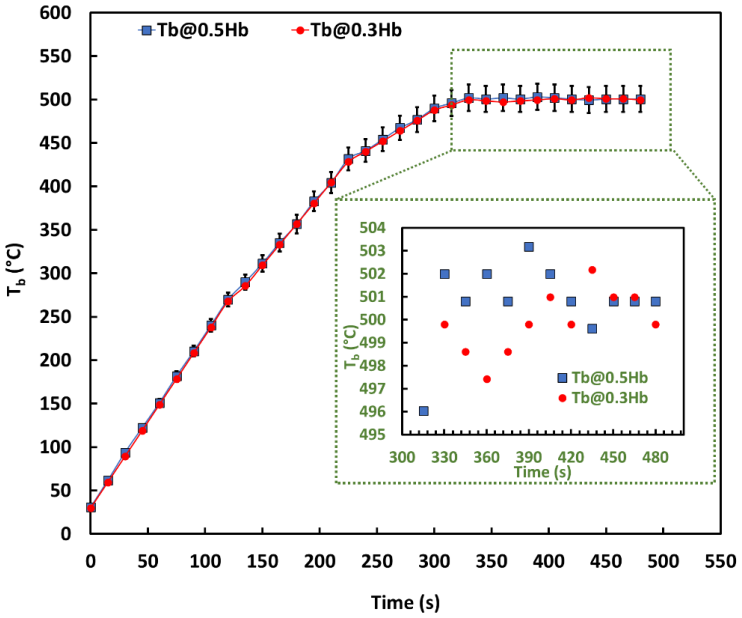

Figure 7.4: Monitored T_b at different bed heights for the nitridation stage at 500 °C.

7.3.2. Mass transfer limitations

Gas-solid reactions consist of five stages: (i) the transfer of reactive compounds from the gas phase to the solid surface, (ii) the internal diffusion of reactive gases into the reactive solid, (iii) the chemical reaction between the gas and solid phases, (iv) the transport of the reaction products from the internal pores to the particle surface, and (v) the transfer of these products from the particle surface to the bulk gas phase. To accurately determine intrinsic kinetic parameters, it is crucial to eliminate the effects of both internal and external mass transfers [41].

The external mass transfer becomes reaction-limiting when the mass transfer rate to the solid surface is slower than the reaction rate. In this study, we adopted varying solid inventories for nitridation and hydrogenation reactions. Collected results showed negligible variations in nitridation and hydrogenation reaction conversions, indicating that external mass transfer was not a limiting factor. Please refer to Section

7.3.6 for further details, where it is shown that variations in NC mass did not affect the extent of nitridation and hydrogenation reactions.

To assess the impact of internal mass transfer limitations, we applied the Mears and Weisz–Prater criterion to determine the maximum allowable particle size. For particles smaller than this threshold, the internal mass transfer becomes negligible (see Eq. (7.24)) [42].

$$\frac{\rho_p \, d_p^2 \, r_{max} \, R \, T_{rxn}}{P_i \, D_e} < 1 \tag{7.24}$$

where ρ_p, d_p, r_{max}, T_{rxn}, P_i, and D_e represent the particle density, particle diameter, maximum reaction rate (for nitridation and hydrogenation), maximum reaction temperature (T_s), partial pressure of component i (i=H_2 or N_2), and effective diffusion coefficient, respectively. We determined that internal mass transfer becomes negligible for particle diameters smaller than approximately 500 μm. Since the mean particle size (MPS) in our study was considerably smaller, at only around 35 μm, the impact of internal mass transfer was effectively insignificant.

T_s reflects the actual temperature of active reaction sites, making it the basis for intrinsic kinetic parameter calculations. In contrast, parameters derived from the T_b are classified as apparent kinetic parameters. By eliminating mass transfer limitations, we ensured the accuracy of kinetic parameter evaluations independent of the reactor type/hydrodynamics, providing reliable data for modeling and further technological developments.

7.3.3. Cyclic performance of NC

We performed a stability analysis on synthesized Mn-Fe-BaH_2 NCs to identify the optimal temperature ranges for maintaining consistent performance in the nitridation-hydrogenation cycle without compromising ammonia production rates over repeated cycles. The nitridation stage, conducted at elevated temperatures up to T_b=630 °C, was found to significantly affect ammonia production rates in the MHCLAS process following multiple cycles. To investigate this, we carried out nitridation at two temperatures, 630 °C and 565 °C, followed by hydrogenation at 320 °C. This approach enabled us to evaluate variations in

ammonia production rates across successive cycles, providing valuable insights into the system's long-term performance (see Figure 7.5).

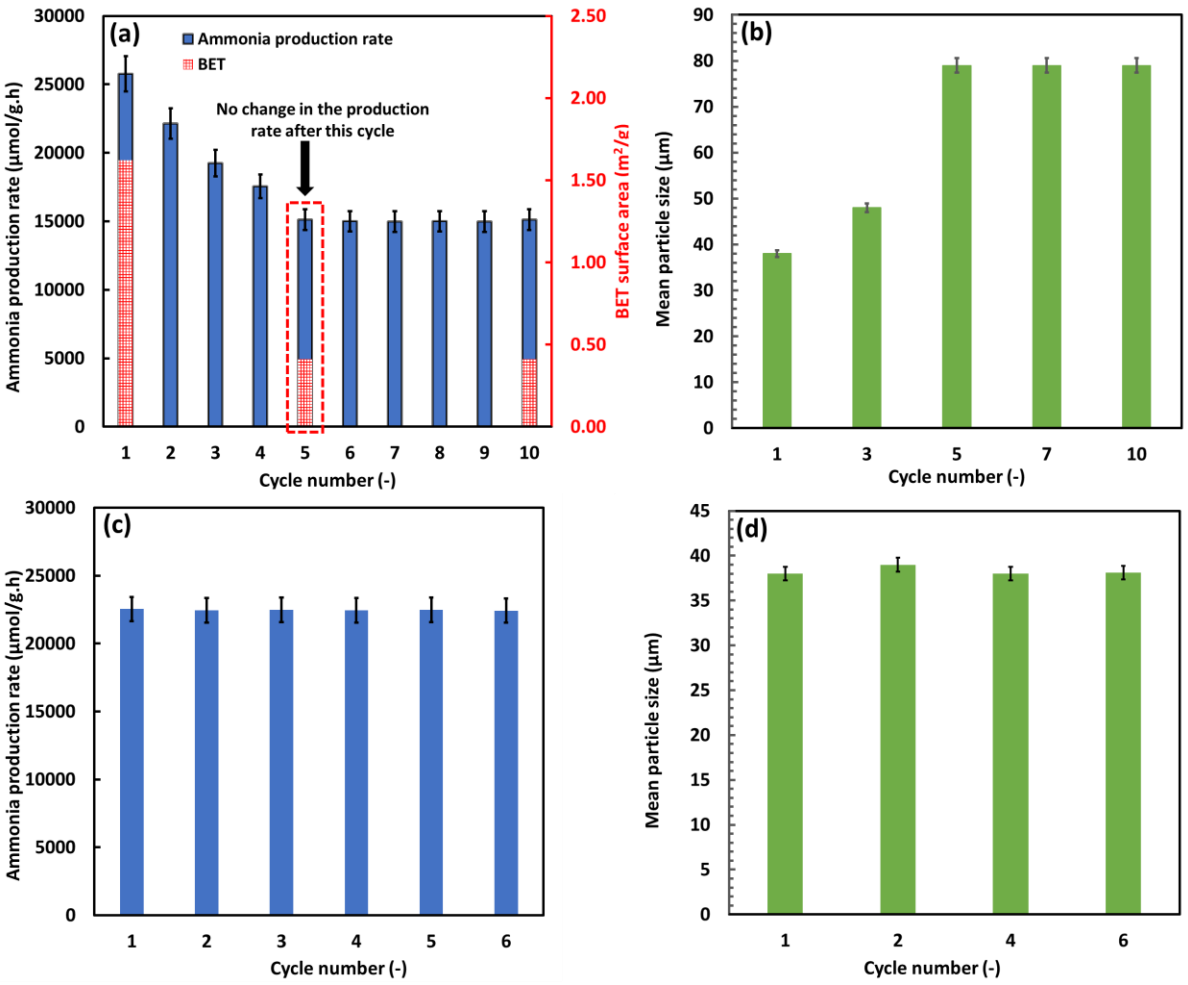

Figure 7.5: Ammonia production rate and BET surface area vs. number of cycles (nitridation T_b of 630 °C, hydrogenation T_b of 320 °C), b) MPS of NCs at different cycle numbers for nitridation T_b= 630 °C, c) ammonia production rate vs. number of cycles (nitridation T_b of 565 °C, hydrogenation T_b of 320 °C), d) MPS of NCs at different cycle numbers for nitridation T_b= 565 °C, initial NC mass: 10 g without alumina.

As shown in Figure 7.5a, at a nitridation T_b of 630 °C and a hydrogenation temperature of 320 °C, the ammonia production rate declined from approximately 26,000 µmol/g·h in the first cycle to around 15,000 µmol/g·h by the fifth cycle. In addition, the surface area of the NCs decreased from 1.6 m^2/g to 0.4 m^2/g.

After the fifth cycle, the production rate stabilized at around 15,000 μmol/g·h, aligning with the results from BET analysis. Moreover, mean particle size analysis revealed an increase until the fifth cycle, and it reaches a relatively constant value (see Figure 7.5b). In contrast, when we conducted the nitridation reaction at T_b of 565 °C, while maintaining the hydrogenation T_b at 320 °C (Figure 7.5c), the ammonia production rate exhibited a minimal variation after six cycles with a value of around 22,000 μmol/g·h. These results are consistent with the variation of mean particle size, which showed negligible changes by increasing cycle number (Figure 7.5d). In addition, the surface area of the NC remained approximately constant after six cycles, i.e., around 1.7 m²/g, further confirming the negligible extent of sintering at the nitridation T_b of 565 °C.

The optimal operating T_b for the nitridation stage is recommended to be 565 °C, while for hydrogenation, a T_b around 320 °C is suggested to prevent particle sintering at elevated temperatures and maximize ammonia production rate. In addition, the application of a dense fluidized bed reactor can significantly decrease the risk of hot spot formation within the system compared to a fixed bed reactor, which can otherwise lead to catalyst sintering and the generation of unwanted byproducts [38].

7.3.4. Nitridation kinetics of Mn-Fe-BaH2 NC

In the nitridation stage, we subjected the synthesized Mn-Fe-BaH_2 NC to a N_2 stream at various T_b. Obtained results indicate that increasing T_b from 360 °C to 630 °C led to an increase in the nitridation conversion fraction of NC (Figure 7.6a). We calculated the nitridation conversion fraction by applying Eq. (7.18) and presented it in the form of $100\times\alpha_N$ in Figure 7.6a.

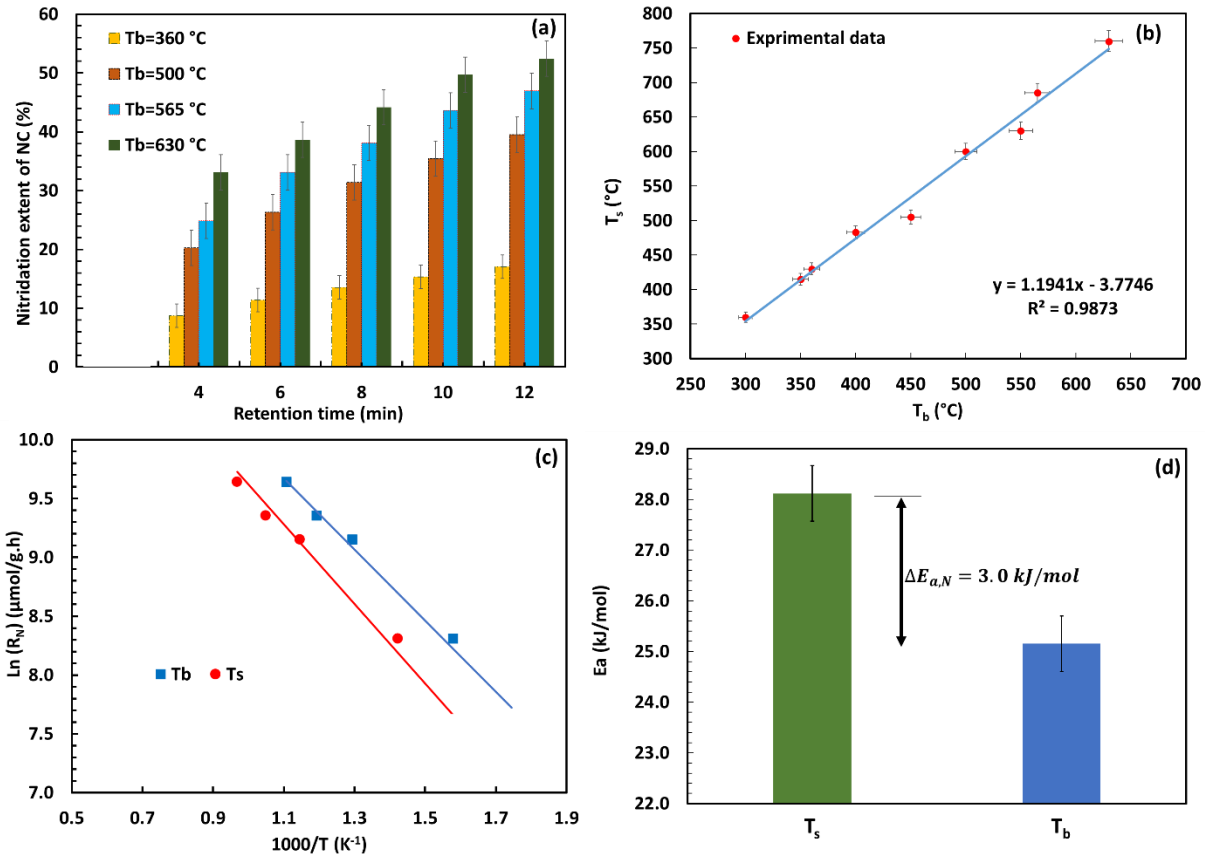

Figure 7.6: a) Mass variations of NC under N_2 flow and MW irradiations at various T_b and retention times, b) T_s as a function of T_b, c) Ln(R_N) vs. 1000/T for estimation of activation energy, d) apparent and intrinsic activation energies calculated by the model-free approach based on T_b and T_s during the nitridation reaction.

Due to selective heating of MWs in a gas-solid reactor, T_b of the particulate bed is lower than T_s. This temperature difference depends on factors such as particle size/shape and electromagnetic properties at operating conditions, U_g, operational temperature, and if the reaction is exothermic or endothermic [38]. As shown in Figure 7.6b, increasing T_b from 300 °C to 630 °C resulted in T_s between 360 °C to 760 °C, respectively. The pyrometer measures the temperature of the outer layer of the particulate bed toward the reactor wall. However, given the adequately mixed particles in the adopted bed in this study due to their fluidization, we can consider that measurements by pyrometer are a close approximation of T_s throughout the fluidized bed.

By employing a model-free approach and the nitridation reaction rate calculated from Eq. (7.25), we determined the apparent and intrinsic activation energies for the nitridation reaction based on both T_b and T_s (refer to Figure 6c).

$$R_N = \frac{m_{\infty,N}}{m_{0,N} t_N Mw_{Nitrogen}} \tag{7.25}$$

where R_N is the nitridation rate of NC, t_N is the nitridation reaction time, and $Mw_{Nitrogen}$ is the molecular weight of a nitrogen atom.

The estimated apparent activation energy based on T_b and intrinsic activation energy based on T_s were about 25.2±0.5 and 28.3±0.4 kJ/mol, respectively (see Figure 7.6d). In most kinetic studies involving MW heating in literature, researchers applied T_b to estimate kinetic parameters, resulting in apparent kinetic parameters. Researchers frequently reported a lower apparent activation energy for reactions taken place under MW heating compared to conventional heating methods. They often attributed this to the non-thermal effects of MW. However, many researchers overlooked the potential underestimation of adopted temperature in developed reaction kinetics during MW irradiations, as measurements typically reflected T_b rather than the actual T_s on the solid phase being involved in the reaction. There is no solid evidence supporting a non-thermal effect in gas-solid reactions under MW heating. Instead, the observed decrease in the apparent activation energy is likely due to inaccuracies in temperature measurement [15]. For reactions with higher activation energies, this effect is more pronounced. In our case, for the nitridation reaction, this variation is limited to around 3 kJ/mol. We presented the apparent and intrinsic activation energies for the nitridation stage for various NCs reported in literature and those estimated in this work in Table 7.3. The activation energies reported in literature are derived under conventional heating conditions, where commonly $T_b = T_s$. However, in these studies, the authors did not address external and internal mass transfer limitations. Therefore, we refer to their reported activation energies as the apparent activation energy, noting the limited information presented in those references. The comparison indicates that

compared to other NCs, the Mn-Fe-BaH_2 applied in this work helps achieve a lower activation energy and faster reaction rate based on both T_b and T_s measurements.

Table 7.3: Reported apparent and intrinsic activation energies of CLAS technology in literature and this work for the nitridation stage.

NC	Heating method	E_a, kJ/mol	Kinetic type	Ref.
Ni-BaH_2	Conventional heating	46.4±4.8	Apparent	[21]
BaH_2	Conventional heating	109.3±11.6	Apparent	[21]
LiH	Conventional heating	102.2±12.3	Apparent	[43]
Zn-8LiH	Conventional heating	50.3±2.7	Apparent	[43]
Mn-Fe-BaH_2	MW heating (based on T_b)	25.0±0.5	Apparent	This work
Mn-Fe-BaH_2	MW heating (based on T_s)	28.0±0.4	Intrinsic	This work

According to SEM-EDS results illustrated in Figure 7.7, we can observe relatively uniform distributions of Mn (Figure 7.7b), Ba (Figure 7.7c), Fe (Figure 7.7d), and nitrogen (Figure 7.7e) in the synthesized NC. These uniform distributions indicate effective interactions between different elements in the NC composite. The application of MW heating can lead to the formation of micro-scale hot spots in each single particle, which facilitates the fixation of nitrogen atoms. Since EDS analysis is a surface technique with a limited penetration depth, the reported compositions reflect surface characteristics, with approximately 9.5 wt.% nitrogen detected on the surface of the NC (see Figure 7.7e). Although this measurement cannot fully represent the nitrogen fixed within the internal structure of the NC, it still provides a valuable insight into the amount of nitrogen fixed on the surface. This value is higher than those measured based on the mass gain of NC during the nitridation stage, i.e., around 6.0 wt.%, which means a lower amount of nitrogen was fixed inside the NC than on the surface. XRD analysis from our previous study revealed that the predominant nitridation phases are manganese (II, III) nitride (Mn_3N_2), manganese (IV) nitride (Mn_4N), and barium imide (BaNH) [20].

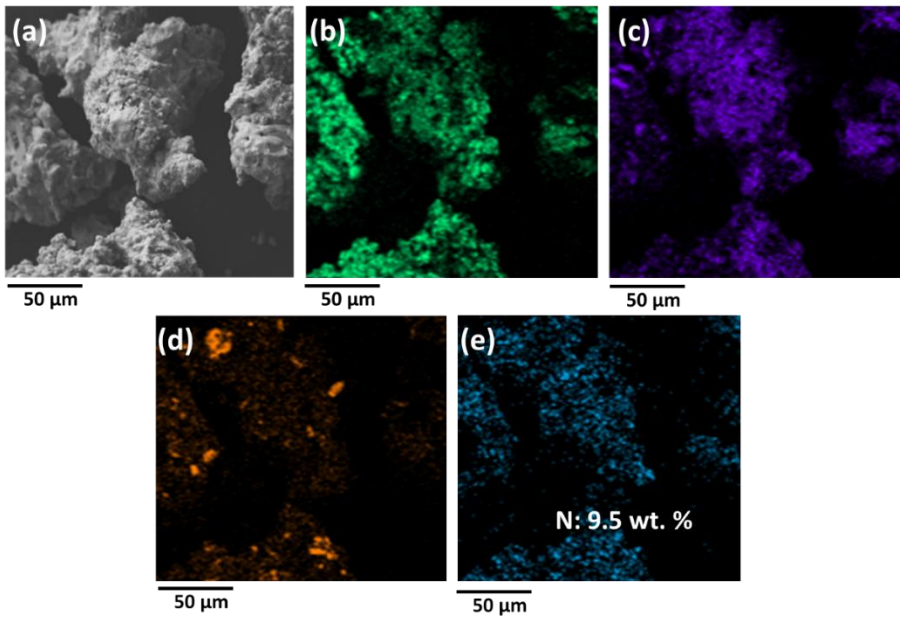

Figure 7.7: a) SEM analysis, b) Mn distribution, c) Ba distribution, d) Fe distribution, e) N distribution in the nitrided Mn-Fe-BaH_2 NC (nitridation T_b= 565 °C).

We adopted a model-fitting approach to test the performance of various kinetic models in estimating nitridation kinetics of Mn-Fe-BaH_2 NC under MW irradiations. We identified diffusion, reaction order, and contracting models (see Table 7.4) as the most suitable models, achieving an $R^2 > 0.90$, for the model-fitting approach. To compare the performances of different models listed in Table 7.2 for the nitridation kinetics of Mn-Fe-BaH_2 NC, we considered three parameters: R^2, RSS, and the proximity of estimated activation energy by the model-fitting approach to apparent or intrinsic activation energy calculated by the model-free approach. The contracting sphere model provided the minimum RSS, i.e., 0.008, and the highest R^2, i.e., 0.9855 (refer to supplementary information, Section S-3 for further details). In addition, when comparing the apparent or intrinsic activation energy calculated via the model-free approach, the contracting models, particularly the sphere contracting model (C3), demonstrated the best fit. Since the model-free approach does not account for the effects of the reaction model and pre-exponential factor in its calculations, the estimated values are more accurate, making it a practical method for identifying the best reaction model that aligns with the reaction mechanism.

Based on the SEM-EDS results presented in Figure 7.7 indicating the presence of around 9.5 wt.% nitrogen at the outer layers of nitrided NC and the mass gain of the NC during the nitridation stage (refer to Figure

7.6a), which was around 6.0 wt.%, a lower amount of nitrogen was fixed in the core of the NC compared to the surface. This observation suggests that the reaction is happening at the surface of the NC, which aligns with the contracting models' assumptions. In the contracting models (Eqs. (7.15) and (7.16)), the reaction rate decreases as the reaction progresses and product layers form, and the amount of fixed nitrogen on the outer layers is higher than internal layers.

MW heating selectively targets solid particles, resulting in significantly higher temperatures within the solid phase while the surrounding gas phase remains comparatively at a lower temperature. This selective energy absorption creates localized hot spots during the nitridation stage, which enhances the dissociation of nitrogen molecules by providing elevated thermal energy at the reaction sites. As a result, even when the bulk temperature appears unchanged, MW heating enables a higher effective temperature in the solid phase, thereby increasing the nitrogen fixation rate. Our previous experimental results confirmed that nitrogen fixation under MW irradiation was notably higher than under conventional heating, supporting this observation [20].

We estimated nitridation kinetic parameters for both T_b and T_s scenarios (see Table 7.4). The results indicate that intrinsic activation energy based on T_s is higher than the apparent activation energy based on T_b. However, the pre-exponential factor calculated for T_s was lower than that calculated with T_b. When the pre-exponential factors based on T_b and T_s are held constant, i.e., $k_{0b} = k_{0s}$, and T_s is applied, the activation energy increases even further. This emphasizes that underestimating the temperature in gas-solid reactions can result in a lower calculated activation energy. This discrepancy may explain the differences observed between kinetic parameters determined under MW irradiation and conventional heating. MW heating in gas-solid reactions does not inherently reduce the activation energy or the pre-exponential factor, which are often attributed to the so-called nonthermal effects in MW systems. Instead, this reduction in activation energy is likely linked to the underestimated reaction temperature. In Table 7.4, E_{0b} and E_{0s} represent the activation energies based on T_b and T_s.

Table 7.4: Nitridation kinetic parameters of Mn-Fe-BaH_2 NC estimated based on T_b and T_s.

Mechanism	E_{0b}, kJ/mol	E_{0s}, kJ/mol (if k_{0s}= k_{0b})	k_{0b}, s^{-1}	k_{0s}, s^{-1}
One-dimensional diffusion-D1	45.5±0.5	49.2±0.5 (51.7)	0.232	0.034
Two-dimensional diffusion-D2	51.1±0.5	54.2±0.7 (58.6)	0.349	0.031
Three-dimensional diffusion-D3	50.4±0.7	54.6±0.6 (59.2)	0.083	0.012
Mampel (first order)-R1	24.0±0.5	27.8±0.4 (29.3)	0.017	0.014
Second order- R2	28.2±0.5	32.7±0.5 (33.9)	0.036	0.031
Third order- R3	32.8±0.6	38.2±0.6 (40.3)	0.097	0.074
Contracting cylinder-C2	26.3±0.4	27.0 (29.4±0.4)	0.0081	0.011
Contracting sphere-C3	25.6±0.5	28.6±0.4 (27.3)	0.0105	0.015

7.3.5. Hydrogenation kinetics of Mn-Fe-BaH2 NC

We determined apparent and intrinsic activation energies of the hydrogenation stage, which is crucial in ammonia production, by model-free approach. We applied Eq. (7.26) to calculate the ammonia production rate (R_{NH_3}).

$$R_{NH_3} = \frac{n_{NH_3}}{m_0 t_H} \tag{7.26}$$

where n_{NH_3} is the produced amount of ammonia, and t_H denotes the hydrogenation reaction time.

We measured R_{NH_3} at T_b ranging between 150 °C to 320 °C and presented the results in Figure 7.8a. We selected the temperature range based on the minimum temperature at which we detected ammonia, i.e.,

T_b=150 °C. Through a linear fit of $Ln(R_{NH_3})$ against $1000/T$, we achieved a highly linear correlation with an R^2 of 0.98 (Figure 7.8b). This analysis yielded apparent and intrinsic activation energy values of 24.0 and 27.5 kJ/mol, respectively.

The apparent activation energy determined in this study is lower than those of other NCs documented in literature (refer to Table 7.5). Specifically, it is lower than the activation energies of Ni-BaH_2-N, BaH_2, Mn_4N-BaH_2, LiH, and Mn_4N-LiH calculated under conventional heating. This decrease in the apparent activation energy is attributed to the incorporation of Fe, which synergistically interacts with Mn and BaH_2, leading to surface energy modification and ultimately lowering the apparent activation energy. In addition, the implementation of BaH_2 in the NC structure can provide additional reasons for a lower value of the apparent activation energy. A less stable NC-N bond that forms in the nitridation stage by applying Fe resulted in a lower ammonia formation temperature. In addition, the measured T_b is lower than T_s, which results in a lower estimated apparent activation energy under MW heating compared to conventional heating.

Thermodynamic calculations performed using FactSage 8.3 in this study serve as a guideline for estimating the reduction behavior of NC–N bonds during ammonia formation. The reduction of Mn–N requires temperatures above 500 °C, whereas the reduction of Fe–N and Ba–N is thermodynamically favorable at temperatures below 100 °C. In addition, DFT study conducted by Fang et al. [44] demonstrated that incorporating Fe into the Mn–Fe NC structure significantly reduces the activation energy for ammonia formation, from 115.94 kJ/mol to 29.78 kJ/mol. This addition of Fe weakens the NC–N bond strength, thereby facilitating the hydrogenation reaction.

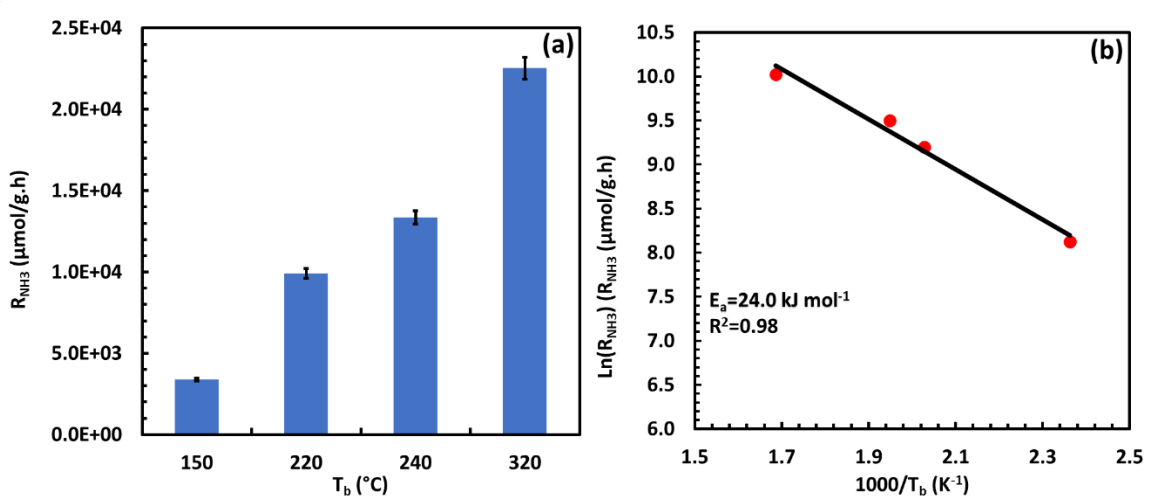

Figure 7.8: a) Ammonia production rate at different hydrogenation T_b (T_b nitridation= 565 °C), b) model-free approach for the estimation of apparent activation energy in the hydrogenation stage.

Table 7.5: Reported hydrogenation apparent and intrinsic activation energies of CLAS technology.

NC	Heating method	E_a, kJ/mol	Kinetic type	Ref.
Mn_4N-LiH	Conventional heating	56.2±1.0	Apparent	[21]
LiH	Conventional heating	62.4±2.5	Apparent	[21]
Mn_4N-BaH_2	Conventional heating	36.4±2.1	Apparent	[21]
BaH_2	Conventional heating	41.6±3.1	Apparent	[21]
Ni-BaH_2	Conventional heating	33.5±2.3	Apparent	[21]
Zn-8LiH	Conventional heating	59.5±4.0	Apparent	[43]
Mn-Fe-BaH_2	MW heating (based on T_b)	24.0±0.5	Apparent	This work
Mn-Fe-BaH_2	MW heating (based on T_s)	25.5±0.4	Intrinsic	This work

The results indicate that increasing T_b from 150 °C to 320 °C significantly enhanced the ammonia production rate (see Figure 7.9a). The implementation of Mn-Fe-BaH_2 can lower the ammonia production reaction temperature to as low as T_b=150 °C. This phenomenon can be attributed to the moderate bond energy between NCs and nitrogen molecules. Fe and BaH_2 play crucial roles in decreasing the nitridation and hydrogenation reaction temperature. Because Fe and BaH_2 form weak bonds with nitrogen atoms, they are particularly favorable for the hydrogenation stage [20]. In addition, the ammonia yield reached a

maximum of approximately 50% at 320 °C, as illustrated in Figure 7.9b. This indicates that roughly 50% of the nitrogen atoms either remained unreacted within the NC (as a lower state of nitride, such as Mn_4N) or released as N_2. The ammonia yield was calculated using a mass balance approach, based on the amount of nitrogen fixed during the nitridation stage (n_N), and the quantity of ammonia generated during the hydrogenation stage (n_{NH_3}), refer to Eq. (7.27).

$$Ammonia\ Yield = \frac{n_{NH_3}}{n_N} \tag{7.27}$$

We estimated the ammonia concentration at the reactor outlet based on the results obtained from ISE, as shown in Figure 7.9c. Initially, the concentration increased before gradually decreasing. At 240 °C, the maximum ammonia content in the outlet gas reached approximately 2.3 vol.%. However, the average ammonia concentrations during the reactions were 1.1%, 0.7%, 0.5%, and 0.2% at T_b of 320 °C, 240 °C, 220 °C, and 150 °C, respectively. This low concentration is linked to a high U_g and the presence of an inert gas.

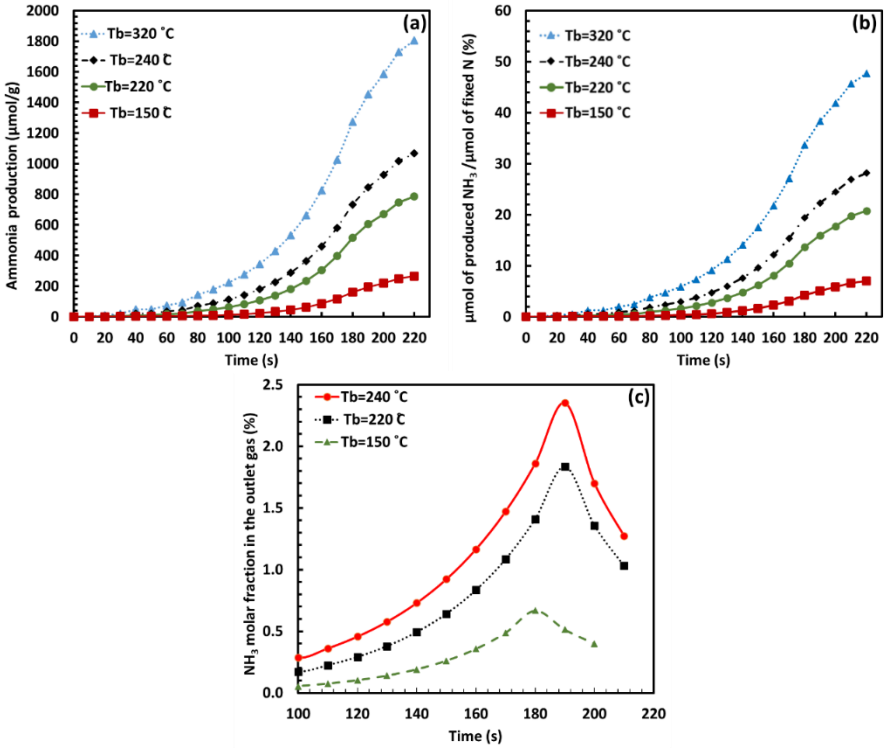

Figure 7.9: a) Online ammonia measurement at different hydrogenation T_b (T_b nitridation= 565 °C), b) ammonia production yield, c) estimated ammonia molar fraction in the outlet gas at different times (NC mass: 2.5 g).

SEM-EDS results of nitrided NCs after hydrogenation are presented in Figure 7.10. They reveal that the nitrogen presented on the surface of the NC was nearly removed after the hydrogenation step, with the nitrogen content decreasing from 9.5 wt.% to 0.2 wt.% on the surface of the NC, a decrease of approximately 97% based on EDS analysis. However, the maximum ammonia yield reached about 50 wt.%, indicating that the remaining nitrogen was released as N_2 due to ammonia decomposition or stayed as lattice nitrogen in NC's structure.

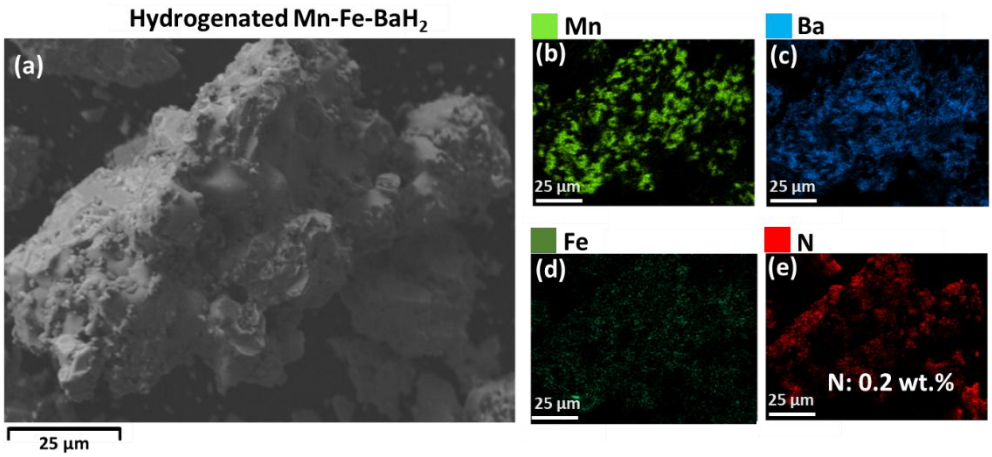

Figure 7.10: a) SEM analysis, b) Mn distribution, c) Ba distribution, d) Fe distribution, e) N distribution in the nitrided Mn-Fe-BaH_2 NC after hydrogenation at 320 °C.

Results obtained from model-fitting approach indicated that Avrami-Erofeev models best describe the hydrogenation reaction of nitrided NC. These models predict that the hydrogenation reaction rate initially increases and then decreases, with nucleation and growth being the primary mechanisms controlling the reaction rate. We presented different proposed reaction mechanisms, E_{0b}, E_{0s}, k_{0b}, and k_{0s} for the hydrogenation stage in Table 7.6. The Avrami-Erofeev-3 model exhibited the highest R^2 (i.e., 0.9863) and lowest average RSS (i.e., 0.0076) compared to other Avrami models (refer to supplementary material, Section S-3 for further details). In addition, the apparent activation energy calculated by the model-free approach in the hydrogenation stage showed a value of 24.0 kJ/mol based on T_b. This value is close to that obtained from the Avrami-Erofeev-3 model based on T_b. We assumed $k_{0b} = k_{0s}$ to evaluate the impact of temperature measurement technique (i.e., T_s or T_b) on the apparent and intrinsic activation energies.

Table 7.6: Hydrogenation apparent and intrinsic kinetic parameters of Mn-Fe-BaH_2 NC estimated based on T_b and T_s.

Mechanism	Code	E_{0b}, kJ/mol	E_{0s}, kJ/mol	$k_{0b} = k_{0s}$, s^{-1}
Avrami-Erofeev-1	A1	31.1±0.7	35.0±0.7	12.60
Avrami-Erofeev-2	A2	20.6±0.4	24.6±0.4	1.20
Avrami-Erofeev-3	A3	23.0±0.4	25.5±0.5	1.026

In Avrami-Erofeev-3 model, it is assumed that (i) nucleation occurs randomly within the bulk or on the surface of the material, (ii) the growth rate of a new phase (e.g., nitrogen-rich or nitrogen-depleted states) is constant, and (iii) the growth is isotropic, occurring at the same rate in all directions [27].

Considering the analogy between the hydrogenation mechanism and the model proposed by the Avrami-Erofeev-3 model, H_2 absorption can be viewed as a phase transformation stage. According to this model, hydrogenation involves nucleation and growth. It is understood that H_2 absorption follows a multistep mechanism: first, H_2 molecules dissociate on the NC surface; then, they penetrate the surface, leading to H^+ diffusion through the bulk of NC structure. Subsequently, hydride nucleation occurs due to H^+ diffusion into interstitial sites within the metal lattice, followed by hydride growth at the phase interface and the formation of ammonia. Nucleation sites can be present on the surface, e.g., in grain boundaries, or within the bulk [27].

7.3.6. Model performance

We reported proposed kinetic models for nitridation and hydrogenation reactions of Mn-Fe-BaH_2 NC based on T_b (apparent) and T_s (intrinsic) in Table 7.7. The choice of kinetic model in the scale-up procedure of MHCLAS depends on the adopted temperature measurement technique when applying MW heating. For instance, if one employs a metallic thermocouple, which measures T_b, the corresponding T_b-based kinetic model should be applied. Conversely, if one applies a technique that measures T_s, the T_s-based kinetic model is recommended.

To evaluate the performances of proposed kinetic models based on T_s and T_b, we compared model predictions for α_N and α_H, i.e., based on the contracting sphere for the nitridation and Avrami-Erofeev-3 for the hydrogenation stage, with associated experimental data in Figure 7.11 (see Section 7.2.4 for details). We estimated the corresponding RSS based on Eq. (7.23). In addition, to evaluate the performances of the kinetic models for different bed inventories, or test the resilience of the models against external mass transfer limitations, we applied two different masses of NCs, i.e., 10 and 20 g, during the nitridation stage, and 2.5 and 5 g during the hydrogenation stage (see Figure 7.11). The obtained results confirmed that the developed kinetic models are unaffected by the external mass transfer resistances, demonstrating their reliability and suitability for application in advancing MHCLAS technology development through its reactor modeling.

Table 7.7: Nitridation and hydrogenation apparent and intrinsic kinetic models of Mn-Fe-BaH_2 NC based on T_b and T_s under MW heating.

Stage	**Proposed kinetic model**
	Apparent reaction kinetic models based on T_b
Nitridation	$\frac{d\alpha_N}{dt} = 0.0105exp\left(\frac{-25600}{RT}\right) \times 3(1-\alpha_N)^{2/3}$
Hydrogenation	$\frac{d\alpha_H}{dt} = 1.026exp\left(\frac{-23700}{RT}\right) \times 4 \times (1-\alpha_H)[-ln(1-\alpha_H)]^{3/4}$
	Intrinsic reaction kinetic models based on T_s
Nitridation	$\frac{d\alpha_N}{dt} = 0.0105exp\left(\frac{-27300}{RT}\right) \times 3(1-\alpha_N)^{2/3}$
Hydrogenation	$\frac{d\alpha_H}{dt} = 1.026exp\left(\frac{-25500}{RT}\right) \times 4 \times (1-\alpha_H)[-ln(1-\alpha_H)]^{3/4}$

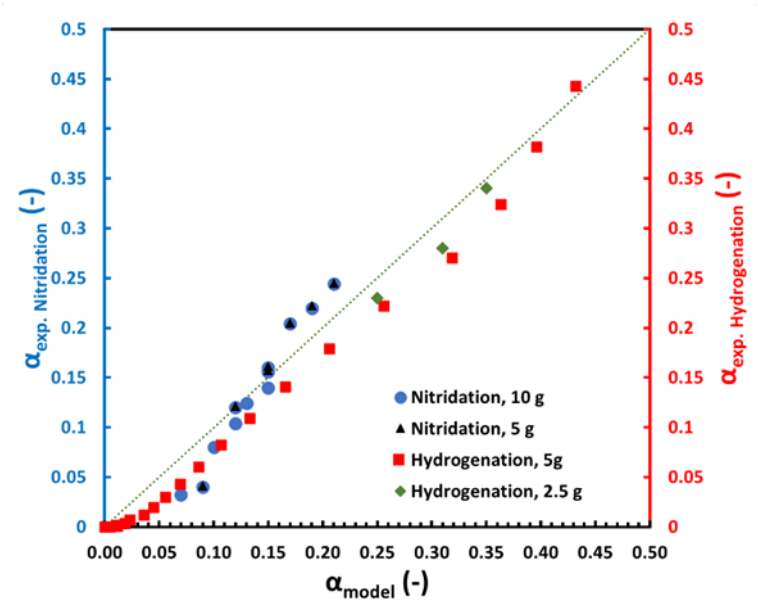

Figure 7.11: Performance evaluation of proposed intrinsic models for nitridation and hydrogenation reactions Mn-Fe-BaH_2 NC under MW irradiation.

7.3.7. NC performance comparison

In Table 7.8, we present the ammonia production rates achieved using MW heating and conventional heating (CH) for NC synthesized in this study, alongside comparisons with data from literature for both MW and CH methods (for details about the conventional heating setup, refer to our recently published article) [20]. The results demonstrate that the CLAS approach achieves a significantly higher ammonia production rate compared to conventional catalytic ammonia synthesis technologies [20,21,45].

Furthermore, a comparison of the Mn-Fe-BaH_2 NC synthesized in this study under CH and MW heating conditions reveals that MHCLAS delivers a significantly higher ammonia production rate at a T_b of 350 °C than systems operated under CH conditions at the same T_b. The selective heating mechanism of MW irradiation generates a lower gas-phase temperature relative to the solid phase, which reduces the risk of ammonia decomposition. To ensure a fair comparison, ammonia production rates were calculated based on the total reaction time, encompassing both the nitridation and hydrogenation stages (as shown in Table 7.8). In catalytic ammonia synthesis, due to the competitive dissociation of N_2 and H_2, operating at elevated pressures is required, while at atmospheric pressure, for BaH_2 and LiH, ammonia was not detected (refer to Table 7.8) [21].

Table 7.8: Comparison of ammonia production rates between Mn-Fe-BaH_2 NC synthesized in this study and those reported in literature based on total reaction time (nitridation time + hydrogenation time).

NC	Ammonia production approach	Operating pressure	Reaction temperature, °C	Ammonia production rate, µmol/g.h	Reference
BaH_2	CLAS-CH	1 bar	300	198±11	[21]
20% Ni-BaH_2	CLAS-CH	1 bar	300	2033±50	[21]
50% Ni-BaH_2	CLAS-CH	1 bar	300	3125±80	[21]
LiH	CLAS-CH	1 bar	350	105±8	[21]
Ni-BaH_2/Al_2O_3	CLAS-CH	1 bar	300	5800±200	[21]
Mn-Fe-BaH_2	CLAS-CH	1 bar	350	3600±100	[20]
Mn-Fe-BaH_2	CLAS-MW	1 bar	350	12000±500	This work
BaH_2	Catalytic-CH	1 bar	300	Undetectable	[21]
LiH	Catalytic-CH	1 bar	350	Undetectable	[21]
50% Ni-BaH_2	Catalytic-CH	1 bar	300	20±3	[21]
Ru/BaO-CaH_2	Catalytic-CH	1 bar	300	7000	[46]
4% Ru/Al_2O_3	Catalytic-MW	1 bar	280	200	[47]
Ru/MgO	Catalytic-MW	1 bar	300	250	[47]
CsRu/MgO	Catalytic-MW	1 bar	260	1250	[45]
$CsRu/CeO_2$	Catalytic-MW	1 bar	260	1500	[48]

7.4. Conclusion

In this work, we investigated the nitridation and hydrogenation reaction kinetics of Mn-Fe-BaH_2 NCs in MHCLAS technology. We conducted the nitridation and hydrogenation reactions within a T_b range of 360–630 °C and 150–320 °C, respectively. During the hydrogenation stage, we set the nitridation T_b at 565 °C to maintain a relatively stable ammonia production rate across multiple cycles. To obtain intrinsic reaction kinetics, we minimized external and internal mass transfer resistances and relied on T_s. We measured T_b and T_s with a grounded metallic thermocouple and a pyrometer/IR camera, respectively. For the nitridation reaction, compared to the results reported in literature, we observed an activation energy of 25.6±0.5 kJ/mol based on T_b under MHCLAS conditions, following a contracting sphere reaction mechanism. For the

hydrogenation reaction, we observed a higher ammonia production rate compared to previously reported values in literature, and the obtained reaction model followed the Avrami-Erofeev-3 kinetic model.

The findings of this study are crucial for advancing MHCLAS technology, in particular, in reactor modeling required for design and performance evaluation. The proposed kinetic models remain independent of reactor type and hydrodynamic conditions due to the elimination of mass transfer limitations. In addition, reaction kinetics based on T_b and T_s provide flexibility for reactor modeling and scaling-up, enabling applications of varying temperature measurement techniques in pilot or industrial MHCLAS reactors.

Acknowledgment

We would like to express our gratitude to OCP Company for financial support of this research.

CRediT authorship contribution statement

Kazem Adavi: Conceptualization, Measurement, Computation, Methodology, Validation, Investigation, Writing - original draft, Visualization, Data-curation. **Adrian Carrillo Garcia:** Conceptualization, Methodology, Writing - review & editing. **Jaber Shabanian:** Conceptualization, Methodology, Writing - review & editing. **Mohammad Latifi:** Methodology, Writing - review & editing. **Jamal Chaouki:** Conceptualization, Resources, Supervision, Writing - review & editing, Funding acquisition.

Nomenclature

Acronyms	
A1	Avrami-Erofeev-1
A2	Avrami-Erofeev-2
A3	Avrami-Erofeev-3
C2	Contracting cylinder model
C3	Contracting sphere model
CH	Conventional heating

CLAS	Chemical looping ammonia synthesis
D1	One-dimensional diffusion
D2	Two-dimensional diffusion
D3	Three-dimensional diffusion
HB	Haber Bosch
ICP	Inductively Coupled Plasma
ISE	Ion selective electrode
MHCLAS	Microwave heating-assisted chemical looping ammonia synthesis
MHFB	Microwave-heated fluidized bed
MW	Microwave
MWH	Microwave heating
NC	Nitrogen carrier
SEM-EDS	Scanning Electron Microscopy with Energy-Dispersive X-ray Spectroscopy
R1	First-order reaction model
R2	Second-order reaction model
R3	Third-order reaction model

Symbols

b	Bulk phase (subscript)
d_p	Particle diameter [μm]
D_e	Effective diffusion coefficient [m^2/s]
E_a	Activation energy [kJ/mol]
H	Hydrogenation stage (subscript)
k_0	Pre-exponential factor [1/s]
m	Number of experimental data points adopted in the model performance evaluation [-]
m_0	The initial mass of the sample [g]

m_t	Mass of the nitrogen carrier at time t [g]
m_∞	The final mass of the nitrogen carrier if fully nitrided [g]
$Mw_{Nitrogen}$	Nitrogen atom molecular weight [g/mol]
n	Number of data points used in model fitting [-]
n_{NH_3}	Amount of produced ammonia [µmol]
n_{NH_3}	Amount of fixed nitrogen [µmol]
N	Nitridation stage (subscript)
P_i	Partial pressure of component I [bar]
R	Universal gas constante = 8.314 [kJ/mol. K]
R_N	Nitrogen fixation rate [µmol/g.h]
R_{NH3}	Ammonia production rate [µmol/g.h]
RSS	Residual sum of squares [-]
S	Solid phase (subscript)
t	Time [s]
T	Temperature [K]
T_b	Bulk temperature [K]
T_{rxn}	Reaction temperature [K]
T_s	Solid temperature [K]
U_g	Superficial gas velocity [m/s]

Greek letters

α	Conversion fraction [-]

α_{exp}	Conversion fraction calculated by experimental results [-]
α_H	Conversion fraction of hydrogenation stage [-]
α_{model}	Conversion fraction calculated by proposed models [-]
α_N	Conversion fraction of nitridation stage [-]
$d\alpha/dt$	Rate of conversion extent [1/s]
$f(\alpha)$	Differential form of the reaction model [-]
$g(\alpha)$	Integral form of the reaction model [-]
ρ_p	Particle density [kg/m^3]

References

[1] G. Zhou, H. Zhao, X. Wang, Z. Wang, Y. Zhang, X. Zhao, Q. Chen, T. Chen, Z. Huang, H. Lin, Plasma-catalytic ammonia synthesis on Ni catalysts supported on Al2O3, Si-MCM-41 and SiO2, Int J Hydrogen Energy 60 (2024) 802–813. https://doi.org/10.1016/j.ijhydene.2024.02.200.

[2] W. Gao, R. Wang, S. Feng, Y. Wang, Z. Sun, J. Guo, P. Chen, Thermodynamic and kinetic considerations of nitrogen carriers for chemical looping ammonia synthesis, Discover Chemical Engineering 3 (2023). https://doi.org/10.1007/s43938-023-00019-4.

[3] S. Brown, J. Hu, Review of chemical looping ammonia synthesis materials, Chem Eng Sci 280 (2023). https://doi.org/10.1016/j.ces.2023.119063.

[4] S. Vinardell, P. Nicolas, A.M. Sastre, J.L. Cortina, C. Valderrama, Sustainability Assessment of Green Ammonia Production To Promote Industrial Decarbonization in Spain, ACS Sustain Chem Eng 11 (2023). https://doi.org/10.1021/acssuschemeng.3c04694.

[5] L. Klaas, D. Guban, M. Roeb, C. Sattler, Recent progress towards solar energy integration into low-pressure green ammonia production technologies, Int J Hydrogen Energy 46 (2021) 25121–25136. https://doi.org/10.1016/j.ijhydene.2021.05.063.

[6] L. Zhou, X. Li, Q. Li, A. Kalu, C. Liu, X. Liu, W. Li, Advances in Nitrogen Carriers for Chemical Looping Processes for Sustainable and Carbon-Free Ammonia Synthesis, ACS Catal 13 (2023) 15087–15106. https://doi.org/10.1021/acscatal.3c03717.

[7] Y. Zhao, Y. Zhao, J. Wang, W. Bao, L. Chang, Highly simplified and efficient process for methanol and ammonia synthesis from coke-oven gas and pulverized coke using chemical looping technology, Int J Hydrogen Energy 48 (2023) 39330–39346. https://doi.org/10.1016/j.ijhydene.2023.08.055.

[8] R.J. Lee Pereira, I.S. Metcalfe, W. Hu, High-throughput screening of suitable nitrogen carriers for chemical looping ammonia synthesis, Applications in Energy and Combustion Science 16 (2023). https://doi.org/10.1016/j.jaecs.2023.100226.

[9] E. Fu, F. Gong, S. Wang, R. Xiao, Chemical Looping Technology in Mild-Condition Ammonia Production: A Comprehensive Review and Analysis, Small 20 (2024). https://doi.org/10.1002/smll.202305095.

[10] S. Feng, W. Gao, J. Guo, H. Cao, P. Chen, Electrodriven Chemical Looping Ammonia Synthesis Mediated by Lithium Imide, ACS Energy Lett 8 (2023) 1567–1574. https://doi.org/10.1021/acsenergylett.2c02730.

[11] H. Ishaq, M.F. Shehzad, C. Crawford, Transient modeling of a green ammonia production system to support sustainable development, Int J Hydrogen Energy 48 (2023) 39254–39270. https://doi.org/10.1016/j.ijhydene.2023.07.036.

[12] P.G. Rutberg, V.A. Kuznetsov, E.O. Serba, S.D. Popov, A. V. Surov, G. V. Nakonechny, A. V. Nikonov, Novel three-phase steam-air plasma torch for gasification of high-caloric waste, Appl Energy 108 (2013) 505–514. https://doi.org/10.1016/j.apenergy.2013.03.052.

[13] P. Peng, P. Chen, M. Addy, Y. Cheng, E. Anderson, N. Zhou, C. Schiappacasse, Y. Zhang, D. Chen, R. Hatzenbeller, Y. Liu, R. Ruan, Atmospheric Plasma-Assisted Ammonia Synthesis Enhanced via Synergistic Catalytic Absorption, ACS Sustain Chem Eng 7 (2019). https://doi.org/10.1021/acssuschemeng.8b03887.

[14] S.W. Brown, B. Robinson, Y. Wang, C. Wildfire, J. Hu, Microwave heated chemical looping ammonia synthesis over Fe and CoMo particles, J Mater Chem A Mater 10 (2022) 15497–15507. https://doi.org/10.1039/d2ta03241d.

[15] K. Adavi, A. Amini, M. Latifi, J. Shabanian, J. Chaouki, Kinetic study of multiphase reactions under microwave irradiation: A mini-review, Frontiers in Chemical Engineering 4 (2022). https://doi.org/10.3389/fceng.2022.1059160.

[16] W. Gao, J. Guo, P. Chen, Hydrides, Amides and Imides Mediated Ammonia Synthesis and Decomposition, Chin J Chem 37 (2019). https://doi.org/10.1002/cjoc.201800586.

[17] R.J.L. Pereira, W. Hu, I.S. Metcalfe, Impact of Gas-Solid Reaction Thermodynamics on the Performance of a Chemical Looping Ammonia Synthesis Process, Energy and Fuels 36 (2022). https://doi.org/10.1021/acs.energyfuels.2c01372.

[18] J. Guo, P. Chen, Interplay of Alkali, Transition Metals, Nitrogen, and Hydrogen in Ammonia Synthesis and Decomposition Reactions, Acc Chem Res 54 (2021). https://doi.org/10.1021/acs.accounts.1c00076.

[19] D.F. Swearer, N.R. Knowles, H.O. Everitt, N.J. Halas, Light-Driven Chemical Looping for Ammonia Synthesis, ACS Energy Lett 4 (2019). https://doi.org/10.1021/acsenergylett.9b00860.

[20] K. Adavi, Z. Chen, A.C. Garcia, J. Shabanian, J. Chaouki, Microwave heating-assisted chemical looping ammonia synthesis over Mn-Fe and Mn-Fe-BaH2 nitrogen carriers, Energy Convers Manag 325 (2025) 119434. https://doi.org/10.1016/j.enconman.2024.119434.

[21] W. Gao, J. Guo, P. Wang, Q. Wang, F. Chang, Q. Pei, W. Zhang, L. Liu, P. Chen, Production of ammonia via a chemical looping process based on metal imides as nitrogen carriers, Nat Energy 3 (2018). https://doi.org/10.1038/s41560-018-0268-z.

[22] Y. Zhao, F. Wu, Y. Miao, C. Zhou, N. Xu, R. Shi, L. Wu, J. Tang, T. Zhang, Revealing Ammonia Quantification Minefield in Photo/Electrocatalysis, Zuschriften (2021) 21896–21899. https://doi.org/10.1002/ange.202108769.

[23] R. Zaffaroni, D. Ripepi, J. Middelkoop, F.M. Mulder, Gas Chromatographic Method for in Situ Ammonia Quantification at Parts per Billion Levels, ACS Energy Lett 5 (2020). https://doi.org/10.1021/acsenergylett.0c02219.

[24] P.L. Yue, F. Khan, L. Rizzuti, Photocatalytic ammonia synthesis in a fluidised bed reactor, Chem Eng Sci 38 (1983). https://doi.org/10.1016/0009-2509(83)85045-3.

[25] A.A. Nair, F. Yu, Quantification of atmospheric ammonia concentrations: A review of its measurement and modeling, Atmosphere (Basel) 11 (2020). https://doi.org/10.3390/atmos11101092.

[26] D. Ripepi, R. Zaffaroni, M. Kolen, J. Middelkoop, F.M. Mulder, Operando isotope selective ammonia quantification in nitrogen reduction studies via gas chromatography-mass spectrometry, Sustain Energy Fuels 6 (2022). https://doi.org/10.1039/d2se00123c.

[27] A. Khawam, D.R. Flanagan, Solid-state kinetic models: Basics and mathematical fundamentals, Journal of Physical Chemistry B 110 (2006). https://doi.org/10.1021/jp062746a.

[28] A.C. García, M. Latifi, J. Chaouki, Kinetics of calcination of natural carbonate minerals, Miner Eng 150 (2020). https://doi.org/10.1016/j.mineng.2020.106279.

[29] A. Carrillo García, M. Latifi, J. Chaouki, Kinetic study of calcination of a rare earth ore, Hydrometallurgy 200 (2021). https://doi.org/10.1016/j.hydromet.2021.105557.

[30] N. Saadatkhah, A. Carillo Garcia, S. Ackermann, P. Leclerc, M. Latifi, S. Samih, G.S. Patience, J. Chaouki, Experimental methods in chemical engineering: Thermogravimetric analysis—TGA, Canadian Journal of Chemical Engineering 98 (2020). https://doi.org/10.1002/cjce.23673.

[31] A.K. and D.R. Flanagan, Solid-State Kinetic Models : Basics and Mathematical Fundamentals, J. Phys. Chem. B (2006) 17315–17328.

[32] M. Mahfud, A. Suryanto, L. Qadariyah, S. Suprapto, H.S. Kusuma, Production of methyl ester from coconut oil using microwave: Kinetic of transesterification reaction using heterogeneous CaO catalyst, Korean Chemical Engineering Research 56 (2018). https://doi.org/10.9713/kcer.2018.56.2.275.

[33] L. Ren, F. Wang, F. Cheng, F. Yang, K. Zhang, Mechanisms of gas generation from conventional and microwave pyrolysis of coal slime, Chemical Engineering Journal 452 (2023). https://doi.org/10.1016/j.cej.2022.139388.

[34] M. Abdi-Khanghah, A. Jafari, G. Ahmadi, A. Hemmati-Sarapardeh, Kinetic modeling and experimental investigation of composition variation in hydrocarbon upgrading: Application to microwave-assisted reactors, J Taiwan Inst Chem Eng 144 (2023). https://doi.org/10.1016/j.jtice.2023.104694.

[35] B.A. Lapshinov, Temperature Measurement Methods in Microwave Heating Technologies, Measurement Techniques 64 (2021). https://doi.org/10.1007/s11018-021-01954-w.

[36] A. Amini, M. Latifi, J. Chaouki, Electrification of materials processing via microwave irradiation: A review of mechanism and applications, Appl Therm Eng 193 (2021). https://doi.org/10.1016/j.applthermaleng.2021.117003.

[37] P. Zhang, C. Liang, X. Chen, D. Liu, J. Ma, Insight into microwave heating patterns for sustainable decomposition of plastic wastes into hydrogen, Appl Therm Eng 260 (2025). https://doi.org/10.1016/j.applthermaleng.2024.124954.

[38] K. Adavi, J. Shabanian, J. Chaouki, Temperature Distribution Assessment in Gas-Solid Reactive and Nonreactive Systems Heated by Microwaves, Ind Eng Chem Res 62 (2023). https://doi.org/10.1021/acs.iecr.3c00575.

[39] S. Nanvakenari, K. Movagharnejad, A. Latifi, Multi-objective optimization of hybrid microwave-fluidized bed drying conditions of rice using response surface methodology, J Stored Prod Res 97 (2022). https://doi.org/10.1016/j.jspr.2022.101956.

[40] Y. Cui, Y. Zhang, L. Cui, W. Zhao, A. Faizan, Microwave heating of silicon carbide and polypropylene particles in a fluidized bed reactor, Appl Therm Eng 232 (2023). https://doi.org/10.1016/j.applthermaleng.2023.121009.

[41] M. Khodabandehloo, J. Shabanian, J.P. Harvey, J. Chaouki, Microwave heating-assisted chemical looping dry reforming of methane, Int J Hydrogen Energy 71 (2024) 1380–1391. https://doi.org/10.1016/j.ijhydene.2024.05.295.

[42] M. Khodabandehloo, J. Shabanian, J.-P. Harvey, J. Chaouki, Kinetic study of microwave heating-assisted chemical looping dry reforming of methane over magnetite, Int J Hydrogen Energy 96 (2024) 1079–1086. https://doi.org/10.1016/j.ijhydene.2024.11.358.

[43] R. Wang, W. Gao, S. Feng, Y. Guan, Q. Wang, J. Guo, P. Chen, Zn Promotes Chemical Looping Ammonia Synthesis Mediated by LiH−Li2NH Couple, ChemSusChem 16 (2023). https://doi.org/10.1002/cssc.202300813.

[44] R. Fang, P. Wang, B. Wang, L. Shen, S. Cao, L.L. Wang, Enhanced chemical looping ammonia synthesis using Fe-doped Mn-based nitrogen carrier: A comprehensive experimental and DFT analysis, Chemical Engineering Journal 510 (2025). https://doi.org/10.1016/j.cej.2025.161424.

[45] Y. Wang, C. Wildfire, T.S. Khan, D. Shekhawat, J. Hu, P. Tavadze, R. Quiñones-Fernández, S. Moreno, Effects of support and promoter on Ru catalyst activity in microwave-assisted ammonia synthesis, Chemical Engineering Journal 425 (2021). https://doi.org/10.1016/j.cej.2021.130546.

[46] M. Hattori, T. Mori, T. Arai, Y. Inoue, M. Sasase, T. Tada, M. Kitano, T. Yokoyama, M. Hara, H. Hosono, Enhanced Catalytic Ammonia Synthesis with Transformed BaO, ACS Catal 8 (2018). https://doi.org/10.1021/acscatal.8b02839.

[47] J. Hu, C. Wildfire, A.E. Stiegman, R.A. Dagle, D. Shekhawat, V. Abdelsayed, X. Bai, H. Tian, M.B. Bogle, C. Hsu, Y. Luo, S.D. Davidson, Y. Wang, Microwave-driven heterogeneous catalysis for activation of dinitrogen to ammonia under atmospheric pressure, Chemical Engineering Journal 397 (2020). https://doi.org/10.1016/j.cej.2020.125388.

[48] A. Araia, Y. Wang, C. Jiang, S. Brown, A. Caiola, B. Robinson, W. Li, J. Hu, Insight into Enhanced Microwave Heating for Ammonia Synthesis: Effects of CNT on the Cs-Ru/CeO2Catalyst, ACS Appl Mater Interfaces 15 (2023). https://doi.org/10.1021/acsami.3c00132.

CHAPTER 8: ARTICLE 5-MODELING AND CFD SIMULATION OF MICROWAVE HEATING-ASSISTED CHEMICAL LOOPING AMMONIA SYNTHESIS

Kazem Adavi [a], Jaber Shabanian [a], Adrian Carrillo Garcia [a], and Jamal Chaouki [a, b]*

[a] *Process Engineering Advanced Research Lab (PEARL), Department of Chemical Engineering, Polytechnique Montreal, P. O. Box 6079, Station Centre-Ville, Montreal, (Quebec) Canada, H3C 3A7.*

[b] *University Mohamed VI Polytechnique, Benguerir, Morocco.*

[*] *Corresponding author: Tel. +1 (514) 340-4711 X 4034, fax: +1 (514) 340-4159, E-mail: jamal.chaouki@polymtl.ca*

Submitted to International Journal of Hydrogen Energy (March 11th, 2025)

Abstract

Microwave (MW) heating is a rapid, selective, and volumetric heating approach that offers significant potential for increasing conversion rates, selectivity, and reducing reaction times. In microwave-assisted chemical looping ammonia synthesis (MHCLAS), MW heating selectively heats the solid phase while the gas phase remains transparent, thereby maintaining a lower gas-phase temperature that can suppress undesired secondary reactions such as ammonia decomposition. However, a major technical challenge remains: the limited penetration depth of MW radiation, which hinders effective scale-up. To address this, we developed a microwave-heated fluidized bed (MWFB) reactor and conducted Eulerian–Eulerian modeling and simulation to investigate the electromagnetic field distribution, energy dissipation, and temperature profiles—a topic scarcely explored in the literature. Model validation was performed using both experimental lab data and established hydrodynamic correlations, ensuring robustness. Our findings demonstrate that the MWFB reactor configuration overcomes the MW penetration depth limitation, making it a viable candidate for industrial-scale applications. The simulations also revealed favorable bulk temperature gradients in the bubbling regime, which help maintain a cooler gas phase—an ideal condition for maximizing ammonia yield. In addition, the MWFB reactor was employed for both the nitridation and hydrogenation stages, allowing us to evaluate reaction conversions and ammonia production rates. We achieved up to 30 g of ammonia per kg of nitrogen carrier per cycle using Mn–Fe–BaH_2 as the nitrogen carrier. To our knowledge, this is the first integrated study that combines dynamic MW-fluidized bed behavior with chemical

looping ammonia synthesis, offering novel insights for scaling up MW-assisted processes and advancing the practical implementation of MHCLAS.

Keywords: Ammonia synthesis, Chemical looping; Microwave heating-assisted fluidized bed reactor; Nitridation; Hydrogenation; Multiphysics modeling.

8.1. Introduction

Ammonia (NH_3) is a promising hydrogen (H_2) carrier for renewable energy storage, decreasing H_2 transportation and storage costs by a factor of three [1,2]. However, the industrial Haber-Bosch (HB) process, which is widely applied for ammonia production, operates under extreme conditions, requiring pressures of 100–300 bar and temperatures of 400–600°C. These harsh conditions make the process economically viable only for large-scale production, typically exceeding 5,000 tonnes of ammonia per day [1,3,4]. However, for renewable energy storage and decentralized ammonia production, lower production rates are necessary, i.e., around 30-100 tonnes per day [1,3,4]. Therefore, addressing the mentioned challenges is crucial for advancing ammonia as a viable solution in these applications.

Among various technologies explored in literature, chemical looping ammonia synthesis (CLAS) has gained significant attention for its ability to overcome the thermodynamic limitations of conventional ammonia production. The CLAS addresses this challenge by decoupling the activation stages of nitrogen (N_2) and H_2. Therefore, it prevents the decomposition of the synthesized ammonia, enabling its production at atmospheric pressure and lower temperatures. This technology offers a more flexible alternative for ammonia synthesis compared to conventional HB process, in particular, in decentralized and renewable energy storage applications. By separating the activation of N_2 and H_2 into independent stages or reactors, the CLAS helps eliminate the issue of competitive adsorption between N_2 and H_2 molecules, which is a major challenge in conventional catalytic ammonia synthesis. However, since the CLAS is a relatively new technology, development of efficient NCs and optimization of reactor design are crucial for improving its performance.

In CLAS, the process begins with a specially designed nitrogen carrier (NC) undergoing a nitridation reaction at temperatures ranging from 300°C to 700°C, where N_2 gas is introduced over the NC [3,5–8]. During this step, N_2 molecules dissociate within the NC, forming lattice nitrogen. Following the nitridation, the NC is exposed to a H_2 stream, facilitating the production of ammonia, while simultaneously regenerating the nitrogen-depleted NC, allowing it to be reused in subsequent cycles [9–11]. Numerous studies have focused on developing NCs by applying various transition metals and metal hydrides [3,5]. However, studies on conventional and microwave (MW) heating-assisted forms of the CLAS technology have been limited to lab-scale [3,5,7,9–13]. In a recent study by the authors [8], we developed MW heating-assisted CLAS (MHCLAS) technology, enabling ammonia production at atmospheric pressure and temperatures as low as 150°C. Through a comprehensive screening of various NCs, we identified a manganese (Mn), iron (Fe), and barium hydride (BaH_2) composite synthesized by coprecipitation approach as the optimal NC. This composite exhibited excellent interactions with MW, resulting in a significantly higher ammonia production rate compared to previously reported ammonia synthesis technologies.

MW heating offers several advantages, such as rapid, selective, and volumetric heating, which can provide the sensible and/or reaction energy needed for both endothermic and exothermic reactions [14,15]. Gaseous phases tend to remain transparent to MW irradiation, while the MW absorber solid phase absorbs the MW energy and heats up [16,17]. This results in a lower gas phase temperature compared to the solid phase, which is beneficial for preserving ammonia and preventing its decomposition [18–25].

An important consideration in the MW heating is the penetration depth of MWs in an object, i.e., the depth at which the electrical field strength drops to 37% of its surface value [26,27]. Dielectric properties of the material, electrical conductivity, MW frequency, and the bed voidage influence the penetration depth [16]. In an earlier study by the group [14], we showed that increasing bed voidage, either by applying larger particles in a fixed bed or by transitioning to a fluidized bed, enhances MW penetration depth in the dense bed. Variations in the bed voidage across different regions of a MW heating-assisted fluidized bed (MHFB) reactor influence the medium's effective dielectric properties, which, in turn, can indirectly change the penetration depth [14].

To scale up ammonia production by applying MHCLAS technology, it is essential to understand the distributions of electrical field, temperature, and heat dissipation within the reactor.

Experimental measurements of these variables in reactors of different dimensions are very challenging. However, modeling and simulation can offer valuable insights into MW irradiation behavior in various media, in particular, in fluidized bed reactors. It can, hence, help accelerate deployment of the MHCLAS technology at industrial scale.

Some studies reported MW heating simulation by applying computational fluid dynamic (CFD) tools in the fixed beds [28–31]. These studies revealed that electromagnetic (EM) waves cause non-uniform temperature distributions in the bed, leading to the formation of hot and cold spots, especially in large fixed-bed reactors (reactor IDs > 20 cm) [14,32]. Macroscale hot spots, resulting from the non-uniform distribution of EM waves, pose significant challenges for kinetic studies in MW systems [15]. One promising strategy to mitigate the issue of hot spots in MHFB reactors is application of dense gas-solid fluidized bed reactors. In the bubbling fluidization regime, particle mixing can help homogenize the temperature distribution, decreasing adverse effects, such as particle sintering and non-uniform product distribution [15,33]. In the study by Mokhtari et al. [34], the authors developed a Eulerian-Eulerian model to study MW heating-assisted dry reforming of methane in gas-solid fluidized bed reactors. This study represents the most comprehensive instance of simulation of MHFB reported in literature for catalytic systems, while there is a research gap of similar studies in noncatalytic reactors, including those for MHCLAS technology. We presented reported modeling and simulation studies of MHFB reactors for various applications in literature in Table 8.1. In most cases documented in literature, which are relatively scarce, the focus was on reaction conversions or there was a deficiency in comprehensive coupling of different phenomena occurring within the MHFB reactor, including EM field, bed hydrodynamics, heat and mass transfers, and reaction kinetics.

In earlier studies of the group [39], we focused on lab-scale experiments for proof of concept of MHCLAS technology and its kinetic investigations. Obtained results demonstrated the great potential of the MHCLAS for further development. However, to the best of the authors' knowledge, no reports in literature have provided simulation data on MHCLAS or conventionally heated CLAS. In this study, we aim at addressing this gap by developing a comprehensive model in COMSOL Multiphysics 6.1 and offering valuable insights into the EM field distribution, heat dissipation, temperature profiles, and reactions conversions in MHCLAS fluidized bed reactors through simulations. The developed model is a novel application of Multiphysics modeling

approach for non-catalytic MHFB reactors. In this model, we coupled Maxwell's equations with bed hydrodynamics, heat and mass balance equations, and nitridation and hydrogenation reaction kinetics of adopted Mn-Fe-BaH_2 NC. We validated the developed model by applying experimental data from a lab-scale setup. We, subsequently, conducted parametric studies to investigate the effects of reaction temperature, superficial gas velocity, and solid inventory, i.e., the mass of loaded NC, on the MHCLAS.

Table 8.1: Reported MHFB models in literature.

Main objective	Model type	Remarks	Ref.
MW heating-assisted dry reforming	Eulerian-Eulerian model	• Did report EM field distribution. • The model was based on catalytic reactions.	[34]
MW heating-assisted lignite drying	Eulerian-Eulerian model	• Did not report EM field distribution in the bed. • Did not report temperature distribution in the bed.	[35]
MHFB simulation	Single-particle model	• Penetration depth evaluation. • It has high computational skills and is studied at the lab-scale. • It did not include hydrodynamic.	[36]
Drying moist particles by MW heating	Eulerian-Eulerian model	• Did estimate drying efficiency. • Did not present EM field. • Did not report the effect of hydrodynamic on EM field distribution.	[37]
MW heating effect on catalytic oxidation of n-butane	1D two phase model	• Did estimate temperature distribution between the gas and solid phases. • Did not consider EM field distribution. • The simulation does not show radial temperature and EM field distributions.	[38]

In Section 8.2, we reported the developed model in this study, including adopted assumptions and governing equations. In Section 8.3, we presented numerical simulation cases, including geometry and model parameters, boundary conditions, and grid independency analysis. In addition, we presented the adopted experimental setup in this work in Section 8.4. We, subsequently, presented dielectric properties of the NC (Section 8.5.1), model validation (Section 8.5.2), hydrodynamics

of the fluidized bed (Section 8.5.3), electrical field, and temperature distributions (Section 8.5.4), nitridation (Section 8.5.5), and hydrogenation reactions parametric studies (Section 8.5.6).

8.2. Model development

8.2.1. Assumptions

We applied the following assumptions for the modeling of MHCLAS fluidized bed reactor:

(i) Gas phase properties vary as a function of temperature.

(ii) Solids are spherical and they have identical properties, e.g., thermal conductivity, heat capacity, dielectric properties and density, that remain constant during nitridation and hydrogenation stages.

(iii) We performed modeling and simulation in 2D to study MHFB.

(iv) We performed 3D models based on the average dense bed voidage for electrical field distribution evaluation.

(v) Gas phase compounds (N_2, H_2, and NH_3) are transparent to MWs.

(vi) The reactor's/cavity's walls made of materials like stainless steel are fully MW reflective.

(vii) We conducted the nitridation and hydrogenation reactions by alternating the inlet gas supply, i.e., N_2 during nitridation and H_2 during hydrogenation. This method decreases process complexity and mitigates the risk of particle attrition.

8.2.2. Governing equations

In this section, we present applied equations to model MHCLAS reactors during nitridation and hydrogenation stages. A schematic representation of the proposed reactor configuration for MHCLAS technology is shown in Figure 8.1a. In this configuration, the transition between nitridation and hydrogenation stages is achieved by switching the inlet gas from N_2 to H_2. We solved the momentum balance equations for both gas and solid phases (Section 8.2.2.1). These equations are coupled with Maxwell's equations (Section 8.2.2.2), as well as heat (Section 8.2.2.3) and mass (Section 8.2.2.4) balance equations. We schematically show the relationship between different equations employed in this model in Figure 8.1b.

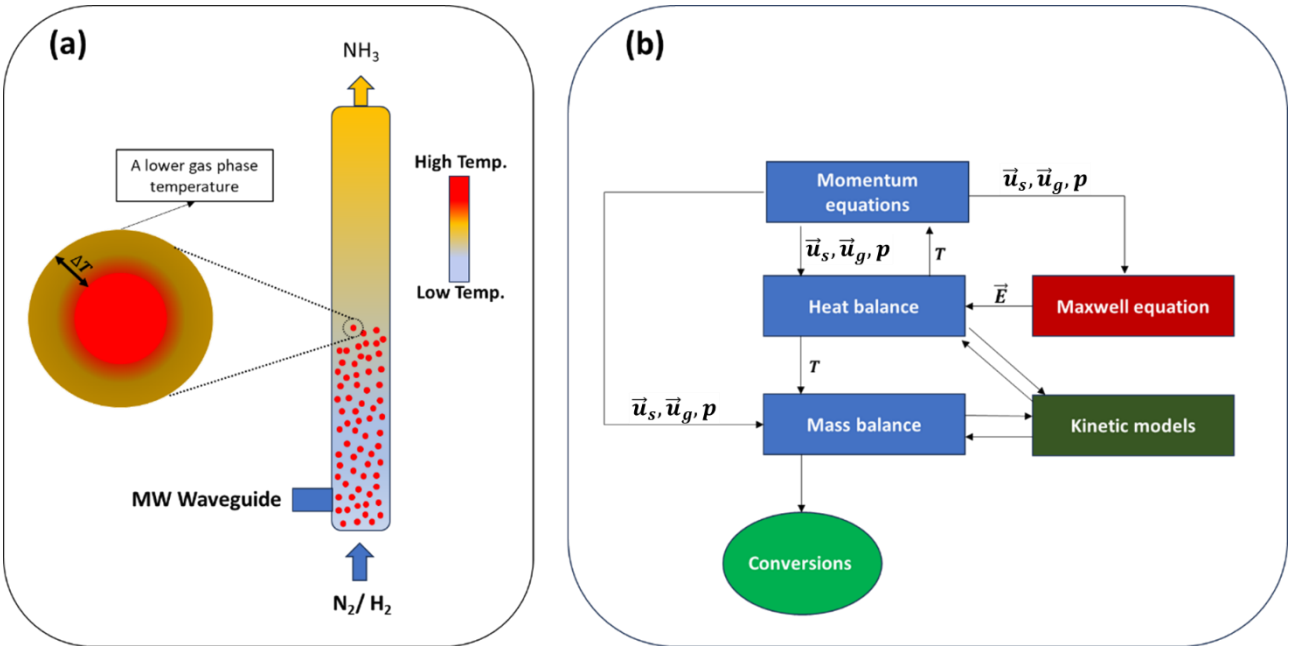

Figure 8.1: (a) A schematic representation of the MHCLAS technology, and (b) an overview of the governing equations applied in the developed model.

8.2.2.1. Hydrodynamic equations

To calculate the hydrodynamic parameters, such as gas/solid velocities, pressure distribution, and gas/solid phase fractions, we solved the momentum balance equations for each phase based on the Eulerian-Eulerian model. Momentum balance for gas phase ($i = g$) and solid phase ($i = s$) is presented in Eqs. (8.1) [34,40].

$$\frac{\partial}{\partial t}(\emptyset_i \rho_i \vec{u}_i) + \nabla.(\emptyset_i \rho_i \vec{u}_i \vec{u}_i) + \emptyset_i \nabla p = \emptyset_i \rho_i g_{grav} + \nabla.\emptyset_i(\tau_i + \tau_i^T) + M_i \tag{8.1}$$

where ρ_i represents the density of phase i, $\vec{u}_i$ denotes the velocity of phase i, p is the pressure field, and τ_i is the stress tensor of phase i. g_{grav} is the gravitational acceleration vector, M_i represents the external force acting on phase i, including drag, lift, and interphase intersection forces, and $\emptyset_i$ is the volume fraction of phase i. We applied $k - \epsilon$ model for modeling the turbulent model in fluidized bed. In addition, we employed the Gidaspow model [41] for drag force calculation, which proved to be a reliable choice to estimate gas-solid drag force in dense fluidized beds [42]. We can apply Eq. (8.2) for the calculation of τ_i.

$$\tau_i = (\mu_i^m + \mu_T)\left(\nabla \vec{u}_i + (\nabla \vec{u}_i)^T - \frac{2}{3}(\nabla.\vec{u}_i)I\right) - \frac{2}{3}\rho_i k I \tag{8.2}$$

$$\mu_T = \rho C_\mu \frac{k^2}{\epsilon} \tag{8.3}$$

where C_μ=0.09, which is an empirical constant, and k and ϵ represent the kinetic energy and dissipation rate in the turbulent model that can be calculated by employing Eqs. (8.4) and (8.5). In addition, μ_i^m and μ_T are the molecular dynamic and turbulent viscosities, respectively [42].

$$\rho \frac{\partial k}{\partial t} + \rho(\vec{u}_m.\nabla)k = \nabla.\left[\left(\mu_m + \frac{\mu_T}{\sigma_k}\right)\nabla k\right] + P_k - \rho\epsilon \tag{8.4}$$

$$\rho \frac{\partial \epsilon}{\partial t} + \rho(\vec{u}_m.\nabla)\epsilon = \nabla.\left[\left(\mu_m + \frac{\mu_T}{\sigma_k}\right)\nabla \epsilon\right] + C_{\epsilon,1}\frac{\epsilon}{k}P_k - C_{\epsilon,2}\rho\frac{\epsilon^2}{k} \tag{8.5}$$

where σ_k, $C_{\epsilon,1}$, and $C_{\epsilon,2}$ are model constants and $\vec{u}_m$ is the mixture velocity.

Eq. (6), i.e., the continuity equation for a two-phase system, is presented as follows:

$$\frac{\partial}{\partial t}(\emptyset_i \rho_i) + \nabla.(\emptyset_i \rho_i \vec{u}_i) = m_i \tag{8.6}$$

$$m_i = r_j \rho_i \tag{8.7}$$

where m_i is the mass transfer from the solid to the gas phase, and r_j denotes the reaction rate for nitridation ($j = N$) and hydrogenation ($j = H$) stages.

To verify the hydrodynamic parameters evaluated by applying the aforementioned equations, we utilized empirical correlations from literature to estimate the minimum fluidization velocity (U_{mf}), bubble voidage (ε_b), emulsion voidage (ε_e), and the fraction of bubbles (f_b) in a pilot-scale bubbling fluidized bed reactor (see Eqs. (8.8)-(8.12)) [43,44].

$$U_{mf} = \frac{\mu_g}{d_p \rho_g}\left[\left(28.7^2 + 0.0494\frac{d_p^3 \rho_g g(\rho_s - \rho_g)}{{\mu_g}^2}\right)^{1/2} - 28.7\right] \tag{8.8}$$

$$\varepsilon_b = 0.784 - 0.139 exp\left(-\frac{U_g - U_{mf}}{0.272}\right) \tag{8.9}$$

$$\varepsilon_e = \varepsilon_{mf} + 0.00061 exp\left(-\frac{U_g - U_{mf}}{0.262}\right) \tag{8.10}$$

$$f_b = 1 - exp\left(-\frac{U_g - U_{mf}}{0.62}\right) \tag{8.11}$$

$$\emptyset_{g,avg} = \varepsilon_b f_b + \varepsilon_e(1 - f_b) \tag{8.12}$$

where d_p is particle diameter, and U_g denotes the superficial gas velocity.

8.2.2.2. Maxwell's equation

We applied Maxwell's equation (Eq. (8.13)) to calculate EM field distribution within MHFB.

$$\nabla \times \mu_{r,eff}^{-1}\left(\nabla \times \vec{E}\right) - k_0^2\left(\varepsilon_{r,\,eff} - \frac{j\sigma_{r,\,eff}}{\omega\varepsilon_0}\right)\vec{E} = 0 \tag{8.13}$$

where $\mu_{r,\,eff}$ is the effective relative permeability, $\vec{E}$ is the electric field strength, and k_0 is the wavenumber in the vacuum. $\varepsilon_{r,\,eff}$ is the effective relative permittivity, $\sigma_{r,\,eff}$ is the effective electrical conductivity, ω is the angular frequency of the EM, and ε_0 is the permittivity of free space. To estimate the dielectric properties and electrical conductivity in the fluidized bed, we applied effective parameters (see Eqs. (8.14)-(8.16)) [14]. $\mu_{r,\,eff}$ can be presented as:

$$\mu_{r,\,eff} = \emptyset_g \mu_{r,\,g} + \emptyset_s \mu_{r,\,s} \tag{8.14}$$

where $\mu_{r,\,g}$ is the relative permeability of the gas phase and $\mu_{r,\,s}$ is the relative permeability of the solid phase. We can estimate $\varepsilon_{r,\,eff}$ by:

$$\varepsilon_{r,\,eff} = \emptyset_g \varepsilon_{r,\,g} + \emptyset_s \varepsilon_{r,\,s} \tag{8.15}$$

where $\varepsilon_{r,\,g}$ is the relative permittivity of the gas phase and $\varepsilon_{r,\,s}$ is the relative permittivity of the solid phase. $\sigma_{r,\,eff}$ can be calculated by:

$$\sigma_{r,\,eff} = \emptyset_g \sigma_g + \emptyset_s \sigma_s \tag{8.16}$$

where σ_g is the electrical conductivity of the gas phase and σ_s is the electrical conductivity of the solid phase.

8.2.2.3. Heat balance equation

To calculate the temperature distribution inside the reactor, we utilized the heat balance equation, as presented in Eq. (8.17) for gas phase and Eq.(8.18) for solid phase [14].

$$\emptyset_g \rho_g C_{p,g} \frac{DT_g}{\partial t} = \nabla.\left(\emptyset_g k_g \nabla T_g\right) + Q_{sg} \tag{8.17}$$

$$\emptyset_s \rho_s C_{p,s} \frac{DT_s}{\partial t} = \nabla.\left(\emptyset_s k_s \nabla T_s\right) + Q_{gs} + Q_{MW} + Q_{rxn} \tag{8.18}$$

where $C_{p,i}$ represents the specific heat capacity of phase i, T_i is the temperature of phase i, and k_i is the thermal conductivity of the phase i. Q_{MW} is the heat dissipation rate due to MW irradiations, Q_{rxn} is the reaction heat, and $Q_{sg} = -Q_{gs}$ is the heat transfer between the gas and solid phases.

The heat dissipation rate under MW irradiation can be calculated by Eq. (8.19) [16].

$$Q_{MW} = \frac{1}{2}\sigma_{r,\,eff}\left|\vec{E}\right|^2 + \pi f \varepsilon_0 \varepsilon_{r,\,eff}\left|\vec{E}\right|^2 + \pi f \mu_0 \mu_{r,\,eff}\left|\vec{H}\right|^2 \tag{8.19}$$

where $\vec{H}$ is the magnetic field strength. This equation has three terms, including Joule heating (first term), dielectric losses (second term), and magnetic losses (third term).

Q_{rxn} for both nitridation and hydrogenation stages can be calculated by applying Eq. (8.20).

$$Q_{rxn} = \Delta H_{rxn,j} \times r_j \tag{8.20}$$

where $\Delta H_{rxn,j}$ represents the change in reaction enthalpy during the reactions, with j denoting the nitridation (N) and hydrogenation (H) stages.

The composition of the synthesized NC influences Q_{rxn} during nitridation and hydrogenation stages. We estimated Q_{rxn} for the nitridation stage of Mn-Fe-BaH_2 to be -20 kJ/mol, while it was -40 kJ/mol for the hydrogenation stage. We estimated the heat of the nitridation and hydrogenation reactions by HSC 6.0 software based on the NC's composition that we developed in our prior research [8].

Conventional heat transfer between gas and solid phases can be calculated by applying Eq. (8.21) [45].

$$Q_{gs} = -Q_{sg} = \frac{5\emptyset_s}{d_p} h_{gs}\left(T_g - T_s\right) \tag{8.21}$$

where h_{gs} is the convection heat transfer coefficient between the gas and solid phases that can be calculated by applying Eq. (8.22). In addition, we can estimate in-bed Nu number by employing Eq. (8.23)-(8.25) [45].

$$h_{gs} = \frac{k_g Nu}{d_p} \tag{8.22}$$

$$Nu = \left(7 - 10\emptyset_g + 5\emptyset_g^2\right)\left(1 + 0.7Re_p^{0.2}Pr^{\frac{1}{3}}\right) + \left(1.33 - 2.4\emptyset_g + 1.2\emptyset_g^2\right)Re_p^{0.7}Pr^{\frac{1}{3}} \tag{8.23}$$

$$Re_p = \frac{\emptyset_g d_p \rho_g \left|\vec{u}_s - \vec{u}_g\right|}{\mu_g} \tag{8.24}$$

$$Pr = \frac{\mu_g C_{p,g}}{k_g} \tag{8.25}$$

Where Re_p is the Reynolds number and Pr is the Prandtl number.

8.2.2.4. Mass balance equation

We can estimate concentration distributions of various chemical compounds by employing Eq. (8.26).

$$\frac{\partial(\emptyset_i \rho_i \omega_{k,i})}{\partial t} + \nabla.\left(\emptyset_i \rho_i \vec{u}_i \omega_{i,k}\right) = \nabla.\left(\emptyset_i \rho_i D_{i,k}^e \nabla \omega_{i,k}\right) + r_k(\rho_{s,\infty} - \rho_{s,0}) \tag{8.26}$$

where $\omega_{k,i}$ represents the mass fraction of the compound k in phase i, and $D_{i,k}^e$ is the effective diffusion coefficient of the compound k in phase i. In addition, $D_{i,k}^e$ can be calculated by applying Eq. (8.27).

$$D_{i,k}^e = \frac{\emptyset_g}{\tau_k} D_{i,k} \tag{8.27}$$

$$\tau_k = \emptyset_g^{\,-1/3} \tag{8.28}$$

Here, τ_k denotes the tortuosity factor, which is calculated by applying the Millington and Quirk model (refer to Eq. (8.28)).

Eqs. (8.29) and (8.30) show the nitridation and hydrogenation reactions kinetics that we obtained based on our earlier experimental study [15].

$$r_N = 0.0105exp\left(\frac{-25600}{RT}\right) \times 3(1 - \alpha_N)^{2/3} \tag{8.29}$$

$$r_H = 1.026exp\left(\frac{-23720}{RT}\right) \times 4(1 - \alpha_H)[-ln(1 - \alpha_H)]^{3/4} \tag{8.30}$$

where α_N and α_H are reaction extents in the nitridation and hydrogenation stages, respectively. r_N and r_H represent the reaction rate during nitridation and hydrogenation stages, respectively.

8.3. Numerical simulation

8.3.1. Geometry and model parameters

To validate the model developed in this study, we utilized results obtained from a lab-scale MHFB reactor operated for MHCLAS. We placed a quartz tube, with an inner diameter of 2.86 cm, at the center of the MW cavity (width × height × depth: 32.5 × 23.0 × 37.5 cm) to maximize MW interaction. Due to its transparency to MW irradiation, the quartz reactor allowed only the MW absorber solid particles within the tube to absorb the MWs and undergo heating (Figure 8.2a).

The pilot-scale MHCLAS reactor model adopted in this work for simulation studies consists of a single fluidized bed with 15 cm ID and 45 cm fixed bed height (L_0), where both nitridation and hydrogenation take place alternatively as discussed in Section 8.2.2, and L_b is dense bed height. The reactor consists of three main sections: the MW waveguide, the dense bed zone, and the freeboard zone (refer to Figure 8.2b). The primary difference between the lab-scale setup and the pilot-scale reactor system lies in the configuration of the MW waveguide. In the lab-scale setup, the quartz reactor walls are transparent to MWs, whereas, in the pilot-scale system, the reactor walls are conductive, reflecting MWs and serving the same function as the MW cavity. The parameters applied in this study, such as dimensions, material properties, and operating conditions, are detailed in Table 8.2. We applied the properties of the gas phase (i.e., N_2, H_2, and NH_3) by the data available in the COMSOL Multiphysics database.

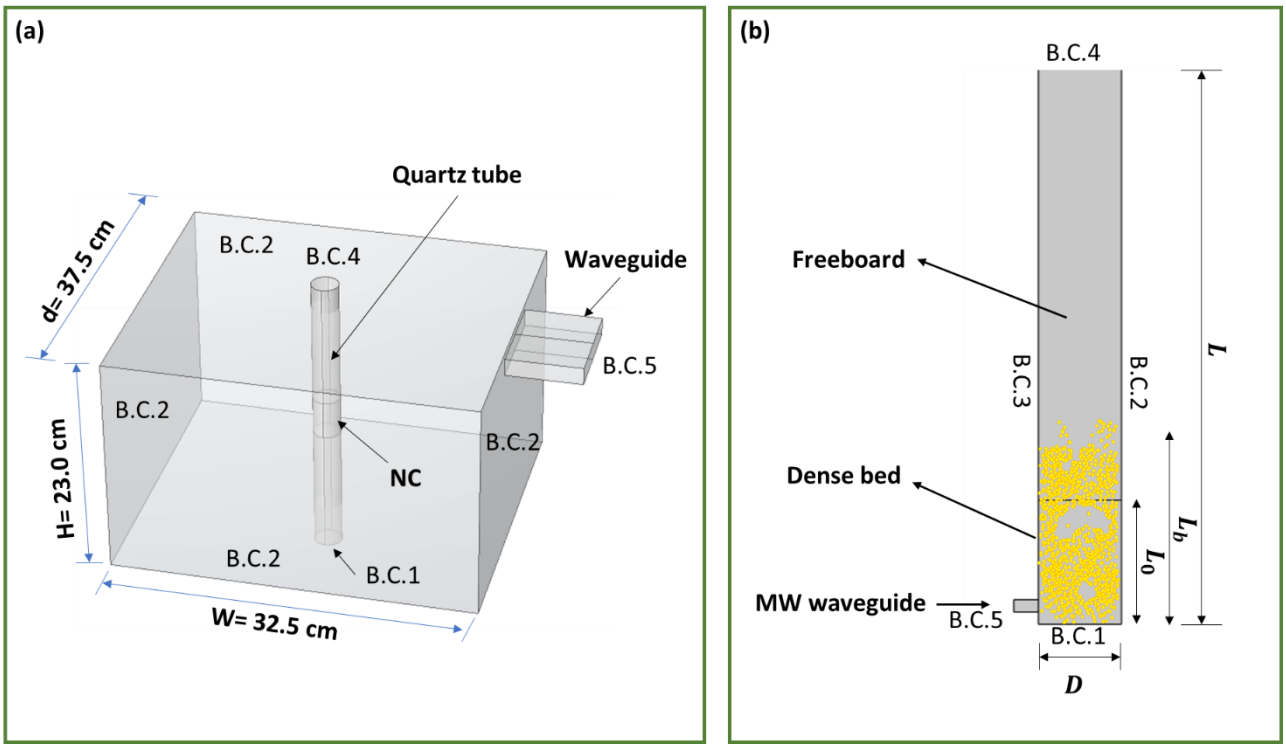

Figure 8.2: Applied geometry and corresponding dimensions and boundary labels in the present study for (a) a lab-scale, and (b) a pilot-scale MHCLAS reactor.

Table 8.2: Implemented parameters in the current study for experimental setup and pilot-scale reactor simulation.

Parameter	Value
Lab-scale particle size, (μm)	50
Pilot-scale particle size, (μm)	150
Particle density in nitridation stage (ρ_p), (kg/m^3)	4550
Particles density in hydrogenation stage (ρ_p), (kg/m^3)	4800
NC thermal conductivity, (W/(mK))	18
NC permittivity- nitridation stage, (-)	11.9-2.34j
NC permittivity- hydrogenation stage, (-)	12.5-2.19j
Gas phase permittivity and permeability, (-)	1.0
Lab-scale reactor diameter, (cm)	2.86
Lab-scale MW input power (W)	Up to 1100
Initial bed voidage, (-)	0.5
Superficial gas velocity (U_g), (cm/s)	6-40
Pilot-scale reactor inner diameter, (cm)	15
Pilot-scale MW input power, (kW)	Up to 100
L_0/D,(-)	3.0

8.3.2. Boundary conditions

To calculate the gas and solid phases velocity profiles, electrical field distribution, and temperature distributions, and reaction extents in the nitridation and hydrogenation stages, we applied boundary conditions (B.C.) that are reported in Table 8.3. We implemented B.C.1 to B.C.5 for momentum balance, heat balance, Maxwell's equation, and mass balance equations for both lab- and pilot-scale units (see Figure 8.2 for the label of boundaries).

For the reactor inlet, the selected boundary conditions include the inlet superficial gas velocity ($U_g = U_{g0}$), inlet temperature (T= 25°C), and the initial concentration of the feedstock. At the reactor outlet, the pressure is maintained constant and equal to ambient pressure ($p = P_0$), with no mass or heat transfer in the z-direction. For reactor walls, we applied slip and no-slip boundary conditions for solid and gas phases, respectively. In addition, cavity walls are insulated to prevent heat and mass transfer.

In the lab-scale reactor, the reactor walls are exposed to air within the MW cavity. We applied the convective heat transfer coefficient by applying Eq. (8.31) [14,46].

$$Nu_L = \frac{h_L L}{k_g} = \frac{4}{3}\left(\frac{7Ra_L Pr}{5(2+21\mathrm{Pr})}\right)^{0.25} + \frac{4(272+315\mathrm{Pr})L}{35(64+63\mathrm{Pr})D} \tag{8.31}$$

where Nu_L is the wall Nusselt number, and Ra_L represents the Rayleigh number.

Table 8.3: Boundary conditions in the present study.

Boundary label	Expression
B.C.1	$U_g = U_{0g}$ $T = T_{in-gas}$ $n \times (\nabla \times \vec{E}) - jkn \times (\vec{E} \times n) = 0$ $\omega_k = \omega_{0,k}$
B.C.2, 3	$\vec{u}_g = 0$ $\vec{u}_s . n = 0$ $-n.\vec{q} = 0$ $-n.\vec{J}_{\omega_k} = 0$
B.C.4	$P = P_0$ $\vec{u}_g . t = 0$ $\vec{u}_s . t = 0$ $-n.\vec{q} = 0$ $n \times (\nabla \times \vec{E}) - jkn \times (\vec{E} \times n) = 0$ $n.D_k \nabla C_k = 0$
B.C.5	$Input\ Power = P_{in}$

8.3.3. Grid independency analysis

The developed model in this study is grid independent, meaning its accuracy is not affected by the number of mesh elements in the reactor. To verify this, we tested multiple mesh resolutions with 26694, 39812, 68489, 305261, and 845125 elements for the pilot-scale reactor.

To evaluate grid independency, we calculated the average T_b in the fluidized bed for each number of elements. We selected this variable as it is highly sensitive to changes in mesh resolution and effectively reflects the impact of various physical phenomena, making it a more reliable indicator than hydrodynamic variables alone. The results showed that increasing the number of elements beyond 39812 (up to 845125) did not affect the average T_b. Therefore, we determined 39812 elements as the optimal mesh resolution for the pilot-scale reactor (see Figure 8.3). By applying a similar approach, we determined that the optimal mesh resolution for the lab-scale MW reactor simulation (3D model) is 612964 cells.

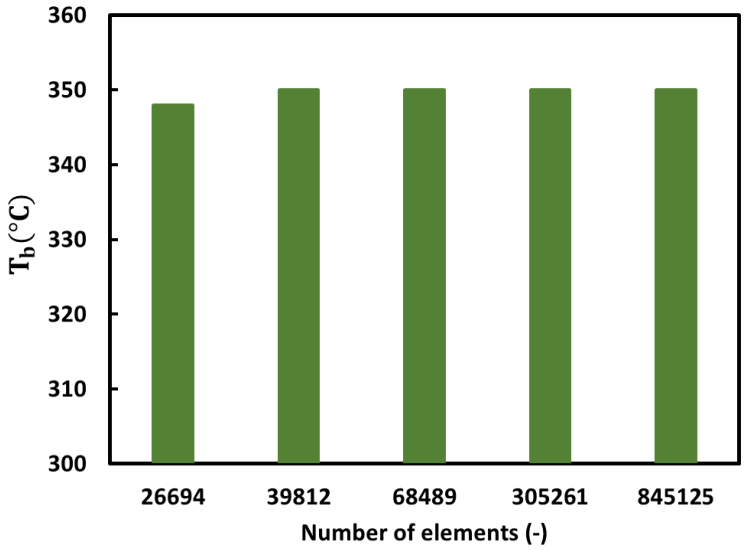

Figure 8.3: Grid independency analysis of the pilot-scale unit adopted in the present study.

8.4. Experimental study

We presented the adopted experimental setup (MHFB reactor) employed in this study to collect experimental data for model validation in Figure 8.4. We placed 5–20 g of NC inside a quartz tube in experiments. During the nitridation stage, we injected a high-purity N_2, 99.9999 vol.%, into the reactor. For the hydrogenation stage, we introduced H_2 with a concentration of up to 20 vol.%, balanced with argon (Ar). We recorded bulk temperature, representing the gas-solid mixture

temperature, with the help of a thermocouple, positioned at the center of the bed. Meanwhile, we measured the temperature of the NC's outer layer, while fluidizing, by a pyrometer/IR camera. Due to high solid mixing in bubbling fluidized beds compared to fixed beds, we can reasonably assume that the recorded temperature by the pyrometer/IR-camera is close to the actual solid phase temperature in the bed. For more details about the experimental setup, please refer to our previous study [8]. In addition, for parameters adjusted for the lab-scale setup, please refer to Table 8.3.

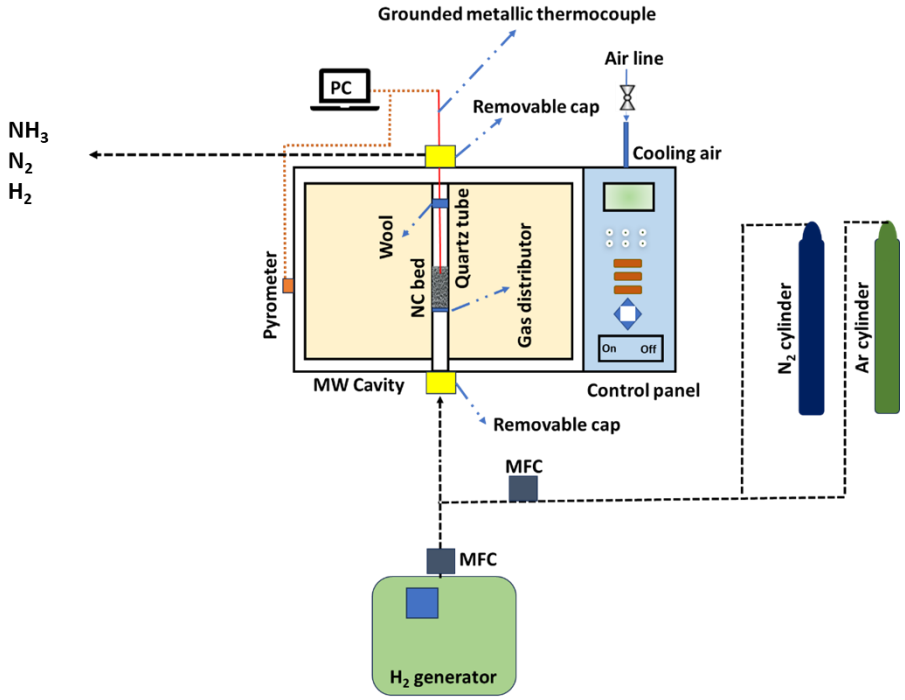

Figure 8.4: Experimental setup applied for MHCLAS technology development in this work [8].

To determine the dielectric properties of the applied NC in this study, we utilized a vector network analyzer (VNA). The complex dielectric properties are expressed as $\varepsilon = \varepsilon' - j\varepsilon''$, where ε' represents the real part (the dielectric constant), indicating the material's ability to store MWs. The imaginary part ε'' corresponds to the dielectric loss factor, which reflects the material's capacity to convert the transmitted MWs into heat. This heating capability is commonly described by the loss tangent ($tan\delta$), calculated as follows [47]:

$$Tan\delta = \frac{\varepsilon''}{\varepsilon'} \tag{8.32}$$

where δ is the phase angle between the phase angle and the polarized dielectric materials. Materials with a low $Tan\delta$ allow MWs to pass through with a minimal absorption, while materials with a high $Tan\delta$ efficiently convert MW energy into heat under irradiation.

8.5. Results and discussion

8.5.1. Dielectric properties of NC

The primary factor influencing the EM field distribution within a MHFB is the dielectric properties of the applied NC. We evaluated the dielectric properties of post-nitridation and post-hydrogenation NCs, as illustrated in Figure 8.6, and observed slight variations throughout the reaction process.

Measurements of ε' and ε'' components of the dielectric constant revealed that they ε' and ε'' were slightly higher after hydrogenation compared to their post-nitridation values. The $Tan\delta$ for nitrided NC was 0.2, which slightly decreased to 0.18 after hydrogenation at a frequency of 2.45 GHz, commonly employed in MW heating applications to prevent interference with other MW-dependent technologies.

Nitrided materials exhibited superior interaction with MWs compared to metallic elements. However, $Tan\delta$ variation during nitridation and hydrogenation is negligible, supporting the assumption that dielectric properties remain constant throughout these stages [8]. In addition, the response of dielectric properties to frequency variations was distinct. At higher frequencies, ε' decreased as the dipoles in the compounds lacked sufficient time to align with the EM field. Conversely, ε'' increased with frequency, indicating a greater MW dissipation into heat due to the intensified bipolar effect (refer to Figure 8.6).

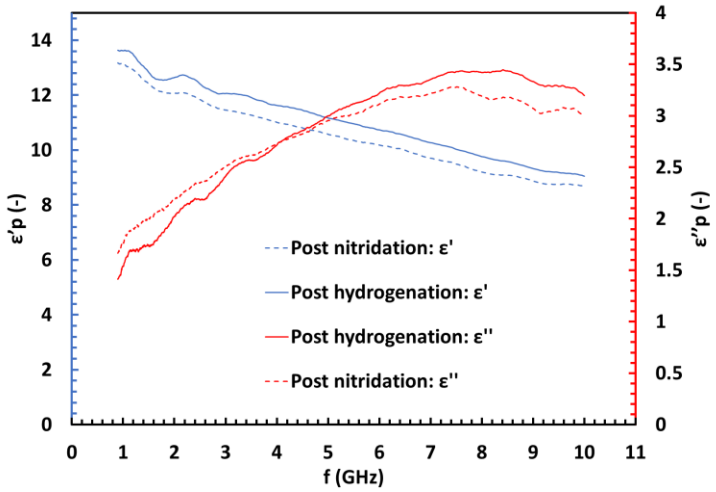

Figure 8.5: ε' and ε'' of dielectric properties for NCs particles after nitridation and hydrogenation stages as a function of MWs frequency measured by VNA.

8.5.2. Model validation

We utilized experimental data obtained from lab-scale setup, including bulk (T_b) and solid (T_s) temperature profiles of NCs under MW irradiations, α_N, and α_H, to validate the model.

In the first step, we estimated the average T_b in the dense bed and freeboard as a function of time in the lab-scale unit by the developed model. The simulation results indicate that T_b initially increases and then stabilizes at around T_b=400°C, reaching thermal equilibrium within the bed (see Figure 8.6a). At the stabilized temperature, we evaluated the axial temperature distribution by the developed model, and we compared the simulation results with the experimental T_b measurements obtained by applying a metallic thermocouple. The comparison demonstrated a close agreement between the model predictions and experimental data (see Figure 8.6b).

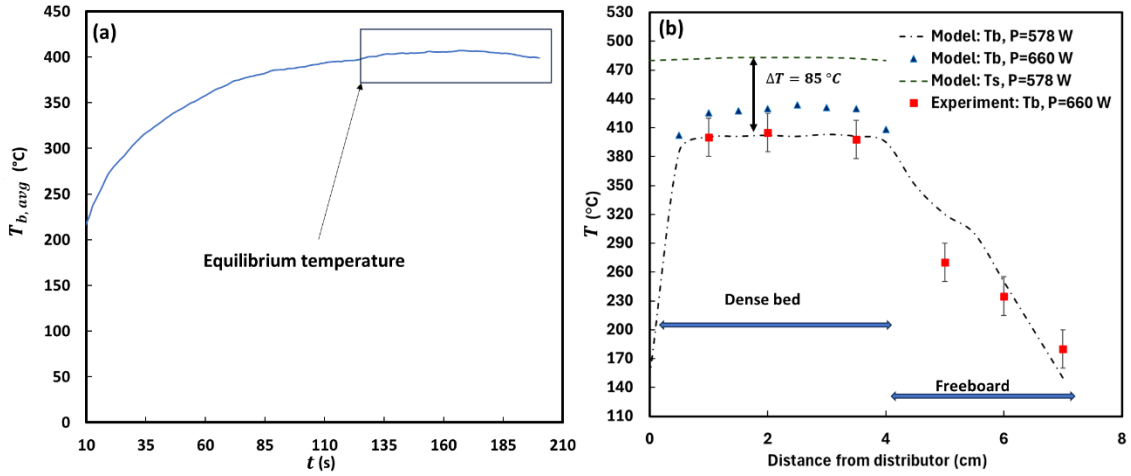

Figure 8.6: (b) Predicted average T_b as a function of time in the lab-scale unit, (b) local T_b and T_s at different dense bed heights in the lab-scale with a comparison with experimental data obtained in this study; U_g= 6.5 cm/s, nitridation stage, and d_p=50 µm.

The bulk temperature at the bed entrance, just above the distributor, was initially low but rapidly increased to approximately 400°C. Within the MHFB, temperature uniformity was higher due to the small particle size and the bubbling fluidization regime. In the freeboard region, T_b started to decline as the influence of particle temperature diminished (see Figure 8.6b). In addition, significant heat loss from the gas to the reactor walls in the freeboard contributed to the observed temperature drop [38,46]. Moreover, we estimated the temperature difference between gas and

solid phases of 85°C in the dense bed, which showed a good agreement with experimental data (Figure 8.6b).

To further validate the model, we compared the experimentally measured α_N, Figure 8.7a, and α_H, Figure 8.7b, with values predicted by the developed model for the lab-scale unit. The results demonstrated a great agreement between the simulation and experimental data, confirming the model's accuracy in predicting reactor performance under MW irradiations. This set of successful validations allows us to confidently apply the validated model for subsequent parametric studies.

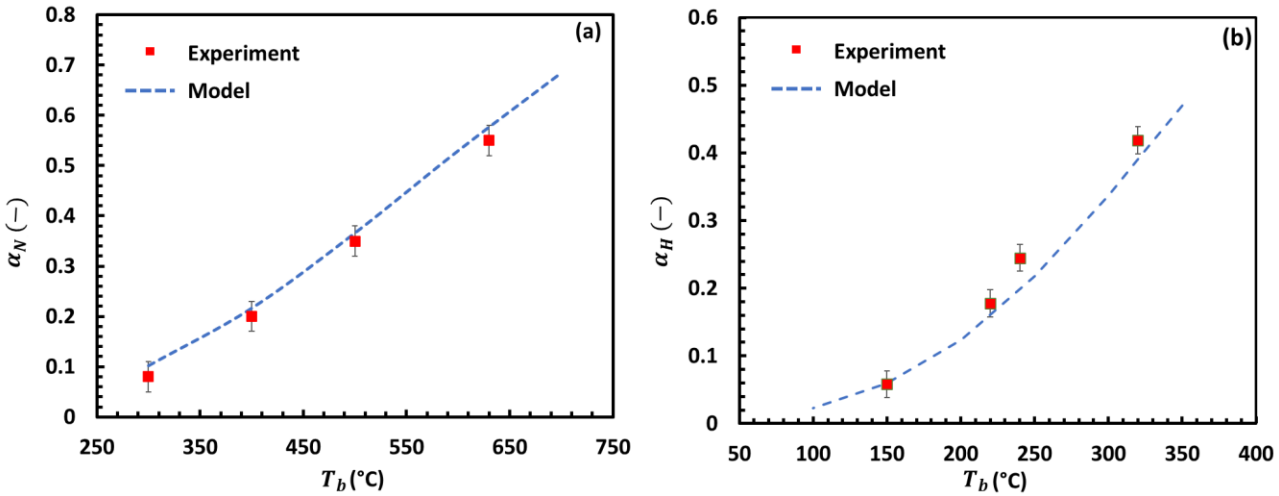

Figure 8.7: Model validation by reactive experimental result obtained from lab-scale unit in (a) nitridation stage, U_g= 6.5 cm/s, and (b) hydrogenation stage, U_g= 7.0 cm/s; d_p=50 µm.

8.5.3. Pilot-scale fluidized bed hydrodynamics verification

We applied the momentum equations to estimate the gas and solid phase fractions in the pilot-scale MHFB reactor at different time intervals and U_g (see Figure 8.8a and b). In addition, we applied reported correlations from literature (Eqs. (8.8)-(8.11)) to verify the estimated bed voidage by the developed Eulerian-Eulerian model. We considered N_2 as the fluidization agent and d_p=150 µm for the pilot-scale setup and model verification.

The predicted average bed voidage/solid fraction obtained from the Eulerian-Eulerian model for pilot-scale MWFB showed an agreement with those estimated by Eqs. (8.8)-(8.11) though the model exhibited a slight overestimation of up to 10% (refer to Figure 8.8c). This discrepancy is likely due to the implementation of a 2D model for these simulations, which can cause further bubble stabilization, thus average bed voidage compared to the 3D unit for which the adopted correlations were developed.

The developed hydrodynamic model plays a crucial role in evaluating EM field distribution, heat dissipation, and temperature profiles in the MHFB. While 3D models provide more detailed insights into the hydrodynamics of fluidized beds, incorporating EM field distribution, heat and mass balances in a 3D simulation significantly increases computational cost and decreases numerical stability compared to 2D models. Given these challenges, the implementation of a 2D model is justified. In the following sections, we applied the verified and validated model to perform a set of parametric studies for MHCLAS technology.

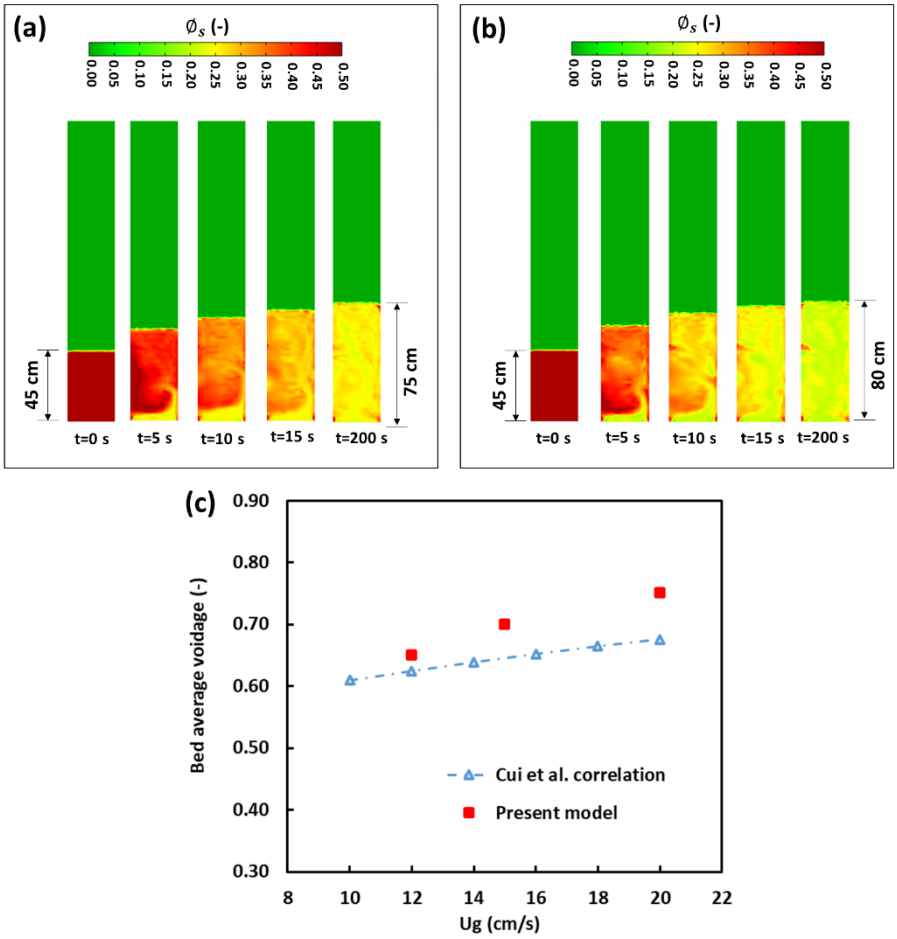

Figure 8.8: NC fraction at (a) U_g=15 cm/s, average T_b =380°C and (b) U_g= 20 cm/s, average T_b=380°C, under MW irradiations, (c) comparison between average voidages of pilot-scale MHFB obtained from the developed Multiphysics model and those estimated by correlations reported in literature as a function of U_g , T=380°C.

8.5.4. Electrical field and temperature distributions in the MHFB

We solved Maxwell's equation to determine the electrical field distribution within the pilot-scale MHFB, see Figure 8.9a. Given the dynamic nature of the MHFB, the electrical field exhibited corresponding fluctuations. These variations in the electrical field led to differences in heat dissipation across the reactor (Figure 8.9b). In the bubbling fluidization regime, the nitridation and hydrogenation reactions primarily occur in the emulsion phase, where the produced gas, ammonia in the hydrogenation case, can be transferred into the bubble phase. The bubble phase is characterized by a high gas concentration and a low solid content, making it relatively transparent to MWs. This results in a significantly lower heat dissipation and temperature within the bubble phase, allowing the produced ammonia to exit with a minimal decomposition. As illustrated in Figure 8.9c, the presence of bubbles in the bed yields regions with lower temperatures. In a bubbling MHFB, three distinct domains interact differently with MWs. In the emulsion phase, solid particles absorb MW energy directly, while the gas remains largely transparent to MWs. The gas velocity in the emulsion phase is approximately equal to or slightly higher than that required for particle fluidization. Any excess gas migrates into the bubble phase, where, due to the high gas concentration, the bubbles remain nearly transparent to MWs.

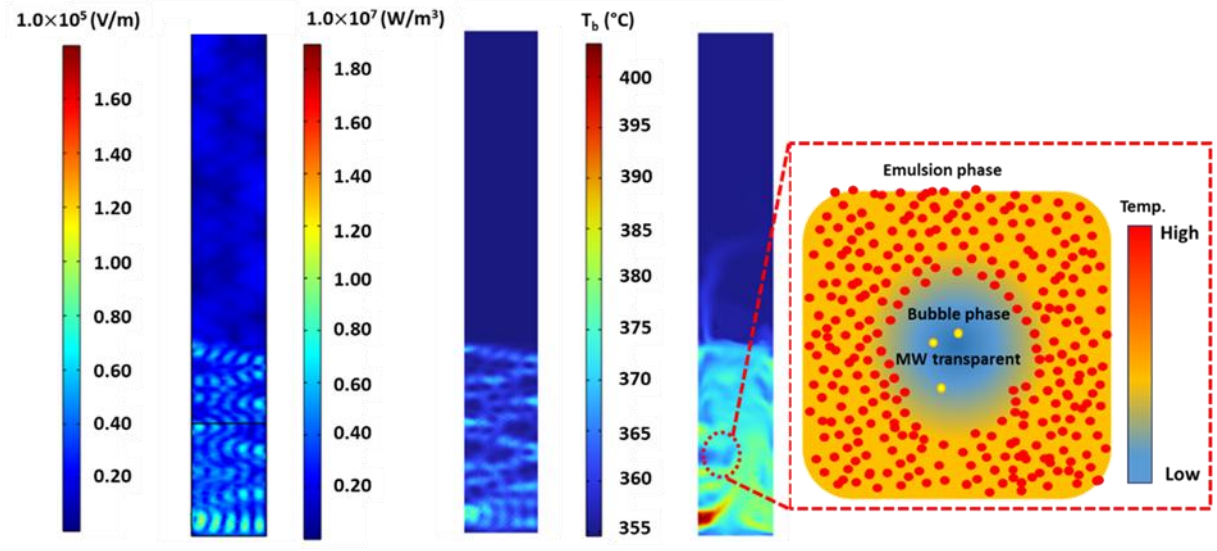

Figure 8.9: (a) Electrical field distribution, (b) heat dissipation rate, and (c) T_b distribution in the pilot-scale MHFB reactor; U_g= 20 cm/s and for the nitridation stage.

The MW penetration depth in the MHFB is influenced by variations in bed voidage, which can result from either the transition from a fixed bed to a fluidized bed or an increase in gas velocity. To better understand this effect, we evaluated the radial distribution of electric field in a pilot-scale MHFB by solving Maxwell's equations in 3D. We varied the average bed voidage from 0.5 to 0.75 to cover a broad range of typical operating conditions. As shown in Figure 8.10, increasing the bed voidage from 0.5 to 0.75 significantly decreases MW attenuation, improving MW penetration throughout the bed.

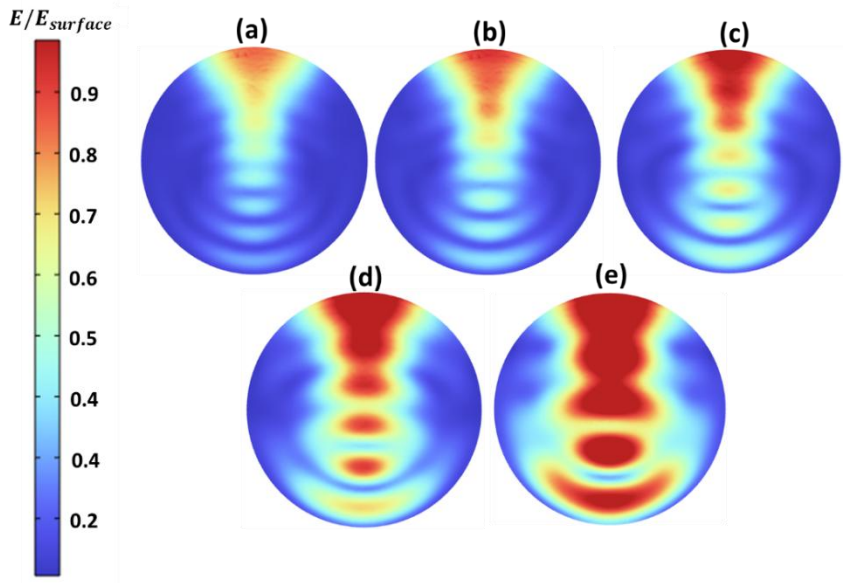

Figure 8.10: Effect of bed voidage in pilot-scale MHFB on its electrical field distribution for $\emptyset_{g,avg}$ of (a) 0.5, (b) 0.55, (c) 0.6), (d) 0.65), and (e) 0.75.

One of the main challenges in MWFB reactors is the limited penetration depth of MWs. While fluidization helps mitigate MW attenuation and improves temperature uniformity within the bed to some extent, this limitation remains a critical factor to address during scale-up. In this study, we adopted a pilot-scale reactor with an internal diameter of 15 cm. However, larger reactor diameters tend to exhibit the electrical field non-uniformity. One potential solution to this issue is to apply multi-waveguide MHFB systems. However, careful design and implementation are essential to avoid interference between waves originating from different waveguides.

8.5.5. Parametric study of nitridation reactor

The first stage of MHCLAS technology is the nitridation stage. During this step, the NC developed in our previous study, i.e., Mn-Fe-BaH_2, is exposed to a N_2 stream. This exposure initiates the nitridation reaction, incorporating nitrogen atoms into the NC structure as lattice nitrogen [14,15]. The nitridation reaction is exothermic; however, initiating the reaction requires reaching the desired T_b to surpass the energy needed to initiate the reaction. MW heating offers an energy-efficient approach by selectively heating the solid phase. In contrast, conventional heating increases gas and solid temperatures simultaneously, resulting in similar temperatures for each and less efficient energy utilization [38,46]. In addition, implementing the fluidized bed reactor ensures that external mass transfer is not the limiting factor in the nitridation and hydrogenation reactions.

We applied the reaction kinetics model developed in our previous study [39] to simulate the nitridation stage in a pilot-scale MHCLAS reactor. Specifically, we investigated the influences of T_b and solid-phase retention time (τ) on α_N. As illustrated in Figure 8.11, the results indicate that increasing T_b from 300°C to 600°C significantly enhances α_N. In addition, a longer solid-phase retention time further increases α_N.

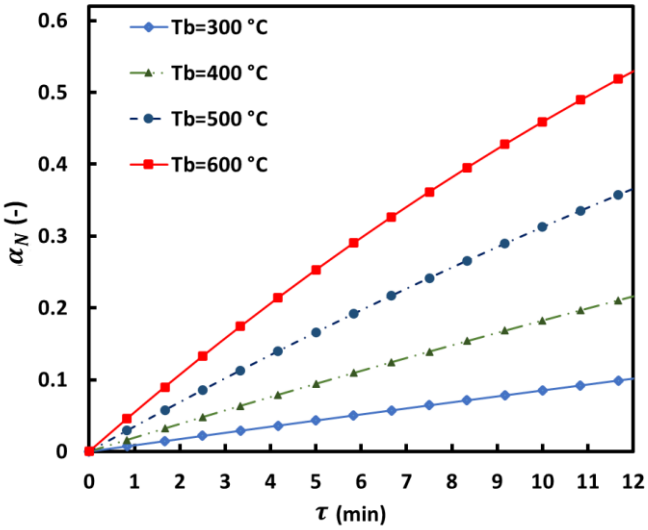

Figure 8.11: Effects of T_b and τ on average α_N in the simulated pilot-scale MHCLAS, U_g=20 cm/s.

The maximum nitrogen fixation capacity of NCs is determined by their composition. In the NC examined in this study, theoretical calculations indicated a potential weight gain of up to 13.5 wt.% under exposure to a nitrogen stream. Pilot-scale results showed a α_N of 55% at 600°C after 720 s, i.e., around 7.5 wt% weight gain (refer to Figure 8.11). These findings are in agreement with

experimental data. The primary cause of the discrepancy between the theoretical nitrogen fixation amount and the actual maximum nitrogen fixation is attributed to the occupation of active sites by oxygen remained from the NC activation stage and potential mass transfer limitations within the internal regions of the particles.

MW heating significantly decreases the nitridation reaction time, addressing a key bottleneck for scaling up MHCLAS technology. In contrast, conventionally heated reactors reported in literature exhibit considerably longer τ. Specifically, nitridation times range from 30 to 45 minutes, three to four times longer than τ achieved with MW heating in this study [3,5,48].

We investigated the effect of U_g on N_2 conversion during the nitridation stage. As shown in Figure 8.12a, the results show that increasing U_g from 15 cm/s to 40 cm/s decreases N_2 conversion from approximately 45% to 17%. Conversely, increasing T_b from 300°C to 600°C enhances N_2 conversion from 8% to 40% (refer to Figure 8.12b). Increasing U_g increases the gas phase residence time within the MHFB, leading to a reduction in N_2 conversion. However, during the nitridation stage, any unreacted nitrogen can be recycled back into the reactor inlet. Consequently, the net nitrogen consumption corresponds to the amount of nitrogen stored as lattice nitrogen.

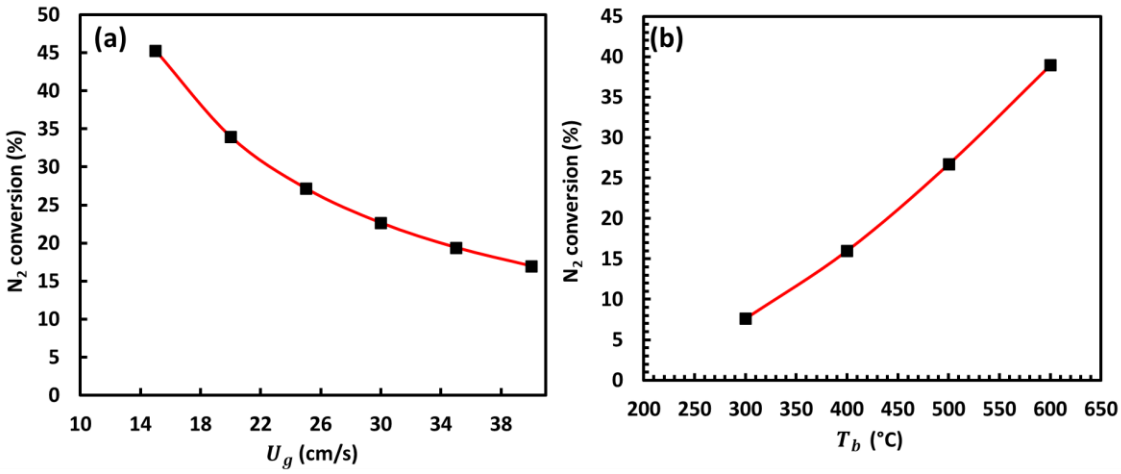

Figure 8.12: Effects of (a) U_g on average N_2 conversion, T_b=565°C, and (b) T_b on average N_2 conversion, U_g=20 cm/s for the simulated pilot-scale MHCLAS in the nitridation stage.

8.5.6. Parametric study of hydrogenation reactor

The second stage of the MHCLAS process is the hydrogenation phase, where the nitrided NC is exposed to a H_2 stream, resulting in the production of ammonia and nitrogen-depleted NC. α_H is

defined as the ratio of ammonia synthesized to the theoretical maximum that could be produced, assuming full conversion of nitrogen atoms in NC's structure into ammonia. We maintained the T_b at 565°C, while the hydrogenation temperature varied between 100°C and 350°C for the modeling and simulation of the pilot-scale MHCLAS.

We presented the effects of T_b and τ on average α_H in the simulated pilot-scale MHCLAS reactor in Figure 8.13a. The data shows that at t=200 s and T_b=350°C, α_H reaches approximately 0.5, maximizing the daily ammonia production rate. Decreasing the retention times at fixed conversions for nitridation and hydrogenation minimizes the overall time required to complete a full cycle, thereby increasing the number of loops that can be conducted in a single day. Therefore, we assumed T_b= 350°C and a retention time of 200 s for the hydrogenation stages. In addition, Figure 8.13b depicts the ammonia production rate per loop per kg of NC. As T_b increases from 150°C to 350°C, α_H increases significantly from 0.05 to approximately 0.5, corresponding to an increase in ammonia production from 2.5 g to 30 g/(kg of NC.loop). Elevated temperatures enhance the reaction kinetics, leading to an increased rate of ammonia formation. However, temperatures exceeding 500°C cause ammonia decomposition, ultimately decreasing the reactor's production efficiency.

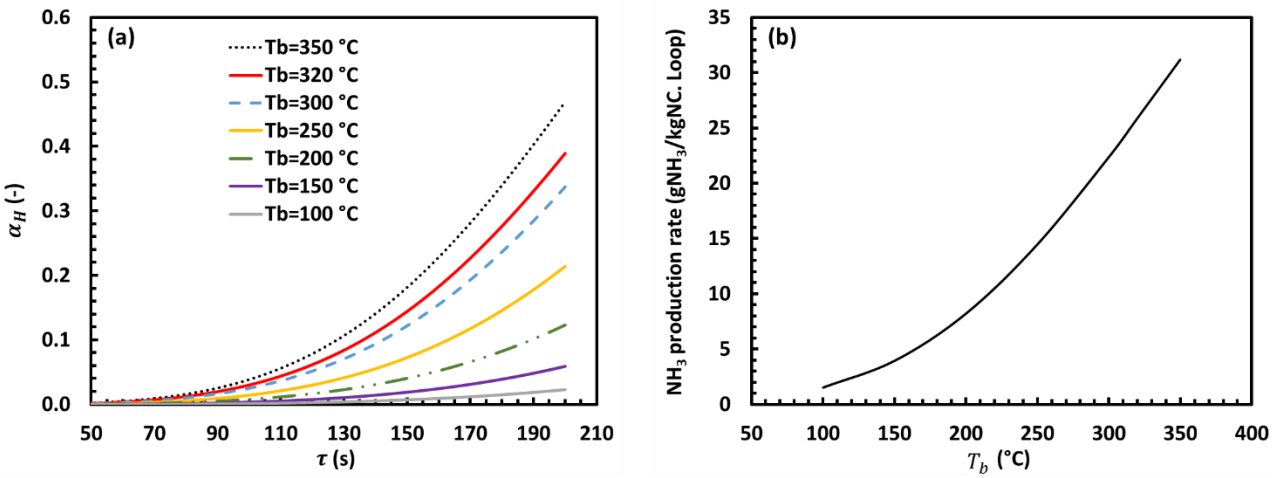

Figure 8.13: (a) Effects of as a function of T_b and τ on average α_H, and (b) ammonia production rate in the hydrogenation stage at different T_b for the simulated pilot-scale MHCLAS.

Influences of hydrogenation T_b and the NC solid inventory on H_2 conversion are shown in Figure 8.14a. As hydrogenation T_b and NC solid inventory increase, the H_2 conversion also increases. At

T_b = 300°C with a solid inventory of 10 kg, the H_2 conversion was approximately 35%. However, increasing the NC solid inventory to 18 kg increased this value to about 65%. In addition, while increasing gas velocity during the hydrogenation stage enhances fluidization, it decreases the H_2 conversion. For instance, when U_g increases from 20 cm/s to 40 cm/s at 300°C, the H_2 conversion declines from 75% to 40% (see Figure 8.14b).

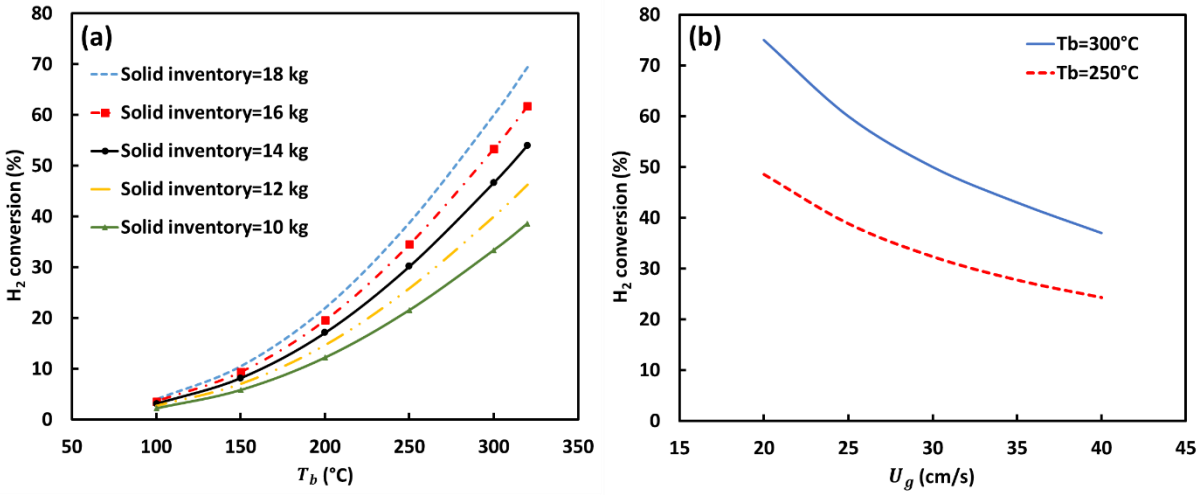

Figure 8.14: Effects (a) of T_b and solid inventory, U_g=25 cm/s, and (b) U_g and hydrogenation T_b on average H_2 conversion in the simulated pilot-scale MHCLAS with 18 kg solid inventory.

8.6. Conclusion

In this study, a comprehensive multiphysics model was developed to investigate the interaction of MW with fluidized bed systems and to simulate key aspects of microwave-assisted chemical looping ammonia synthesis (MHCLAS), including electromagnetic field distribution, heat dissipation, temperature profiles, and reaction conversions during both the nitridation and hydrogenation stages. This work addresses a significant research gap, as few studies have explored MW-fluidized bed interactions or pilot-scale modeling of MHCLAS systems.

The results demonstrated that the MWFB configuration effectively overcomes the penetration depth limitations of microwave heating, enabling the application of volumetric and selective heating on a larger scale. In addition, the analysis of temperature distribution under MW irradiation revealed lower gas-phase temperatures in the bubble phase compared to the emulsion phase, a condition that helps suppress undesired ammonia decomposition reactions and enhances overall reaction efficiency.

Parametric studies on U_g and T_b showed that increasing T_b and decreasing U_g increase nitrogen and hydrogen conversion. In addition, increasing the solid inventory of the NC increases nitrogen can hydrogen conversions. These insights are critical for optimizing reactor performance and guiding the scale-up of MHCLAS technology toward industrial implementation.

Ultimately, the model predicts that ammonia production rates up to 30 g per kg of NC per cycle are attainable, confirming the feasibility and promise of the MHCLAS process for sustainable ammonia synthesis and energy storage applications.

Acknowledgment

We extend our deepest gratitude to OCP Group of Morocco for their financial support of this research.

CRediT authorship contribution statement

Kazem Adavi: Conceptualization, Methodology, Software, Validation, Formal analysis, Investigation, Data curation, Writing - original draft, Visualization. **Jaber Shabanian:** Conceptualization, Methodology, Writing - review & editing. **Adrian Carrillo Garcia:** Conceptualization, Methodology, Writing - review & editing. **Jamal Chaouki:** Conceptualization, Resources, Supervision, Writing - review & editing, Funding acquisition.

Nomenclature

α_j	Extent of reaction j, [-]
ΔH_{rxn}	Reactions enthalpy, [J/mol]
ε_0	Permittivity of free space, [F/m]
ε'	Dielectric constant, [F/m]
ε''	Dielectric loss factor, [F/m]
ε_e	Emulsion voidage, [-]
ε_b	Bubble voidage, [-]
$\varepsilon_{r,eff}$	Effective permittivity, [-]
ϵ	Dissipation rate, [m^2/s^3]
μ_i^m	Molecular dynamic viscosity, [Pa.s]
$\mu_{r,eff}$	Effective permeability, [H/m]
μ_T	Turbulent viscosity, [Pa.s]
$\sigma_{r,eff}$	Effective electrical conductivity, [S/m]
τ_i	Stress tensor of phase i, [Pa]
ω	Angular frequency of the EM, [rad/s]

ω_k	Mass fraction of component k, [-]
ρ_i	Density of phase i, [kg/m^3]
$\emptyset_i$	Fraction of phase i, [-]
$C_{\epsilon 1}$	Turbulent model constant, [-]
$C_{\epsilon 2}$	Turbulent model constant, [-]
C_μ	Empirical constant, [-]
c_k	Concentration of compound k, [mol/m^3]
C_p	Heat capacity, [J/(kgK)]
d_p	Particle diameter, [µm]
$D_{e,k}$	Effective diffusion coefficient, [m^2/s]
$\vec{E}$	Electrical field, [V/m]
f_b	Bubble fraction, [-]
F_i	External force on phase i, [N]
g	Gas phase
g_{grav}	Gravitational acceleration constant, [m/s^2]
h_{gs}	Convection heat transfer coefficient between gas and solid phases, [W/m^2.K]
$\vec{H}$	Magnetic field, [A/m]
H	Hydrogenation stage
J_k	Diffusive mass transfer of compound k
k	Kinetic energy of turbulent model, [m^2/s^2]
k_0	Wavenumber in the vacuum, [1/m]
k_{eff}	Effective conduction heat transfer coefficient [W/(mK)]
m_{sg}	Mass transfer from solid phase to gas phase, [kg/s]
M_i	External force acting on phase i, [N/m^3]
N	Nitridation stage
Nu	Nusselt number, [-]
p	Pressure, [atm]
P_k	Production term of turbulent kinetic energy, [m^2/s^3]
Pr	Prandtl Number, [-]
q	Conductive heat transfer rate, [W/(m^{2}K)]
Q_{MW}	Heat dissipation rate, [W/m^3]
Q_{rxn}	Heat of reaction, [W/m^3]
Q_{sg}	Heat transfer rate between solid and gas phases, [W/m^3]
r_j	Reaction rate, [mol/(m^{3}s)]
Re_p	Reynolds Number, [-]
s	Solid phase
t	Time, [s]
T	Temperature, [K]
$\vec{u}_g$	Gas phase velocity, [m/s]
$\vec{u}_s$	Solid phase velocity, [m/s]
$\vec{u}_m$	Gas solid mixture velocity, [m/s]
U_g	Superficial gas velocity, [m/s]

U_{mf}	Minimum fluidization velocity, [m/s]

References

[1] M. Tawalbeh, S.Z.M. Murtaza, A. Al-Othman, A.H. Alami, K. Singh, A.G. Olabi, Ammonia: A versatile candidate for the use in energy storage systems, Renew Energy 194 (2022). https://doi.org/10.1016/j.renene.2022.06.015.

[2] S. Giddey, S.P.S. Badwal, C. Munnings, M. Dolan, Ammonia as a Renewable Energy Transportation Media, ACS Sustain Chem Eng 5 (2017). https://doi.org/10.1021/acssuschemeng.7b02219.

[3] S. Brown, J. Hu, Review of chemical looping ammonia synthesis materials, Chem Eng Sci 280 (2023). https://doi.org/10.1016/j.ces.2023.119063.

[4] A. Hellman, K. Honkala, S. Dahl, C.H. Christensen, J.K. Nørskov, Ammonia Synthesis: State of the Bellwether Reaction, in: Comprehensive Inorganic Chemistry II (Second Edition): From Elements to Applications, 2013. https://doi.org/10.1016/B978-0-08-097774-4.00725-7.

[5] S. Feng, W. Gao, H. Cao, J. Guo, P. Chen, Advances in the Chemical Looping Ammonia Synthesis, Acta Chimi Sin 78 (2020). https://doi.org/10.6023/A20060207.

[6] S.W. Brown, B. Robinson, Y. Wang, C. Wildfire, J. Hu, Microwave heated chemical looping ammonia synthesis over Fe and CoMo particles, J Mater Chem A Mater 10 (2022). https://doi.org/10.1039/d2ta03241d.

[7] W. Gao, R. Wang, S. Feng, Y. Wang, Z. Sun, J. Guo, P. Chen, Thermodynamic and kinetic considerations of nitrogen carriers for chemical looping ammonia synthesis, Discover Chemical Engineering 3 (2023). https://doi.org/10.1007/s43938-023-00019-4.

[8] K. Adavi, Z. Chen, A.C. Garcia, J. Shabanian, J. Chaouki, Microwave heating-assisted chemical looping ammonia synthesis over Mn-Fe and Mn-Fe-BaH2 nitrogen carriers, Energy Convers Manag 325 (2025) 119434. https://doi.org/10.1016/j.enconman.2024.119434.

[9] E. Fu, F. Gong, S. Wang, R. Xiao, Chemical Looping Technology in Mild-Condition Ammonia Production: A Comprehensive Review and Analysis, Small 20 (2024). https://doi.org/10.1002/smll.202305095.

[10] W. Gao, J. Guo, P. Wang, Q. Wang, F. Chang, Q. Pei, W. Zhang, L. Liu, P. Chen, Production of ammonia via a chemical looping process based on metal imides as nitrogen carriers, Nat Energy 3 (2018). https://doi.org/10.1038/s41560-018-0268-z.

[11] S. Yang, T. Zhang, Y. Yang, B. Wang, J. Li, Z. Gong, Z. Yao, W. Du, S. Liu, Z. Yu, Molybdenum-based nitrogen carrier for ammonia production via a chemical looping route, Appl Catal B 312 (2022). https://doi.org/10.1016/j.apcatb.2022.121404.

[12] M.M. Sarafraz, F.C. Christo, Sustainable three-stage chemical looping ammonia production (3CLAP) process, Energy Convers Manag 229 (2021). https://doi.org/10.1016/j.enconman.2020.113735.

[13] B. Wang, X. Yin, P. Wang, L. Shen, Chemical looping ammonia synthesis at atmospheric pressure benefiting from synergistic effect of Mn- and Fe-based nitrogen carriers, Int J Hydrogen Energy 48 (2023). https://doi.org/10.1016/j.ijhydene.2022.10.132.

[14] K. Adavi, J. Shabanian, J. Chaouki, Temperature Distribution Assessment in Gas-Solid Reactive and Nonreactive Systems Heated by Microwaves, Ind Eng Chem Res 62 (2023). https://doi.org/10.1021/acs.iecr.3c00575.

[15] K. Adavi, A. Amini, M. Latifi, J. Shabanian, J. Chaouki, Kinetic study of multiphase reactions under microwave irradiation: A mini-review, Frontiers in Chemical Engineering 4 (2022). https://doi.org/10.3389/fceng.2022.1059160.

[16] A. Amini, M. Latifi, J. Chaouki, Electrification of materials processing via microwave irradiation: A review of mechanism and applications, Appl Therm Eng 193 (2021). https://doi.org/10.1016/j.applthermaleng.2021.117003.

[17] M. Khodabandehloo, J. Shabanian, J.P. Harvey, J. Chaouki, Microwave heating-assisted chemical looping dry reforming of methane, Int J Hydrogen Energy 71 (2024) 1380–1391. https://doi.org/10.1016/j.ijhydene.2024.05.295.

[18] S. Hamzehlouia, S.A. Jaffer, J. Chaouki, Microwave Heating-Assisted Catalytic Dry Reforming of Methane to Syngas, Sci Rep 8 (2018). https://doi.org/10.1038/s41598-018-27381-6.

[19] C. Jiang, I.W. Wang, X. Bai, S. Balyan, B. Robinson, J. Hu, W. Li, A. Deibel, X. Liu, F. Li, L.M. Neal, J. Dou, Y. Jiang, R. Dagle, J.A. Lopez-Ruiz, G. Skoptsov, Methane Catalytic Pyrolysis by Microwave and Thermal Heating over Carbon Nanotube-Supported Catalysts: Productivity, Kinetics, and Energy Efficiency, Ind Eng Chem Res 61 (2022). https://doi.org/10.1021/acs.iecr.1c05082.

[20] A. Araia, Y. Wang, B. Robinson, C. Jiang, S. Brown, C. Wildfire, D. Shekhawat, J. Hu, Microwave-assisted ammonia synthesis over Cs-Ru/CeO2 catalyst at ambient pressure: Effects of metal loading and support particle size, Catal Commun 170 (2022). https://doi.org/10.1016/j.catcom.2022.106491.

[21] C. Wildfire, V. Abdelsayed, D. Shekhawat, R.A. Dagle, S.D. Davidson, J. Hu, Microwave-assisted ammonia synthesis over Ru/MgO catalysts at ambient pressure, Catal Today 365 (2021). https://doi.org/10.1016/j.cattod.2020.06.013.

[22] Y. Wang, C. Wildfire, T.S. Khan, D. Shekhawat, J. Hu, P. Tavadze, R. Quiñones-Fernández, S. Moreno, Effects of support and promoter on Ru catalyst activity in microwave-assisted ammonia synthesis, Chemical Engineering Journal 425 (2021). https://doi.org/10.1016/j.cej.2021.130546.

[23] A. Araia, Y. Wang, C. Jiang, S. Brown, A. Caiola, B. Robinson, W. Li, J. Hu, Insight into Enhanced Microwave Heating for Ammonia Synthesis: Effects of CNT on the Cs-Ru/CeO2Catalyst, ACS Appl Mater Interfaces 15 (2023). https://doi.org/10.1021/acsami.3c00132.

[24] Y. Wang, T.S. Khan, C. Wildfire, D. Shekhawat, J. Hu, Microwave-enhanced catalytic ammonia synthesis under moderate pressure and temperature, Catal Commun 159 (2021). https://doi.org/10.1016/j.catcom.2021.106344.

[25] A. Araia, Y. Wang, C. Jiang, S. Brown, A. Caiola, B. Robinson, J. Hu, Intuitive study on the effect of support morphology over Cs-Ru/CeO2 catalyst for microwave-initiated ammonia synthesis, Catal Commun 172 (2022). https://doi.org/10.1016/j.catcom.2022.106551.

[26] P. Yan, A.I. Stankiewicz, F. Eghbal Sarabi, H. Nigar, Microwave heating in heterogeneous catalysis: Modelling and design of rectangular traveling-wave microwave reactor, Chem Eng Sci 232 (2021). https://doi.org/10.1016/j.ces.2020.116383.

[27] P.D. Muley, Y. Wang, J. Hu, D. Shekhawat, Microwave-assisted heterogeneous catalysis, Catalysis 33 (2021). https://doi.org/10.1039/9781839163128-00001.

[28] M. Laza Bulc, T. Leuca, F. Slovac, Numerical modeling of heating process in an electromagnetic microwave field using comsol multiphysics software, Journal of Electrical and Electronics Engineering 7 (2014).

[29] S.A. Halim, J. Swithenbank, Simulation study of parameters influencing microwave heating of biomass, Journal of the Energy Institute 92 (2019). https://doi.org/10.1016/j.joei.2018.05.010.

[30] D. Salvi, D. Boldor, J. Ortego, G.M. Aita, C.M. Sabliov, Numerical modeling of continuous flow microwave heating: A critical Comparison of COMSOL and ANSYS, Journal of Microwave Power and Electromagnetic Energy 44 (2010). https://doi.org/10.1080/08327823.2010.11689787.

[31] D. Salvi, D. Boldor, G.M. Aita, C.M. Sabliov, COMSOL Multiphysics model for continuous flow microwave heating of liquids, J Food Eng 104 (2011). https://doi.org/10.1016/j.jfoodeng.2011.01.005.

[32] R.R. Mishra, A.K. Sharma, Microwave-material interaction phenomena: Heating mechanisms, challenges and opportunities in material processing, Compos Part A Appl Sci Manuf 81 (2016). https://doi.org/10.1016/j.compositesa.2015.10.035.

[33] S. Nanvakenari, K. Movagharnejad, A. Latifi, Multi-objective optimization of hybrid microwave-fluidized bed drying conditions of rice using response surface methodology, J Stored Prod Res 97 (2022). https://doi.org/10.1016/j.jspr.2022.101956.

[34] M. Mokhtari, J. Shabanian, J. Chaouki, Methane dry reforming in a microwave heating-assisted dense fluidized bed, Powder Technol 449 (2025). https://doi.org/10.1016/j.powtec.2024.120444.

[35] C. Si, J. Wu, Y. Zhang, G. Liu, Q. Guo, Experimental and numerical simulation of drying of lignite in a microwave-assisted fluidized bed, Fuel 242 (2019). https://doi.org/10.1016/j.fuel.2019.01.002.

[36] M. Salakhi, M.J. Thomson, A particle-scale study showing microwave energy can effectively decarbonize process heat in fluidization industry, IScience 28 (2025). https://doi.org/10.1016/j.isci.2024.111732.

[37] M. Ranjbaran, D. Zare, CFD Modeling of Microwave-Assisted Fluidized Bed Drying of Moist Particles Using Two-Fluid Model, Drying Technology 30 (2012). https://doi.org/10.1080/07373937.2011.642913.

[38] S. Hamzehlouia, J. Shabanian, M. Latifi, J. Chaouki, Effect of microwave heating on the performance of catalytic oxidation of n-butane in a gas-solid fluidized bed reactor, Chem Eng Sci 192 (2018). https://doi.org/10.1016/j.ces.2018.08.054.

[39] K. Adavi, A. Carrillo Garcia, J. Shabanian, M. Latifi, J. Chaouki, Kinetic study of microwave heating-assisted chemical looping ammonia synthesis over Mn-Fe-Ba-based nitrogen carrier, n.d.

[40] L. Mu, K.A. Buist, J.A.M. Kuipers, N.G. Deen, Hydrodynamic and heat transfer study of a fluidized bed by discrete particle simulations, Processes 8 (2020). https://doi.org/10.3390/PR8040463.

[41] D. Gidaspow, Multiphase Flow and Fluidization: Continuum and Kinetic Theory Descriptions, 2012. https://doi.org/10.1016/C2009-0-21244-X.

[42] M. Adnan, N. Ahmad, P. Piumsomboon, B. Chalermsinsuwan, Coarse-graining dense discrete phase model for modeling particle dynamics in a 3D tapered fluidized bed coater: Analysis of different drag models, J Food Eng 365 (2024). https://doi.org/10.1016/j.jfoodeng.2023.111831.

[43] F. Laasri, N. Mostoufi, A.C. Garcia, J. Chaouki, Simulation of a bubbling fluidized bed reactor for phosphogypsum decomposition with carbon monoxide, Canadian Journal of Chemical Engineering (2025). https://doi.org/10.1002/cjce.25618.

[44] H. Cui, N. Mostoufi, J. Chaouki, Characterization of dynamic gas-solid distribution in fluidized beds, Chemical Engineering Journal 79 (2000). https://doi.org/10.1016/S1385-8947(00)00178-9.

[45] Y. Zhang, Z. Chao, H.A. Jakobsen, Modelling and simulation of chemical looping combustion process in a double loop circulating fluidized bed reactor, Chemical Engineering Journal 320 (2017). https://doi.org/10.1016/j.cej.2017.03.046.

[46] A. Malhotra, W. Chen, H. Goyal, P.J. Plaza-Gonzalez, I. Julian, J.M. Catala-Civera, D.G. Vlachos, Temperature homogeneity under selective and localized microwave heating in structured flow reactors, Ind Eng Chem Res 60 (2021). https://doi.org/10.1021/acs.iecr.0c05580.

[47] S. Farag, A. Sobhy, C. Akyel, J. Doucet, J. Chaouki, Temperature profile prediction within selected materials heated by microwaves at 2.45GHz, Appl Therm Eng 36 (2012). https://doi.org/10.1016/j.applthermaleng.2011.10.049.

[48] R. Wang, W. Gao, S. Feng, Y. Guan, Q. Wang, J. Guo, P. Chen, Zn Promotes Chemical Looping Ammonia Synthesis Mediated by LiH−Li2NH Couple, ChemSusChem 16 (2023). https://doi.org/10.1002/cssc.202300813.

CHAPTER 9: TECHNO-ECONOMIC ASSESSMENT OF MICROWAVE HEATING-ASSISTED CHEMICAL LOOPING AMMONIA SYNTHESIS TECHNOLOGY

9.1. Introduction

In previous chapters, we introduced the microwave heating chemical looping ammonia synthesis (MHCLAS) technology, which enables ammonia production by decoupling nitrogen and hydrogen activation and applying selective and volumetric microwave (MW) heating. Our research demonstrated the effectiveness of a Mn, Fe, and Ba-based nitrogen carrier, which exhibited superior performance under both conventional and MW heating. Furthermore, we developed a reaction model to simulate and analyze pilot-scale reactor performance. This chapter presents a general techno-economic analysis of the developed MHCLAS technology, assessing economic constraints and identifying key areas for improvement in future developments. We performed all calculations based on USD currency, showing as $.

9.2. Process development

9.2.1. Process flow diagrams

To implement MHCLAS technology, we proposed two different process flow diagrams (PFDs). In the first PFD, both the nitridation and hydrogenation stages are performed in a single reactor by simply switching the inlet gas from nitrogen to hydrogen (see Figure 9.1). This approach offers a simpler process and eliminates the need for solid circulation, thereby decreasing the risk of solid attrition. In the first stage, the nitridation process, nitrogen with 99.995% purity, produced by a membrane system, is introduced into a MW-heated fluidized bed containing NCs. Membrane systems are one method of nitrogen purification, though the specific process can vary depending on manufacturing requirements and technical factors. Other common techniques for nitrogen production include pressure swing adsorption (PSA) and the cryogenic method.

The nitrogen molecules dissociate and form lattice nitrogen (Figure 9.1a). In the second stage, the hydrogenation process, the inlet gas is switched to a hydrogen stream. The nitrided NCs are exposed to the hydrogen stream, resulting in ammonia production (Figure 9.1b). Hydrogen can be

supplied from various sources, such as water electrolysis [1], chemical looping dry reforming [2,3], or catalytic waste pyrolysis [4]. In the second PFD (refer to Figure 9.2), solid NCs circulate between the nitridation and hydrogenation stages. This approach requires a detailed reactor design to ensure stable solid circulation. However, it may also increase the risk of solid attrition.

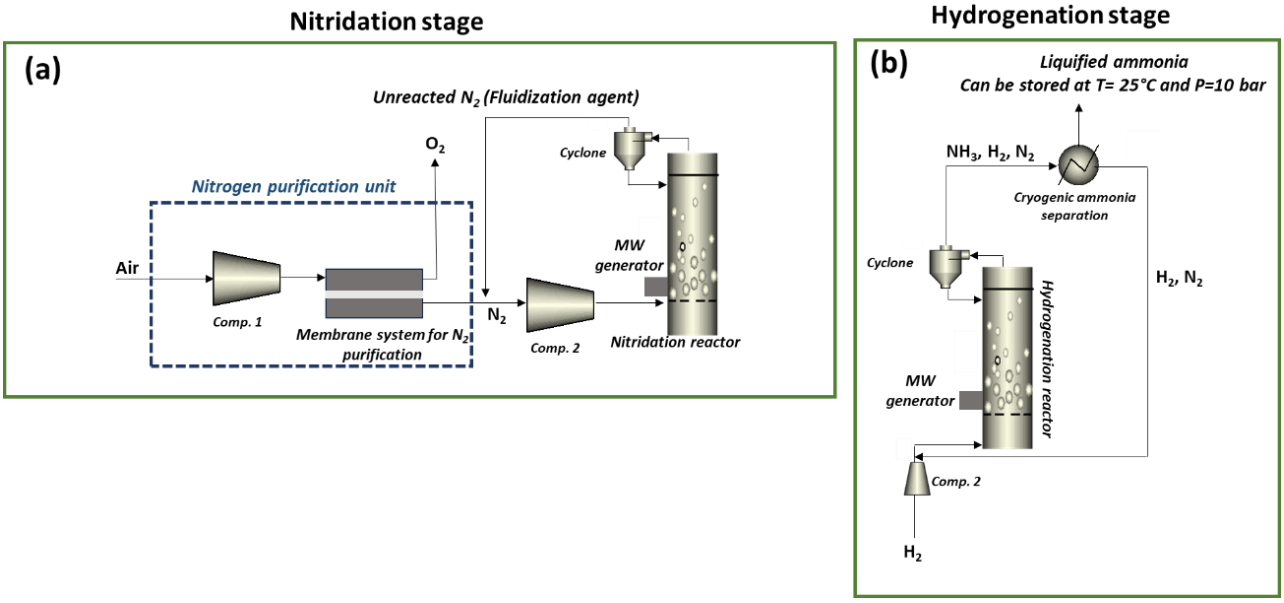

Figure 9.1: Scenario 1-MHCLAS PFD without solid circulation and performing the nitridation and hydrogenation stages by switching the inlet gas, (a) Nitridation stage, (b) Hydrogenation stage.

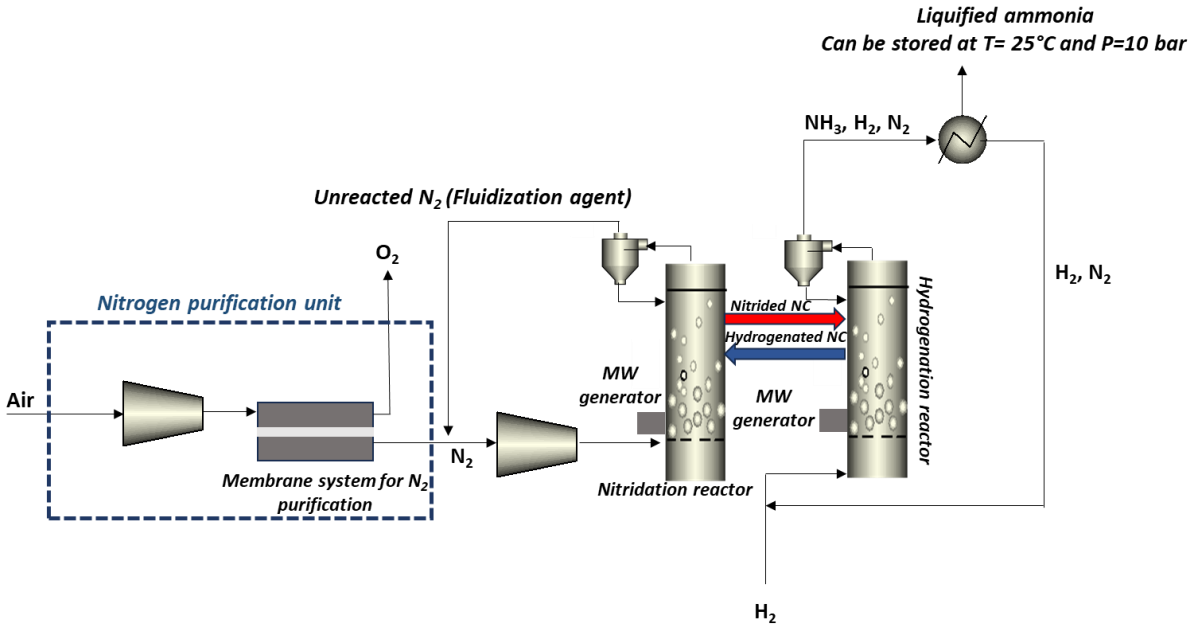

Figure 9.2: Scenario 2-MHCLAS PFD with two reactors: nitridation and hydrogenation reactors.

9.2.2. Reactor design

A major challenge in scaling up MW-heated reactors is the limited penetration depth of MWs. To overcome this, we proposed a double waveguide system that effectively expands the reactor's diameter while maintaining efficient MW interaction. We conducted a COMSOL Multiphysics simulation to analyze the radial distribution of the electric field during both the nitridation and hydrogenation stages. As shown in Figure 9.3, a diameter of 50 cm appears optimal; increasing the diameter beyond this may lead to non-uniform temperature distributions within the bed. The simulation methodology is similar to that described in Chapter 8, and Table 9.1 details the reactor parameters for both stages.

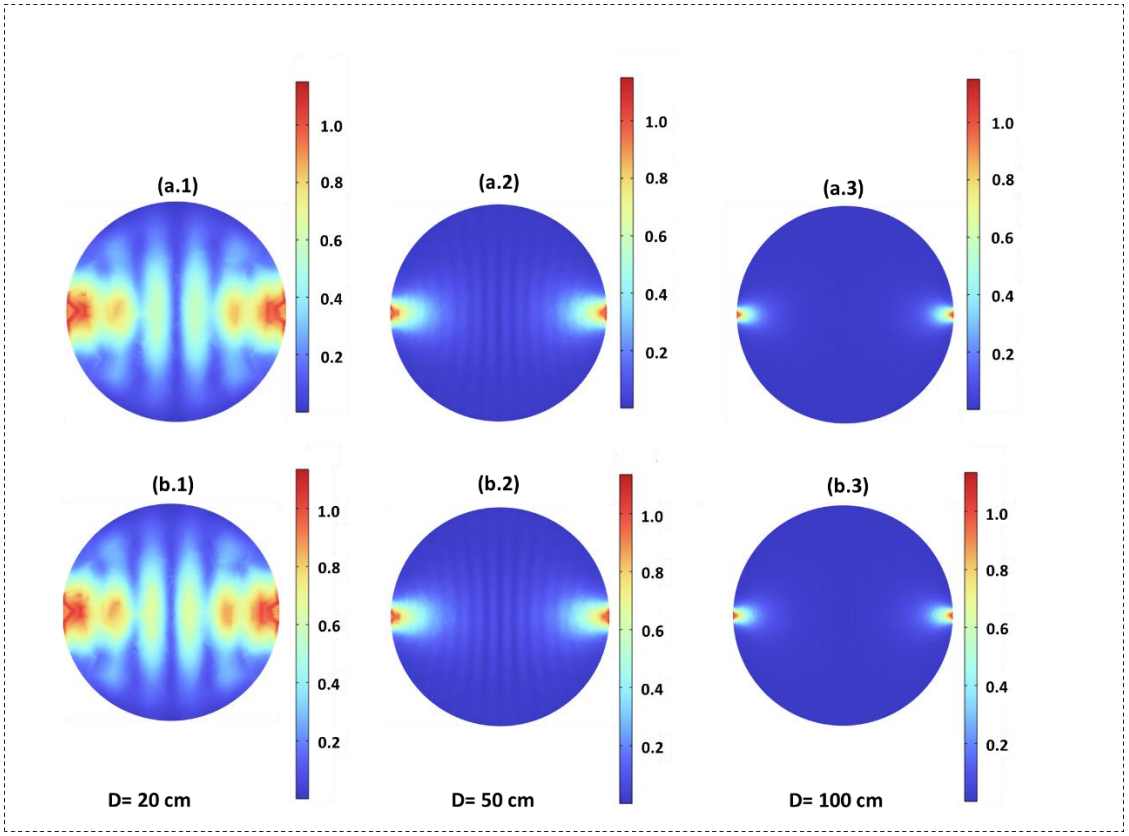

Figure 9.3: Normalized electrical field distribution for (a) nitridation and (b) hydrogenation stages for reactors with different diameters.

Table 9.1: MHCLAS reactor characterizations.

Particle diameter, μm	250
Average particle density, kg/m^3	4700
Minimum fluidization velocity, U_{mf}, cm/s	12
Superficial gas velocity, U_g, cm/s	20-40
Nitrogen carrier weight per reactor, kg	700
Reactor diameter, m	0.5
Bed length, m	1.5
Reactor material	Stainless steel + Alumina
Nitridation bulk temperature, °C	565
Nitridation pressure, bar	1
Nitridation time, min	10.0
Minimum flow of N_2/mass of NC, NL/kg per loop for nitridation reaction	4.7
Hydrogenation bulk temperature, °C	350
Hydrogenation pressure, bar	1
Hydrogenation time, min	5.0
Nitridation to hydrogenation transition time, min	5.0
Minimum flow of H_2/mass of NC, NL/kg per loop	19.2
Operation time, hr/year	8000
Operation year	10

The ammonia production rate in each reactor is directly influenced by the amount of solid inventory that can be loaded. One of the key challenges of MW heating systems is the limited MW penetration depth. However, by utilizing two MW waveguides instead of one, we can increase the reactor diameter to 0.5 meters, thereby enhancing the ammonia production rate to approximately 1.7 tonnes per day per reactor (see Figure 9.4).

This approach plays a crucial role in the industrialization of MHCLAS technology. By adopting a modular plant design, the total production capacity can be scaled up simply by increasing the number of reactors, making the system more flexible and efficient for large-scale applications.

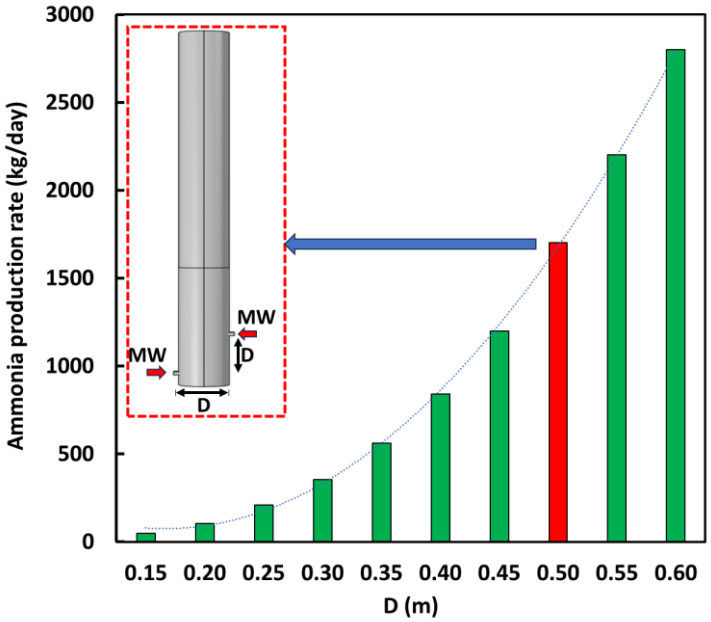

Figure 9.4: Effect of reactor diameter on ammonia production rate per reactor.

We designed the reactor to achieve a production rate of approximately 1.7 tonnes of ammonia per day. The proposed reactor has a diameter of 0.5 meters and a bed height of 1.5 meters before fluidization. We can construct the reactor from stainless steel and lining it with alumina. Alumina, being nearly transparent to MWs at MHCLAS operating temperatures, serves as a protective barrier in the bed [5]. Its presence prevents reaction gases from contacting the MW generator and protects it from potential damage, allowing MWs to pass through while keeping the gases separated from the generator. In addition, thermal insulators can be used to enhance thermal isolation and minimize heat loss from the system.

For the first scenario, a single reactor is designed to perform both the nitridation and hydrogenation stages (see Figure 9.1). The nitridation reaction occurs over 10 minutes, while hydrogenation takes around 5 minutes, with an additional 5 minutes allocated for the transition from the nitridation bulk temperature (565°C) to the hydrogenation bulk temperature (350°C). Under these operating conditions, the ammonia production rate is around 30 $g_{ammonia}$/ kg_{NC} per loop.

9.3. Economic calculations

9.3.1. CAPEX costs calculation

In MHCLAS, the MW generator provides the required energy for the advancement of nitridation and hydrogenation reactions, this supplied heat supports the required energy for surpassing the

required activation reaction and the required energy for endothermic reaction (for hydrogenation stage when only Mn presents as NC). There are two main types of MW generators including magnetron-based and solid-state-based MW generators [link].

Magnetrons are cheaper but have a shorter lifetime, i.e. up to 10,000 hours, compared to solid-state magnetrons, i.e., around 100,000 hours. In addition, the available power for magnetrons on the market is limited to a maximum of 100 kW [link].

Table 9.2 presents the capital expenditure (CAPEX) costs that we considered in this work for different items. Here, ISBL (Inside Battery Limits) refers to the equipment and their installation required within the process boundary, such as valves, safety equipment, and control systems. In contrast, OSBL (Outside Battery Limits) includes components external to the main process, such as utilities (see Eqs. (9.1) and (9.2)). For more details about ISBL and OSBL factors refer to Table 9.3.

$$ISBL\ Cost = Total\ equipment\ cost \times ISBL\ factor \quad (9.1)$$

$$OSBL\ Cost = Total\ equipment\ cost \times OSBL\ factor \quad (9.2)$$

The equipment cost was estimated using equations from the literature [6], while the cost of the solid-state MW generator was obtained through market inquiries.

Table 9.2: Price of compounds contributing to CAPEX estimation.

Item	Rate
Reactor	70,000 $/reactor
Solid state MW generator	2 $/W
Compressor	25,000 $/unit
Separators	8,000 $/unit
Cyclones	27,000 $/unit
ISBL factor	0.70
OSBL factor	0.20
Engineering cost factor	0.05
Contingency factor	0.05

Table 9.3: Factors associated with ISBL and OSBL.

ISBL factor	
Installation costs	0.35
Piping and instrumentation	0.15
Construction and labor	0.15
Electrical and utilities infrastructure	0.05
Total	0.7
OSBL factor	
Storage	0.04
Safety and environmental systems	0.04
Support facilities	0.08
Project management and indirect costs	0.04
Total	0.20

Figure 9.5 presents the CAPEX cost distribution for an ammonia production capacity of 1.7 tonnes per day for scenario 1 and 3.5 ton/day for scenario 2, with a total CAPEX of $0.7 million and $1.4 million, respectively. After ISBL costs, the MW generator and reactor represent the largest contributors to CAPEX.

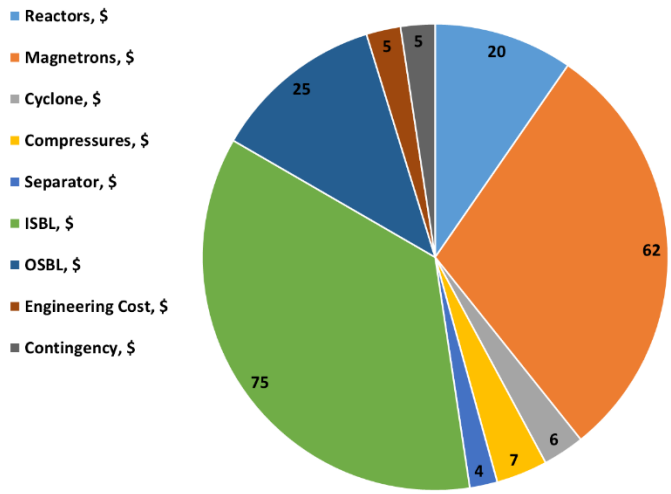

Figure 9.5: CAPEX costs distribution in percentage.

9.3.2. OPEX costs calculation

Hydrogen prices vary based on several factors, including production technique, country, environmental policies, feedstocks, and the energy source used for hydrogen generation. Various methods for hydrogen production are reported in the literature, including steam methane reforming

(SMR), gasification, pyrolysis, water electrolysis, and fermentation. In addition, the feedstocks required for these processes can range from fossil fuels to plastic and food waste [7–10].

The hydrogen color classification system is used to represent the environmental impact of different production techniques, for example, gray hydrogen is produced by fossil fuel reforming, which results in CO_2 emissions. Blue hydrogen is derived from fossil fuels but incorporates carbon capture technologies to minimize CO_2 emissions, and green hydrogen refers to zero-carbon emission hydrogen production such as water electrolysis. The price of green hydrogen is higher than blue hydrogen, and blue hydrogen is higher than green hydrogen [11,12].

Hydrogen prices usually range from 1$ to 5$ per kilogram [13]. Electricity prices vary across different countries and regions. In Canada, electricity costs range from 0.03$ to 0.2$ per kWh, whereas in countries such as Morocco, prices can reach 0.116$ per kWh.

Nitrogen is a crucial component in MHCLAS, with its cost varying based on production capacity and required purity levels. For nitrogen with 99.995% purity, the estimated energy consumption is 0.68 kWh per cubic meter. Given regional electricity price differences, the cost of nitrogen can range from 0.03$ to 0.30$ per kilogram for a facility producing more than 500,000 m^3/year. For more details associated with OPEX cost calculations, refer to Table 9.4 [link]. However, further research is needed to evaluate the impact of lower nitrogen purity on MHCLAS performance.

Table 9.4: Price ranges of compounds contributing to OPEX estimation.

Item	Rate
Hydrogen	1-5 $/kg
Nitrogen	0.03-0.3 $/kg
Electricity	0.03-0.20 $/kWh
Nitrogen carrier	10 $/kg
NC lifetime	2 years
Electricity-to-MW efficiency	50%
Maintenance and repair cost	0.03 total CAPEX
Ammonia separation cost based on the cryogenic technique	10 $/ton ammonia
Return on investment (ROI) factor	0.2

9.4. Sensitivity analysis

9.4.1. Effect of hydrogen price

Hydrogen prices range from 1$/kg to 5$/kg, depending on the production method, with green hydrogen costing between 2.5$/kg and 5$/kg. (see Figure 9.6).

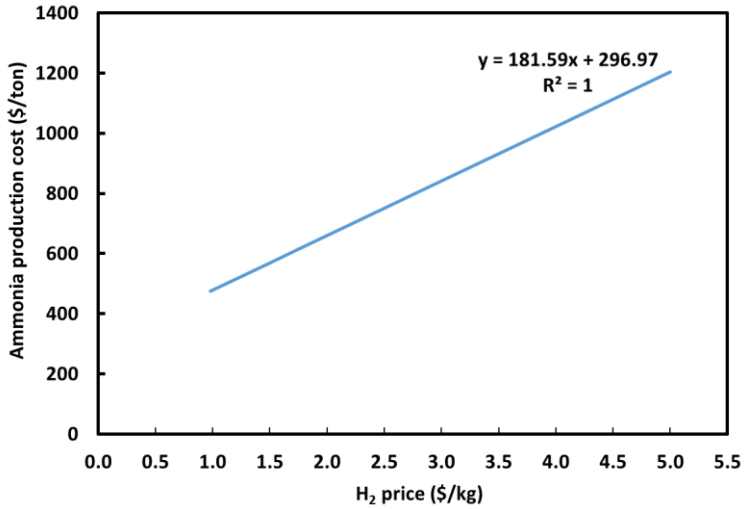

Figure 9.6: Effect of hydrogen price on ammonia production cost, electricity price: 0.054$/kWh, nitrogen price: 0.05 $/kg.

An increase in hydrogen price from 1$/kg to 5$/kg increases the ammonia production cost from approximately 470 $/ton to 1200 $/ton, highlighting the critical need for cost-effective, sustainable hydrogen production methods to minimize environmental impact. (see Figure 9.6).

9.4.2. Effect of nitrogen price

Nitrogen prices vary significantly depending on its purity. The primary methods for nitrogen production are pressure swing adsorption (PSA), cryogenic separation, and the membrane system. PSA can produce nitrogen with a concentration ranging from 95% to 99.999%, meeting the needs of various industries [link].

Higher nitrogen purity, which corresponds to lower oxygen content, increases production costs. As nitrogen prices rise, ammonia production costs can increase from approximately 730 $/ton to 900 $/ton (see Figure 9.7). Therefore, developing cost-effective nitrogen production methods is essential to reducing overall ammonia production costs.

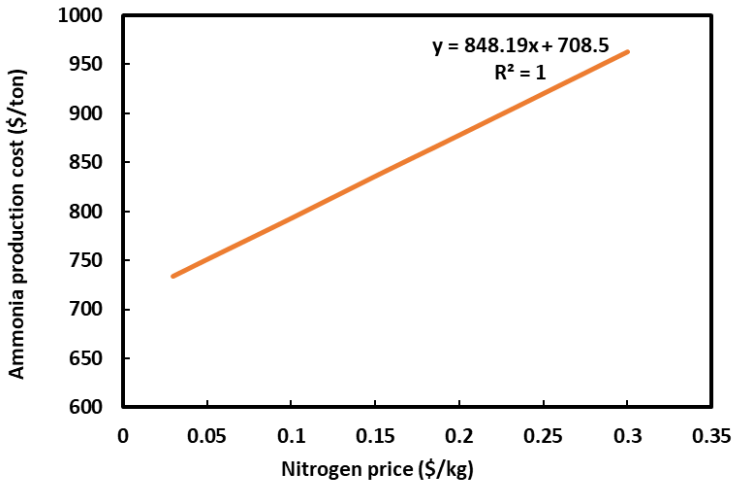

Figure 9.7: Effect of nitrogen price on ammonia production cost, hydrogen price: 2.5 $/kg, electricity price: 0.054 $/kWh.

9.4.3. Effect of electricity price

To assess the electricity price effect on ammonia production cost, we analyzed a wide range of electricity prices (see Figure 9.8). When electricity prices increase from 0.03$/kWh to 0.2$/kWh, ammonia production costs increase from approximately 750 $/ton to 860 $/ton. However, with ongoing advancements in renewable energy technologies, we anticipate that electricity costs will decrease further, potentially lowering ammonia production costs in the future (refer to Figure 9.8). In our calculations, we assumed an electricity-to-MW conversion efficiency of 50%.

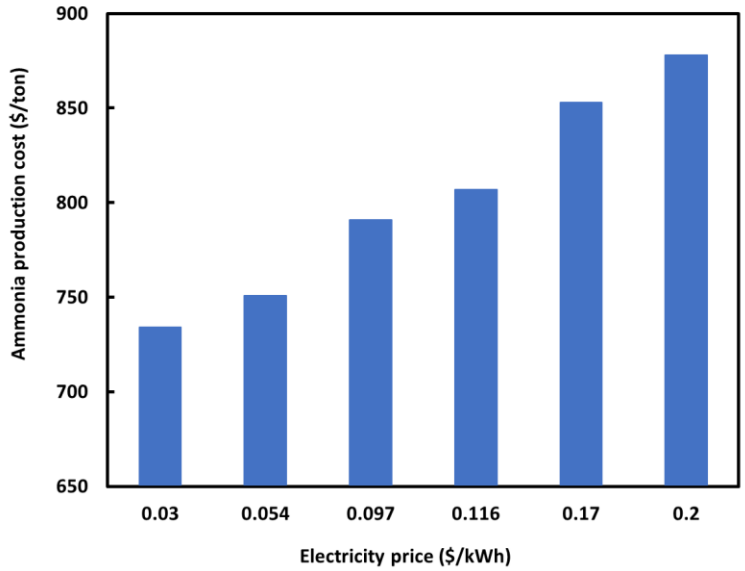

Figure 9.8: Effect of electricity price on ammonia production cost, hydrogen price: 2.5 $/kg, nitrogen price: 0.05 $/kg.

The efficiency of converting electricity into MW energy varies depending on the type of generator used. Magnetron-based systems typically achieve electricity-to-MW efficiencies of up to 65%, whereas solid-state MW generators reach up to 60%. In our techno-economic assessment, we assumed a conservative electricity-to-MW conversion efficiency of 50%, acknowledging that this value may improve with ongoing advancements in MW heating technologies. Although solid-state MW generators generally exhibit lower conversion efficiency, they offer superior control over frequency and power output, making them suitable for precision applications. Moreover, solid-state systems demonstrate significantly longer operational lifespans, with lifetimes reaching up to 100,000 hours, compared to a typical maximum of 10,000 hours for magnetron-based systems (see Table 9.5).

Table 9.5: Comparison between magnetron and solid-state MW generators.

Parameter	Magnetron	Solid-State MW Generator
Electricity-to-MW efficiency	50–70%	30–60%
Power Range	Up to ~100 kW (for a single unit)	Up to ~30 kW (for a single unit); scalable by modular installation up to 400 kW
Frequency Stability	Poor	Excellent
Lifetime, hours	2,000–10,000	20,000–100,000
Maintenance	Non-repairable; should be replaced after damage	Commonly, components are replaceable
Price (CAPEX)	Low	High (~2–4× magnetron for same power)
Operating Cost (OPEX)	Higher	Lower
Scalability	Limited due to the maximum available power	Excellent (modular systems can be combined)

In terms of OPEX, hydrogen costs represent the largest portion, accounting for approximately 70% of total OPEX. This is followed by electricity costs, which make up 11%. In this calculation, labor and land costs are excluded due to their variability across different operating regions.

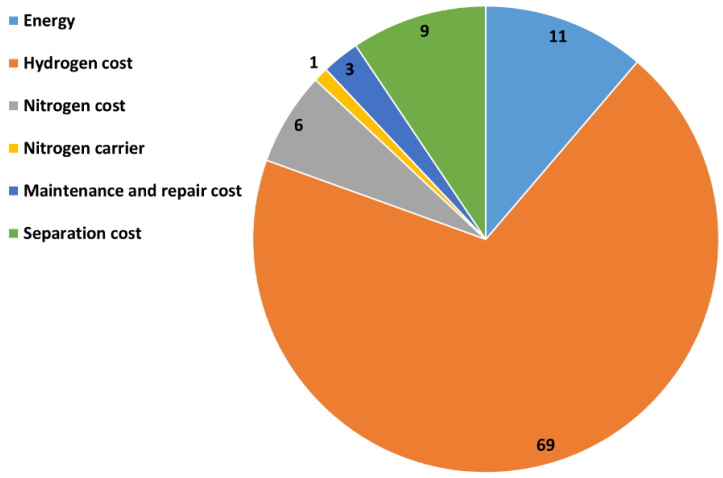

Figure 9.9: OPEX costs distribution, hydrogen price: 2.5 $/kg, nitrogen price: 0.05 $/kg, electricity price: 0.054 $/kWh.

9.5. Conclusion

In this chapter, we presented a general techno-economic analysis and reactor design to provide an overview of the MHCLAS technology scale-up. The results indicated an ammonia production cost of approximately 700 $/ton, with the potential to decrease to 400 $/ton. However, more detailed reactor design and techno-economic studies are necessary to support the further industrialization of MHCLAS technology.

References

[1] R.B. Harikrishna, H. Deka, T. Sundararajan, G.R. Rao, Green hydrogen production by water splitting using scrap metals at high temperature, Int J Hydrogen Energy (2023). https://doi.org/10.1016/j.ijhydene.2023.08.366.

[2] M. Khodabandehloo, J. Shabanian, J.P. Harvey, J. Chaouki, Microwave heating-assisted chemical looping dry reforming of methane, Int J Hydrogen Energy 71 (2024) 1380–1391. https://doi.org/10.1016/j.ijhydene.2024.05.295.

[3] M. Khodabandehloo, J. Shabanian, J.-P. Harvey, J. Chaouki, Kinetic study of microwave heating-assisted chemical looping dry reforming of methane over magnetite, Int J Hydrogen Energy 96 (2024) 1079–1086. https://doi.org/10.1016/j.ijhydene.2024.11.358.

[4] F. Vatankhah, A. Carrillo García, J. Chaouki, Hydrogen and carbon nanotube production from microwave-assisted catalytic decomposition of plastic waste, Chemical Engineering Journal 503 (2025). https://doi.org/10.1016/j.cej.2024.158189.

[5] A. Amini, M. Latifi, J. Chaouki, Electrification of materials processing via microwave irradiation: A review of mechanism and applications, Appl Therm Eng 193 (2021). https://doi.org/10.1016/j.applthermaleng.2021.117003.

[6] G. Towler, R. Sinnott, Chemical Engineering Design: Principles, Practice and Economics of Plant and Process Design, 2021. https://doi.org/10.1016/B978-0-12-821179-3.01001-3.

[7] J. Zhao, D. Wang, L. Zhang, M. He, W. Ma, S. Zhao, Microwave-enhanced hydrogen production: a review, RSC Adv 13 (2023). https://doi.org/10.1039/d3ra01898a.

[8] J.J. Lamb, M. Hillestad, E. Rytter, R. Bock, A.S.R. Nordgård, K.M. Lien, O.S. Burheim, B.G. Pollet, Traditional Routes for Hydrogen Production and Carbon Conversion, in: Hydrogen, Biomass and Bioenergy, 2020. https://doi.org/10.1016/b978-0-08-102629-8.00003-7.

[9] H.F. Abbas, W.M.A. Wan Daud, Hydrogen production by methane decomposition: A review, Int J Hydrogen Energy 35 (2010). https://doi.org/10.1016/j.ijhydene.2009.11.036.

[10] A.I. Osman, N. Mehta, A.M. Elgarahy, M. Hefny, A. Al-Hinai, A.H. Al-Muhtaseb, D.W. Rooney, Hydrogen production, storage, utilisation and environmental impacts: a review, Environ Chem Lett 20 (2022). https://doi.org/10.1007/s10311-021-01322-8.

[11] J. Incer-Valverde, A. Korayem, G. Tsatsaronis, T. Morosuk, “Colors” of hydrogen: Definitions and carbon intensity, Energy Convers Manag 291 (2023). https://doi.org/10.1016/j.enconman.2023.117294.

[12] J.M.M. Arcos, D.M.F. Santos, The Hydrogen Color Spectrum: Techno-Economic Analysis of the Available Technologies for Hydrogen Production, Gases 3 (2023). https://doi.org/10.3390/gases3010002.

[13] R. Yukesh Kannah, S. Kavitha, Preethi, O. Parthiba Karthikeyan, G. Kumar, N.V. Dai-Viet, J. Rajesh Banu, Techno-economic assessment of various hydrogen production methods – A review, Bioresour Technol 319 (2021). https://doi.org/10.1016/j.biortech.2020.124175.

CHAPTER 10: GENERAL DISCUSSION

In this study, we successfully developed the MHCLAS technology, which separates the N_2 and H_2 dissociation reactions into two independent stages named nitridation and hydrogenation. To provide the energy required for these reactions, we utilized MW heating. MW heating offers selective, rapid, and volumetric energy transfer, enabling direct interaction with solid phases while the gas phase remains transparent. This unique characteristic creates a temperature gradient between the gas and solid phases, reducing the gas-phase temperature and thereby minimizing the risk of secondary reactions, such as ammonia decomposition.

We employed COMSOL Multiphysics to model and simulate the interaction of MWs with various systems, including a single MW-absorbing particle, monoliths, and fixed beds containing solid MW-absorbing particles. Our study explored the influence of key variables—such as U_g, reaction heat, and the placement of temperature measurement probes at the microscale—on the temperature differential between gas and solid phases. To ensure the accuracy and reliability of our model, we first verified and validated it using data from the literature as well as our own laboratory measurements. In addition, we estimated the solid surface temperature and temperature at specific distances from the surface by implementing a virtual thermocouple.

The simulation involved exposing a single particle to a gas stream with different U_g ranging from 0 to 3 m/s. The results indicated that increasing U_g led to a rise in the temperature difference between the gas and solid phases. However, the rate of change in this temperature difference decreased when U_g was increased beyond 1 m/s. At an operational temperature of approximately 470°C, the maximum observed temperature difference was 276°C.

We also examined this temperature difference under various reaction conditions, including non-reactive, endothermic, and exothermic scenarios. The results revealed a decreasing trend in the temperature difference as the reaction type shifted from endothermic to non-reactive and finally to exothermic. In addition, we evaluated the impact of a virtual thermometer probe on the estimated gas-solid temperature difference. It was found that this variable significantly influenced the measurement outcomes. For instance, increasing the probe distance from the particle's surface from 50 µm to 1000 µm resulted in a temperature difference increase from 36 °C to 261 °C. These

findings showed the potential inaccuracies of bulk temperature measurement techniques and highlighted the importance of precise measurement methods in MW-heated systems.

We investigated the distribution of EM field in fixed-bed reactors at laboratory scale. The findings revealed a high probability of hotspot formation in fixed-bed reactors, making small reactor sizes (with an inner diameter <3 cm) preferable for kinetic studies. In addition, to mitigate the effects of hotspots during MW irradiation, we recommended the use of fluidized bed reactors.

We examined the impact of bed voidage on the penetration depth of MWs in fixed-bed reactors, a critical factor for scaling MW reactor designs for industrial applications. For SiC particles, an increase in bed voidage from 0.2 to 0.9 resulted in a significant enhancement of MW penetration depth, expanding from approximately 5 cm to 55 cm. This observation underscores the importance of the bed voidage and reactor diameter for efficient MW energy distribution in both fixed and fluidized bed systems.

After confirming the effectiveness of MW heating for various reaction types, including endothermic and exothermic reactions, we conducted a systematic study to identify suitable NCs for MHCLAS. This process involved analyzing information from literature, conducting thermodynamic studies, and evaluating key factors such as availability, toxicity, and melting point. An ideal NC should form nitride phases under a nitrogen stream and allow these nitrides to react with a hydrogen stream to produce ammonia and nitrogen-depleted NCs.

Based on these criteria, we selected Mn, Fe, and Ba as the core elements for our NCs and explored different synthesis strategies. We developed three NCs: Mn-Fe: mechanical, Mn-Fe: coprecipitation, and Mn-Fe-BaH_2: coprecipitation. The proposed NCs demonstrated effective interactions with MWs during all stages of MHCLAS, including the nitridation and hydrogenation phases.

Among the synthesized NCs, those produced via the coprecipitation method exhibited superior MW interactions compared to the mechanical approach. This improvement is attributed to the presence of small amounts of residual oxide phases formed during the activation stage. In addition, Mn-Fe: coprecipitation outperformed Mn-Fe-BaH_2: coprecipitation due to the weaker MW interaction of BaH_2. While BaH_2 showed a higher activity for ammonia synthesis by employing CLAS technology, its limited MW responsiveness reduced the overall interaction efficiency in Mn-

Fe-BaH_2 compared to Mn-Fe. However, the incorporation of Mn and Fe into the NC structure helped partially offset the weak MW interaction of BaH_2.

We conducted nitridation reactions at temperatures ranging from 350 °C to 700 °C over three synthesized NCs. The formation of nitride phases in the NCs was confirmed through SEM-EDS, XRD, and TGA analyses. For NCs produced by the coprecipitation method, nitrogen distribution was more uniform compared to those synthesized through the mechanical approach, indicating effective interaction among the elements within the NC structure.

While Fe does not form nitride phases as a single metallic element under atmospheric pressure, combining it with elements that establish strong nitrogen bonds facilitated the formation of iron nitrides. Mass gain measurements during the nitridation process revealed up to a 10 wt% increase under a nitrogen stream. Furthermore, the application of MW heating enhanced NC weight gain in the nitridation stage compared to conventional heating methods, attributable to the elevated solid-phase temperatures achieved through MW heating.

We performed the hydrogenation stage by introducing a H_2 stream over the nitrided NCs, with the resulting ammonia absorbed by applying two/three sequential gas washers. The reaction of ammonia with deionized water produced ammonium hydroxide, and its concentration was monitored by employing a calibrated ion-selective electrode (ISE) that measures ammonia solely.

The results demonstrated that MW heating significantly enhanced the ammonia production rate compared to conventional heating. This improvement is attributed to the lower gas-phase temperatures in MW-heated systems, in contrast to conventionally heated reactors where the gas and solid phases commonly are maintained at equal temperatures.

Among the synthesized NCs, Mn-Fe-BaH_2 exhibited superior performance. This was attributed to the presence of BaH_2 and Fe, which facilitate the hydrogenation process by modifying the NC-N bond and decreasing its strength. The hydrogenation reaction was studied across a temperature range of 150 °C to 350 °C, with results indicating a consistent increase in ammonia production rates as the temperature increased.

After establishing the proof of concept and identifying the most suitable NC for MHCLAS, we conducted a comprehensive intrinsic kinetic study for both the nitridation and hydrogenation stages. The developed kinetic models were designed to be independent of external and internal

mass transfer limitations, making them highly applicable for subsequent stages of technology development such as reactor modeling and design.

Our studies revealed that activation energies estimated by applying bulk temperatures were lower than those calculated based on solid-phase temperatures. This discrepancy suggests that previous studies in the literature may have underestimated temperatures, often attributing the differences to the non-thermal effects of MW heating. However, in gas-solid reactions under MW irradiation, neither activation energy nor pre-exponential factors should change when compared to those obtained under the conventional heating approach. However, the selective heating nature of MWs can, under certain conditions, lead to variations in reaction mechanisms. These findings emphasize the critical need for precise temperature measurement in MW-heated systems to ensure accurate and reliable kinetic analyses.

To ensure the accuracy of the developed models, we studied temperature distribution in the MHFB to achieve isothermal conditions suitable for kinetic studies. In addition, a stability analysis was conducted to identify the optimal temperatures for the nitridation and hydrogenation reactions to maintain the ammonia production rate nearly constant across multiple cycles.

In this study, the intrinsic activation energy for the nitridation reaction was determined to be 27.3 kJ/mol, while the hydrogenation reaction exhibited an activation energy of 25.5 kJ/mol in the MHCLAS process, based on solid-phase temperature measurements. The nitridation reaction was best described by the contracting sphere or shrinking core model, whereas the hydrogenation stage was most accurately represented by the Avrami-Erofeev models. These findings provide a solid foundation for further MHCLAS technology development and reactor design.

In the next phase, we applied the developed reaction kinetic models to model and simulate lab and pilot-scale MHCLAS reactors for both nitridation and hydrogenation stages. By employing COMSOL Multiphysics, we integrated Maxwell's equations with mass balance, heat balance, hydrodynamics, and reaction kinetics. We proposed a design in which these two stages could be conducted within a single reactor by alternating the inlet gas, while applying N_2 for nitridation and H_2 for hydrogenation. First, we validated the lab-scale model by comparing its results with experimentally obtained bulk and solid temperatures, as well as the extents of nitridation and hydrogenation reactions. The strong agreement between the model predictions and experimental data confirmed the model’s accuracy and reliability.

Next, we applied the validated model to simulate pilot-scale MHFB reactors—an approach that, to the best of our knowledge, remains rare in MHFB system simulations and not only for MHCLAS technology. Our analysis of EM field distribution, temperature dissipation, and bulk temperature uniformity revealed that, due to the selective nature of MW heating, regions with higher gas concentrations exhibited lower bulk temperatures. This phenomenon was attributed to the MW transparency of the gas phase. In addition, the EM field distribution within the fluidized bed demonstrated that implementing fluidization effectively mitigates MW penetration depth limitations and the exponential attenuation of MWs in MW-heated reactors. Moreover, we investigated the impact of bulk temperature, solid inventory, and superficial gas velocity on gas and solid-phase reaction conversions. These findings offer valuable insights for optimizing key operating parameters to enhance MHCLAS performance—specifically, maximizing ammonia production rates while minimizing energy and material consumption.

In the final stage of this thesis, we conducted a general techno-economic analysis and proposed an industrial-scale ammonia production plant utilizing MHCLAS technology. Our findings suggest that implementing two MW waveguides could effectively overcome the challenge of limited MW penetration depth. In addition, our analysis estimates that the ammonia production cost can be reduced to as low as $400 per ton. Further reactor design studies are required to facilitate the industrialization of MHCLAS. However, the results of this study show a promising pathway for its implementation.

CHAPTER 11 CONCLUSION AND RECOMMENDATIONS

11.1. Conclusion

We conducted a comprehensive study to advance the development of MHCLAS technology. The project began with identifying a key research gap in the transition to renewable energy storage, such as the need for mild-condition ammonia synthesis. MHCLAS addresses this challenge by decoupling nitrogen and hydrogen activation, thereby overcoming the competitive molecular activation issues between N_2 and H_2 inherent in conventional catalytic ammonia synthesis approaches. In addition, by utilizing selective MW heating, we supplied heat to the solid phase while maintaining a lower temperature in the gas phase. This approach not only enhances reaction control but also supports process electrification, contributing to the decarbonization of the chemical industry. Beyond its environmental advantages, MW heating has the potential to reduce energy consumption while improving reaction rates and selectivity.

As part of this thesis, we developed and simulated models to assess the microscale temperature gradients between gas and solid phases, which are critical in suppressing secondary gas-phase reactions such as ammonia decomposition.

Following this, we systematically evaluated potential NC elements, ultimately synthesizing the most promising candidates by applying mechanical and coprecipitation approaches. We tested the activation of Mn-Fe and Mn-Fe-BaH_2 NCs under both nitridation and hydrogenation conditions. The results demonstrated that Mn-Fe-BaH_2 exhibited superior activity compared to Mn-Fe NCs synthesized through either approach. Moreover, the developed NCs not only showed strong reactivity during both reaction stages but also effectively interacted with MWs, enhancing their overall performance.

After successfully proving the concept, we conducted an in-depth kinetic study to estimate intrinsic kinetic parameters for both nitridation and hydrogenation stages. These kinetic models were subsequently implemented for lab- and pilot-scale MHCLAS reactor modeling and simulation.

Through a comprehensive approach encompassing proof of concept, kinetic analysis, and reactor modeling, our findings demonstrate that MHCLAS is a promising solution for the decarbonization and decentralization of ammonia production. This technology holds great potential not only for renewable energy storage but also for competing with the industrial HB process at large production scales for other application.

11.2. Recommendations for future studies

11.2.1. NCs screening by applying DFT tools

To enhance the ammonia production rate in MHCLAS technology, exploring a diverse range of elements and their combinations is a practical approach. The use of DFT tools can play a crucial role in analyzing the interactions of various elements/metals during the nitridation and hydrogenation stages. In this study, we implemented an initial selection strategy for NCs based on factors such as the thermodynamic favorability of nitridation and hydrogenation reactions, melting points, toxicity, and cost. Complementing this approach with DFT analysis offers deeper insights into the interactions between different metals [1]. In addition, conducting an aging test can be an effective approach to investigate the behavior of Mn–Fe solid solutions during the nitridation and hydrogenation stages. The formation of such solutions alters the redox characteristics of the nitrogen carriers throughout both steps. Mn and Fe exhibit mutual solubility across a wide temperature range, and their interaction may enhance the performance of ammonia synthesis. However, studying their behavior under more severe operating conditions and extended durations can yield valuable insights into long-term stability and potential degradation mechanisms.

This study revealed that the presence of oxides can enhance the MW heating efficiency of the NCs. However, these oxides may also exhibit catalytic properties, which should be explored in future studies.

11.2.2. Reactor design for MHCLAS

MW heated reactors face several challenges, including limited MW penetration depth, constraints on reactor size, spark formation, and difficulties in accurate temperature measurement. However, these limitations can be addressed by implementing optimally designed reactors, paving the way for the industrial adoption of MW heating not only for MHCLAS but also for a wide variety of chemical reactions.

To mitigate the issue of limited MW penetration depth, a multi-waveguide strategy offers a promising solution. Simulation tools like COMSOL Multiphysics can help in designing reactors that minimize the risk of standing wave formation and ensure more uniform temperature distribution.

Spark formation poses another significant challenge in MW-heated reactors. Sparks can arise from the presence of solid particles or metallic components, such as thermocouples, reactor connections, or reactor walls. These sparks generate extremely high temperatures (exceeding 1200 °C in some cases), which can damage catalysts/reactive solids and decrease their reactivity. Conducting dedicated studies to design reactors with minimal risk of spark formation is essential for improving reactor performance and safety.

Despite extensive efforts to develop temperature measurement techniques under MW irradiation, there remains a lack of reliable, safe, stable, and non-intrusive methods for accurately measuring temperatures in bulk, gas, and solid phases. This challenge is further intensified in larger reactors, making the development of advanced temperature measurement solutions a critical area of research.

11.2.3. Plasma-MW-assisted CLAS

Plasma implementation in the hydrogenation stage can elevate the risk of ammonia decomposition after its formation due to direct ionization of the gas phase in plasma-assisted reactors. However, the nitridation stage is well-suited for plasma application, as it requires nitrogen molecule dissociation.

To safeguard the produced ammonia during the hydrogenation stage, maintaining a lower gas-phase temperature is essential, and MW heating provides an effective solution for this purpose. Therefore, designing reactors capable of utilizing plasma for nitridation and MW heating for hydrogenation is crucial for optimizing the performance and advancing this technology.

REFERENCES

[1] C. Elkadiri, I. Bouziani, H. A. Ousaleh, M. Naji, J. Chaouki, G. Abbas, A. Faik, A computational study of Fe3CuN and Fe3ZnN antiperovskite nitrides for chemical looping ammonia synthesis, International Journal of Hydrogen Energy, Volume 111, 2025, Pages 623-634, https://doi.org/10.1016/j.ijhydene.2025.02.364.

APPENDIX 1: ATTRITION TEST

To assess the NC's resistance to attrition in a fluidized bed reactor, we utilized a jet fluidized bed to measure the erosion rate of particles. The inlet gas flow was maintained at 5 L/min for 1 hour, and bed attrition was quantified based on the mass of particles collected at the fluidized bed exit.

$$A_h = \frac{\dot{m}_{fins}}{m_0} \quad (1)$$

Where $\dot{m}_{fins}$ is the mass rate of collected particles and m_0 it the initial NC weight which is 40 g.

We conducted the test three times, and the results indicated a solid attrition rate of approximately 0.08%/h. Under these conditions, applying a jet with an orifice velocity of around 260 m/s (orifice diameter=d_o=0.63 mm), the attrition rate was significantly higher than that observed under standard operating conditions in the bed. However, when compared to the values reported by Lyngfelt et al. [1], our findings suggest that the NCs exhibit a lower attrition rate than those documented in the literature (i.e., 0.05–0.33%/h) for chemical looping combustion using Mn-based ore. Figure S1-1 shows the experimental setup that was applied for attrition measurement.

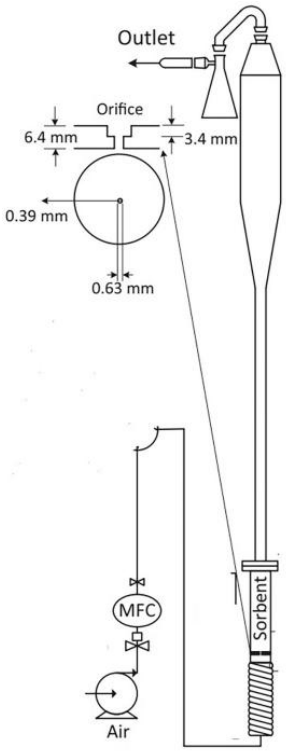

Figure S1-1: Experimental setup for NCs attrition measurement in this study [2]**.**

References

[1] A. Lyngfelt, P. Moldenhauer, M. Biermann, K. Johannsen, D. Wimmer, M. Hanning, Operational experiences of chemical-looping combustion with 18 manganese ores in a 300W unit, International Journal of Greenhouse Gas Control 127 (2023). https://doi.org/10.1016/j.ijggc.2023.103937.

[2] P. Asiedu-Boateng, N.Y. Asiedu, V. Zivkovic, G.S. Patience, Attrition characteristics of limestone in gas-solid fluidized beds, Powder Technol 419 (2023). https://doi.org/10.1016/j.powtec.2023.118342.

APPENDIX 2: THERMODYNAMIC CALCULATIONS

A2.1. Thermodynamics of conventional catalytic ammonia synthesis

We performed thermodynamic calculations by applying FactSage 8.3 to analyze the behavior of conventional catalytic ammonia synthesis, such as the Haber-Bosch (HB) process. Our study focused on a nitrogen-to-hydrogen molar ratio of 1:3, evaluating the impact of temperature (25–1000 C) and pressure (1–750 bar) on the equilibrium composition of ammonia.

As illustrated in Figure S2.1, since ammonia synthesis is an exothermic reaction, higher temperatures thermodynamically hinder ammonia formation. However, increasing the operating pressure can suppress the adverse effect of elevated temperatures on ammonia decomposition.

Due to the high stability of nitrogen molecules compared to hydrogen, ammonia synthesis by HB process requires catalysts, e.g., iron-based catalysts, to proceed effectively at temperatures above 400°C. Ammonia becomes thermodynamically unstable at these temperatures and tends to decompose (see Figure S2.1). This is why the HB process operates under harsh conditions (400–600°C, 100–300 bar) to overcome thermodynamic and kinetic limitations.

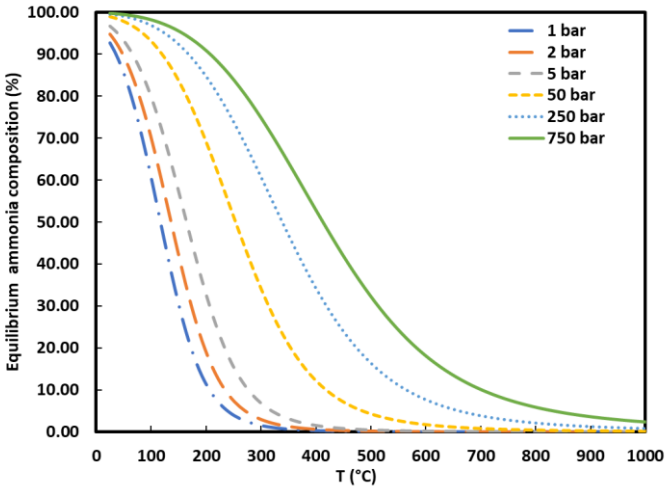

Figure S2.1: Thermodynamic calculations of catalytic ammonia synthesis at different temperatures and pressures performed by FactSage 8.3.

A2.2. Thermodynamics of nitridation stage

As shown in Figure S2.2, Mn and BaH_2 react to form nitrides, with the specific nitride phase depending on temperature and the N_2/NC mass ratio. For instance, increasing the temperature sequentially transforms Mn nitrides from Mn_6N_4 to Mn_3N_2, then to Mn_2N, and finally to Mn_4N

(see Figure S2.2a). In addition, a lower N_2/NC mass ratio can promote the formation of Mn_3N_2 and Mn_4N at lower temperatures (Figure S2.2b).

Nitridation of BaH_2 to Ba_3N_2 begins at 250°C and is fully completed around 550°C. However, alkali hydride imides were not included in the FactSage database. During the nitridation process, BaH_2 initially forms BaNH or $Ba(NH_2)_2$, and with increasing temperature, Ba_3N_2 can subsequently be produced.

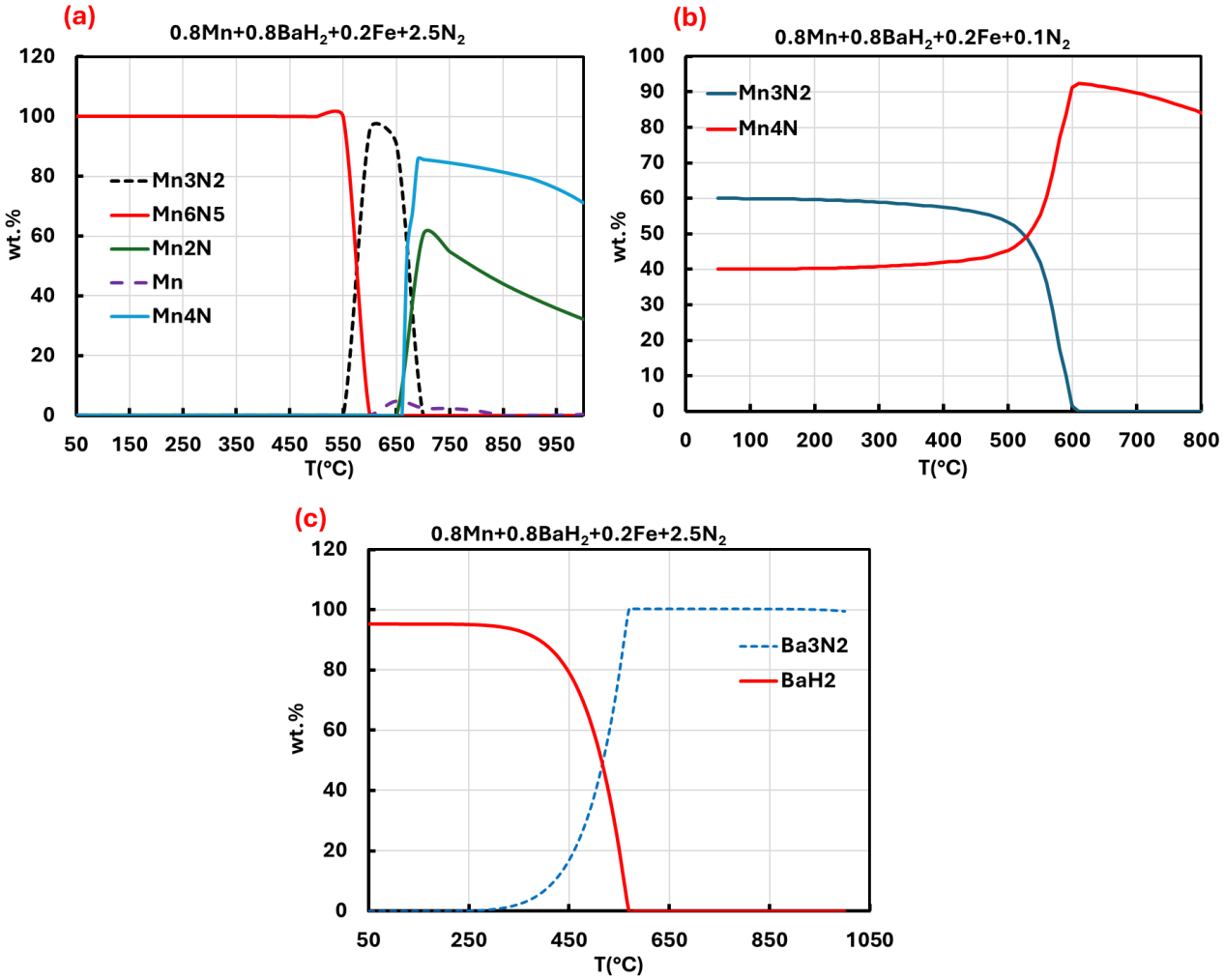

Figure S2.2: Thermodynamic calculations of nitridation reaction based on Mn-Fe-Ba-based NC (a) Mn, (b) BaH_2.

A.2.3. Thermodynamics of hydrogenation stage

Following the nitridation stage, we identified the formed nitrided compounds and exposed them to a hydrogen stream. The results indicated that ammonia remained stable below 200°C but

gradually decomposed as the temperature increased, reaching complete decomposition at 700°C (see Figure S2.3a). However, in the HB process, at atmospheric pressure, ammonia decomposes completely at 350°C (Figure S2.3b). MHCLAS, benefiting from the separation of nitridation and hydrogenation stages along with the implementation of selective MW heating, can be conducted at a bulk temperature of 300 °C, while the gas-phase temperature for the hydrogenation stage can be as low as 250 °C. In contrast, the HB process operates at temperatures ranging from 400 to 600 °C.

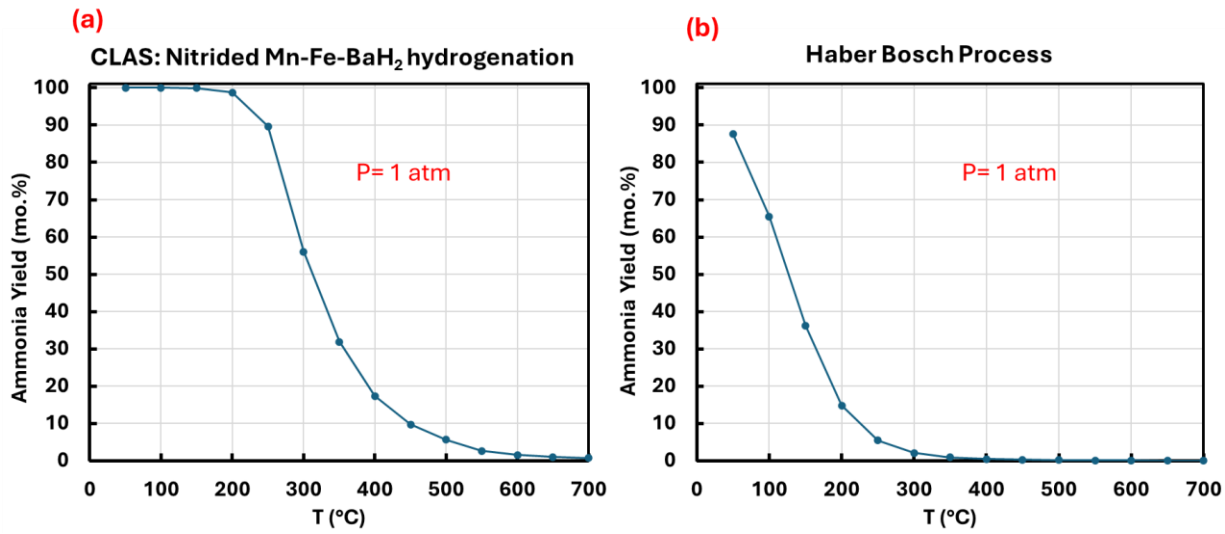

Figure S2.3: Thermodynamic calculations of ammonia yield for (a) CLAS, (b) HB process at atmospheric pressure.

In addition, thermodynamic analysis of the solid phase during the hydrogenation stage revealed that full conversion of nitrided compounds requires temperatures between 400–550°C (see Figure S2.4). However, optimizing the temperature is crucial to achieving a balance between ammonia formation and solid-phase conversion. This is why we conducted the hydrogenation stage at bulk temperatures up to 350°C. Moreover, in MHCLAS, the gas-phase temperature is lower than the bulk temperature, which helps prevent ammonia decomposition, while the solid-phase temperature is higher, enhancing the thermodynamics of nitride conversion to ammonia.

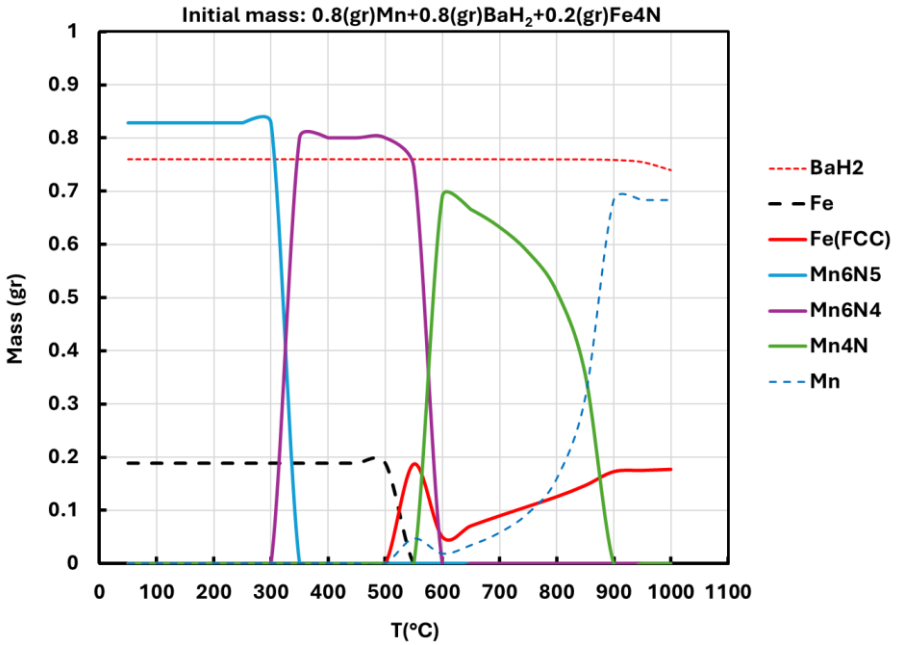

Figure S2.4: Thermodynamic of solid phase during the hydrogenation stage.

APPENDIX 3: NITROGEN CARRIER SELECTION STRATEGY

We systematically selected potential elements for NC selection by identifying those capable of forming a nitride solid phase (highlighted in blue and green). In addition, we excluded rare, toxic, radioactive elements, as well as those with low melting points (i.e., lower than 400°C). As a result, we finalized a selection of 10 elements: Mg, Ca, Ti, Zr, Cr, Mo, Mn, Fe, Zn, and Al (see Figure S3.1). We determined the potential for nitride formation in various elements through thermodynamic calculations.

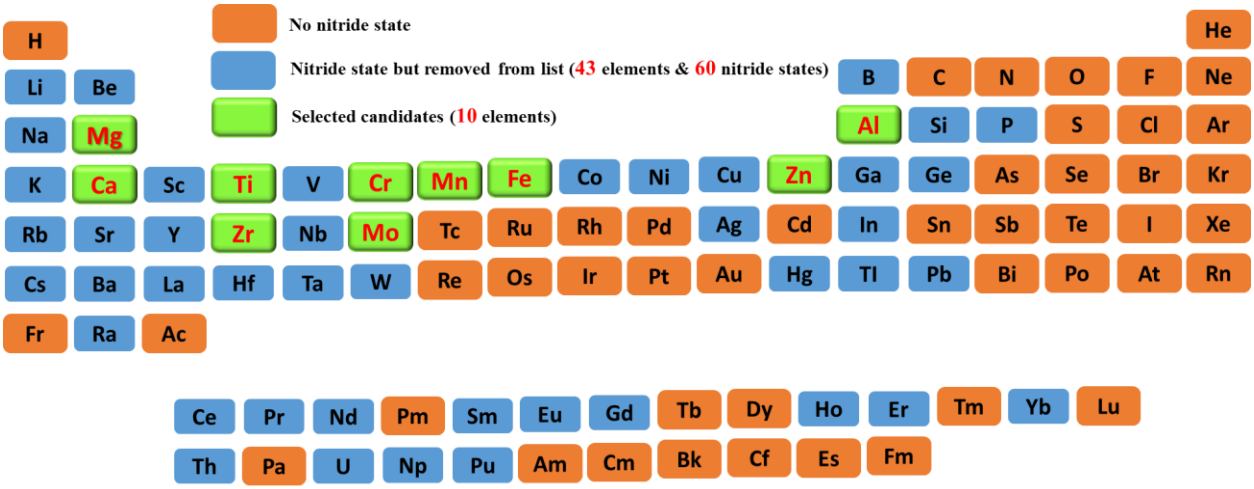

Figure S3.1: Potential NC elements identification.

When the Gibbs free energy variation of the transient metals (TMs) nitride is more negative, the resulting nitride compounds are more stable. In this context, elements with Gibbs free energy variation values closer to zero ($\Delta G \approx 0$) are more favorable, as their nitrides are less stable and can be more easily reduced during the hydrogenation stage for ammonia formation. Based on this criterion, Fe, Mn, and Cr emerge as promising candidates (see Figure S3.2). For more information, please refer to Chapter 6, Article 3. We applied a similar strategy for the hydrogenation stage, where elements with Gibbs free energy variations close to $\Delta G = 0$ are more favorable candidates (see Figure S3.3).

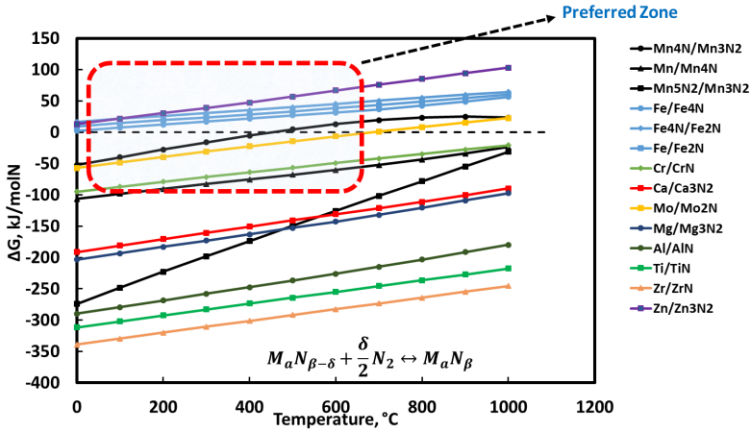

Figure S3.2: Gibbs free energy variation of different TMs in the nitridation stage (P=1 atm).

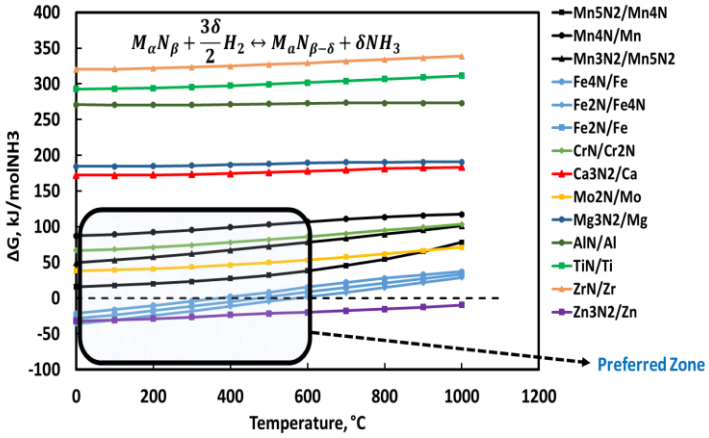

Figure S3.3: Gibbs free energy variation of different elements in the hydrogenation stage (P=1 atm).

APPENDIX 4: SUPPLEMENTARY MATERIALS OF ARTICLE 3

Microwave heating-assisted chemical looping ammonia synthesis over Mn-Fe and Mn-Fe-BaH_2 nitrogen carriers

Kazem Adavi [a], Zhaohui Chen [b], Adrian Carrillo Garcia [a], Jaber Shabanian [a], and Jamal Chaouki [a,c,*]

[a] Process Engineering Advanced Research Lab (PEARL), Department of Chemical Engineering, Polytechnique Montreal, P. O. Box 6079, Station Centre-Ville, Montreal, (Quebec) Canada, H3C 3A7

[b] State Key Laboratory of Mesoscience and Engineering, Institute of Process Engineering Chinese Academy of Sciences, Beijing 100190, China

[c] University Mohamed VI Polytechnique, Benguerir, Morocco

**Corresponding author: Tel. +1 (514) 340-4711 X 4034, fax: +1 (514) 340-4159, E-mail:* jamal.chaouki@polymtl.ca

1. Nitrogen carrier's optimization

In our preliminary studies (refer to Section 6.2.4 for the experimental procedure), we optimized compositions of adopted nitrogen carriers (NCs) based on their ammonia production rates and ability to be heated under microwave (MW) irradiations (see Figure S4.1 below).

For Mn-Fe mechanical NCs, we investigated the effect of iron (Fe) wt.% relative to manganese (Mn) wt.%. Results indicated that increasing the Fe content initially enhances the ammonia production rate, but it declines beyond a certain threshold. The highest ammonia production rate was at a Mn: Fe mass ratio of 4: 1.

We observed a similar trend for Mn-Fe NCs synthesized via coprecipitation. However, due to more uniform interactions between the elements (i.e., Mn, Fe) in this approach, we recorded a higher ammonia production rate with this NC compared to what was synthesized through the mechanical approach. For the Mn-Fe NCs synthesized via coprecipitation, we achieved the maximum rate of ammonia production at a manganese nitrate ($(Mn(NO_3)_24.H_2O$) to iron nitrate ($Fe(NO_3)_39.H_2O$) mass ratio of 1: 1.5.

For Mn-Fe-BaH_2 NCs, we examined the effect of the barium fluoride (BaF_2): ($Mn(NO_3)_2 \cdot 4H_2O$) solution mass ratio was examined. Increasing this ratio initially led to an increase in the ammonia production rate, followed by a decline. The maximum ammonia production rate was at a BaF_2:

$Mn(NO_3)_2 \cdot 4H_2O$ mass ratio of 1: 4. The presence of Fe in the Mn-Fe-BaH_2 NCs with a BaF_2: $Fe(NO_3)_3 9.H_2O$ mass ratio of 1: 1 enhanced MW heating capability of the synthesized NCs, enabling them to reach the required temperatures in this work.

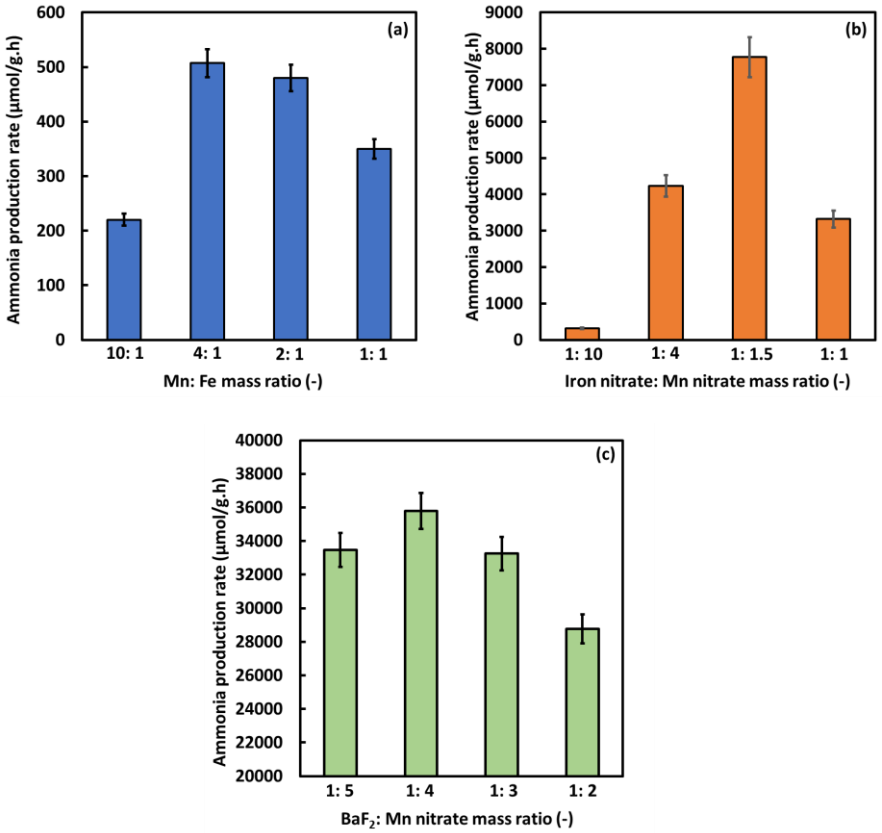

Figure S4.1: Optimization of NC compositions during the synthesis process: (a) Mn-Fe: mechanical, (b) Mn-Fe: coprecipitation, and (c) Mn-Fe-BaH_2: coprecipitation.

APPENDIX 5: SUPPLEMENTARY MATERIALS OF ARTICLE 4

Kinetic study of microwave heating-assisted chemical looping ammonia synthesis over Mn-Fe-Ba-based nitrogen carrier

Kazem Adavi [a], Adrian Carrillo Garcia [a], Jaber Shabanian [a], Mohammad Latifi [a], and Jamal Chaouki [a, b,*]

[a] Process Engineering Advanced Research Lab (PEARL), Department of Chemical Engineering, Polytechnique Montreal, P. O. Box 6079, Station Centre-Ville, Montreal, (Quebec) Canada, H3C 3A7.

[b] University Mohamed VI Polytechnique, Benguerir, Morocco.

[*] Corresponding author: Tel. +1 (514) 340-4711 X 4034, fax: +1 (514) 340-4159, E-mail: jamal.chaouki@polymtl.ca

S-1. Ion-selective electrode standard curve

The following figure presents the standard calibration curve obtained using the ion-selective electrode (ISE) employed in this study. A high-performance ammonia ISE (9512HPBNWP) was used, and calibration was cross-verified before each measurement to ensure analytical accuracy.

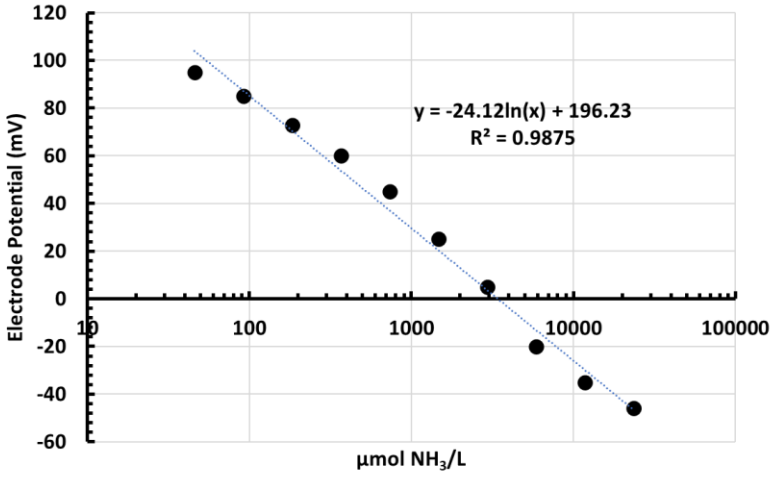

Figure S5-1: Standard curve of ISE applied for ammonia quantification in this study.

S-2. BET isotherms

Figure S5-2 presents the BET adsorption–desorption isotherms of the synthesized nitrogen carriers after one and 10 cycles at a bulk nitridation temperature of 630 °C. As shown in Figure S5-2a, the sample after one cycle exhibits a H4 hysteresis loop, indicative of mesoporosity. In contrast, Figure S5-2b displays a significantly reduced adsorption volume after ten cycles, corresponding to a surface area decrease from 1.6 m^2/g to 0.4 m^2/g, suggesting notable textural degradation.

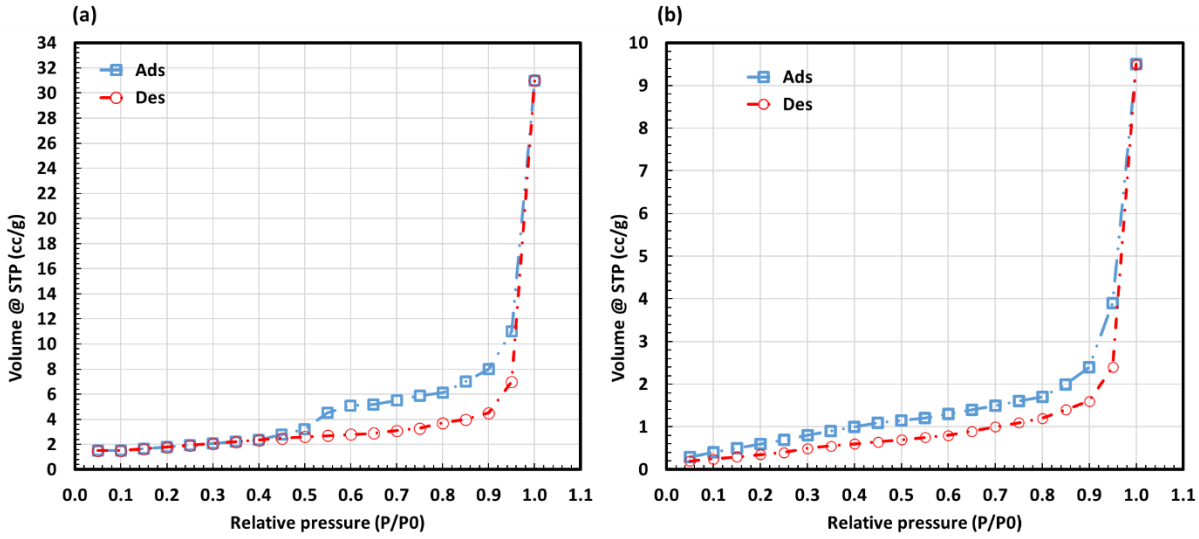

Figure S5-2: a) BET adsorption–desorption isotherms of the sample after one cycle at a nitridation bulk temperature of 630 °C; b) BET isotherms of the same sample after 10 cycles at a nitridation bulk temperature of 630 °C.

S-3. R^2 and RSS of different reaction models

Tables S5-1 and S5-2 present the R^2 and RSS values for various kinetic models applied to study the kinetics of the nitridation and hydrogenation stages.

Table S5-1: R^2 and RSS values for different kinetic models applied for the nitridation stage.

Mechanism	R^2	RSS
One-dimensional diffusion-D1	0.9820	0.0097
Two-dimensional diffusion-D2	0.9830	0.0091
Three-dimensional diffusion-D3	0.9744	0.0112
Mampel (first order)-R1	0.9561	0.0226
Second order- R2	0.9614	0.0106
Third order- R3	0.9656	0.0118
Contracting cylinder-C2	0.9781	0.0103
Contracting sphere-C3	0.9855	0.0080

Table S5-2: R^2 and RSS values for different kinetic models applied for the hydrogenation stage.

Mechanism	R^2	RSS
Avrami-Rrofeev-1	0.9270	0.0183
Avrami-Rrofeev-2	0.9760	0.0198
Avrami-Rrofeev-3	0.9863	0.0076

APPENDIX 6: ADDITIONAL EXPLANATIONS

Conventional heating

To compare MW heating with conventional heating systems, we used a stainless-steel reactor with walls heated by induction. Due to the skin effect, the magnetic field does not penetrate the reactor walls, and heat is transferred from the walls toward the interior of the bed, effectively simulating conventional heating conditions.

Alternative methods for mimicking conventional heating include placing resistive wires or heating elements inside the reactor. In such configurations, heat is transferred to the gas–solid system via conduction and convection. However, achieving uniform temperature distribution within the bed is more challenging in these setups.

In our comparisons, we maintained a constant bulk temperature for both MW and conventional heating systems. Under conventional heating, the gas and solid phases were assumed to be at thermal equilibrium, and temperature was measured by a thermocouple that was placed in the dense bed. In contrast, under MW heating, the solid-phase temperature, measured by a pyrometer, was higher than the bulk temperature due to selective heating of the solids.

The primary goal of MW heating in MHCLAS is to maintain a lower gas-phase temperature to suppress ammonia decomposition. Therefore, preheating of the inlet feedstock is not recommended. For future industrial-scale development, a detailed energy optimization strategy is necessary to minimize the overall energy consumption of the MHCLAS process.

Lamina flow assumption

Based on the following calculations, the Reynolds number for a single particle with a diameter of 500 μm exposed to a nitrogen gas stream at 500 °C and a superficial gas velocity of up to 3 m/s indicates a laminar flow regime. Since our operating conditions remain below this velocity, the laminar flow assumption is valid for the analysis presented in Article 2. Furthermore, comparisons with results obtained using Navier–Stokes and k-ε turbulence models at higher velocities show negligible deviations, confirming the robustness of this assumption.

$$Re_p = \frac{\rho U_g d_p}{\mu} = \frac{0.375 \times 3 \times 500 \times 10^{-6}}{4.1 \times 10^{-5}} = 13.7$$

Table S6-1: Different flow regimes for a single particle exposed to nitrogen flow.

$Re_p < 1$	Creeping flow
$1 < Re_p < 20$	Laminar flow
$20 < Re_p < 1000$	Transient flow
$Re_p > 1000$	Turbulent flow

Theoretical NCs' weight gain

The maximum weight gain of NCs depends on their composition and the specific nitride phases formed. For Mn, the formation of Mn_3N_2 results in a theoretical maximum weight gain of approximately 17 wt.%. In the case of iron, the formation of Fe4N corresponds to a weight gain of about 6.5 wt.%. For barium, the formation of BaNH yields a maximum weight gain of around 11 wt.%. These theoretical values were calculated based on the elemental composition of the components within the NCs.

Nitridation and hydrogenation reactions

Reactions during the nitridation stage:

$$4Mn + 0.5N_2 \rightarrow Mn_4N$$

$$4Mn_4N + N_2 \rightarrow 3Mn_3N_2$$

$$4Fe + 0.5N_2 \rightarrow Fe_4N$$

$$BaH_2 + 0.5N_2 \rightarrow BaNH$$

Reactions during the hydrogenation stage:

$$Mn_3N_2 + H_2 \rightarrow Mn_4N + NH_3$$

$$Mn_4N + H_2 \rightarrow Mn + NH_3$$

$$Fe_4N + H_2 \rightarrow Fe + NH_3$$

$$BaNH + H_2 \rightarrow BaH_2 + NH_3$$

Corrections

1. Fe_xO_y in Figure 6.6 refers to Fe_2O_3.
2. In Eq. (5.1) μ_r is relative permeability.
3. In Table 5.1, relative permittivity is unitless